Structural and photoelectrochemical properties of CdSe and CdS thin films

Furlong, Mark Justin

Award date:
1996

Awarding institution:
University of Bath

Structural and Photoelectrochemical Properties of CdSe and CdS Thin Films

submitted by Mark Justin Furlong

for the degree of PhD

of the University of Bath

1996

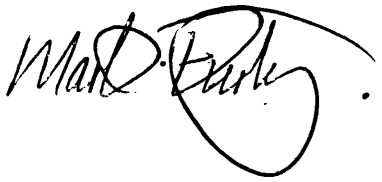

COPYRIGHT

ProQuest LLC
789 East Eisenhower Parkway
P.O. Box 1346
Ann Arbor, MI 48106-1346

Abstract

CdSe thin films have been electrodeposited onto conducting glass substrates from selenosulfite based solutions. Deposits were characterised by capacitance voltage, photocurrent, and electrolyte electroabsorption (EEA) techniques. Film composition, structure and morphology were assessed by wavelength dispersive x-ray analysis (WDX), x-ray diffraction (XRD), and atomic force microscopy (AFM), respectively. It is proposed that CdSe is deposited by a "under potential deposition (UPD)" like process to give 1:1 stoichiometries. Film properties were found to be insensitive to deposition potential. Monochromatic photocurrent conversion efficiencies of upto 30% suggests possible application of the films in photovoltaic devices.

CdS thin films grown by the chemical bath route were characterised by capacitance voltage and electrolyte electroreflectance methods following annealing under different conditions. Changes in film structure were determined by field enhanced scanning electron microscopy (FSEM) and high resolution transmission electron microscopy (HRTEM). Low values of the broadening parameter determined by EEA were correlated with the improved crystallinity of the $CdCl_2$ flux annealed layers. However, the presence of pinholes highlighted the unsuitability of $CdCl_2$ annealed films for use in CdS/CdTe based heterojunction solar cells. Annealing in air was identified as the most promising heat treatment for improving properties of CdS thin films.

Scanning microscopy for semiconductor characterisation (SMSC) and photoelectrochemical microscopy (PEM) were used to spatially map the photocurrent response of related to the grain structure of the underlying substrate. Image contrast mechanisms are discussed and related to images observed in microscopy. EEA measurements have demonstrated the highly defective nature of the anodised CdS layers.

The work in this thesis has established the relationships between the structure, morphology and composition of thin semiconductor films and their electrochemical and photoelectrochemical performance. This approach has provided an improved understanding of materials which have applications in thin film solar cells

Acknowledgements

I wish to express my sincere thanks to my supervisor, Professor Laurence Peter, for his supervision and constant encouragement over these last three years.

My thanks are also due to the many past and present members of the research group for being good companions in the lab and for providing a stimulating working environment. I would particularly like to mention Rob, Greg, Pete and Anthony with whom I spent much time whilst studying in Bath.

I would also like to thank Steve, Mark, Steven, and Simon for providing a pleasant time during my first year spent at the University of Southampton. I shall always remember the great times we had during the early days of our postgraduate study.

My thanks are also due to Professor Pedro Salvador and Dr Antonio Martinez Chapparo at the Instituto de Quimicafisica "Rocosolano" in Madrid for use of their scanning microscope for semiconductor characterisation (SMSC) and for the highly enjoyable time spend in Spain during the 42°C heat.

My thanks are extended to Professor David Williams and Dr Roger Hutton at University College, London for the opportunity to use their photoelectrochemical microscope (PEM).

My gratitude is extended to Mr Hugh Perrott of the electron optics centre for help in obtaining the SEM images and WDX data. Thanks are also due to Dr Pete Weglicki for assistance in operating the Atomic Force Microscope.

I would like to thank Dr Mike Bailes for developing the automated electrolyte electroreflectance (EER) setup.

Finally, but most importantly I would like to thank Jenny for all her love and support

The Universities of Southampton and Bath are acknowledged for financial support.

To my
parents

Contents

Chapter 1

Introduction

1.1 Introduction

Electricity is a highly refined form of energy. Globally, 66% of today's electricity is produced by burning fossil fuels [1]. However, although the reserves of coal, natural gas, and petroleum are projected to last for the next 200 years [2], environmental concerns are increasing the demand for cleaner sources of energy. At present alternative sources of energy include:

(i) Nuclear	Limited due to the technical and political risks associated with the use of plutonium. Severe problems are associated with the disposal of nuclear waste.
(ii) Hydropower	Hydroelectric dams are becoming increasingly popular, especially in developing countries with poor energy infrastructures. Wave and tide power have not yet proved to be economically viable.
(iii) Windpower	Limited to certain geographical locations and costly to set up wind farms.
(iv) Biomass	Commercial extraction of oil and tar from related fossil fuels is often complex and costly

One of the more promising technologies which fulfils the demands of both the cleanliness and future power generation requirements is solar energy. It has been estimated that each day the earth receives solar energy corresponds to 200,000 times the total world electrical-generating capacity [2]. This vast and unlimited supply of free energy has therefore presented an increasingly attractive source for meeting today's ever increasing power needs.

Figure 1.1 illustrates the basic structure of a thin film heterojunction solar cell in which solar energy is converted directly into electricity

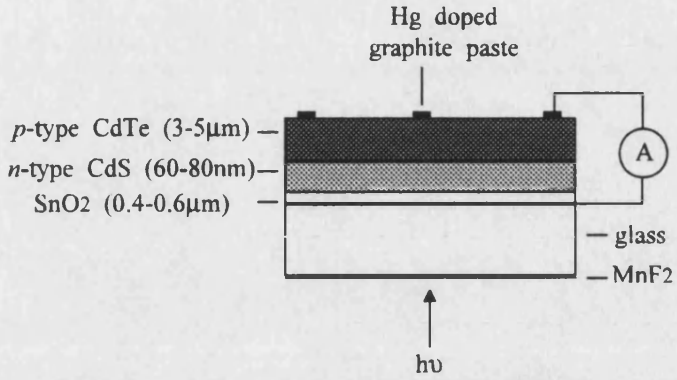

Figure 1.1 Illustration of a typical CdS/CdTe based heterojunction solar cell.

Incident photons are absorbed by a *p*-type semiconductor such as CdTe and in the process generate charge carriers known as electrons and holes. The *pn* junction formed at the interface with the *n*-type CdS layer separates the charge carriers resulting in a voltage and current flow in the external circuit. However at present, the low solar energy conversion efficiencies of terrestrial photovoltaic cells makes them unattractive for wide scale use. For example, the commercial CdS/CdTe based Appolo™ solar illustrated in figure 1.1 has an efficiency of only ≈ 10% [3,4]. Consequently, individual cells measuring 30 cm x 30 cm are combined into larger and more expensive arrays to generate sufficient power for practical applications. The chief driving force in photovoltaic research has therefore been to develop cells with higher efficiencies and at a lower cost. This has involved a cooperative effort in all research fronts in the areas of chemistry, physics, and material science. In each case, particular emphasis has been placed on the influence that film structure, morphology, and composition have on the photovoltaic characteristics of the deposit. For example, poorly crystalline semiconductor layers have been found to severely limit cell efficiencies by promoting the recombination of charge carriers [5,6]. This has stimulated renewed interest in inexpensive

routes to the fabrication of high quality thin film semiconductors, such as CdS [7,8], CdTe [9,10], CdSe [11,12], ZnSe [13,14], and $CuInSe_2$ [15,16]

An alternative approach to the design of solar cells involves replacing one of the solid materials by an electrolyte. The reaction of holes (or electrons) with chemical species in the solution is used to drive current through an external circuit. These photoelectrochemical solar cells have achieved relatively high efficiencies [17,18], but they suffer from serious stability problems arising from the chemical reactivity of their components.

CdSe has shown great promise as a semiconductor material for photoelectrochemical solar cells (PECs). In aqueous polysulfide electrolytes, solar energy conversion efficiencies of 8.4% [19] and 7.2% [20] have been reported for single crystal and electrodeposited thin film CdSe, respectively. Electrodeposition is a simple and versatile method for preparing thin film CdSe and is based on the co-reduction at a suitable cathode (SnO_2 coated glass) of the metal ion (Cd^{2+}) and chalcogen (Se^{2-}) [20]. However, contamination of the target material with side products, e.g. Se, is often a problem with this technique. The presence of excess Se centres has been shown to be highly detrimental to cell efficiency. This is the case when selenious acid (H_2SeO_3), which appears to be the most favoured precursor, is used as the Se source [21]. In this work, stoichiometric CdSe thin films have been electrodeposited from solutions containing selenosulfite ($SeSO_3^{2-}$) and $Cd(NTA)^-$ ions. CdSe is formed by the reaction sequence

$$Cd(NTA)^- \rightarrow NTA^{3-} + Cd^{2+} \quad (1.1)$$

$$Cd^{2+} + 2e^- \rightarrow Cd \quad (1.2)$$

$$Cd + SeSO_3^{2-} \rightarrow CdSe + SO_3^{2-} \quad (1.3)$$

Based on a preliminary voltammetric study a mechanism has been proposed for the formation of CdSe. Extensive characterisation by photoelectrochemical and surface analytical techniques reveals the optical, structural, and electrical properties of CdSe thin films are remarkably insensitive to deposition potential. Atomic force microscopy (AFM) images revealed that air annealing partially recrystallised the electrodeposited layer. So far conversion efficiencies of $\approx$ 7% have been obtained for annealed CdSe films electrodeposited from selenious acid solutions [20]. Based on the superior properties of the as-deposited films grown here, it has been suggested that under carefully optimised annealing conditions, films with greater efficiencies than this may be obtained.

CdS is used as a heterojunction partner in high efficiency CdTe [4] (see figure 1.1) and $CuInSe_2$ [22] based solar cells. In this work CdS films have been grown by chemical bath deposition (CBD) onto conducting substrates (SnO_2 coated glass). CBD of thin semiconducting films is the solution analogue, of the well known chemical vapour deposition in the gas phase. The CBD process is based on the reaction of $CdCl_2$ with thiourea ($SC(NH)_2$) in aqueous solution according to [8,23]

$$Cd(NH_3)_4^+ + SC(NH_2)_2 + 2OH^- \rightarrow CdS + CH_2N_2 + 4NH_3 + 2H_2O \qquad (1.4)$$

Chapter 5 describes the use of capacitance voltage and electrolyte electroreflectance measurements to asses the changes in film properties that accompany various post deposition heat treatments. These changes were related to differences in film morphology observed in scanning electron (SEM) and transmission electron (HRTEM) micrographs. Air annealing has been identified as the optimum heat treatment for CBD CdS implemented in CdTe based photovoltaic cells.

Anodic electrodeposition offers an alternative approach to the growth of thin photosensitive films of CdS [24,25]. Anodisation involves oxidation of the metal followed by reaction with sulfide ions

$$Cd \rightarrow Cd^{2+} + 2e^{-} \quad (1.5)$$

$$Cd^{2+} + S^{2-} \rightarrow CdS \quad (1.6)$$

Gerisher [26] has demonstrated that conversion efficiencies of >5% could be obtained in the cell configuration (single crystal n-CdS/$Fe(CN)_6^{4-}$, $Fe(CN)_6^{3-}/SnO_2$). However, the high cost of single crystal photoelectrodes promoted the use of anodisation as an inexpensive route to preparing photoactive layers of CdS. Miller and Heller [27] showed that photosensitive sulfide layers could be grown on Cd electrodes in solutions of polysulfide and used *in-situ* as photoanodes. However there are a number of disadvantages associated with CdS prepared by this method Of particular concern is that it results in discontinuous films with many defects that can act as recombination centres. It is also difficult to obtain films that are thick enough to be useful. Maximum thicknesses are typically 500 nm. For this reason, the polycrystalline liquid junction solar cells failed to compete with more efficient and reliable solid state devices. Nevertheless, a number of questions still need to be answered in order to understand the poor performance of anodically grown films. This provided the stimulus in the present study to investigate the role that the underlying substrate morphology plays in film growth. Two localised photoelectrochemical techniques [28,29] were used; photoelectrochemical microscopy (PEM) [30,31] and scanning microscopy for semiconductor characterisation (SMSC) [32,33]. These techniques have been used to spatially map the photocurrent response at the illuminated Cd/CdS interface. Localised

imaging has revealed that the photoresponse maps the grain morphology of the underlying substrate. Far superior image resolution and contrast were obtained in the continuous scan direct detection method (PEM). Mechanisms have been presented to explain the origin of image contrast. The effect of substrate etching on the photoresponse of anodised CdS layers was assessed by photocurrent spectroscopy. The properties of anodised CdS films were also studied by electrolyte electroreflectance spectroscopy (EER). In a comparison with single crystal CdS, EER revealed CdS films grown on etched substrates were highly defective.

References

1 T. Suntola, 11th E. C. Photovoltaic Solar Energy Conference, 12-16th October 1992, Montreaux, Switzerland, (E.C), 1992, p. 977

2 Comptons Interactive Encyclopedia for Windows on PC CD-ROM, Comptons NewMedia, 1995

3 M. E. Özsan *et al*, *Int. Jnl. Solar Energy*, **12**, 79 (1992)

4 J. M. Woodcock, A. K. Turner, M. E. Özsan, and J. G. Summers, in *Prceedings of the 22nd IEEE Photovoltaic Solar Energy Conference*, Lisbon, Portugal, 11-14 April 1991, (H. S. Stevens and Associates, Bedford, U.K), 1991, p. 931

5 R. Memming, *Electrochim. Acta*, **25**, 77 (1980)

6 D. Lincot and J. Vedel, *J. Electroanal. Chem.*, **220**, 179 (1987)

7 G. Goodlet, M. J. Furlong, L. M. Peter, A. A. Shingleton, M. E. Özsan, D. R. Johnson, M. Sadeghi, and D. Sivapathasundaram, *J. Mat. Sci: Electronic Materials.*, in press

8 M. Froment, D. Lincot, R. Ortega-Borges, *Philosophical Magazine B*, 68(2), 185 (1993)

9 B. M. Basol, *J. Appl. Phys.*, **55**, 601 (1984)

10 A. Kampman, P. Cowache, J. Vedel, and D. Lincot, *J. Electroanal. Chem.*, **387**, 53 (1995)

11 G. Hodes, D. Cahen, J. Manassen, and M. David, *J. Electrochem. Soc.*, **127**, 2252 (1980)

12 R. K. Pandey, S. R. Kumar, A. J. N. Rooz, and S. Chandra, *Thin Solid Films*, **200**, 1 (1991)

[13] V. Krishnan, D. Ham, K. K. Mishra, and K. Rajeshwar, *J. Electrochem. Soc.*, **139**(1), 23 (1992)

[14] C. Natarajan, M. Sharon, C. Lévy-Clément, and M. Neumann-Spallart, *Thin Solid Films*, **237**, 118 (1994)

[15] L. Stolt, J. Hedström, M. Ruckh, J. Kessler, K. O. Velthaus, and H. W. Schock, *Appl. Phys. Lett.*, **62**, 597 (1992)

[16] C. Guillén and J. Herrero, *J. Electrochem. Soc.*, **141**(1), 225 (1994)

[17] M. A. Butler and D. S. Ginley, *J. Mat. Sci.*, **18**, 1 (1979)

[18] A. Heller, *Solar Energy*, **29**, 153 (1982)

[19] A. Heller, K. C. Chang, and B. Miller, *J. Electrochem. Soc.*, **124**, 697 (1977)

[20] J. P. Szabo and M. Cocivera, *J. Electrochem. Soc.*, **133**, 1247 (1986)

[21] F. Decker, J. R. Moro, J. L. S. Ferreira, and M. Vanzi, *Ber. Bunsenges. Phys. Chem.*, **91**, 408 (1987)

[22] D. Cahen and Y. W. Chen, *Appl. Phys. Lett.*, **45**, 746 (1983)

[23] D. Lincot and R. Ortega Borges, *J. Electrochem. Soc.*, **139**, 1880 (1992)

[24] L. M. Peter, *Electrochim. Acta*, **23**, 165 (1978)

[25] L. M. Peter, *Electrochim. Acta*, **23**, 1073 (1978)

[26] H. Gerisher, *J. Electroanal. Chem.*, **58**, 263 (1975)

[27] B. Miller and A. Heller, *Nature* (Lond.), **262**, 680 (1976)

[28] M. A. Butler, *J. Electrochem. Soc.*, **131**, 2185 (1984)

[29] T. E. Furtak, D. C. Cranfield, and B. A. Parkinson, *J. Appl. Phys.*, **51**, 6018 (1980)

[30] R. Peat, A. R. J. Kucernak, D. E. Williams, and L. M. Peter, *Semicond. Sci. Tech.*, **5**, 914 (1990)

[31] R. S. Hutton and D. E. Williams, *Electrochim. Acta*, **39**(5), 701 (1994)

[32] A. Martinez Chaparro, P. Salvador, B. Coll, and M. Gonzalez, *Surf. Sci.*, **293**, 160 (1993)

[33] A. Martinez Chaparro, P. Salvador, A. Mir, B. Coll, and V. Caselles, in *Proceedings of the 5th International Conference on Defect Recognition and Image Processing in Semiconductor Devices*, Santander, Spain, 1993

Chapter 2

Theory

2.1. Structural Properties of CdS and CdSe

CdS and CdSe may assume one of two crystalline structures, zinc blende and wurtzite, both of which are characterised by tetrahedral lattice sites.

Cadmium forms tetrahedral lattice sites with sulfur and selenium as the combination of a Group II and IV elements gives rise to 4 valence electrons. Each Cd atom is surrounded symmetrically by 4 S or Se atoms. This is illustrated in figure 2.1.

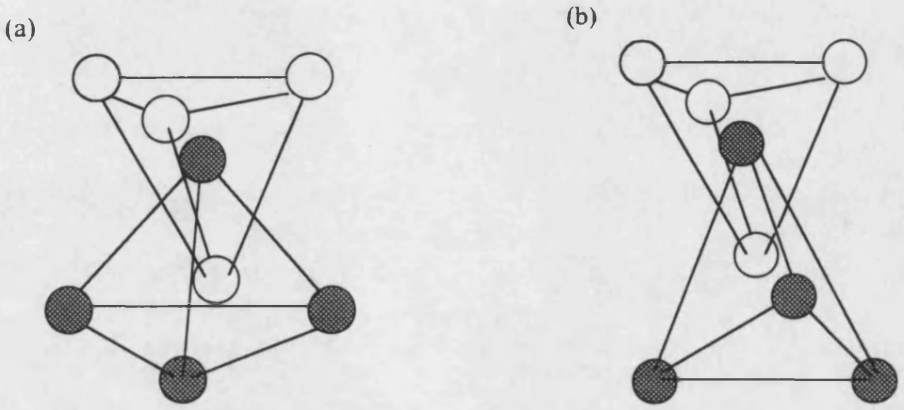

Figure 2.1. Tetrahedral sites for Cd (solid circles) and S or Se (hollow circles) where bases of tetrahedra are parallel and (a) lie in line vertically and (b) lie 60° out of line

The combination of tetrahedral sites takes two possible forms, wurtzite and zinc blende. The wurtzite or hexagonal crystal form consists of two interpenetrating close packed hexagonal lattices displaced with respect to one another by a distance 3/8c along the hexagonal c-axis. This is illustrated in figure 2.1 showing the combination of tetrahedral sites in figure 2.2.

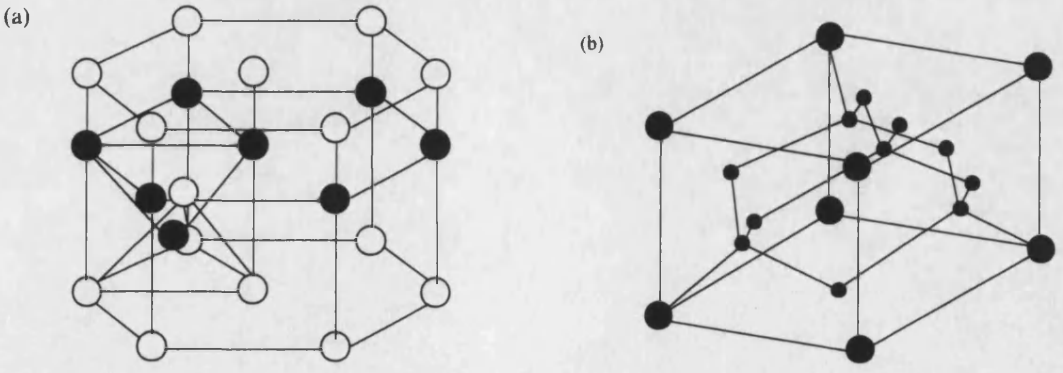

Figure 2.2. Crystal structure of the (a)wurtzite and (b)zinc blende lattices

The zinc blende structure is in the cubic class and has the combination of tetrahedral sites illustrated in figure 2.1(b). It is composed of two interpenetrating cubic close packed lattices. Shown in figure 2.2(b) is the crystal structure of cubic zinc blende

2.2. Band Structure

In a crystalline solid, the overlap of atomic orbitals extends throughout the lattice giving rise to crystal orbitals. In a finite solid though, there can only be a finite number of crystal orbitals, equal to the number of valence atomic orbitals. However since there are so many orbitals, we can neglect the energy spacing between them, and assume that they form continuous bands of energy levels. These are separated by regions of energy known as the forbidden gap or band-gap (E_g). This is shown in figure 2.3. The two highest bands are known as the valence (VB) and conduction (CB) bands.

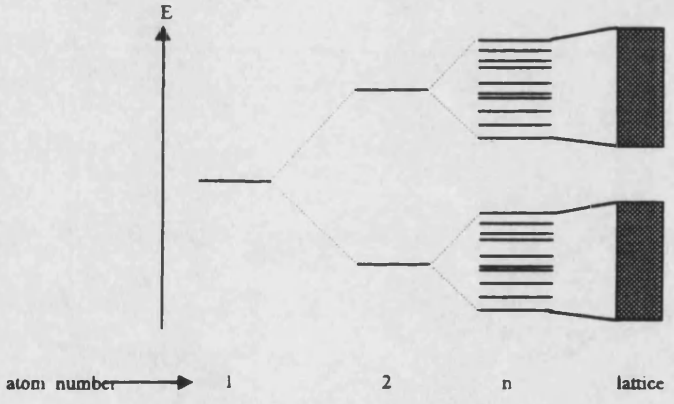

Figure 2.3. Orbital energies for the overlap of a pair of atoms through to all the atoms in a solid

The crystal will behave as an insulator if the allowed energy bands are either filled or empty as no electrons can move in an electric field or as a metal if one or more bands are partly filled. Semiconducting properties arise if one or two bands are strongly filled or slightly filled. In order to describe the origin of band structure in a semiconductor we

must consider the wave functions which describe the overlapping atomic orbitals in the crystal lattice.

For a free electron in three dimensions the energy values (ε_k) for the wave functions (k) are given by

$$\varepsilon_K = \frac{\hbar}{2m}(k_x^2 + k_y^2 + k_z^2) \tag{2.1}$$

If we then confine the electron within a periodic boundary condition L where

$$k_x, k_y, k_z = 0; \quad +2\pi/L; \quad +4\pi/L; \ldots \tag{2.2}$$

The free electron wave function is of the form of a travelling plane wave and is given by

$$\varphi_k(v) = \exp(ik.r) \tag{2.3}$$

Hence any form of the wave function is of the form $2n\pi/L$ where n is a positive or negative integer. However in the case where L is very large in all three dimensions, the energy separation between consecutive allowed k values becomes negligibly small. This leads to a continuum of bands and is illustrated in figure 2.3. This is inaccurate as it does not account for the presence of a band-gap. The band structure of a crystal can be explained by the nearly free electron model for which the band electrons are treated as perturbed only weakly by the periodic potential of ions in the lattice. Equation 2.3 now becomes

$$\varphi(x) = u_k(x)e^{ikx} \tag{2.4}$$

where $u_k(x)$ has a period a and k is the wave vector of the state. As a result of the periodic lattice potential the electron is accelerated and decelerated. The value of p therefore changes and no longer equals that for a free electron. According to the Bloch theorem one of the main observations is that the wave functions no longer have unique values of k. Hence the term $p=\hbar k$ is no longer a true momentum and may be considered as a quantum number of the wave function. For a periodic lattice we can represent the changes in the quantum number k as

$$k = k' + 2\pi m/a \tag{2.5}$$

The quantity $2\pi/a$ is used to describe the variation of φ with k. Illustrated in figure 2.4 is the "nearly free" electron-band structure with the effect of lattice potential illustrating the discontinuities in wavefunction structure.

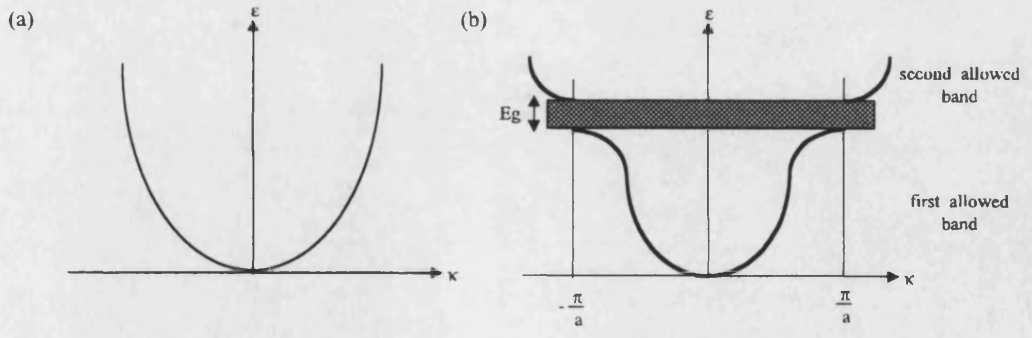

Figure 2.4. (a) Plot of ε versus k for a free electron and (b) same plot but for an electron in a monatomic linear lattice.

However how do the ranges in energy where no states of real k exist arise?. We can understand this in terms of a Bragg-like condition for the interaction of free electrons with the periodic potential in the lattice. The Bragg condition for the diffraction of a wave-vector k in one dimension is given by

$$k = \pm 1/2G = \pm n\pi/a \qquad (2.6)$$

where $G=2\pi n/a$ is reciprocal lattice vector and n is an integer. The first reflection and first energy gap occur at $k=\pm\pi/a$ where wave-like solutions of the Schrödinger equation do not exist. Other gaps are found at $\pm n\pi/a$ for integral values of n. The region in which $-\pi/a < k < \pi/a$ is called the first Brillouin zone. The situation in real crystals is far more complicated. Shown in figure 2.5 is the first Brillouin zone for the zinc blende and wurtzite structures which both CdS and CdSe can adopt.

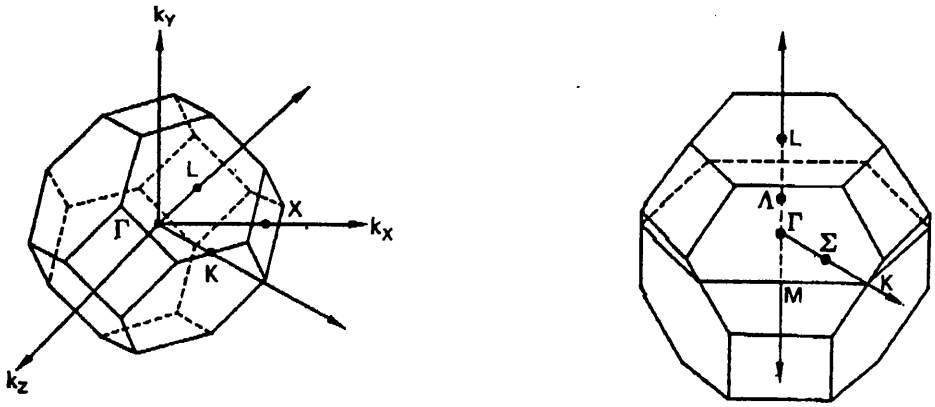

Figure 2.5. Brillouin Zone for (a) zinc blende and (b) wurtzite structures [1]

In both cases the Γ corresponds to the zone centre and the remaining symbols represent points and directions of high symmetry. The band structures of CdS and CdSe have been determined by Cohen *et al* [2] and are illustrated in figure 2.6.

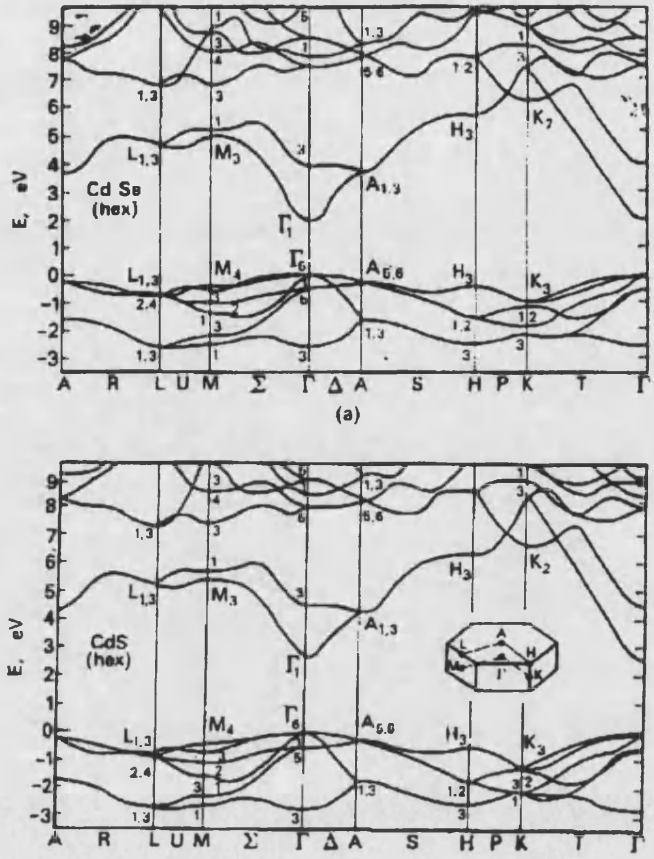

Figure 2.6. The band structure of CdSe (top) and CdS (bottom) [2]

It is interesting to note there remains a region of energy above 0 eV where no states are present which is the band gap region. States below the gap are occupied and comprise the valence band, whilst states above the gap comprise the conduction band.

2.3. Band Theory of Solids

The occupancy of electrons in bands determines the conductivity of a material in an applied electric field. This differs for metals, insulators, and semiconductors. The prerequisite for electrical conduction is the availability of electron states into which electrons can be promoted as they gain kinetic energy in the electric field. The three cases are illustrated in figure 2.7

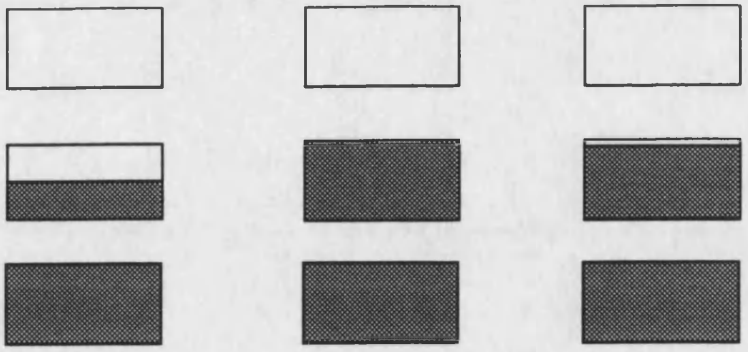

Figure 2.7. Occupancy of bands by electrons in (a) metal, (b) insulator and (c) semiconductor

2.3.1. Metals

The structure of a metal permits very close overlap of adjacent atomic orbitals giving a continuous band of orbitals. In metals, the important feature is that there are empty levels located very close to the uppermost filled level, the Fermi level, and so it requires hardly any energy to excite the uppermost electrons (thermal energy (kT) at room temperature is sufficient). This results in highly mobile electrons which give rise to electrical conductivity.

2.3.2. Insulators

If the valence electrons exactly fill one or more of the bands constructed from the overlap of atomic orbitals, leaving others empty, the material will be an insulator at absolute zero. The energy gap typically several eV is much greater than kT at room temperature and therefore there is no way of changing the momentum of the electrons if every state in the band is filled. Electrons are therefore unable to accelerate in an applied electric field and hence the electrical conduction is negligibly small at room temperature.

2.3.3. Semiconductors

Materials which posses a small band gap (< 1 eV) where a proportion of the electrons can be excited thermally into the valence band of the solid are known as intrinsic semiconductors. Semiconductivity can also be brought about by impurity doping of wide band gap materials. Silicon for example is insulating in its pure state but it can be made *p*- or *n*-type by doping. Wide gap materials which are defective may also show semiconductivity. This is due to the presence of atomic vacancies or interstitials in the lattice which mimic impurity effects.

Impurities and defects are subdivided into donors and acceptors. Donors provide excess electrons to the conduction band thus providing electron or *n*egative conductivity (*n*-type). Acceptors capture valence electrons from the atoms of the semiconductor in which they have been introduced resulting hole or *p*ositive conductivity (*p*-type). In doped silicon, the donor and acceptor ionization energies are comparable to kT and the thermal ionization of donors and acceptors therefore dominates the electrical conductivity at room temperatures.

2.4 The Fermi Level

The probability of occupation of energy levels in a solid is determined by the Fermi-Dirac distribution function [3].

$$f(E) = \frac{1}{1+\exp[(E-E_f)/kT)} \tag{2.7}$$

where E_f is the Fermi energy, k the Boltzmann constant, T the absolute temperature and E the energy of the state. At low temperatures, E_f represents the boundary between

filled and empty energy levels. In a semiconductor, E_f is located in the region between the valence and conduction band edges, i.e. the band gap.

In an intrinsic semiconductor, the Fermi level is located approximately in the middle of the band gap. Here the number of excited electrons located in the conduction band must be the same as the number of holes remaining in the valence band. If we describe the conduction band as N_C energy levels at an energy E_C, where N_C is the effective density of energy levels in this region of the conduction band and N_V as the effective density of valence band energy levels at an energy E_V, the Fermi level can be conveniently used to describe the density of electrons in the conduction band and holes in the valence band. These are given in equations 2.8 and 2.9

$$n = N_c \exp[-(E_c - E_f)/kT] \tag{2.8}$$

$$p = N_v \exp[-(E_f - E_v)/kT] \tag{2.9}$$

where n is the density of electrons in the conduction band, p the density of holes in the valence band. Combining equations 2.8 and 2.9 we obtain

$$np = N_c N_v \exp(-E_g/kT) \tag{2.10}$$

$$n = p = (N_c N_V)^{1/2} \exp-(E_g/2kT) \tag{2.11}$$

For an *n*-type semiconductor, where electrons are donated to the conduction band, the Fermi level is located at an energy close to the donor level. In the *p*-type case, the Fermi level is located close to the acceptor level. We can determine the position of the Fermi level in an *n*-type semiconductor if we consider the relative occupancy of the electrons in the donor level (N_d) to be small compared with the density of states in the

conduction band (N_c). From this we can define an occupancy ratio $R_{d/c} = N_d/N_c$ and equate this to the Fermi-Dirac function given in equation 2.7.

$$R_{d/c} = 1/[1+\exp[(E_c-E_f)/kT] \quad (2.12)$$

As the exponential term is much greater than 1 this becomes

$$R_{d/c} = \exp[-(E_c-E_f)kT] \quad (2.13)$$

From this the Fermi level is given by

$$E_f = E_c - kT \ln(N_c/N_D) \quad (2.14)$$

The density of electrons in the conduction band may also be determined using equation 2.15

$$n = N_c \exp[(E_f-E_c)/kT] \quad (2.15)$$

The situation is identical for a *p*-type semiconductor apart from the fact that the occupancy ratio becomes $R_{a/v}=N_a/N_v$ which is determined by the number of acceptor levels N_a and the density of states in the valence band N_v. The Fermi energy for electrons and holes are given by equations 2.16 and 2.17.

$$E_f = E_c - \ln(N_c/N_a)kT \quad \text{where } n = N_D \quad (2.16)$$

$$E_f = E_v - \ln(N_v/N_d)kT \quad \text{where } p = N_A \quad (2.17)$$

So far we have considered the Fermi level under conditions of thermodynamic equilibrium. However when the semiconductor is subjected to some non-equilibrium condition such as illumination [4], a "steady state" Fermi level or "quasi Fermi level" is obtained. In the steady state a dynamic equilibrium is established between the processes of generation and recombination of the electron hole pairs. Under illumination the electron and hole densities become

$$n^* = n_o + \Delta n \tag{2.18}$$

$$p^* = p_o + \Delta p' \tag{2.19}$$

where n_o and p_o are the electron and hole densities in the dark and Δn and Δp are the changes in the electron and hole densities under illumination. In the case of an *n*-type semiconductor, the density of majority carriers is not appreciably increased by the illumination, so the position of the quasi Fermi level, E_{sFn} for majority carriers is nearly identical to E_f. However the concentration of holes is drastically increased from the dark value with illumination, i.e. $\Delta p >> p$. In which case the quasi Fermi level, E_{sFp} for minority carriers is obtained at an energy level considerably higher than E_{VB}. An energy level diagram showing the thermodynamic equilibrium Fermi level and quasi level is given in figure 2.8.

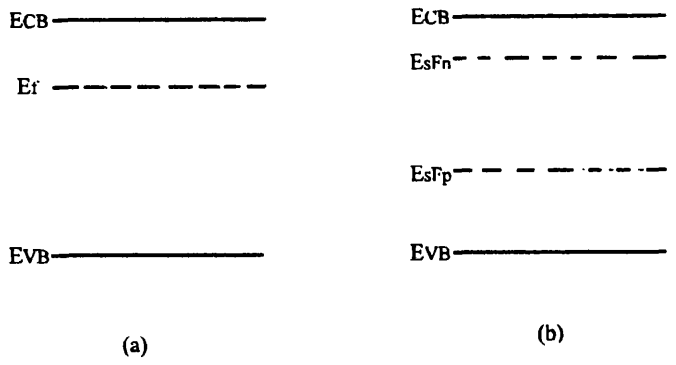

Figure 2.8. Energy level diagram showing (a) thermodynamic and (b) quasi equilibrium Fermi levels

Under non-equilibrium conditions equation 2.10 becomes.

$$n^* p^* = n^2 \exp(E_{sFn} - E_{sFp}) / kT \tag{2.20}$$

If $\Delta n << n_o$, it follows from equation 2.16 that for an *n*-type semiconductor, $E_{sFn} = E_f$. We can describe the position of E_{sFn} in terms of the hole occupancy using equation 2.21

$$E_f - E_{sFp} = \ln(\Delta p / p_o)kT \quad (\text{where } \Delta p >> p_o) \tag{2.21}$$

Similarly for a *p*-type semiconductor, if $\Delta p << p_o$

$$E_{sFn} - E_f = \ln(\Delta n / n_o)kT \tag{2.22}$$

Equations 2.21 and 2.22 are only valid for low levels of illumination, i.e. the magnitudes of Δn and Δp are proportional to intensity and therefore the shifts in the quasi Fermi levels are also proportional to intensity. When of Δn and Δp are extremely high, effects due to the degeneracy of the carriers must be taken into account. Equations 2.21 and 2.22 are then no longer valid [5].

The thermodynamic description of the Fermi level is that it corresponds to the electrochemical potential of an electron in a solid. This is a very useful concept for understanding the movement of electrons between solids. When two solids are brought into contact with one another, electrons flow from one solid to another when the Fermi levels of both solids are the same. The concept of E_f is thus extremely important in understanding charge transport at semiconductor/metal interfaces

2.5. Potential Distribution at the Interface

Several texts have been published which describe the fundamentals of the semiconductor electrolyte interface (Peter [6], Morrison [7], Finklea [8], and Pleskov and Gurevich [5]).

When a semiconductor is brought into contact with an electrolyte an electrical double layer forms at the interface between the two phases. Three regions may be distinguished within the electrical double layer: the diffuse layer in the solution, an intermediate layer called the Helmholtz layer and the space charge region in the semiconductor. This is illustrated in figure 2.9 for an *n*-type semiconductor under conditions of depletion.

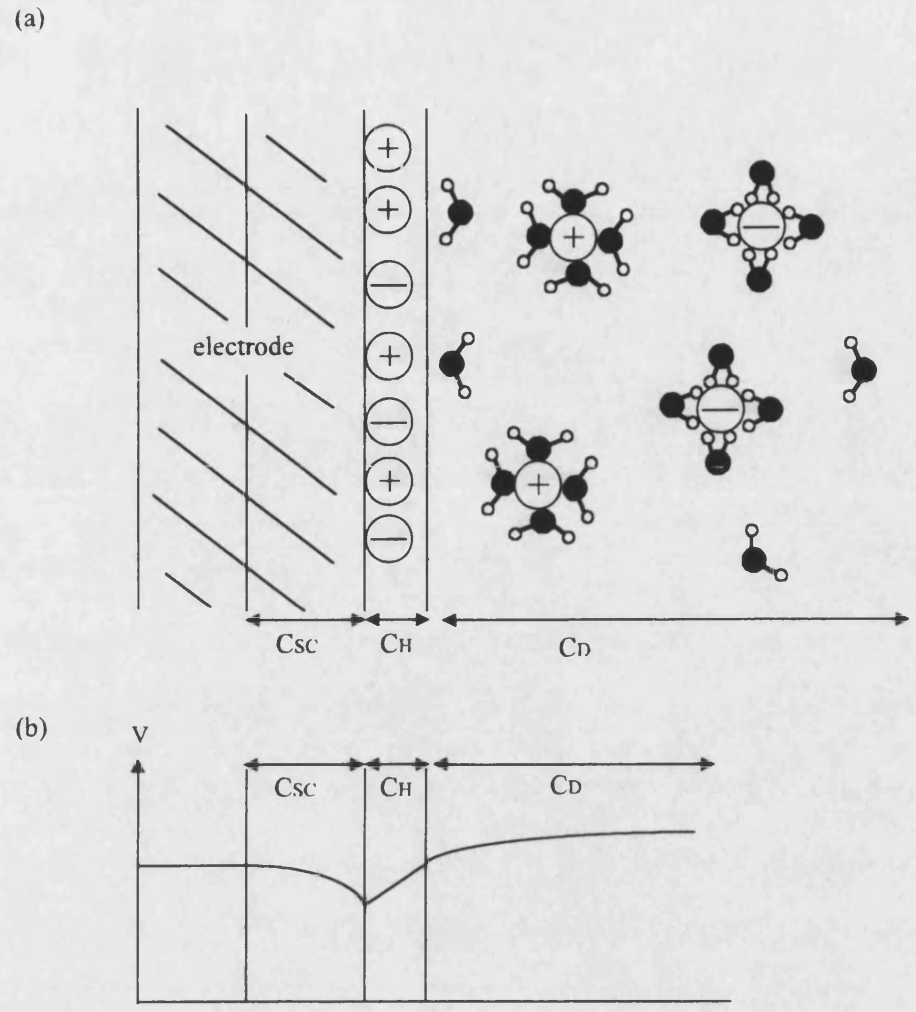

Figure 2.9. (a) The structure of the semiconductor electrolyte interface showing the space charge (C_{SC}), Helmholtz (C_H) and diffuse (C_D) regions. (b) Band diagram showing the electrical potential drop across the interface.

The Helmholtz layer is formed by ions attracted to the electrode surface, and also by molecules of the solvent. Its thickness is of the order of the size of an ion. Outside this is the diffuse double layer (also known as the Gouy-Chapman layer) of variable thickness. The formation of a space charge region in the semiconductor leads to a potential drop between its surface and the neutral bulk and results in a change in potential energy of the electrons with distance. The extent of this perturbation is described by the term "band bending", $\Delta\Phi$. If the potential at the surface is given by Φ_{bulk} and at the surface by $\Phi_{surface}$, then $\Delta\Phi=\Phi_{surface}-\Phi_{bulk}$. Therefore the bands bend upwards if the potential drop

across the space charge layer is greater than zero and downwards if the drop is less than zero. A unique case exists where the potential drop between the surface and the bulk of the electrode is zero, i.e. there is no space charge layer and the bands remain flat right upto the surface. The potential at which this occurs is known as the flat band potential (E_{fb}). These three cases are shown in figure 2.10.

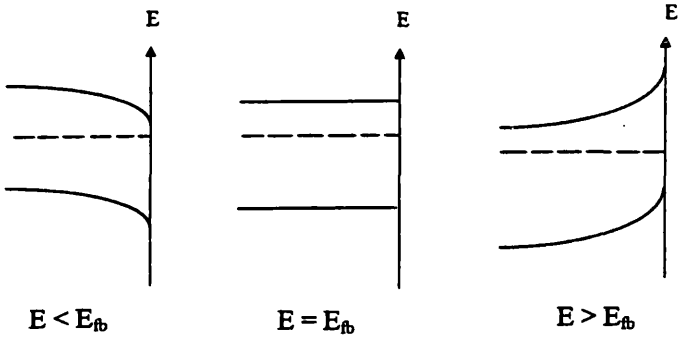

Figure 2.10. Effect of applied potential on the band bending of an intrinsic semiconductor. E_{fb} is the flat band potential.

If the electrode is biased positive to E_{fb}, the width of the space charge layer is given by

$$W = (2\varepsilon\varepsilon_o / qN_D)^{1/2}.(E - E_{fb})^{1/2} \qquad (2.23)$$

where $\varepsilon\varepsilon_o$ is the permittivity of the semiconductor and ($E-E_{fb}$) the degree of band bending.

The space charge region can be classified into three different types depending on the dc bias applied to the sample, i.e. the band bending. At potentials more negative than flat-band the space charge region becomes an accumulation layer where the majority carriers (electrons in the conduction band) are drawn towards the electrode surface. At sufficiently negative potentials H_2 may be evolved. This is shown in figure 2.11(a). If the potential E is made more positive than E_{fb}, electrons are removed from the surface and a depletion layer is formed. The probability of an electron transferring to solution is

therefore low as will be any current produced and the electrode is said to be blocking (figure 2.11(d)). Under illumination however, photogenerated holes are produced, giving rise to an anodic photocurrent. Recombination of these electrons with conduction band holes may also occur as shown in figure 2.11(b). Finally if the potential is made further positive under illumination, limiting anodic currents are obtained as surface recombination will no longer play an important role. This is illustrated in figure 2.11(c).

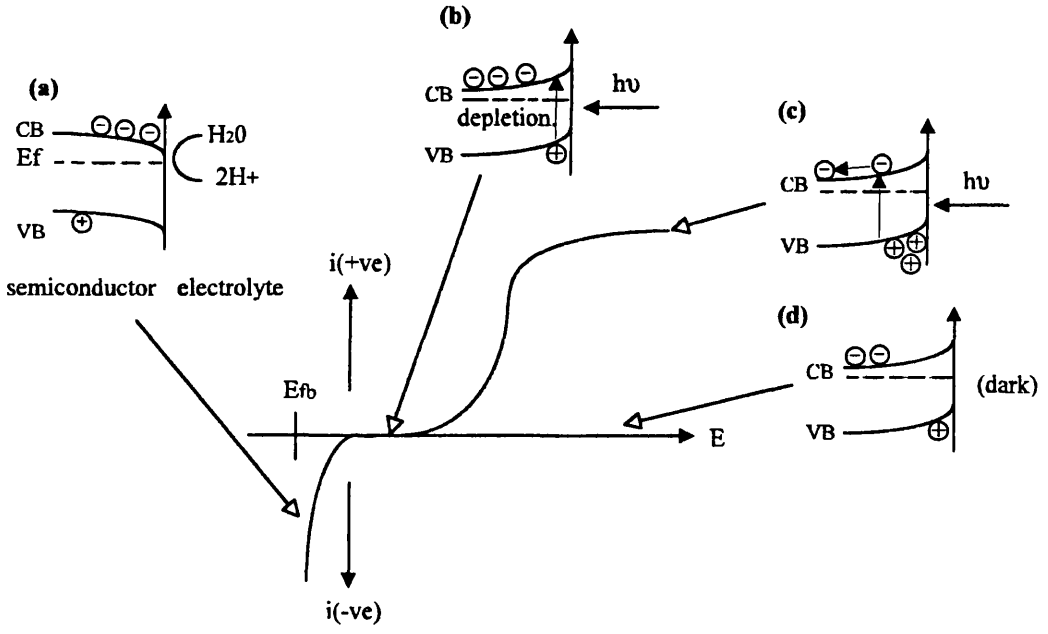

Figure 2.11. Current voltage curve for an *n*-type semiconductor in the dark and under illumination in an indifferent electrolyte. Insets (a) to (d) are the various charge transfer processes that occur under different degrees of band bending (see text)

A term which later will be seen to be important in characterising semiconductors is the capacitance associated with the space charge layer. C_{SC} is given by

$$C_{SC} = \frac{\varepsilon\varepsilon_0}{W} = \left[\frac{q\varepsilon\varepsilon_0 N_D}{2(E - E_{fb})}\right]^{1/2} \qquad (2.24)$$

The derivation of expression 2.23 assumes that all the potential drop takes place across the space charge layer. The magnitude of the electric field across this layer is given by equation 2.25

$$E = \frac{Q_{SC}}{\varepsilon\varepsilon_o} = \left[\frac{2qN_D(E - E_{fb})}{\varepsilon\varepsilon_o}\right]^{1/2} \qquad (2.25)$$

There are however a number of cases in which changes in the applied potential does not appear just across the space charge region; instead a fraction of the change may also appear across the Helmholtz layer. This is mainly due to the presence of electronic states confined to the surface of the electrode. An important case arises when a high density of surface states exists within the band gap region. If the energy of the Fermi level coincides with the energy of the surface states, then their occupancy and consequently the surface charge become sensitive to the applied potential. If the density of surface states is high, all of the externally applied potential appears across the Helmholtz layer and the electrode behaves essentially like a metal. and the band bending is fixed. This situation is known as Fermi level pinning (Flp) as the surface level of the Fermi level is pinned with respect to the band edges. Surface states are important as their presence must be accounted for into theories of the semiconductor electrolyte interface. For a description of surface states and the role they play at the interface see e.g Allongue and Cachet [9], and Vanmaekelbergh and Cardon [10].

2.6. Electron Transfer Reactions at Metal/Electrolyte and Semiconductor/Electrolyte Interfaces

The theory of electron transfer will firstly be considered for the metal/electrolyte interface. In figure 2.12(a) we consider a metal electrode immersed in an electrolyte containing a redox species (E_{rdx}).

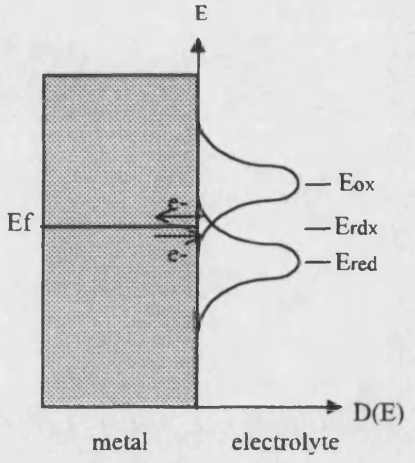

Figure 2.12 (a). Band diagram for a metal/electrolyte contact showing charge transfer across the interface

Also shown are the oxidised (E_{OX}) and reduced (E_{RED}) form of this species. The relative amounts of these present are described by the term D(E) which represents the density of redox energy. For the purpose of this discussion, the concentration of oxidised and reduced species are assumed to be identical. Electron transfer takes place between the metal and the electrolyte via a single energy band. This may either take place from the solution to the metal ($E_{rdx} \rightarrow E_{ox} + e^-$) or from the metal into solution ($E_{ox} + e^- \rightarrow E_{red}$) via an isoenergetic or adiabatic process [8]. Electron transfer occurs so rapidly that there is no significant change in the atomic coordinates of the system. Hence the electron moves horizontally across the interface in figure 2.12(a).

This model may be applied to semiconductors, although the presence of a band gap introduces complications. The theory was first developed for semiconductor

electrodes by Gerischer [7]. Firstly electron exchange can only occur at energies above the conduction band edge or below the valence band edge Secondly the solution redox levels may overlap appreciably with only one of the semiconductor bands. Figure 2.12(b) shows an *n*-type semiconductor in contact with an electrolyte containing a redox couple with a standard potential more positive than the equivalent potential of the conduction band. Under depletion conditions, the amount of current flowing depends on the degree of overlap between the conduction band and energy of the E_{OX} levels. If the oxidised form of the redox couple is exchanged for the reduced form with a redox level matched in energy to the valence band as illustrated in figure 2.12(c), high electron transfer rates are expected.

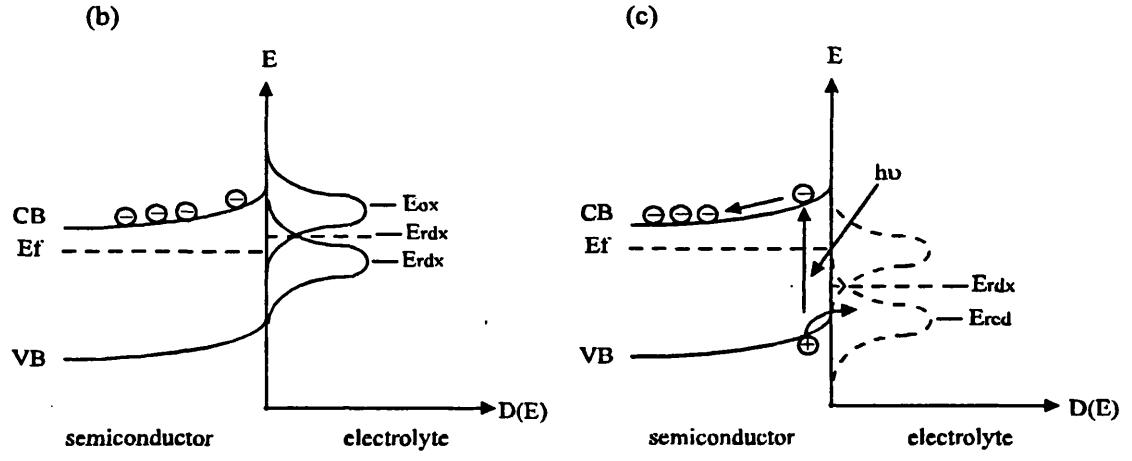

Figure 2.12 (b) and (c): Energy level representation for (b) electron transfer to the oxidised form of the redox couple and (c) photogenerated hole transfer to the reduced form of the couple. The shaded oval represents the presence of surface states.

In the presence of surface states, the redox reactions between semiconductor and electrolyte are not so straightforward. If we consider the case when the electrode is biased close to flatband, the concentration of minority carriers at the surface is so low that minimal currents are expected in the absence of surface states. However electrons are able to tunnel through the space charge layer to the surface states and transfer to E_{OX} species in solution, and small currents are therefore observed. This is illustrated in figure 2.12(d). The importance of surface states in mediating electron transfer reaction is

further emphasised in figure 2.12(e). In the case of redox couples chosen with formal potentials located positive of the valence band adge, a decreasing current flow would be expected as the redox energy level moves upwards. However currents flow in spite of the reduction in overlap because holes in the valence band are captured by surface states which then oxidise E_{RED} molecules.

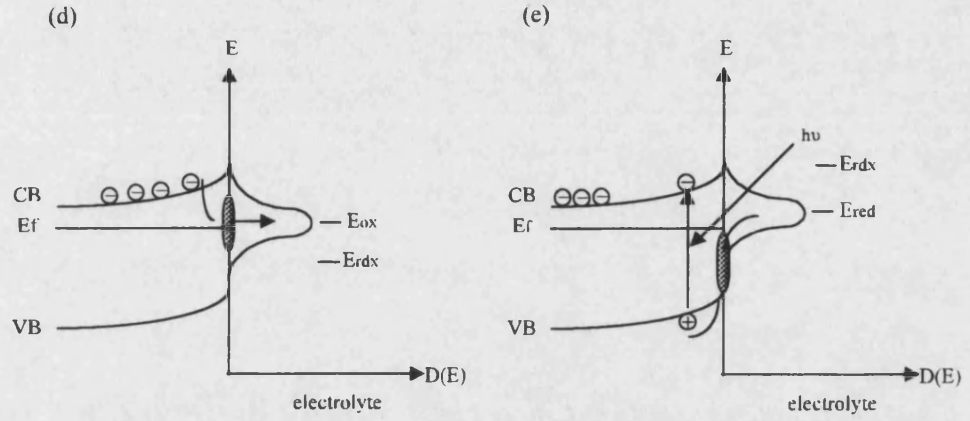

Figure 2.12 (d) and (e): Energy level diagram illustrating the role of surface states on charge transfer to E_{RDX} by (d) majority carrier injection and (e) photogenerated minority carrier injection.

2.7. Mott-Schottky Relationship

The Mott Schottky (M-S) relationship [11] given in equation 2.26 is based on measurement of the capacitance associated with the space charge layer.

$$\frac{1}{C_{sc}^{\ 2}} = \frac{2}{q\varepsilon\varepsilon_o N_D A}(E - E_{fb} - kT/q) \qquad (2.26)$$

where $\varepsilon\varepsilon_o$ is the permittivity of the film, V is the applied potential, $(E\text{-}E_{fb})$ is the potential difference across the space charge region, and C_{sc} is the capacity of the space charge region. Given the linear relationship between the potential across the space charge region and C_{SC}^{-2}, the flatband potential and donor density may be determined. The derivation of the Mott-Schottky relationship assumes that changes in the potential drop

only takes place across the space charge layer though there are additional capacitances associated with the electrolyte side if the SEI, *viz.* with the diffuse (C_d) and Helmholtz (C_h) layer. The three capacitances are in series where $C_{SC} << C_h$ and C_d. Hence C_{SC} must dominate the measured capacitance which can be assigned to the space charge layer. This is summarised in equations 2.27 to 2.29.

$$C_{MEAS} = (C_{SC}^{-1} + C_h^{-1} + C_d^{-1})^{-1} \quad (2.27)$$

$$C_{SC}^{-1} >> C_h^{-1}, C_d^{-1} \quad (2.28)$$

$$C_{MEAS} = C_{SC}^{-1} \quad (2.29)$$

Equation 2.26 may be modelled experimentally by a single capacitor. The simplest equivalent circuit assumes that the electrochemical cell is described by the space charge capacitance in series with an uncompensated resistance (solution + electrode contact) [12]. The analysis is only valid if the measured space charge capacitance data give linear M-S plots. Often, however deviations from linearity are observed as are frequency dependent values of C_{SC} and the uncompensated solution resistance. There are several reasons why such non-ideal behaviour is observed.

(a) Surface States: These lead to Fermi level pinning where an appreciable change in the potential drop also takes place across the Helmholtz region (equation 2.26 only considers the potential drop across the space-charge region). An appreciable contribution from the Helmholtz layer is often observed in heavily doped semiconductors, since C_{SC} is much larger. Pleskov and Gurevich [5] have pointed out that it is possible to diminish the contribution from surface states by increasing the frequency of the applied ac voltage. In this case, species with a long relaxation time, whose concentration is relatively large,

become gradually less important, until at sufficiently high frequencies the measured capacitance represents the space charge capacitance.

(b) Deep Donors [13]: In the absence of an electric field these are not ionised in the semiconductor bulk, but become ionised in the electric field of the space charge layer, contributing to the low frequency capacitance.

(c) Fast Surface States: Species on the electrode surface may respond to the alternating electric field. The total capacitance will then include a contribution from the charging of these "fast states". In many cases, fast surface states are thought to contribute to the measured capacity. However in measurements made on ZnO electrodes, Dewald [14] has pointed out that this is one of the few cases where no contribution of such states to the measured capacity was found.

Experimentally Mott-Schottky plots showing a frequency dependence as a result of processes such as those described above may be classified in two ways.

(a) The slope may or may not change but the intercept on the potential axis is shifted.

(b) Only the slope changes whilst the intercept on the potential axis remains constant.

In the analysis of the capacitance measurements reported in this thesis, a modified form of the Mott-Schottky relationship has been used to asses the importance of surface roughness $\Re$ in the capacitance voltage behaviour of polycrystalline thin film CdS[15]. The relationship given in equation 2.26 can be recast in a form that takes the effective interfacial surface roughness into account

$$C_{SC} = A\,\Re.(qN_D\varepsilon\varepsilon_o / 2)^{1/2}.(E - E_{fb} - kT/q)^{-1/2} \qquad (2.30)$$

where A is the contact area. Saturation in the capacitance is expected to occur when the space charge region extends throughout the film to the underlying tin oxide coated glass substrate, and under these conditions the limiting geometric capacitance C_{GEO} is given by

$$C_{GEO} = \frac{A\Re.\varepsilon\varepsilon_o}{d} \qquad (2.31)$$

C_{GEO} is the capacitance associated with the entire film of thickness d and of area A. By comparing equations 2.30 and 2.31 it can be seen that saturation of the junction capacitance should occur at a transition voltage, V_{TR}, defined by

$$V_{TR} = d.(qN_D / 2\varepsilon\varepsilon_o) \qquad (2.32)$$

Comparison of equations 2.30 and 2.31 show that both contain $\Re$ as an unknown quantity. This may be eliminated by writing equation 2.30 in a normalised form that can be used to construct Mott-Schottky plots.

$$(C_G / C_{SC})^{1/2} = (2\varepsilon\varepsilon_o / d^2 qN_D).(E - E_{fb} - kT/q) \qquad (2.33)$$

This allows the ratio ε/N_D to de determined without assuming a value for $\Re$. Using a value for the permittivity of the film N_D may be calculated. The transition from Mott-Schottky behaviour to the geometric capacitance at the potential V_{TR} is illustrated in figure 2.13. This is determined experimentally by linear extrapolation of the linear regions of the plot.

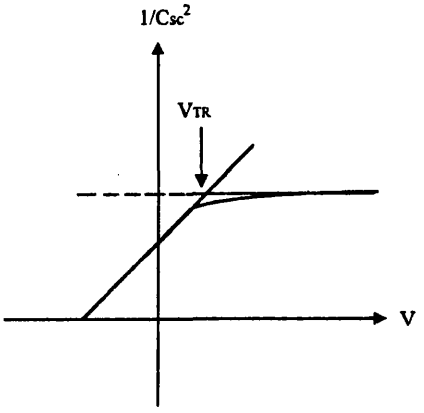

Figure 2.13. Mott-Schottky plot showing the transition from space charge to geometric capacitance at V_{TR}

2.8. Absorption of Light and Photocurrent Generation in Semiconductors

2.8.1. Optical Properties of Crystalline Solids

The response of a crystal to an electromagnetic field is described by the dielectric function $\varepsilon(\omega,k)$ which depends sensitively on the electronic band structure of that crystal. Studies of the dielectric function are made using optical spectroscopy which yields information on the band structure of semiconductors. This may at first seem surprising, as absorption and reflection bands of crystals are broad and often featureless functions of photon energy (for $E>E_g$). However when derivatives are taken of the reflectance or absorbance with respect to electric field in the case of modulation spectroscopy highly, structured spectra are obtained that can be related to the band structure of the crystalline material.

The dielectric function is not directly accessible experimentally from optical measurements. The directly accessible functions are the reflectance $R(\omega)$, the refractive index $n(\omega)$, and the extinction coefficient $K(\omega)$. To obtain a more detailed picture of the optical properties of a solid we must see how the complex dielectric function given in equation 2.34 relates to the reflectivity or absorptivity from a crystal surface.

$$\varepsilon = \varepsilon'(\omega) + i\varepsilon''(\omega) \tag{2.34}$$

where ε' is the real and ε'' the imaginary component of the dielectric function. The complex refractive index **n** of a solid is given by

$$\mathbf{n} = \mathrm{n}\text{-}i\mathrm{k} \tag{2.35}$$

where n represents normal refraction, and k the absorption strength. The refractive index is normally taken as a real number, but at wavelengths where some absorption occurs, it is convenient to represent the absorbance as an imaginary contribution to **n**. The proportion of light reflected from the solid is given by

$$\mathrm{R} = \frac{(1-\mathrm{n})^2 + \mathrm{k}^2}{(1+\mathrm{n})^2 + \mathrm{k}^2} \tag{2.36}$$

We can now relate $\mathrm{n}(\omega)$ and $\mathrm{k}(\omega)$ to the dielectric function $\varepsilon(\omega)$ by

$$(\varepsilon(\omega))^{1/2} = \mathrm{n}(\omega) + i\mathrm{k}(\omega) \equiv \mathbf{n}(\omega) \tag{2.37}$$

Kramers Kronig analysis is then used to determine the variation in phase (θ) of the reflected wave as an integral over the reflectance $\mathrm{R}(\omega)$ [16]. From equations 2.36 and 2.37 $\varepsilon'(\omega)$ and $\varepsilon''(\omega)$ may also be determined. By plotting the real and imaginary components of the dielectric function versus wavelength it is shown that the peak in the imaginary

part of the dielectric function corresponds to the region of strongest absorption, i.e. the band-gap.

2.8.2. Charge Transfer under Illumination

In a semiconducting material, where there is an energy gap between the filled valence band (VB) and the empty conduction band (CB), only photons with energy greater than the gap will be absorbed. Photons of longer wavelength will pass through having insufficient energy to excite an electron. In photocurrent spectroscopy and voltammetry we follow the onset in the absorption by measuring the variation in the current/voltage due to charge carrier generation with wavelength. The threshold energy for optical absorption corresponds to the band-gap (E_g).

Optical transitions between the valence band and conduction band are governed by the selection rule $\Delta k=0$. Transitions are only allowed between Bloch functions with the same wavenumbers. This selection rule may alternatively alternatively be expressed as forbidding changes in the momentum of the electron undergoing the transition. For a direct gap semiconductor, where the top of the valence band and the bottom of the conduction band correspond to orbitals with the same value for **k** space, the lowest energy transition between the bands is allowed. This is the case for the Group II-VI materials studied here (CdS, CdTe, CdSe). For an indirect material such as silicon, the lowest energy transition requires a change in wavenumber, and so is forbidden ($\Delta k\neq 0$). However the forbidden transitions are observed, although more weakly than allowed ones. The **k**-selection rule breaks down as it depends on lattice periodicity which is broken by lattice vibrations. Absorption coefficients for direct and indirect processes are typically $10^5\ cm^{-1}$ and $10^3\ cm^{-1}$, respectively [17]. Values of the optical absorption

coefficient for thin films electrodes can be derived from optical transmission and reflection data using the expression

$$T = (1 - R)^2 \exp(\alpha L_f) \tag{2.38}$$

where R represents the fractional reflection and L_f is the film thickness. For a direct band gap material with parabolic bands, α is related to E_g by

$$\alpha = C(h\nu - E_g)^{1/2} \tag{2.39}$$

where C is a constant. The band gap is determined by extrapolation of the linear portion of the plot of $\alpha h\nu^{1/n}$ versus $h\nu$ to the energy axis. The exponent n assumes the values of 0.5 for a direct allowed transition, and 2 for a indirect allowed transition. In this chapter we shall only consider direct-gap semiconductors where n=1/2.

2.8.3. Charge Carrier Generation in an Illuminated Semiconductor

Illumination of a semiconductor ($E>E_g$) results in the generation of electron-hole pairs. In the *n*-type case under depletion conditions, the electron (majority carrier) moves towards the back contact and the hole (minority carrier) to the front surface where its fate may be determined by a number of charge transfer processes. Charge separation in a semiconductor takes place in two regions.

(a) Space Charge Region (thickness = W). The potential drop across this depleted layer drives holes to the surface and electrons into the bulk of the semiconductor.

(b) Diffusion Layer (thickness = L). This is the layer in which photogenerated holes can diffuse to the edge of the depletion layer where they are collected and transfered to the interface

These two characteristic lengths are illustrated in figure 2.14.

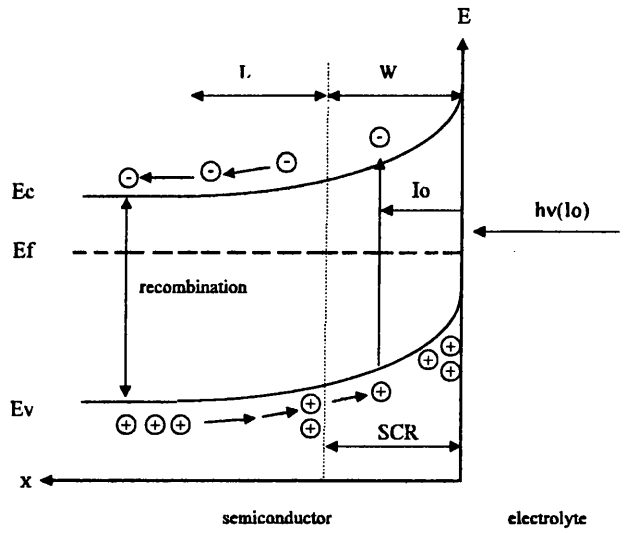

Figure 2.14. Schematic diagram for an *n*-type semiconductor under depletion showing the various carrier processes that take place under illumination.

The thickness of the depletion layer for a homogeneously doped semiconductor is given by

$$W = (2\varepsilon\varepsilon_o / qN_D)^{1/2}(E - E_{fb})^{1/2} \qquad (2.40)$$

where N_D is the donor density, E the applied potential, and E_{fb} the flat band potential. The thickness L of the diffusion layer is determined by the lifetime, τ, and mobility, D, of the photogenerated holes ($L = (\pi D\tau)^{1/2}$). For high quality low doped semiconductors,

the diffusion length may be several microns whereas for low doped defective materials it may be a few nanometers [18]. At the semiconductor electrolye interface holes may undergo charge transfer processes associated with photodecomposition of the semiconductor lattice or with a electron exchange involving a redox species in solution

The original expression describing charge carrier generation and collection at an illuminated semiconductor under depletion was obtained by Gärtner [19]. For a description of the Gärtner model the reader is directed to a review by Peter [20]. However this represents the case for a metal contact to the semiconductor (Schottky configuration). Butler [21] subsequently used the Gärtner model to fit the behaviour of the semiconductor electrolyte interface. The flux of minority carriers is given in equation 2.41.

$$j_{min} = I_o\left(\frac{1-\exp(\alpha W)}{1+\alpha L}\right) \tag{2.41}$$

where I_o is the incident photon flux after correction for reflection losses, $L = (\pi D\tau)^{1/2}$ is the minority carrier diffusion length, W is the depletion layer width, and α the absorption coefficient. Equation 2.42 may be used to define the photocurrent conversion efficiency Φ

$$\Phi = \frac{j_{min}}{I_o} = 1-\left(\frac{\exp(-\alpha W)}{1+\alpha L)}\right) \tag{2.42}$$

A summary of the assumptions made in the derivation of equation 2.42 [20] are as follows:

(a) Complete collection of minority carriers takes place from the space-charge region (no space chargerecombination)

(b) no surface recombination

(c) no contribution of trapped electrons or holes to the total space-charge, which is attributed with only ionised doping levels.

(d) semi-infinite crystals (no influence of the back contact)

The above treatment corresponds to the case where the thickness of the sample, L_f, is greater than all the characteristic lengths. This is the case for thick single crystalline semiconductors. However, for thin semiconducting films a different description is required in which the magnitudes of W, L, and $1/\alpha$ are compared with the film thickness, L_f.

If the thickness of the film is similar to the penetration depth of the light as is often the case for anodic layers grown on metals, a portion of the incident light will be reflected at the film/metal interface and pass through the film for a second time. An additional current may also arise due to excitation of electrons from the metal to the film. In Bi_2O_3 films grown anodically on Bi, Metikos-Hukovic [22] has observed a contribution to the cathodic photocurrent from photoemission processes involving the excitation of electrons from the Bi electrode into the oxide overlayer.

If the film thickness is less than the width of the space charge region, the applied electric field stretches across the whole of the film, and as a result, the term associated with the diffusion of minority carriers (holes) can be ignored and equation 2.42 becomes

$$\Phi = I_o[1 - \exp(\alpha L)] \qquad (2.43)$$

For minimal rates of charge carrier recombination in the space charge region and at the film surface, the photocurrent therefore depends linearly on the flux of photons absorbed by the film. Although space charge recombination may not be important in single crystalline semiconductors, high densities of defects are expected in polycrystalline thin films (grown by anodic or cathodic electrodeposition, or by the chemical bath route). Figure 2.15(a) illustrates the effect of recombination on the photoresponse of an illuminated semiconductor and the equivalent response modelled by the Gärtner equation. Information on the kinetics of charge carrier generation and decay can be obtained by analysis of i-t transients such as those illustrated schematically in figure 2.15(b). However, the lack of consideration of recombination effects in the Gärtner theory is highlighted by the absence of structure in the i-t trace.

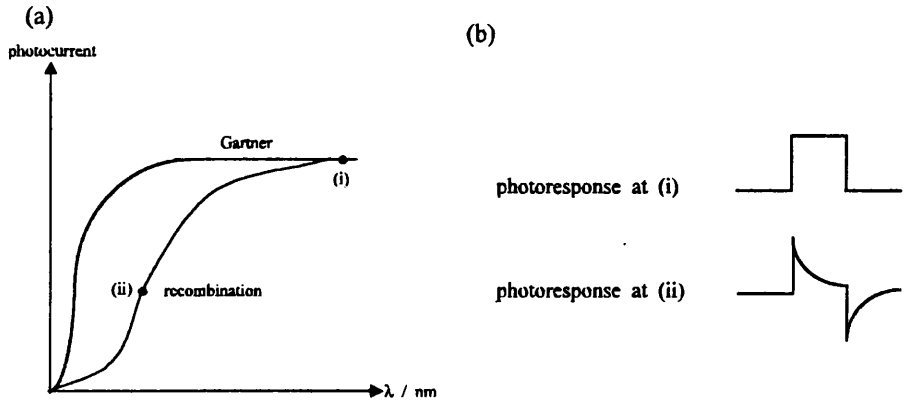

Figure 2.15. (a) Schematic representation of the experimental photoresponse (dotted line) and the equivalent response modelled by the Gärtner theory (solid line) for a semiconductor under illumination. (b) Current-time transients recorded at points (i) and (ii) in (a).

Lemasson[23] subsequently used a modified form of the Gärtner equation to determine the flatband potential

$$J_{min} = I_o \alpha (L_p + W) / (1 + \alpha L_p) \qquad (2.44)$$

where $\alpha W << 1$. If $\alpha L_p << 1$ then equation 2.44 becomes

$$j_{min} = I_o \alpha (L_p + W) \tag{2.45}$$

In addition if the minority carrier diffusion length is much smaller than the width of the space-charge region (i.e. L_p+W) the photocurrent is given by

$$j_{min} = I_o W \alpha \tag{2.46}$$

$$j_{min} = 2I_o \alpha^2 \varepsilon\varepsilon_o (E-E_{fb}) / N_D \tag{2.47}$$

Plots of j_{min}^2 versus E may be extrapolated to give values for the flatband potential. Such plots are equivalent to Mott-Schottky plots scaled by the absorbance coefficient and in principle they offer an alternative method for the determination of doping densities. However unless $L_p << W$, appreciable differences between the values determined by the two methods arise.

However there are a number of limitations to the Gärtner model. The reason for this lies in the assumptions found within the theory which for many systems are invalid. The most important process that leads to a substantial deviation in the photocurrent response between experiment and theory is the recombination of charge carriers either in the bulk or at the surface of the electrode. In the following section a semi-qualitiative description of recombination will be given.

2.8.4. Recombination Processes

A number of models that have been presented to describe recombination come under the heading of quasi-equilibrium theories of space-charge recombination [24].

In all cases, if the rate of charge transfer at the semiconductor surface is sufficiently small, the build-up of minority carriers in the space charge region will lead to recombination. The flux in the region 0<<x<<W may then be related to equation 2.48

$$dJ/dx=G(x) - R(x) \tag{2.48}$$

where G(x) and R(x) are the generation and recombination rates of minority carriers, respectively. G(x) is given by

$$G(x) = \alpha I_o(\exp(-\alpha x)) \tag{2.49}$$

Following the integration of equation 2.48 several assumptions are necessary which depend on the particular model applied to the system before evaluation of the integral $\int_0^W R(x)dx$. The three main models used to determine the effects of space-charge recombination are those of El Guibaly and Reichmann [25,26], Hanemann and Mcann [27], and Albery *et al* [28]. Details of these approaches have been given by Peter [20].

We can divide recombination processes as taking place either in the bulk or at the surface of the electrode. If the electron-hole pair created by illumination is not separated by an electric-field, recombination will occur via a radiative or non-radiative route. The radiative mechanism depends on the occupancy of the electronic states before and after the electron and hole recombine. In the case of non-radiative recombination, electron-hole recombination takes place at regions with bulk defects, or impurities. These may be located at any position in energy between the valence and conduction bands. In bulk

recombination, the non-radiative process is far more likely as the probability of energy emission is considerably higher than emission by one large single step.

A further important recombination process concerns the fate of photogenerated carriers in anodically grown films (e.g. CdS) on metals (e.g. Cd). In these films the substantial long range disorder leads to a range of defective states between the two bands reducing the efficiency of charge carrier separation. The incorporation of impurities from the metal substrate and the metal-film interface itself also contributes to processes which limit high photocurrent conversion efficiencies.

Surface recombination effects are dominated by the presence of surface states. Much speculation exists on the actual nature of these states. They may be electronic, ionic, or structural entities, all of which have a high affinity for trapping electrons and holes. Surface states may be classified as extrinsic or intrinsic. Extrinsic states are created when a new phase is formed at the sample interface, e.g. when an oxide forms or when the electrode comes into contact with an electrolyte. Intrinsic states arise from the abrupt termination of the crystal lattice at the electrode surface. From this a dangling bond arises which may react with a solution species and subsequently behave as a surface state [8].

Using steady state photocurrent techniques it is difficult to distinguish between the many recombination processes described above. Peter *et al* [29,30] have developed time resolved photocurrent techniques in order to allow deconvolution of these processes. The authors have developed a mathematical model to show the influence of surface recombination on photocurrent voltage characteristics by investigating the response of the semiconductor electrolyte interface to light modulation. This technique is known as Intensity Modulated Photocurrent Spectroscopy (IMPS).

2.9. Modulation Spectroscopy

Modulation spectroscopies are powerful methods used for the study and characterisation of many of the important parameters of bulk and thin-film semiconductors. The techniques are based upon introducing a small periodic perturbation in some physical property of the sample and then measuring the differential change in the optical response of the material using phase sensitive detection. The differential changes in the optical constants are very small, typically 1 part in 10^5. These small changes can be related theoretically to a derivative of the absolute spectrum with respect to the modifying parameter. Herein lies one of the principal advantages of modulation spectroscopy, i.e. it yields sharp, derivative optical spectra corresponding to interband transitions, and suppresses background effects. Because of its derivative nature, a large number of sharp spectral features can be observed even at room temperature (298 K). The modulation of semiconductors by a small ac potential perturbation will be discussed here. Other sources of perturbation include heat pulse [31] (thermomodulation) and stress [32] (piezomodulation).

A great amount of work has been published on the topic of modulation spectroscopy. Important contributions to the field have been made by Aspnes [33,34], Blossey and Handler [35], Polak and Shen [36], Cardona [37] and Raccah [38]. Shen and Pollak [39] have recently provided an excellent and comprehensive review of modulation spectroscopy, including a section on electrochemical modulation spectroscopy.

2.9.1. Origin of the modulated response

To understand the origin of the modulated spectra we must consider the correlation between optical absorption processes and semiconductor band structure [3,35]

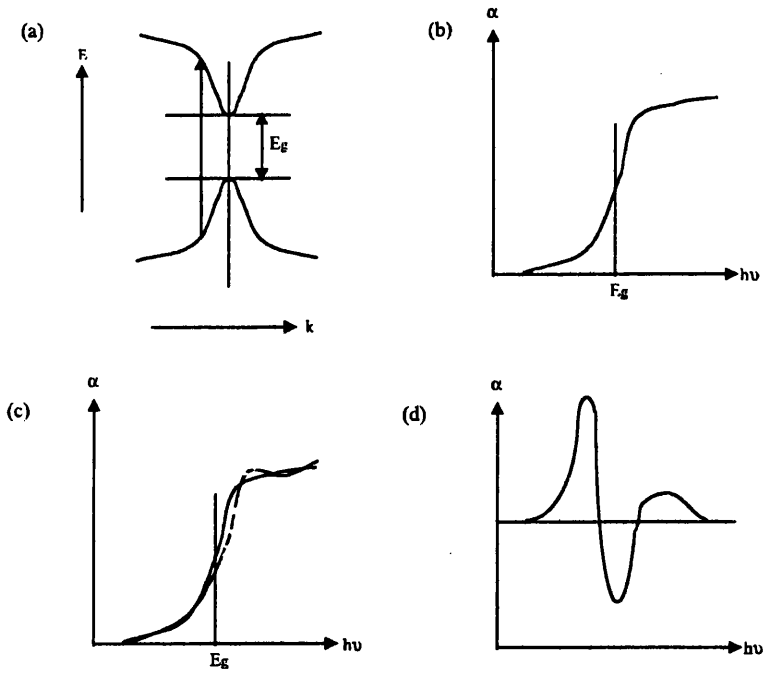

Figure 2.16. Absorption spectrum and its correlation with band structure: (a) two-band semiconductor. (b) absorption spectrum, (c) finite- (dashed line) and zero- (solid line) field case, (d) modulated electroabsorption spectra (After Blossey and Handler [35])

Figure 2.16(a) shows a simple parabolic band structure where absorption of a photon leads to a direct electronic transition. The resulting absorption spectrum is shown in figure 2.16(b) with a thermally broadened absorption edge. We must then consider how an externally applied field modifies the absorption spectrum. The change with applied field is shown as the broken line in figure 2.16(c). The oscillatory behaviour arises from the fact that the absorption coefficient which is proportional to the probability of creating an electron-hole pair shows electric field induced oscillations. Figure 2.16(d) shows the type of experimental spectra obtained. EEA spectra correspond to the difference in value between the two curves shown in 2.16(c). The exact shape of the curve shown in 2.16(d) depends on the degree of ionicity, the crystal structure of the compound and the relative strength of the external electric field with respect to the coulomb integral. In this example the change in the imaginary component of the dielectric constant is illustrated but experimentally we determine either the field induced change in transmittance ($\Delta T/T$)

for thin film samples or reflection ($\Delta R/R$) for single crystal samples. In each case third derivative spectra are obtained. In the next section a more quantitative description of the modulation effect will be discussed.

Modulation of some perturbation of a semiconductor material gives rise to differential changes in the reflectivity of the sample. This can be related to the perturbation of the complex dielectric function $\varepsilon(=\varepsilon_1+i\varepsilon_2)$ as given in equation 2.50

$$\Delta R/R = a(\varepsilon_1,\varepsilon_2)\Delta\varepsilon_1 + b(\varepsilon_1,\varepsilon_2)\Delta\varepsilon_2 \qquad (2.50)$$

where R is the reflectivity, and $\Delta\varepsilon_1$ and $\Delta\varepsilon_2$ are the changes in the real and imaginary components of the dielectric function. The quantities a and b are known as the Seraphin coefficients and are functions of the unpeturbed dielectric constant [40]. In general a and b are non-zero quantities but near the band-gap of the bulk semiconductor, $b\approx 0$. Equation 2.50 therefore simplifies to

$$\Delta R/R \approx a(\varepsilon_1, \varepsilon_2)\Delta\,\varepsilon \qquad (2.51)$$

The effects of external modulation on $\Delta\,\varepsilon_1$ and $\Delta\,\varepsilon_2$ can be divided into two categories. The first case is where the perturbation does not destroy the translational symmetry of the material and so electrons are not accelerated. In this case the lineshape is first derivative as is found in thermo- and piezomodulation. Where translational symmetry of the solid is removed by the perturbation and charge carriers are accelerated, the lineshape is related to the third derivative of the unpeturbed dielectric function. These two cases are illustrated in figure 2.17.

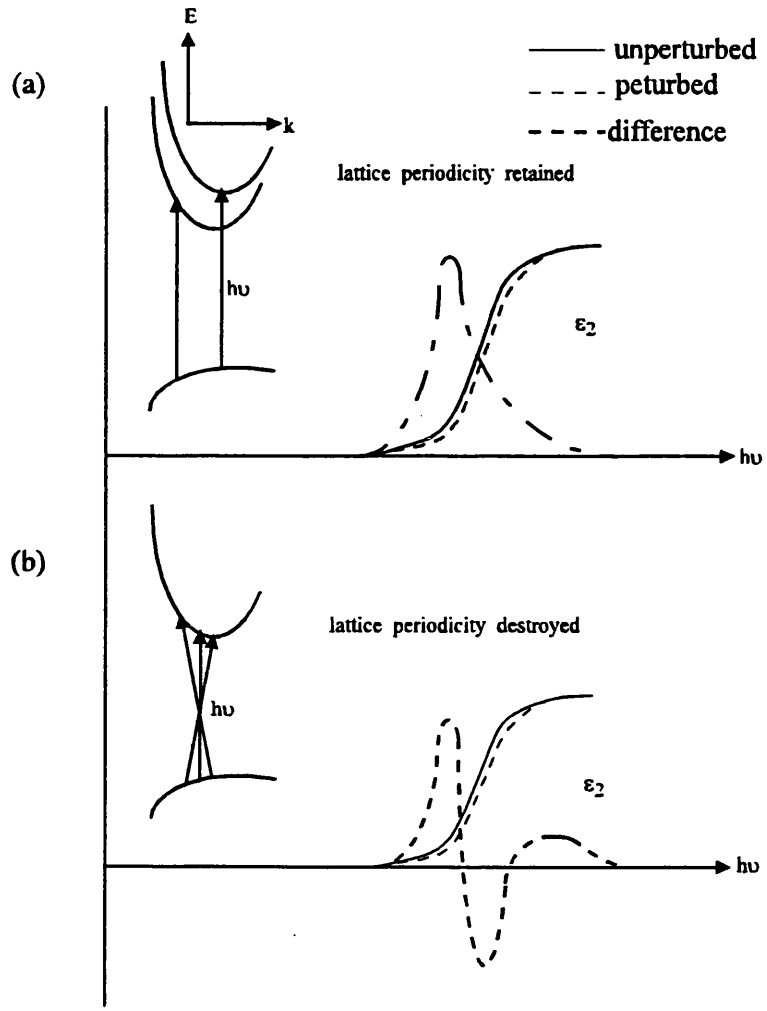

Figure 2.17. Schematic diagram showing the effect of changes in lattice periodicity have on the imaginary dielectric constant, ε_2. Case (a) corresponds to piezo- or thermomodulation and (b) to electromodulation

The electroreflectance effect has been modelled using first order perturbation theory by D. E. Aspnes [33] in the low-field regime and is described as follows. The Hamiltonian term for an electron in a crystal is given by H_o. The change in the complex dielectric function is obtained by adding a perturbation term, H' to the Hamiltonian, H_o, of the unperturbed crystal lattice. The change in the complex dielectric constant may then be calculated by first-order perturbation theory. If H' is not lattice periodic as in the case of electromodulation, the translational invariance of the Hamiltonian in the field direction is destroyed. This is the principal reason for the complex nature of ER spectra and accounts for the relationship between low-field ER spectra and the third derivative of the unpeturbed dielectric function.

Electromodulation can be classified into low-, intermediate-, and high field regimes depending on the strength of the applied field with respect to the characteristic energies of the solid. The three ranges for electroreflectance spectra are classified in terms of the relative strengths of the perturbation and system energies for interband optical absorption processes. Table 2.1 compares the energy $\hbar\Omega$ of a particle of mass $\mu_{||}$, which is accelerated in a uniform field with the broadening parameter Γ which determines the width of the EEA structure. The former can be thought of as indirect measure of the strength of the applied field.

Range	Interband Perturbation	Identifying Spectral Characteristics
Low	$(h\Omega)\leq\Gamma$	Invariant line shape scaling with E^2
Intermediate	$(h\Omega)\geq\Gamma$	Franz Keldysh Oscillations. Exponential absorption edge
High	$(h\Omega)>>\Gamma$	Stark shifts. Selection rules modified

Table 2.1. Summary of electromodulation field regimes and identifying spectral characteristics

We will now consider the origin of the first and third derivative spectra.

The Hamiltonian term for an electron in a crystalline lattice is given by equation 2.52.

$$H_o = p^2/2m + V(r) \qquad (2.52)$$

If the system is perturbed by an electric field, lattice periodicity is lost and a perturbation term H' is added to the Hamiltonian where H' = εE.r. The electron will experience a position dependent potential which accelerates it in one direction. The momentum conservation rule for optical transitions is thus weakened and non-vertical transitions

become allowed. This is equivalent to spreading the formerly sharp vertical transitions over a finite range of initial and final momenta. This is illustrated in figure 2.17(b). For small applied fields, transitions close to the fundamental gap will smear out structure in the unpeturbed dielectric function giving a difference spectrum with a number of sign changes. For electroreflectance under low field conditions this is approximated by a third derivative form with two crossing points. In the case where no external modulation is applied to the sample, momentum is still a good quantum number to within a reciprocal lattice vector. Optical transitions therefore remain vertical. This is illustrated in figure 2.17(a). This represents a first order change and is approximated by a first derivative line shape.

When the low-field criterion is not satisfied, the dielectric function exhibits Franz Keldysh oscillations (FKOs). This regime has been described by Pollak *et al* [41] for a zero broadening parameter and by Studna [42] and Aspnes [43] with broadening. The intermediate field case considers the interaction of a photon with an electron tunnelling from the valence to conduction band, with the width of the energy barrier being reduced by the electron-photon interaction. The probability of transmission through the barrier is given by equation 2.53

$$T = \exp\left(-\int k\, dz\right) \tag{2.53}$$

where

$$\frac{\hbar k^2}{2\mu_{\|}} = E_g - E - qFz \tag{2.54}$$

Integrating equation 2.54 gives

$$T = \exp[-(4/3)\eta^{3/2}] \tag{2.55}$$

with

$$\eta = (E_g - E)/\hbar\theta \tag{2.56}$$

Equation 2.55 shows that for E>Eg the transmission probability becomes oscillatory. The more quantitative expression to model FKO's developed by Aspnes and Studna is given by equation 2.57.

$$\Delta R/R \alpha \exp[-2(E-E_g)^{1/2}\Gamma/(\hbar\theta)^{3/2}]x\cos[(4/3)(E-E_g)^{3/2}/(\hbar\theta)^{3/2} + \chi][E^2(E-E_g)]^{-1} \tag{2.57}$$

where Γ is the broadening parameter and χ is an arbitrary phase factor.

The high field limit corresponds to the breakdown of selection rules, Stark shifts of energy bands, and first derivative contributions to ER spectra similar to those obtained with other modulation techniques. This limit is rarely obtained in practice.

2.9.2. Determination of band structure

Low field electroreflectance spectra may be described by a generalised resonance line shape function of the form

$$\Delta R/R = \mathrm{Re}[Ce^{i\theta}(E - E_g + i\Gamma)^{-n}] \tag{2.58}$$

where C and θ are amplitude and phase factors. n is the lineshape factor and depends on the critical point type. For a 2D, 3D, or excitonic critical point n assumes the values 3, 2, or 2.5, respectively. The bandgap (E_g) and broadening parameter (Γ) determine the energy location and width of the structure. The amplitude (C) and phase (θ) factors

determine the amplitude and asymmetry of the lineshape. The bandgap and broadening parameters can be determined directly from the experimental lineshape using a third derivative fitting function (TDFF) developed by Aspnes and Rowe [44].

The TDFF is based on fitting the lower energy extremum A, with co-ordinates ($\Delta R/R_A$,E_A), the higher energy extremum B, with co-ordinates ($\Delta R/R_B$,E_B), and the base line ($\Delta R/R$). From the asymmetry factor given in 2.59 we E_g and Γ are determined using equations 2.60 and 2.61

$$\rho = -(\Delta R / R_B)(\Delta R / R_A) > 0 \tag{2.59}$$

$$E_g = E_A + (E_B - E_A) f(\rho) \tag{2.60}$$

$$\Gamma = (E_B - E_A) g(\rho) \tag{2.61}$$

The terms $f(\rho)$ and $g(\rho)$ are plotted in figure 2.20 as a function of the asymmetry ratio ρ for the three critical points. From ratioing the peak heights, the asymmetry ratio may be calculated and values of E_g and Γ determined.

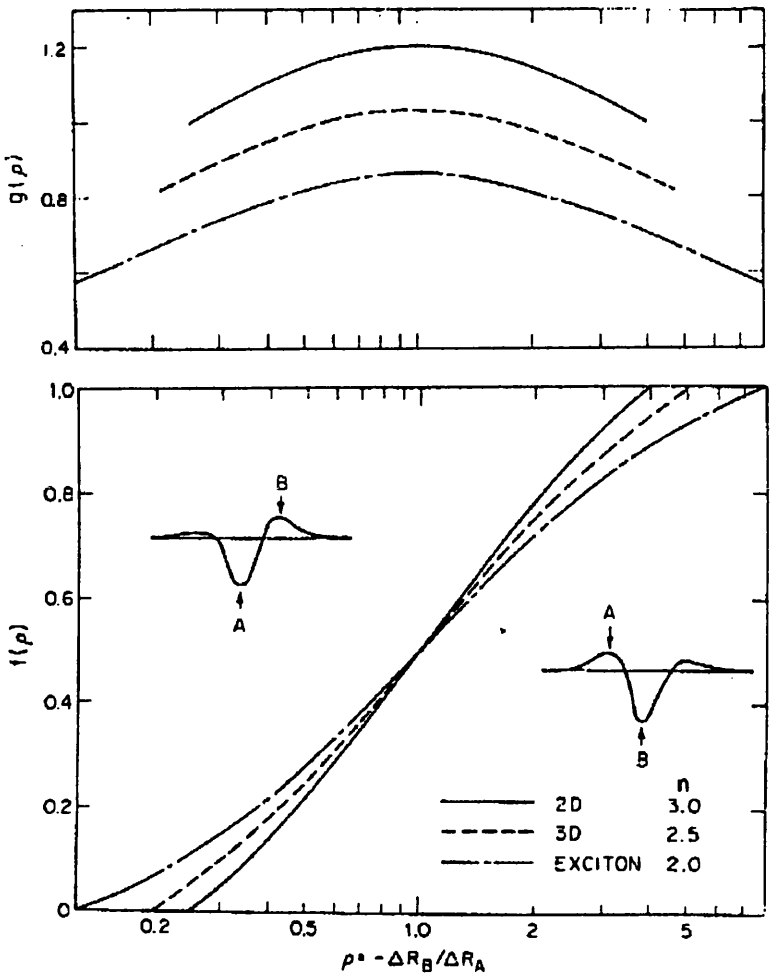

Figure 2.18. The functions f(ρ) and g(ρ) necessary to determine the critical point energy and broadening parameter in terms of the asymmetry ratio ρ (After Aspnes [33])

However there are a number of uncertainties in applying this generalised line fitting function to experimental spectra. In the low-field regime, the lineshape is expected to be independent of the applied dc bias. However in many cases lineshape changes or "spectral rotation" away from the characteristic third derivative form take place. This makes quantitative analysis difficult. The two principal explanations for this are (i) excitonic broadening which will be dealt with in section 2.9.4. and (ii) field inhomogeneities which will be discussed below.

2.9.3. Inhomogeneity and broadening effects

The appropriate form of the dielectric function used to model modulation spectra depends on whether the broadening is inhomogeneous or homogeneous in which case Lorentzian or Gaussain representations are used, respectively. The first case is almost universally applied in the interpretation of modulation spectroscopy results although in certain cases the use of Gaussian line shapes or a combination of both broadening representations can lead to substantially improved fits. The origin of inhomogeneous broadening lies in two effects: (i) inhomogeneity in the space charge layer due to the varying electric field with thickness and (ii) inhomogeneity due to local charge effects. These both result in a poor correlation between theory and experiment. The two effects are discussed below.

(i) Inhomogenity due to the variation of potential within the space charge layer

The lineshape analysis assumes that the electric field and therefore ε is constant across the space charge region. In practise these two parameters vary with distance away from the surface. It is particularly important to include the inhomogeneity of the electric field for band gap transitions, because the low absorption coefficient allows the incident light to penetrate far into the semiconductor and sample a wide range of fields. A number of attempts have been made by different groups to model this effect. Aspnes and Frova [45] used a first order perturbation approach to calculate $\Delta R/R$ for a small change in $\Delta\varepsilon$ that disappears at large distances away from the surface. Analysis showed that inhomogeneity can be considered to mix the contribution of ε_1 and ε_2 to $\Delta R/R$. Although this theory is the most widely used treatment of the effect of inhomogeneity on electroreflectance, it cannot be applied to non-normal incidence or to structures that contain sharp dielectric boundaries, such as semiconductors with a surface layer.

Hamnett *et al* [46] presented a more flexible approach based on dividing the space charge layer into a series of layers or "slabs" within which the electric field varies linearly. The number of "slabs" was simply increased until the calculated spectral structure became stable. From their analysis they conclude that certain structures are due to multilayer optical reflections rather than excitonic processes. However, Shen and Pollak [47] using an analytical integral scheme, found no structure due to field inhomogeneity. Jackson and Seebauer [48] revealed a similar conclusion based on solving the inhomogeneous field case by several methods, including that by Hamnett *et al* [46]. An interesting comparison was made between broadening due to an inhomogeneous field distribution and that associated with excitonic transitions for the ER response of *n*-GaAs near to E_o. Behm and Röppisher [49] concluded that owing to the same dc potential dependence of both mechanisms of "spectral rotation", there is no simple way of distinguishing between them.

(ii) Inhomogeneity due to local charge

In addition to the electric field varying across the space charge layer with thickness, the field may also vary locally within this region. The presence of defects, impurities, bound states, and strain can all lead to local variations in the applied field in the semiconductor and therefore changes in ε. By considering that the field distribution is small compared to the total field, various authors have derived first order expressions for the distribution of ε. These interactions that have been considered negligible in previous theoretical treatments, give rise to two additional signals, one proportional to a first order derivative and another to a second order derivative of the dielectric function with respect to energy. The experimental electroreflectance spectrum is a linear combination of these. Raccah *et al* [50] has suggested tentatively that these terms may be interpreted in terms of electrostricture and polarisation of the defects, respectively.

Application of these lower order terms gives substantially improved fits. However with two or more parameters in the description it becomes possible to over-interpret the data. Similarly it seems doubtful whether it is useful to consider an additional contribution from Gaussian lineshapes which has also been suggested for inhomogeneous broadening [50].

Electric field inhomogeneity is not only important in the bulk but also at the electrode surface. The effects of surface inhomogeneity have been assessed by scanning a focused laser spot across the electrode surface and measuring the localised electroreflectance response. Early studies measured inhomogeneity in $\Delta R/R$ on a $\approx$100 μm scale [51], although in a more recent study made by Salvador *et al* [52] on the localised EER response of WSe_2, the resolution was the order of $\approx$10 μm.

It is evident that there are many uncertainties when lineshape theories are used to extract the band gap and broadening parameter from electroreflectance spectra. However, in this work comparisons have been made between spectra recorded for samples grown or treated by different methods. In this case it is the relative rather than the absolute values of these quantities are of interest. In spite of the complex third derivative nature of electroreflectance spectroscopy, excellent fits between experiment and theory are obtained in many cases. However this highlights the need for a physical explanation of this effect for which many theories have been developed. Often the ER response of a system can be fitted to a several different theories, suggesting either that the experimental ER response is a complex superposition of the each of the individual effects modelled, or that the given system is insensitive to the additional parameters which have been incorporated into the particular theory.

2.9.4. Excitons

An exciton is an excited electron hole state where the electron does not escape fully into the conduction band, but remains trapped in the electrostatic potential of the hole left behind in the valence band. Excitons can be classed into either Frenkel or Wannier types. In the first case the exciton is small and tightly bound as is observed in highly ionic or molecular crystals where the electrons are bound to lattice sites. In the second case, the exciton is weakly bound where the electrons are shared amongst lattice sites, as is found in covalently bonded crystals. Excitons formed in the group II-VI semiconductors are considered to be somewhere between the localised and non localised type. The peaks observed in electroabsorption or reflectance spectra are due to either band-to-band transitions, excitonic transitions, or a combination of the two. The contribution of excitons to absorption spectra is shown by the presence of peaks near the band edge. Not all solids show such excitons, but in many of those that do, such as CdS, they are only seen at low temperatures where free carrier formation by exciton dissociation does not occur ($E_{exciton} > kT$).[3]

In the case of CdS, the presence of excitons leads to a change in the third derivative lineshape as the electrode is biased towards depletion. This makes quantitative analysis according to Aspnes TDFF an uncertain process. To understand why we must firstly consider the band structure of CdS. The valence band of CdS is divided into three two-fold-degenerate levels by the spin-orbit interaction and crystal-field splitting. This gives rise to 3 excitonic transitions originating in each of the three valence bands at k=0 [53]. Peaks are also obtained which relate to energy levels of exciton states bound to various types of crystalline defects. Figure 2.19 shows an electroabsorption spectrum reproduced from that measured by B. B. Snavely [54] for polycrystalline CdS at 4.2 K at a field strengths comparable to those used here.

Additional structure is clearly evident in the electroabsorption spectrum at this temperature. However for CdS the situation is further complicated by the fact that the electroabsorption spectrum exhibits a lineshape very similar to that expected for an interband optical transition.

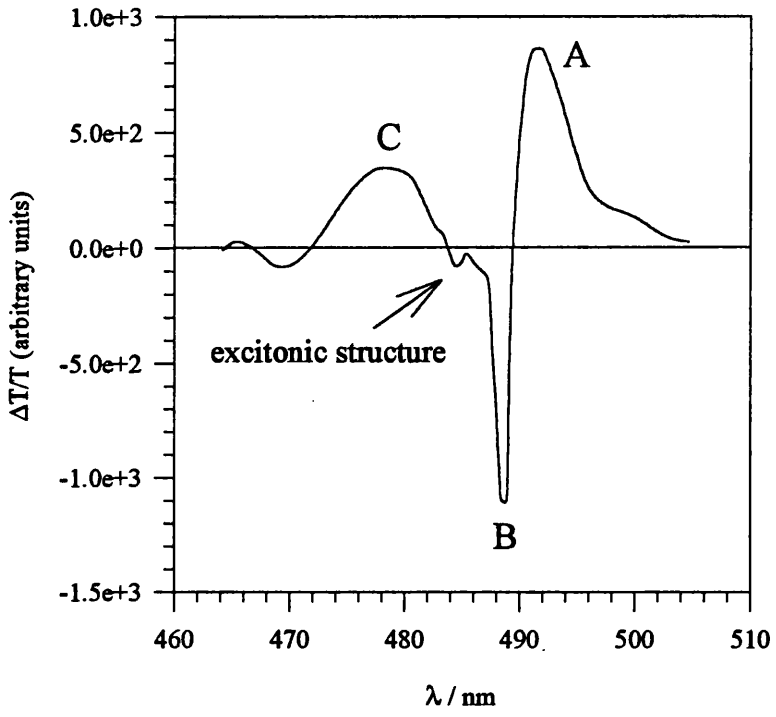

Figure 2.19. Electroabsorption spectrum of thin film CdS at 4.2 K. Exciton energies deduced from thin film optical absorption spectra at 4.2 K are indicated by the arrows (After Snavely [54])

For band-to band electroabsorption it has been shown by Chester and Fritsche[55] that the energy and width of the peak corresponding to the fundamental transition (E_o) changes with applied electric field strength. For CdS neither the position nor the width changed. As the energy and width was independent of the electric field, the electroabsorption does not seem to be associated with band-to-band transitions at a E_o type critical point. It was concluded that electroabsorption must therefore be associated with excitons.

Many workers have attempted to provide physical explanations for the origin of the intrinsic (bulk) and extrinsic (bound) excitonic effects [56, 57, 58] however, because of the close proximity of the two lower energy exciton lines, the electric field effect on either line is not independent of the other [59]. The electric field can cause mixing of exciton states making it a very complicated theoretical problem. It is likely that this is the reason why very little work has been published on the modulation spectroscopy of CdS.

2.10 Electrodeposition

2.10.1. Introduction

Group II-VI compound semiconductors such as CdSe, CdTe, and CdS are important in a wide range of optoelectronic application ranging from solar cells to IR windows and more recently quantum dot structures [60,61,62,63]. Until now films of these materials have mainly been synthesised by a range of techniques including vacuum deposition [64], spray pyrolysis [65], chemical vapour deposition [66], slurry painting [67], and molecular beam deposition [68]. Electrodeposition offers a simple and viable alternative to these cost intensive routes [69,70]. A noteworthy example of the acceptance of electrodeposition is in the commercial BP "Apollo™" CdS/CdTe solar cell. Here CdTe is electrodeposited onto CdS giving cell efficiencies of up to 10% under A.M 1.5 illumination [71]. The advantages of electrodeposition are as follows:

(i) Large areas [72]: Electrodeposition onto large and complex areas is easily achieved. In the BP Solar "Apollo™" cell [71], CdTe is electrodeposited onto substrates 30cm square with excellent stoichiometry and uniformity.

(ii) Low cost [73]: Apart from the much lower equipment costs compared with vacuum deposition apparatus, the most obvious advantage is in terms of the energy saving. The electrodeposition of many materials takes place at 80°C or lower. Deposition baths can also be used for very long periods and only small amounts of tellurium need to be added to the bath to maintain the Te(IV) concentration.

(iii) Toxicity: Chemical vapour deposition (CVD) techniques are based on the thermal decomposition of highly toxic and often air sensitive organometallic precursors such as tetramethyl cadmium. Electrodeposition involves the use of easily handled stable precursors in the condensed phase

In this chapter an overview will be given of the fundamental aspects of electrodeposition as well as the mechanisms of film growth or electrocrystallisation which are responsible for the macroscopic properties of electrodeposited films.

Either cathodic or anodic methods may be employed in aqueous media for film formation by electrodeposition. The first approach is based on the co-reduction at a suitable substrate (cathode) of the metal ion and chalcogen. The second approach is based on the corrosion of a metal (anode) in a chalcogenide environment. In the present work, the cathodic electrodeposition of CdS and CdSe and the anodic deposition of CdS were investigated. These processes will be used to illustrate the theory of electrodeposition.

(i) Cathodic processes

In a cathodic process a solution species is reduced by the transfer of electrons from the cathode, for example

$$H_2SeO_3 + 6H^+ + 6e^- \rightarrow H_2Se + 3H_2O \quad (2.62a)$$

In the formation of CdSe this is followed by the reaction with Cd^{2+} ions

$$Cd^{2+} + H_2Se \rightarrow CdSe \quad (2.62b)$$

(ii) Anodic processes

Conversely charge transfer may be an anodic process where a metal electrode (anode) is oxidised by the removal of electrons. For example

$$Cd \rightarrow Cd^{2+} + 2e- \quad (2.63a)$$

Anodic CdS films may be formed by the reaction with S^{2-} ions

$$Cd^{2+} + S^{2-} \rightarrow CdS \quad (2.63b)$$

Electrocrystallisation is used to describe the process of phase formation associated with reduction of ions in solution or by oxidation of a metal electrode and subsequent reaction with anions. Electrocrystallisation on a foreign surface may involve several steps which are illustrated in figure 2.20 [74].

(i) Transport of solvated ions through the solution to the electrode surface

(ii) Electron transfer

(iii) Formation of adsorbed atoms (ad-atoms) by partial or complete loss of the solvation cage

(iv) Surface diffusion of ad-atoms

(v) Critical nuclei formation by ad-atom clustering

(vi) Incorporation of ad-atoms at lattice sites

(vii) Growth of nuclei by mechanisms

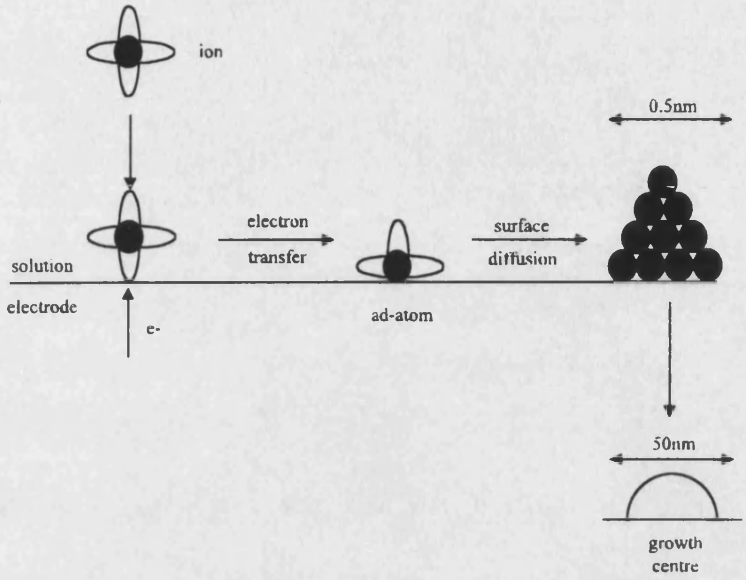

Figure 2.20 Mechanisms involved in the electrocrystallisation on an atomically smooth surface of a foreign substrate

To understand the mechanisms of film growth and the features found at a macroscopic level, the later stages of electrocrystallisation, in particular the formation of nuclei, are of interest. The term electrochemical nucleation refers to the formation of a new phase resulting from electron transfer to ions and subsequent generation of ad-atoms that cluster together to form critical or unstable nuclei on either a perfectly smooth or foreign surface. Electrocrystallisation has many features in common with the growth of a solid phase from its supersaturated vapour. The theory of electrochemical nucleation has been developed from previous considerations made on the thermodynamics and kinetics of vapour phase growth[75].

2.10.2 Electrodeposition of Elemental Semiconductors

Many of the parameters in the electrodeposition of elemental semiconductors are similar to those encountered in the electroplating of metals. In the following section these have been grouped into thermodynamic and kinetic considerations.

(i) Thermodynamics

Electrochemical deposition and dissolution of metals obeys the following general stoichiometric equation

$$[M(z)L_xS_y]_{(aq)} + ne^- \leftrightarrow [M]_{(s)} + [xL]_{(aq)} + [yS]_{(aq)} \quad (2.64)$$

where M is the metal atom, L atoms or atomic groups or molecules of a ligand, S solvent molecules (H_2O) and n is the number of electrons exchanged from the metal to form an anion in the reverse reaction (dissolution), and the corresponding number of electrons required to neutralise the metal ion in the case of cathodic electrodeposition. The multistep nature of metal electrodeposition is influenced by the presence of complexing groups of ligands and solvent molecules around the central metal ion. Only for special conditions (very low pH, absence of complexation) is the species a simple solvated metal ion.

The Nernst equation for reaction 2.64 is given by

$$E_m = E^\circ_m + RT/nF \ln (a_M^{n+}/a_M) \quad (2.65)$$

where E_M is the equilibrium potential of the metal electrode in a given solution, E°_m the standard reduction potential, and a_m^{n+} and a_m, the activities of M^{n+} metal ion in solution

and M in the deposit, respectively. The truly reversible potential of metals, reflecting the equilibrium described by the overall reaction 2.64, can only be established if the following conditions are fulfilled.

(i) Processes involved in the transformation of M^{n+} to M in the lattice are considerably faster than other competing electrochemical reaction of the solvent or other spurious redox processes involving impurities or additives in the solution.
(ii) All soluble intermediate species are present in the solution at equilibrium concentrations.
(iii) The element M is pure and a well defined phase.
(iv) The deposited crystal grains are in their equilibrium (standard) state
(v) The crystals are not too small (i.e. negligible surface energy effects)

In many cases these prerequisites are overlooked in experimental studies of metal deposition and dissolution, leading to ill defined reference potentials in studies of electrode kinetics. For example, it is well known that the properties of metals are affected by small amounts of additives. In the case of steel, the properties may be "tuned" by the addition of relatively small additions of other metals, or minute quantities of C, S, or N which become incorporated into the metal phase. The role of these impurities has been found to be important in the kinetic behaviour of steel electrodes [76].

The influence of crystal size on potential was determined by Kaischew [77] who related the size of the critical nucleus and its equilibrium form to the overpotential. It was found that the smaller crystals had more negative (cathodic) equilibrium potentials.

This may be explained with the aid of equation 2.66 which enables the deviation of the standard potential from the equilibrium potential to be determined.

$$\Delta E = -\Delta(\Delta G)/nF \qquad (2.66)$$

All the above cases of deviation arise from a free-energy change different from that underlying the reversible potential. In equation 2.67 the overall free energy change of the system is determined by contributions from the bulk and surface.

$$\Delta G = (-)\Delta G_{bulk} + (+)\Delta G_{surface}$$

(2.67)

Therefore as crystals decrease in size an increasing contribution of $\Delta G_{surface}$ to ΔG will occur. According to equation 2.67, the reversible potential should shift to more negative values. Fulop and Taylor [78] found that shifts of less than 1 mV were observed for crystallite sizes greater than 25 nm. However, it has been emphasised that the equilibrium between the supersaturated phase above the electrode and the small crystal is metastable and the smallest change of its dimensions can make it either grow or dissolve under the applied overpotential. Although the above conditions are rarely met in practice, Kröger [79] has introduced the concept of "quasi" rest potentials to explain the zero current conditions obtained at potentials shifted from the equilibrium value (E_e). This displacement may be due to a number of factors, for example deviations in deposit morphology or composition from the pure well defined phase. However, lateral variations in these properties create regions of potential difference across the electrode surface over which local anodic and cathodic currents may flow. The zero current

measured at the "quasi" rest potential therefore reflects the current in the external circuit rather than at the electrode surface.

In practice, electrodeposition of M usually occurs at potentials more negative than the equilibrium potential. The additional potential required is $(\eta) = E\text{-}E_m$. This is known as the overpotential. An overpotential may be required for the element to deposit so as to overcome a kinetic barrier associated with phase formation on a different substrate. The overpotential is therefore necessary to drive the kinetics. An important term in the electrochemical formation of a phase on a substrate of the same or different material is the free energy term included in equation 2.66. More elaborate treatment of this enables free energy curves to be calculated for the electrochemical nucleation of a monolayer deposit of a metal on a substrate of the same material. This is illustrated in figure 2.21 [74]. The formation of nuclei of a new phase is always an improbable event which must be forced to occur. This is because small centres of any phase are thermodynamically unfavourable and should redissolve (compare with section 2.11 on the formation of CdS clusters by chemical bath deposition). This is illustrated in equation 2.68.

$$\Delta G_{NUC} = \Delta G_{SURFACE} + \Delta G_{BULK} \qquad (2.68)$$

Small centres are unstable as $\Delta G_{SURFACE}$ is positive and is proportional to surface area, whereas ΔG_{BULK} is negative (under supersaturation conditions) and proportional to the volume of the phase. Owing to the high surface area / volume ratio of the nuclei, ΔG_{NUC} becomes positive. Stable nuclei are formed when they reach a critical size due to rapid ad-atom addition on the substrate surface. The initial stages of film growth are promoted by a very high concentration of ad-atoms favoured by using a high

overpotential and a high concentration of metal ions. Overpotential is clearly important as it determines the critical radius and critical free energy of the nuclei formed. In this case, the driving force for the electrocrystallisation of nuclei is the difference between the equilibrium potential and the electrode potential, i.e. the overpotential.

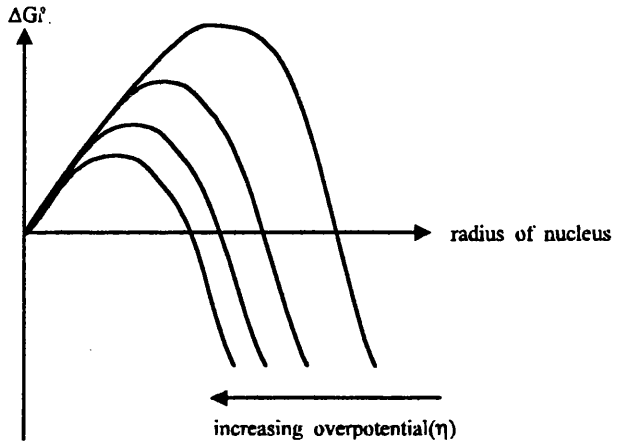

Figure 2.21. Free energy curves for the formation of a monolayer deposit of a metal on a surface of a foreign substrate [74]

Conversely electrodeposition can occur at potentials more positive that the equilibrium potential. The difference in the potential is the underpotential. The driving force for underpotential deposition (UPD) is the formation of a surface phase or compound which is energetically favoured relative to the bulk. This phenomenon can be explained in terms of the existence of a stronger attraction forces between atoms of the depositing material and the foreign atoms of the substrate rather than between atoms of the bulk metal. If the equilibrium potential is considered to reflect the energy needed to take an adatom from the bulk of the metal and transfer it to solution to form the product, the equilibrium established between ad-atoms and the foreign substrate may be used to determine the free energy change associated with the deposition process. Many examples of UPD can be found, for example, Pb on Ag [76] or Cd on Pt [80] . A good example is found in the case of the deposition of Pb on Au where the voltammogram indicates that monolayer deposition occurs ≈400 mV more positive than the bulk

deposition potential of lead [81] (-0.37 V vs SCE). This corresponds to a free energy change of $\approx$ -80 kJmol^{-1}.

UPD can also refer to processes such as the adsorption of hydrogen on a metal, as in the case of hydrogen on Pt [82]. UPD has been used by Stickney *et al* [83] in the electrochemical analogue of atomic layer epitaxy (ECALE) which involves the alternated deposition of atomic layers of elements such as Cd and Te to form high quality, epitaxial compound semiconductors. However, the UPD process is usually limited to a few monolayers. As the deposit thickens, distortions are introduced into the growing layer. Due to lattice mismatch a switch in the growth mechanism to 3-dimensional nucleation occurs. In which case the potential shifts back to normal values. However recently the same workers [84] have deposited a total of approximately 100 layers of Cd and Te atoms using a flow based system in which reagents can be flushed prior to the deposition cycle of the second element. Evidence for epitaxy was found for layers upto 20 nm in thickness.

2.10.3. Electrodeposition of Alloys and Compound Semiconductors

(i) Thermodynamics

The co-deposition of binary, ternary alloy or compound semiconductors can be quite difficult because the conditions favourable for the deposition of one of the metals may differ from the those necessary for the other metals or constituents. Further complications arise if one wishes to achieve a precise control of stoichiometry for the electrodeposited alloy or compound, a critical condition necessary for many semiconductor applications. In general though, interaction between the components in a deposit usually shifts the deposition potential of a deposit to values that are positive

relative to the deposition potential of the less noble element (having a more negative value of the standard potential). A variety of possibilities arise when two or more metals are alloyed together. The exact form of the solid phase depends on both the chemical and electrochemical properties of the individual elements. In the case of metal the phase types that may be formed include (i) eutectic mixtures, (ii) homogeneous solid solutions, (iii) intermetallic compounds, and (iv) alloys. The most important parameter in alloy formation is the stochiometry of the deposit as this determines the bulk properties of the deposit. As the standard potentials for the components in solution are likely to differ from one another, the stochiometry of the deposit will be determined by the standard potential for the less noble metal in the alloy. In equation 2.65 the reversible potential was defined for a pure metal in its standard state ($a_m = 1$). However for an alloy the activity of the metal must be considered according to $a_M = \gamma_M x_M$, where x_M is the mole fraction and γ_M is the activity coefficient. Therefore, for an ideal mixture where $\gamma_m = 1$, the reversible potential for an alloy is given by

$$E'_m = E^\circ_m + RT/nF \ln (a_M^{n+}/x_M) \qquad (2.69)$$

where E'_m is the standard potential of the alloy. This compares with equation 2.65 to give the change of the electrode potential with respect to the pure metal

$$E'_m - E_M = \Delta E = (RT/nF) \ln x_M \qquad (2.70)$$

However this implies the absence of any free energy contributions due to mixing, so few alloys will follow this relationship. The effect of mixing on potential has been determined by Kozin [85] for a series of Cd amalgams of differing composition. The

standard potentials to which they were extrapolated were found to differ considerably from the standard potential of the metal, indicating significant free energies of amalgamation.

If one or more components of the alloy is miscible in the solid, a eutectic is formed. The reversible potential of the alloy in the solution corresponding to the less noble component should be the same as that of the pure, less noble metal. However, eutectics are usually formed of very small crystallites, and hence as previously described, a shift in the potential relative to that of the pure metal is observed.

The third case of alloy which may be formed is an intermetallic compound. The equilibrium potential of a metal alloyed with a component with which it forms an intermetallic compound should be more positive than that of the pure metal as the free energy of formation of the compound, ΔG°_{f}, is always negative, i.e.,

$$\Delta E^{\circ} = -\Delta G^{\circ}_{f} / mnF \qquad (2.71)$$

where m is the stoichiometry coefficient of the metal in the equation of formation. For example zinc, when alloyed with Ag forms AgZn, with $\Delta G^{\circ}_{f} \approx -10$ kJmol^{-1} [76]. Compared to pure zinc, a potential 50 mV more positive due to alloying is obtained.

Important factors in alloy or compound electrodeposition are the reversible potentials of the alloy or compound components, the stability of the resultant deposit, and the activities of ions in solution. From equation 2.65 we can develop the case for the electrodeposition of the compound M_xN_y for which deposition of component M involves x e^- and that of component N y e^-. The equilibrium potentials of M and N are

$$E_M = E^\circ_M + (RT/xF) \ln(a_M^{n+}/a_M) \quad (2.72)$$

and

$$E_N = E^\circ_N + (RT/yF) \ln(a_N^{n+}/a_N) \quad (2.73)$$

The condition necessary to obtain the simultaneous deposition of two different kinds of ions at the cathode can be written as

$$E_M + \eta_{M,iA} = E_N + \eta_{N,iB} \quad (2.74)$$

where $\eta_{M,iA}$ and $\eta_{N,iB}$ are the cathodic overpotentials for the deposition of the two metals at comparable current densities, j_A and j_B, respectively. However, when the standard potentials of metals are far apart, for example where $E^\circ_N < E_M$ two situations can arise according to equations 2.75 and 2.76.

(i) $E^\circ_N < E < E^\circ_M$ Only M deposits (2.75)

(ii) $E < E^\circ_N < E^\circ_M$ Both deposit (2.76)

It is desirable that the two equilibrium potentials potentials are close together in order to achieve a controlled stoichiometry. However where there is a large separation, the deposition potentials may be brought together in the following ways:

(i) adjusting the concentration of the more noble metal ions. For example as Te(IV) is more noble than Cd^{2+}, at the potential where stochiometric CdTe films are obtained (≈ +5 mV vs CdRe), excess Te incorporation in the deposit is avoided by using a very low

concentration of $HTeO_2^+$. As reduction is diffusion controlled, the incorporation of Te in the deposit is determined by the availability of Te(IV) ions at the substrate surface

(ii) Complexation strategies. The activity of discharging metal ions are altered by complexation.

Of particular interest here is the fact that metal ions form complexes with certain components of the solution. The principles behind the complexation of Cd that are relevant to the deposition of CdSe made in this work will be discussed.

The equilibrium constant for the equilibrium established between a metal, M and ligand, L^{n-}, in solution is given by

$$K = \frac{[M(z)L^{(z-n)+}]}{[M(z)^{z+}][L^{n-}]} \qquad (2.77)$$

Common ligands used to complex metal ions include ethylenediaamine tetraacetic acid (EDTA) and nitrilotriacetic acid (NTA). A variety of metal ligand species is formed in solution which participate in equilibria such as those shown in equation 2.78 [86].

$$L^{x-} + Cd^{2+} \leftrightarrow CdL^{2-x} \leftrightarrow CdHL^{3-x} \leftrightarrow CdH_2L^{4-x} \leftrightarrow CdH_3L^{5-x} \qquad (2.78)$$

Each of these species can undergo an electrode reaction according to a corresponding stoichiometric equation of the type

$$[M(n)L^{(z-n)+}]_{(aq)} + ze^- \leftrightarrow [M]_{(s)} + [L^{n-}]_{(aq)}$$

At equilibrium, the electrode potential can be calculated from equations 2.80 and 2.81

$$E = E° + \frac{RT}{zF} \ln \frac{[M(z)L^{(z-n)+}]}{[L^{n-}]} \tag{2.80}$$

$$E = E° - \frac{RT}{nF} \ln K \tag{2.81}$$

where K is the stability constant of the complex. In many cases, under a given set of conditions, a certain species prevails to the extent that concentrations of all others can be neglected. When this is not the case, the concentration of any one of the species may be calculated by solving a series of simultaneous equations using appropriate equilibrium constants.

A particularly important complex interaction with metal ions is the formation of hydroxo- complexes in aqueous solution. In an aqueous solution OH^- ions are always present and their concentration is related to the pH value. Therefore, the presence of hydroxo- complexes is pH dependent and depending on stability constants there are pH regions in which free metal ions are nearly non existent. The effect of pH on electrode potential on M/M^{n+} equilibria is given by a graphical representation known as a Pourbaix diagram [87]. This defines the region of stability of different species involved in the particular metal-water system. Such diagrams represent a useful tool to fix preliminary conditions in electrodeposition and corrosion studies. In the second case they define

conditions under which corrosion of the metal can take place in anaerobic or oxygenated solutions.

2.10.4. Cathodic Electrodeposition

Cathodic electrodeposition is used to deposit a wide range of (i) n-type, (ii) p-type, or (iii) "insulating" or compensated semiconducting materials. In each case it is important that electrons can pass from the cathode through the growing layer to guarantee film growth. However, as the concentration of surface electrons varies between various substrates, different strategies for growth are required. These are described as follows

(i) n-type semiconductor

For growth at potentials ($E°_e$) more negative than flatband (E_{fb}), electrons in the conduction band flow towards the electrode surface to form an accumulation layer. In which case, reduction of species at the film solution interface is not hindered by the availability of electrons. However, in the case where $E°_e < E_{fb}$, deposition requires an overpotential, η. This is associated with the surface density of electrons at a growing deposit and is defined by equation 3.21. This must not be confused with the overpotential required to overcome a kinetic barrier associated with phase formation at a foreign substrate.

$$n_{surf} = n_{bulk} \exp(-q\Delta\varphi/kT) \quad (2.82)$$

where n_{bulk} is the bulk concentration of electrons and $\Delta\varphi$ the band bending ($\Delta\varphi = E_{fb} - E_e$). This case is illustrated well by the reduction of Te (IV) ions according to equation 2.83.

$$HTeO_2^+ + 3H^+ + 4e^- \rightarrow Te + 2H_2O \qquad (2.83)$$

Illustrated in figure 2.23 is a schematic representation of the i-V curves obtained for Te (IV) reduction at glassy carbon (solid line) and CdS (dashed line) cathodes.

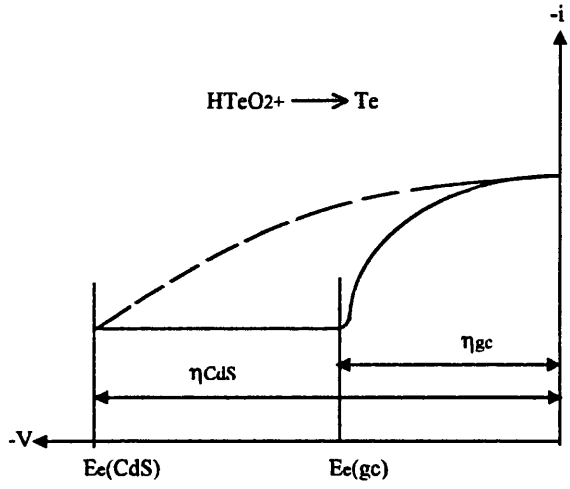

Figure 2.23. Schematic representation of the current voltage behaviour for Te (IV) reduction at glassy carbon (solid line) and CdS (dashed line) electrodes. η_{gc} and η_{CdS} are the overpotential required for growth on glassy carbon and CdS, respectively.

At metallic like substrates such as glassy carbon, the reduction of Te (IV) is not limited by the supply of electrons but rather by electrode kinetics. In contrast, at n-type semiconductor electrodes such as CdS, reduction is controlled by electron supply (majority carriers). In figure 2.23 this is reflected by the sluggish conversion of Te (IV) to Te (0) at the CdS surface. It is therefore important that in the electrodeposition of stoichiometric films such as CdTe, a preliminary assessment is made of the η required to obtain measurable rates of film growth.

(ii) p -type semiconductor

In p-type semiconductors the majority carriers are holes and the surface concentration of electrons is low. In which case the electrode is said to be blocking. Transfer of electrons to the growing deposit can only be achieved under conditions of inversion. In this case ($E^{\circ}_{e} > E_{fb}$), transfer of electrons to the surface can occur as the conduction band moves into the Fermi level. This is generally only possible for highly doped (p^{+}) thin films. An increased surface concentration of electrons cannot be brought about by higher field strengths as dielectric breakdown of the semiconductor will occur. An alternative approach to generating electrons is by illumination of the electrode surface. Hippel and Bloom [88] found in the electrodeposition of p-type Se from selenious acid (H_2SeO_3), reduction ceased in darkness after the formation of a Se layer of $\approx$ 5 nm on the substrate surface. However, under illumination the film continued to grow due to the photogenerated supply of electrons which could participate in H_2SeO_3 reduction.

(iii) Compensated

During the growth of a compensated or "insulating" deposits, the field strength must be continuously increased to maintain measurable rates of film growth. This is observed in the deposition of CdS from a solution of dimethyl sulfoxide (DMSO) containing Cd^{2+} and S [89]. The insulating nature of the deposit is due to its highly nanocrystalline morphology. Because the high density of grain boundaries at the film surface act as traps, electron movement to the solution-film interface is severely restricted. Figure 2.24 illustrates schematically the presence of these traps between the valence and conduction bands.

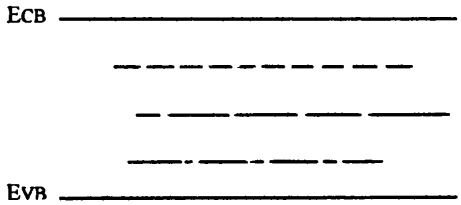

Figure 2.24. Schematic representation of the electron traps (dashed lines) in CdS thin films electrodeposited from dimethyl sulfoxide (DMSO) solution

The effect of an electric field on the movement of electrons in an insulating deposit has been considered by Stimming *et al* [90] in terms of the Poole Frenkel [91] effect. In the zero field case (figure 2.25 (a)), the potential barrier posed by the traps is too high for the electrons to escape. However in the presence of a field the barrier is effectively lowered permitting the thermally assisted tunnelling of electrons out of the traps and towards the film-solution interface to participate in growth (figure 2.25 (b)).

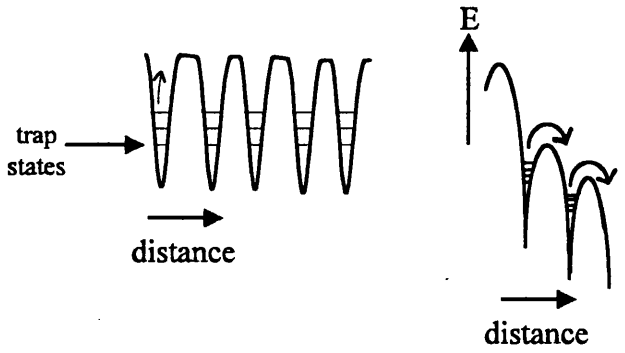

Figure 2.25. Schematic potential energy profiles for electron tunnelling in an compensated deposit at (a) zero field and (b) in the presence of an electric field

2.10.5. Anodic film growth

When anodic oxidation of a metal is followed by chemical reaction with a component present in solution, insoluble substances are formed which coat the surface of the electrode. Considerable attention has been devoted to the study of solid phases formed on metals by anodic electrodeposition, since this involves a number of electrochemical systems of great practical importance, e.g. the dissolution of lead in

lead-acid batteries to form $PbSO_4$[92], the formation of calomel in reference electrodes[93], and the growth of photoactive CdS during the anodisation of Cd in sulfide media[94].

In the early stages of nucleation and growth of an anodic film a thin continuous layer of insulating material is formed at the electrode surface. Such films are said to be passivating and are typically a few nm in thickness. However, as the deposit is insulating, the only way that growth can continue is if ions migrate through the solid phase. This is achieved by using high applied field strengths whereby growth proceeds by *field assisted migration.*

For films such as anodically grown CdS, transport numbers (t) from 1 (highly mobile) to 0 (static) are used to describe the mobility of ions. This reflects that the two components of the film (Cd^{2+} and S^{2-}) have to come from different sides of the deposit to participate in growth. Illustrated in figure 2.26 is a schematic representation of anodic film formation.

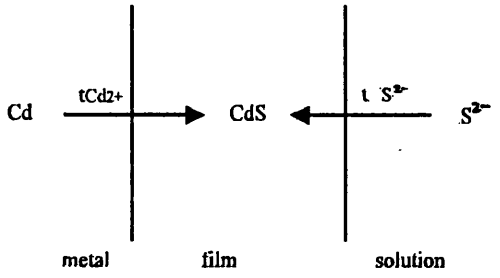

Figure 2.26. Schematic representation of the movement of Cd^{2+} and S^{2-} ions during growth of an anodic CdS layer. t_{Cd}^{2+} and t_S^{2-} are the transport numbers for Cd^{2+} and S^{2-}, respectively

The effect electric field on the mobility of the ions determines whether growth occurs at the film-solution or metal-film interface. In general though it is assumed that film formation occurs by the movement of Cd^{2+} ions or Cd^{+} interstitials in the metal lattice. The potential barrier to ion movement in an insulating deposit is illustrated in figure 2.27

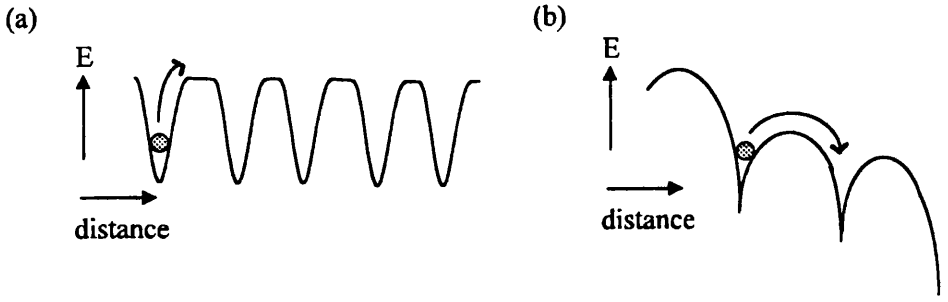

Figure 2.27 Schematic potential energy profiles for ion transport across an anodised layer at (a) zero field and (b) in the presence of an electric field

In the zero field case (figure 2.27 (a)) film growth is prevented as the barrier is too high for ion movement to occur. However, in the presence of a high field the barrier is effectively lowered so that ions are able to cross, resulting in film growth (figure 2.27 (b)). Theories have been presented for the movement of ions over a potential barrier The Cabrera-Mott [95] theory considers the largest energy barrier to be located at the metal film interface (figure 2.28 (a)), whereas in the Verwey [96] theory the rate controlling activation energy barrier is assumed to be within the bulk anodised layer (figure 2.28 (b)). A detailed description of anodic growth theories can be found elsewhere.

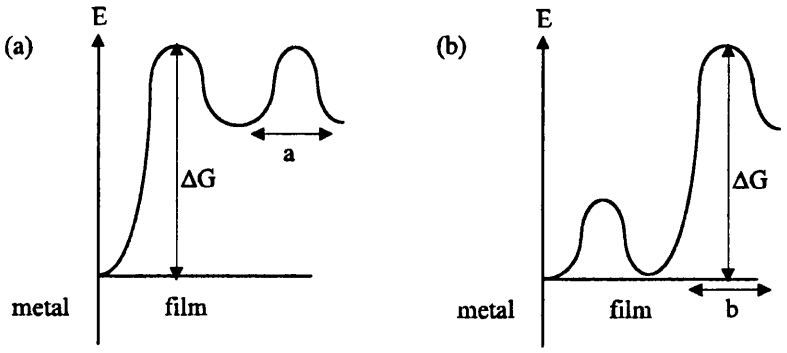

Figure 2.28. Schematic potential energy profiles for ion transport across an anodised film (zero field) showing the cases corresponding to (a) the Cabrera Mott [95] theory and (b) the Verwey [96] theories

As the insulating film thickens it becomes increasingly difficult to move ions through the deposit. To maintain the same rate of growth, higher field strengths must be applied. However, there becomes a point where film cracking occurs due to dielectric breakdown ($E > 10^6\ Vm^{-1}$). This is typical of anodised layers grown in the transpassive region (see chapter 6) This is accompanied by pore formation and the precipitation of S and CdS at the electrode surface. As a drastic change in film morphology occurs, Peter [97] has suggested that growth proceeds by a different electrode process involving the tunnelling of electrons. Similar models have been presented to explain pore formation in anodically grown oxide layers on Al [98]. At sufficiently high field strengths, the valence and conduction bands in CdS bend to such an extent that tunnelling of electrons from the valence band of CdS into the metal surface can occur. Figure 2.29 illustrates this case.

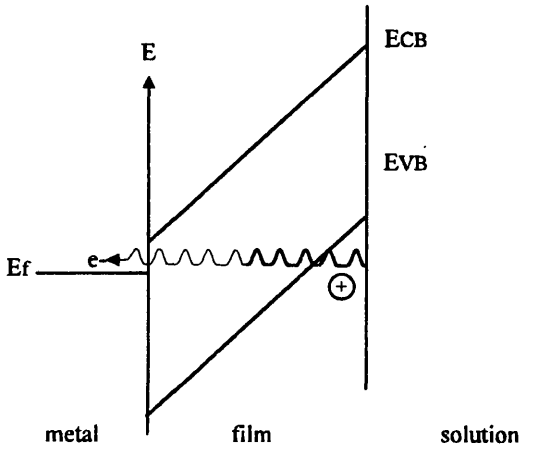

Figure 2.29. Tunnelling of electrons from the valence band (V_{CB}) into the metal surface in a thin anodic film

This leads to the production of a high density of holes at the film surface which result in the dissolution-precipitation shown in reactions (2.84) and (2.85).

$$CdS + 2h^{+} \rightarrow Cd^{2+} + S \qquad (2.84)$$

$$Cd^{2+} + S^{2-} \rightarrow CdS \qquad (2.85)$$

This mechanism is responsible for the formation of S and CdS at the electrode surface. Figure 2.30 illustrates the how these reactions participate in the development of the film morphology in the breakdown regime

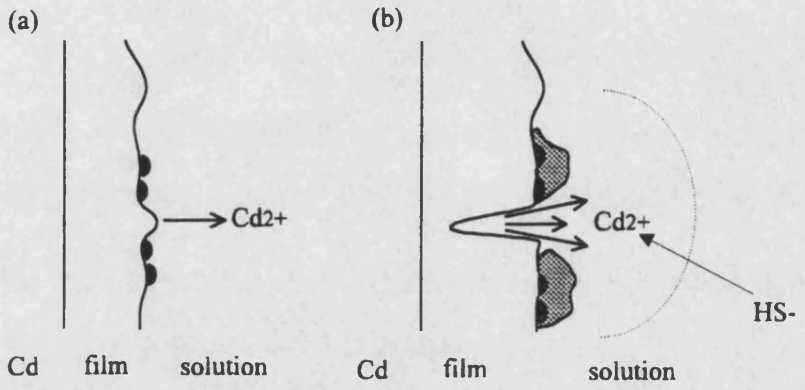

Figure 2.30. Schematic representation of the (a) early and (b) later stages of film dissolution leading to the creation of a pore and the formation of S (black semi-circles) and precipitated CdS (shaded regions)

As the anodised CdS films are not smooth, the strength of the electric field varies at different points across the deposit surface. At protrusions where the field strength is enhanced, an increased rate of film dissolution occurs according to reactions 2.84 and 2.85. (figure 2.30 (a)). At higher field strengths, accelerated localised thinning results in the formation pores at the film surface. The high flux of Cd^{2+} accompanying this combine with S^{2-} ions to precipitate CdS around the pore circumference. In figure 2.30 (b) the shaded regions represent CdS formation. Cross section SEM micrographs have confirmed the presence of pores in CdS films grown in the transpassive regime [97]

The processes described are responsible for the poor film morphology obtained when attempting to grow anodic CdS layers of a useful (≈ μm) thickness.

Film growth is controlled by similar laws as cathodic metal deposition, i.e. oxidation at kinks, nucleation and dendrites all have similar roles to the cathodic case. An example is the kinetics of formation of a calomel film on mercury. The time dependence of the current has been found to obey the case for two dimensional electrocrystallisation.

2.10.6. Electrocrystallisation and Phase Formation

The morphology of an electrodeposited layer is strongly dependent on the crystallographic character of the growing surface which itself is dominated by the structure of the underlying substrate. This can give rise to a particularly complex surface for the growing deposit. As growth proceeds, phase changes at the microscopic level give rise to macroscopic features such as grain boundaries and regions with differing crystallographic orientation. The role of the underlying substrate on film formation will be illustrated by metal deposition on (i) a perfect crystal face and (ii) a real surface with defects.

(i) Metal Deposition on a Perfect Crystal Face

A perfect crystal bound by singular faces exhibits no sites for growth. The only way the layer can grow is by the formation of 2D clusters of ad-atoms giving rise to lattice growth [99]. This is because a single atom deposited on the crystal face has a smaller bond energy to the crystal than for example, a kink atom and so stays temporarily on the surface as an adatom. As these surface atoms cluster together thereby increasing their stability, they are able to act as potential nuclei for subsequent layer growth. This is known as the 2D nucleation mechanism of growth and will be discussed later in this section. However, defect-free crystals with flat atomically smooth

surfaces are rarely found or produced. In the presence of defects, the step connected with defects perpetuates during growth and produces a sufficient number of growth sites to make the 2D nucleation not unnecessary. Budevski *et al* [100] have prepared dislocation free silver surfaces by electrolytically depositing metal layers from a single crystal seed onto the capillary endings of a glass tube. In this way a perfect dislocation free crystal face fitting the whole cross section of the capillary were grown. The preparation technique of dislocation free faces of silver single crystals and their properties have been described elsewhere [101].

(ii) Growth on a defective surface

During phase growth, atoms are incorporated into different sites across the substrate surface. All polycrystalline and most single crystal surfaces present a variety of different features at which lattice growth may occur. The various types of sites first discussed by Kossel and Stranski [102] in the theory of phase growth are illustrated in figure 2.31. These include surface and edge vacancies, kink, edge and surface sites.

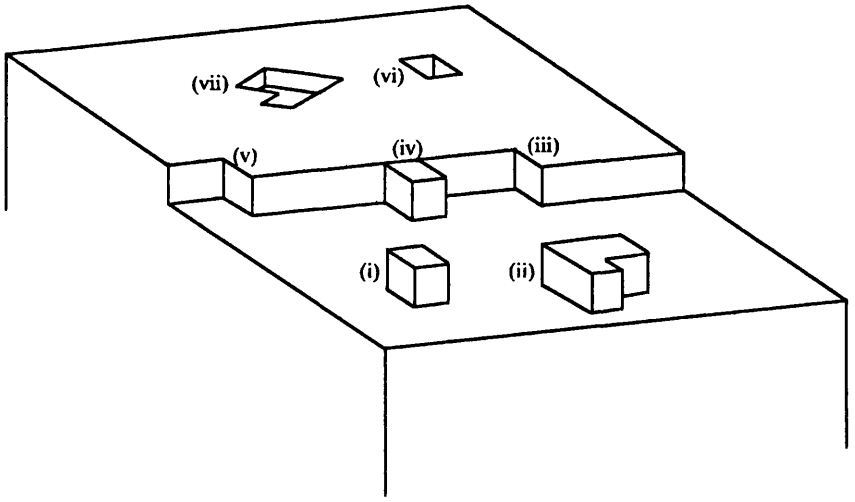

Figure 2.31. The structure of a crystalline singular face and the various types of defects present. (i) ad-atom, (ii) adatom cluster, (iii) kink (half-crystal) position, (iv) edge site, (v) edge kink position, (vi) vacancy, (vii) vacancy cluster [102].

Based upon this formalism, the features that dominate the surface of a metal are as follows.

(i) The crystal faces forming the metal surface are not ideal planes but contain steps
(ii) A kink is formed at the point where one step ends and the next begins, which is of great importance in crystal growth.
(iii) If charge transfer at the electrode surface results in the incomplete or complete loss of the solvation sphere associated with the metal ion, metal ad-ions or ad-atoms are formed, respectively. The atoms inside the crystal have the lowest energy, followed by the atoms incorporated in the crystal plane and then by atoms in steps and kinks and by ad-atoms and ad-ions.

Kinks or half-crystal positions are one of the most important defects playing a role in crystal growth. During the initial stages of growth, two mechanisms have been presented for the incorporation of atoms in steps and for subsequent step propagation.

(i) The metal ion is reduced at the electrode surface to an ad-atom that is transported to a step by surface diffusion. It then becomes incorporated in a kink.
(ii) The metal ion reacts directly with a kink, without an intermediate ad-atom stage

In both cases, the rate of deposition depends on both the current density and overpotential, although in the first case the equilibrium concentration of ad-atoms is important as are the geometrical factors of the surface where ad-atoms are not involved. Rates of electrocrystallisation have been found to differ across the surface of the electrode[76], for example at s screw dislocation type of defect at where faster rates of

lattice growth are observed. During deposition the wedge shaped structure fills up and after completion slowly moves across the crystal face and appears as a spiral. This provides a large number of sites for subsequent growth which no longer requires nucleation and continues at low overpotentials. The most important property of this defect is that as atoms are incorporated into the dislocation, the growth process becomes energetically more favourable.

2.10.7. Nucleation and Growth of Monolayers on Foreign Substrates

The electrode surface reaches a stage where it becomes covered with a large density of nuclei. Interference between diffusion fields of neighbouring nuclei is followed by their physical overlap. Nuclei develop morphology (e.g. cone or hemispherical) which are determined by the interaction between the deposited material, the substrate, and the electrolyte. As growth proceeds there is an increase in area where electron transfer can occur between the substrate and depositing ions. The increase in current accompanying growth is used to deconvolute the processes involved in film formation.

There are several of ways in which the layer can grow. Growth may either be (i) two dimensional when only a monolayer can be deposited without further nucleation or (ii) three dimensional, e.g. as cones or hemispheres where thicker layers can be formed by a continuation of the growth process. Figure 2.32 illustrates these cases

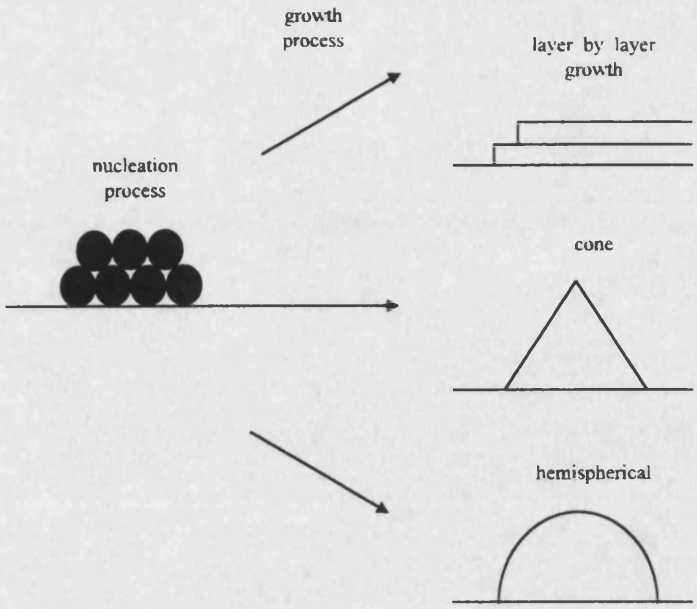

Figure 2.32. Layer-by-layer, two dimensional, and three dimensional growth processes

Each dimensionality of growth may proceed by either *progressive* or *instantaneous* nucleation and growth may occur under kinetic or mass transfer control. A brief description of the major types of growth follows.

(i) Two dimensional growth

Theoretical treatments have considered monolayer growth as a cylindrical centre of constant height growing two dimensionally where the rate determining step in the electrocrystallisation process is the incorporation of atoms at the periphery of the growing centre. Figure 2.33 illustrates this case.

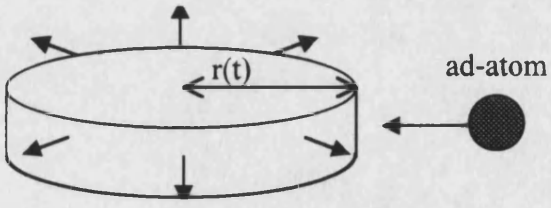

Figure 2.33. Atom incorporation into a growing 2-dimensional centre.

For a single centre the current increases linearly with time for multinuclear growth. However, modifications need to be introduced into the theory to account for overlap.

This is known as the overlap problem and has been treated by the Avarami theorem[74]. If growth proceeds by a layer-by-layer process, oscillations in the current time behaviour are observed. These are shown schematically in figure 2.34(a). The well known process of UPD favours 2D growth, since thermodynamic affinity for the completion of the full layer adjacent to the substrate is larger than that of starting a new layer. However for kinetic reasons, the build up of adatoms of the surface may create a situation where several layers are formed simultaneously on top of each other, preventing further ordered growth.

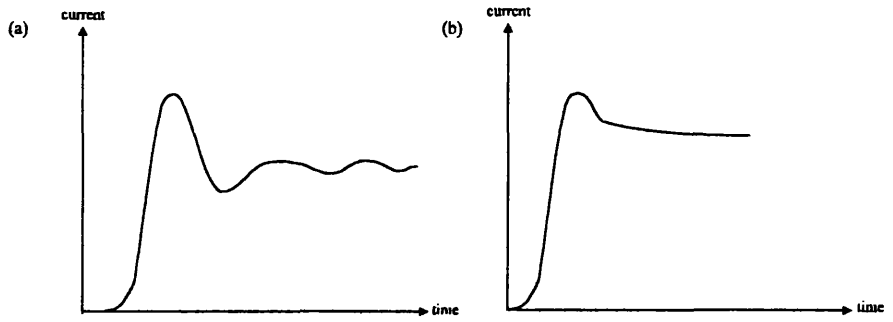

Figure 2.34. Schematic diagram of current-time transient behaviour expected for (a) two dimensional growth on a dislocation free surface and (b) three dimensional growth on a foreign substrate

(ii) Three dimensional growth

The formation of a new phase on a foreign substrate may involve the growth of three dimensional centres. The theoretical current-time behaviour has been predicted for growth centres assuming simple geometrical shapes such as cones or hemispheres. In the first case growth can occur either parallel or perpendicular to the electrode surface with the rate constants k and k′, respectively, as is illustrated in figure 2.35.

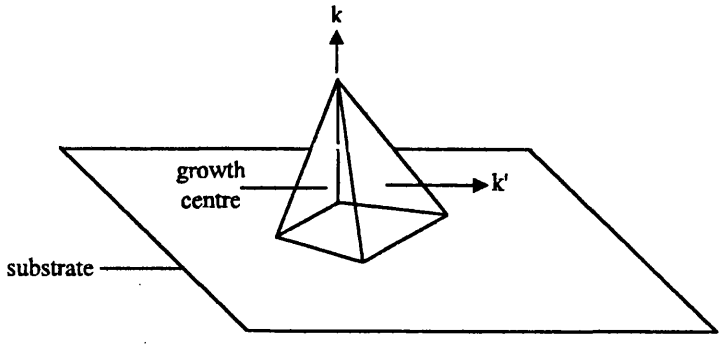

Figure 3.25. Growth of a three dimensional centre represented by a cone. The rate constants k and k' refer to growth parallel and perpendicualr to the substrate

At longer deposition times, overlap of adjacent growing centres occurs which alters the initial rising current behaviour associated with the formation of discrete centres. A schematic representation of the rising current-time transient observed for growth of a cone under diffusion control is illustrated in figure 2.34(b).

Information on the formation of a new phase either on a perfect crystal face or foreign substrate is obtained by fitting current-time curves obtained in potential step experiments to nucleation and growth theories. At short times before overlap occurs, the relationships between current and deposition time t are given by the general form

$$i_t = k\,(t - t_o)^n \qquad (2.86)$$

where k is a constant, t_o is the induction time and n is a particular value for each nucleation and growth system. This relationship is valid in the short time regime (i.e. in the absence of significant overlap of nuclei or diffusion zones). Current transients are plotted as functions of t^n (where n=0.5, 1, 1.5, 2, 3) where n depends on the type of nucleation involved, the geometry of the phase growth, and the rate determining step in phase formation. A more detailed description of the fitting of i-t curves to different types growth processes is given by Gunawardena *et al* [103] and Scharifker *et al* [104].

2.10.8. The Role of the Substrate on Grain Structure and Orientation

As nucleation and growth proceeds, the effect of the underlying substrate on the morphology of the growing substrate is diminished. One of the major features of an

electrodeposited layer is the presence of grain boundaries. These are particularly important in electrodeposited layers used in photovoltaic devices as they act as efficient recombination centres, thus lowering the density of charge carriers. The aim is therefore to grow deposits with large grains and a low density of grain boundaries. Following the initial stages of nucleation and growth, the grain size of the deposit is determined by the number of grain producing dislocation as well as the number of nuclei produced during the deposition process. The larger the density of grain precursors, the finer the grain structure of the deposit will be. The factors which promote the formation of dislocations or nucleation contributing to a reduction in grain size are high overpotentials and/or high current densities which lead to high degree of supersaturation at the surface by adatoms. In addition, disorder in the growing deposit can be brought about by the incorporation of additives or impurities at the surface.

As the layer thickens the influence of the underlying substrate is diminished and the deposit may develop an orientation. A number of theories have been presented for interpreting the origin of orientation. Pangarov [105] has related the energetics of nuclei formation to overpotential, showing that, at different overpotentials, different crystal planes become more or less energetically favourable. If such a condition is maintained, repeated nucleation of the same orientation should produce oriented crystals. Other factors can also promote oriented growth, for example, different rates of deposition have been found on different crystal planes leading to orientation in the growing deposit [106]. Moreover, these effects have been shown to be enhanced by the preferential absorption of foreign molecules at sites across the electrode surface.

2.10.9. Kinetics

There are a number of steps in electrocrystallisation which can control the overall rate. For example, any one or a selection of the steps illustrated in figure 2.20 may determine the overall reaction rate. These may be simplified into three rate determining events.

(i) Transport of the reacting species from the bulk of the solution to the position where charge transfer can take place, i.e. $O_{BULK} \rightarrow O_{ELECTRODE}$ (mass transfer).

(ii) The reaction or reaction sequence leading to a change in the valency of the depositing species, i.e. $O_{ELECTRODE} \rightarrow R_{ELECTRODE}$ (electron transfer, ne^-)

(iii) Transport of the surface species as an atom into the metal lattice.

(iv) Chemical steps such as where the rate of metal deposition is determined by ligand dissociation, for example $ML_n \rightarrow ML_{n-x} + xL$; $Ml_{n-x} \rightarrow M$.

In the case of anodic dissolution, the steps are in reverse order.

In treating the kinetics associated with film growth, a number of assumptions are made so that the rate determining step can be deconvoluted from the many steps that can take place. For example, we can assume that electron transfer and changes in the solvation sphere surrounding the depositing species are rapid. Zeldovich[107,74] has constructed a series of equilibria corresponding to the formation of clusters of adatoms by atom addition from which a steady state nucleation rate was determined.

So far we have considered a perfectly smooth surface, i.e. it is assumed that the sites where nuclei form are all identical. In section 2.10.6 it was shown that a real surface contains a rich array of defect centres, many of which influence the process of nucleation. For heterogeneous nucleation on a foreign substrate we can define N_o as the

number of sites available to participate in nucleation at the electrode surface. In which case the formation of nuclei assumes first order growth kinetics according to

$$N(t) = N_o [1\text{-}\exp (At)] \quad (2.87)$$

where N(t) is the number density, and A is the rate constant for nucleation. Limiting cases of nucleation are termed progressive and instantaneous. In the first case the nucleation rate is proportional to the number of free active sites. If the first order rate constant for the process is low ($A \ll 1$), for progressive nucleation

$$N(t) = N_o At \quad (2.88)$$

At higher values of the rate constant ($A \gg 1$), all of the active sites are occupied by nuclei within a very short time. In this case

$$N(t) = N_o \quad (2.89)$$

The basic treatment of the two limiting forms of nucleation described above have been developed in greater detail for a more rigorous description of 2D and 3D nucleation processes [108]

2.10.10 Mass Transfer

The kinetics of nucleation and growth of a growing layer can be strongly influenced by mass transfer effects for which there are three regimes:

(i) Diffusion. This involves the movement of charged species across a concentration gradient. At the potential where O is reduced to R, a boundary layer forms, over which the concentration of O and R vary away from the electrode surface. As the concentration of R is greater at the surface than in the bulk, R diffuses away from the electrode.

(ii) Migration. This is the mechanism by which charge passes through an electrolyte due to a potential gradient. As the forces leading to migration are purely electrostatic, charge can be carried by any ionic species in solution. The effects of migration on the movement of electroactive species can be minimised by the addition of a large excess of inert electrolyte. This is able to accommodate charge transfer between the anode and cathode.

(iii) Convection. This is brought about by mechanical disturbance of the solution, for example stirring, agitation, or flowing the solution through a cell. Convection effects due to density differences can also be diminished by immersing the cell in a thermostated bath.

The balance between mass transfer and kinetic control is also affected by the overpotential or current density applied to the electrode. At low overpotentials of growth, the diffusion of reagents to the electrode surface is usually fast compared with electron transfer. This leads to the growth of a well defined deposit. If the overpotential

is further increased, the rate of nucleation of additional growth centres rises. This can lead to the formation of a less ordered structure with macroscale features in the deposit. With a further increase in the current density, outward growth of the layer occurs and problems arising from the mass transport control in solution can occur, for example, dendrites or whiskers are formed on the electrode surface. This phenomenon is particularly undesirable in metal finishing operations. Agitation can reduce these effects by lowering the diffusion layer thickness and favour more rapid deposition. For a deposit to be bright, the microscopic roughness of the deposit must be low compared with the wavelength of the incident light so that it is reflected rather than scattered. For example, in the electrodeposition of Ag from its nitrate salt, dendritic growth of the metal is observed as the nucleation and growth is mass transfer controlled. However if Ag is complexed by cyanide ions (as $KAg(CN)_2$ (with excess KCN) then a far smoother deposit forms as the rate of nucleation is controlled by the kinetics of electron transfer [109]. The "quality" of electrodeposits is further improved by the addition of brighteners to the plating bath. In the case of electroplating of Ag, aromatic sulphones or sulphonates are added leading to brighter deposits [110]. These additives are also known as levellers as they eliminate surface irregularities by modifying the nucleation and growth of the metal on the substrate surface.

By varying the mass transfer conditions at an electrode surface, valuable information can be obtained on the kinetics and mechanisms of electrode reactions. In the following section the fundamental aspects of mass transferred controlled growth will be considered at (a) planar and (b) rotating disk electrode geometries.

(a) Linear diffusion at a planar electrode

In the case where the mass transfer of an electroactive species, i, is purely diffusion controlled (i.e. the solution is unstirred and contains an excess of background electrolyte), the simplest model is that of linear diffusion to an atomically smooth electrode of infinite dimensions. In which case, the variation in concentration, c_i, due to diffusion perpendicular to the electrode surface can be characterised by Fick's first law in a one-dimensional form:

$$\text{Flux} = -D_i \frac{dc_i}{d_x} \tag{2.90}$$

where D_O is the diffusion coefficient and x the distance of the species i away from the electrode surface. At the electrode surface (x = 0), equation 2.90 may be used to relate the current flow, I, due to ion movement at the electrode surface to the change in concentration of O (c_O) and R (c_R) according to

$$\frac{I}{nF} = -D_O\left(\frac{\partial c_O}{\partial x}\right)_{x=0} \tag{2.91}$$

$$\frac{I}{nF} = D_R\left(\frac{\partial c_R}{\partial x}\right)_{x=0} \tag{2.92}$$

where D_O and D_R are the diffusion coefficients of species O and R, respectively. Figure 2.36 illustrates the variation in the flux of these species at a planar electrode surface.

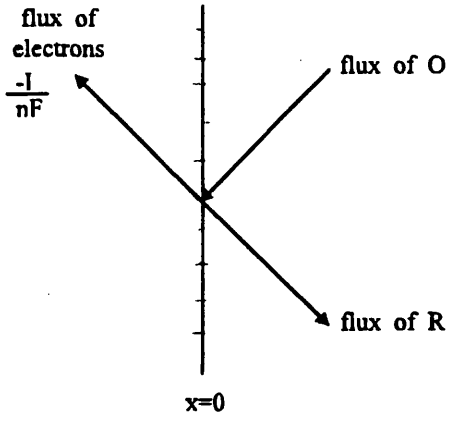

Figure 2.36. Schematic representation of the balance between the flux of O and R at the electrode surface and the corresponding flux of electrons produced following reduction

The region marked from the electrode surface by the dotted line is known as the Nernst diffusion layer (thickness = δ). Over this range the concentration of both O and R differ from the bulk. At the potential where reduction of O occurs, the diffusion layer reaches its maximum thickness ($\approx 10^{-2}$ s) on a time scale of 10 s or less. During this period the concentration changes at the electrode surface are only due to diffusion. However, at longer times, species diffuse away from the boundary layer, so the effects of convection must be taken into account.

The change in concentration of O or R with time due to diffusion is described by Fick's second law. This considers the variation in concentration of an electroactive species at a point, x, located between two planes (x + dx and x- dx) parallel to the electrode, between which diffusion can occur. This gives

$$\frac{\partial c_i}{\partial t} = D_O \frac{\partial^2 c_i}{\partial x^2} \qquad (2.93)$$

By solving equation 2.93 for the appropriate boundary conditions at a planar electrode, the Cottrell [108] relationship is obtained:

$$I = \frac{nFD^{1/2}c_O^{\infty}}{\pi^{1/2}t^{1/2}} \qquad (2.94)$$

From potential step experiments, current-time data can be used to construct plots of I versus $t^{-1/2}$. A straight line that passes through the origin confirms that the electrode reaction is diffusion controlled, and the diffusion coefficient can be obtained from the slope. However, when using the Cottrell [108] equation to test for diffusion control it is important to consider the following points: (i) during the initial potential step, current due to charging of the cell flows in addition to the Faradaic current. In this case a sharp spike at the beginning of the i-t transient is recorded. Since the current at t = 0 cannot be recorded, it is necessary to extrapolate the transient response. (ii) At longer times effects of convection can contribute to the measured current. For these reasons it is important that transients are recorded over a large time scale to ensure currents recorded are principally diffusion controlled.

In the above analysis, the effects of mass transfer have been discussed for electrodes that are not encountered in practise. In reality, wire, disc or drop geometries with less than ideal surfaces are used. However, it has been found that for many electrochemical systems, the solution of diffusion equations for three dimensional surfaces leads to similar conclusions as the one-dimensional model. Details of the diffusion problem at three dimensional electrode surface can be found elsewhere [74].

(ii) Rotating disk electrode.

The rotating disk electrode (RDE) is a more precise method for studying mass transfer. The rate of mass transfer may be controlled over a large range and in a more controlled manor in comparison with potential step techniques. At the centre of the sheath the electrolyte is pulled up to the active electrode and then propelled across the surface radially. Illustrated in figure 2.37 is a schematic diagram of the mode of convection at an RDE. The electrode may be rotated at speeds ranging typically from 10 to 10,000 r.p.m.

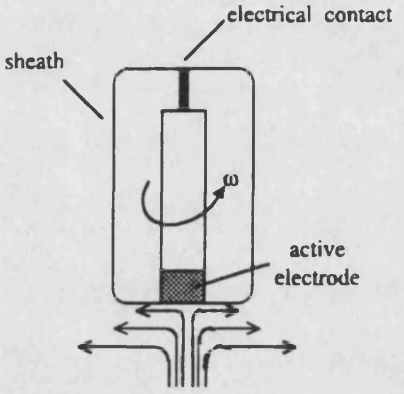

Figure 2.37. Diagram of a rotating disk electrode showing convective flow at the active electrode surface

At the electrode surface, changes in concentration are due to both diffusion and convection. For linear diffusion of an electroactive species to the rotating electrode surface in one dimension, the flux is given by

$$\frac{\partial c_O}{\partial t} = D_O \frac{\partial^2 c_O}{\partial x^2} - V_x \frac{\partial c_O}{\partial_x} \qquad (2.95)$$

where V_x is the velocity of solution movement perpendicular to the active electrode surface. According to Levich [111], the relationship between distance from the electrode surface, x, and rotation rate of the disk, ϖ, is given by

$$V_x = \omega^{3/2} / x^2 \tag{2.96}$$

Therefore, at increasing distances from the electrode surface, the effect of solution movement becomes more important as the velocity rises. Herein lies the important concept that in the boundary layer close to the electrode surface, convection will not be an important form of mass transport and current will solely be due to diffusion. However, outside this layer bulk concentration profiles of O and R are maintained due to high rates of convection. Figure 2.38 illustrates the steady state concentration profiles obtained under this condition.

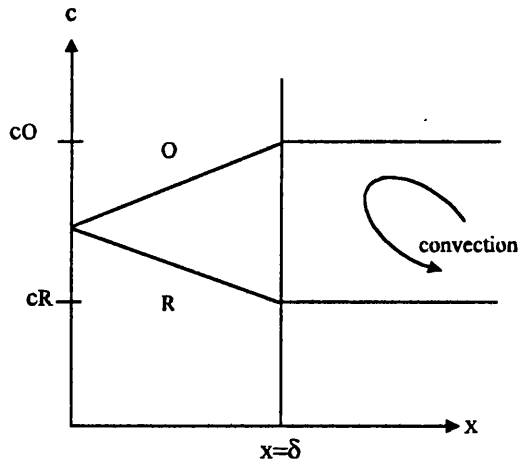

Figure 2.38. Steady state concentration profiles at an rotating disk electrode for $O + ne^- \rightarrow R$

At a given potential the current at the electrode surface is given by

$$I = nFD\frac{c_O^{\sigma} - c_O^{\infty}}{\delta} \tag{2.97}$$

At potentials where the surface concentration of O is zero, Levich [111] has derived a more quantitative expression relating the limiting current density to the rotation rate according to

$$I_L = 0.62nFD^{2/3}\nu^{-1/6}c^{\infty}\omega^{1/2} \qquad (2.98)$$

This expression provides a test that the current is entirely diffusion controlled. By measuring the current over a range of rotation rates, a graph of I versus $\omega^{1/2}$ should be linear, and the slope of the plot can be used to determine the diffusion coefficient of the electroactive species involved

2.10.11. Case Study: The Cathodic Electrodeposition of CdSe

A problem that arises in the cathodic electrodeposition of CdSe from solutions containing seleneous acid is that this may react with cathodically generated H_2Se giving elemental Se in the films, with undesirable effects on its semiconducting properties [112]. This problem has been overcome using alkaline selenosulfite in which Se occurs in a lower valency than seleneous acid [113]. However, in such solutions the Cd ions need to be complexed with NTA in order to avoid hydroxide precipitation and direct reaction between the cadmium and selenosulfite ions.

(i) Cd-H_2O system

The first strategy in devising a route to the electrodeposition of CdSe is to consider the Pourbaix[87] representation for the Cd-H_2O which is given in figure 2.39 for $[Cd^{2+}] = 0.08$ mol dm^{-3}

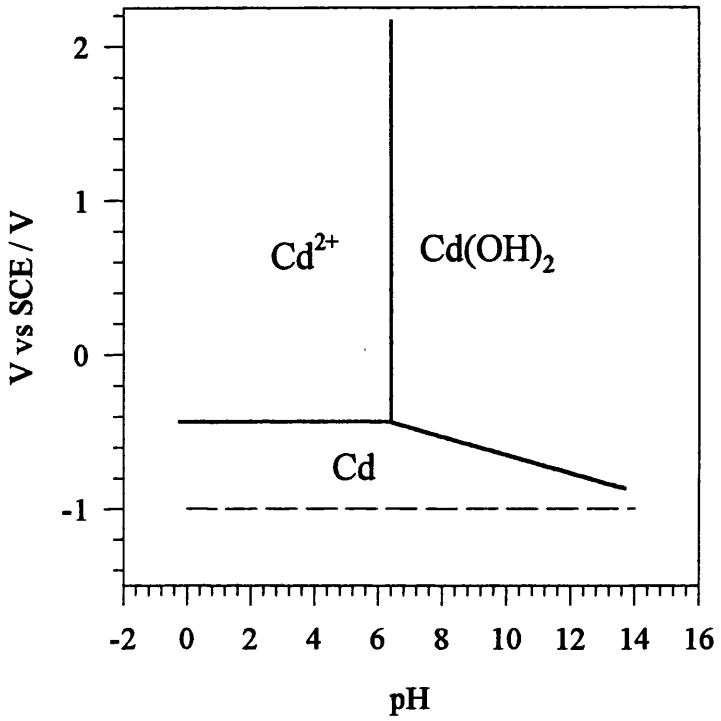

Figure 2.39. Potential-pH diagram for the stable equilibria of the system Cd-H_2O, at 25°C. The dotted line represents the pH independent equilibrium potential for reduction of the $SeSO_3^{2-}$ ion.

The plot was constructed from the following equilibrium relationships that are applicable to the potential pH range in the CdSe electrodeposition bath. The reactions considered are:

$$Cd^{2+} + 2e^- \rightarrow Cd \qquad E = -0.403 + 0.0295\log [Cd^{2+}] \qquad (2.99(a))$$

$$Cd + 2H_2O \rightarrow Cd(OH)_2 + 2H^+ + 2e^- \qquad E = 0.05 - 0.0594pH \qquad (2.99(b))$$

$$Cd^{2+} + 2H_2O \rightarrow Cd(OH)_2 + 2H^+ \qquad \log [Cd^{2+}] = 13.81 - 2pH \qquad (2.99(c))$$

In acidic or neutral solution Cd exists as the colourless Cd^{2+} ions, which is converted into the white hydroxide $Cd(OH)_2$ on increasing the pH of the solution. Depending on the solution pH, $Cd(OH)_2$ formed in equations 2.99 (a) and (b) may also correspond to the formation of "inactive" or "active" $Cd(OH)_2$. These observations have been made from the study of the behaviour of Cd metal in alkaline solution. Huber[87] has shown that the passivating film obtained by the anodic polarisation of Cd consists of $Cd(OH)_2$; the anhydrous oxide CdO initially formed is unstable in water and becomes converted into "active" $Cd(OH)_2$ which turns into "inactive" $Cd(OH)_2$ upon ageing. The $\Delta H_f°$ values for these three compounds are -225, -470, and -473 $kJmol^{-1}$ [87], respectively. Figure 2.40 shows the theoretical diagram of corrosion, immunity, and passivation for Cd. $Cd(OH)_2$ dissolves at high pH to give the colourless bicadmite ion ($HCdO_2^-$) which is the predominant dissolved form of cadmium above pH 11.1.

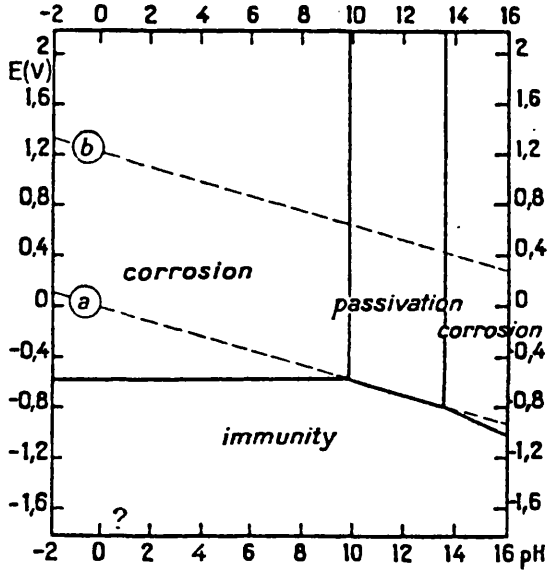

Figure 2.40. Theoretical conditions of corrosion, immunity, and passivation of Cd, at 25°C.

As Cd is complexed by NTA, the Cd-H_2O Pourbaix diagram cannot be used to determine the predominant species at a given potential and pH. However, Lai *et al* [86] have calculated the equilibrium concentration of all species present in the cadmium-NTA system by solving a series of simultaneous equations using appropriate rate constants.

As expected, the distribution of various Cd species depends on the solution pH and the amounts of Cd and chelating agent ions. From the Nernst equation the shift in the Cd/Cd^{2+} potential resulting from complexation may be calculated according to

$$E_{Cd/Cd^{2+}} = E°_{Cd/Cd^{2+}} + (RT/nF) \ln a_{Cd^{2+}} \quad (2.100)$$

since

$$Cd^{2+} + NTA^{3-} \leftrightarrow Cd(NTA)^{-} \qquad K = 6.3x10^{9}\ mol^{-1}\ dm^{-3} \quad (2.101)$$

the activity of the Cd^{2+} may be defined by

$$a_{Cd^{2+}} = \frac{a_{Cd(NTA)^-}}{a_{NTA^{3-}} K} \quad (2.102)$$

Given that there is an excess of NTA^{3-} to Cd^{2+} is the deposition bath, $a_{Cd(NTA)^-} = a_{Cd^{2+}}$. In this case

$$E_{Cd/Cd^{2+}} = E°_{Cd/Cd^{2+}} - (RT/nF) \ln K - (RT/nF) \ln a_{NTA^{3-}} \quad (2.103)$$

Assuming the activity of the complexing agent is unity, from equation 2.103 a shift of ≈250 mV is calculated from the standard potential for bulk Cd. Although it has been suggested that Cd can bind to NTA giving other species which may play a role in the mechanism of Cd reduction, for example $Cd(NTA)_2^{4-}$ and $Cd(NTA)_3^{7-}$, the equilibrium constants for these species have not as yet been determined. At pH≈9, it has been found that $Cd(NTA)^-$ appears to be the predominant solution species [86]. However in the presence of selenosulfite, this may represent a somewhat ideal case as this could form complexes with chelated cadmium which may have quite different properties to

$Cd(NTA)^-$. The possibility of these species participating in reduction to give CdSe will be discussed in Chapter 4.

(ii) Selenium-H_2O

To avoid the incorporation of Se into the films, selenosulfite, prepared by the dissolution of Se in alkaline solution has been used. The presence of excess SO_3^{2-} prevents formation of elemental Se. Free selenide ions, for subsequent reaction with Cd^{2+} ions, are formed electrochemically by the reaction

$$SeSO_3^{2-} + 2e^- \rightarrow Se^{2-} + SO_3^{2-} \qquad (2.104)$$

From a rotating disk study made by Miller *et al* [114], the equilibrium potential for reaction 2.104 was estimated to be -1.0 V vs SCE. A similar study be Toropova [115] obtained a value of -1.06 V vs SCE. Due to the pH independence of reaction 2.104 ,the Pourbaix representation of this equilibrium is given simply by a straight line at ≈-1.0 V parallel to the abscissa (pH). This has been represented by the dotted line included in figure 2.39. However, the Pourbaix diagram suggests HSe^- is also present in the deposition bath suggesting reaction 2.104 may additionally involve a protonated form of Se^{2-}. In which case changing the pH would alter the balance of Se^{2-}/HSe^- in the bath. Due to the scarcity of thermodynamic data on $SeSO_3^{2-}$, the equilibrium potential corresponding to the reduction of selenosulfite was calculated from the free energies for the species listed in table 3.2. Using equation 2.103, the potential calculated on the SCE scale was -1.06 V.

Species	$\Delta G°_{298}$ / kJmol^{-1}
Se^{2-}	+129.3*
$SeSO_3^{2-}$	+199.0
SO_3^{2-}	-486.6

Table 3.2. Values for the free energy of formation for compounds involved in the formation of $SeSO_3^{2-}$ *. From a survey of the literature a range of $\Delta G°$ values are quoted for Se^{2-} formation ranging from +155kJmol^{-1} to +129kJmol^{-1}. The values most often given has been used here.

(iii) CdSe

The use of Pourbaix diagrams to fix the preliminary conditions for the deposition of CdSe has been shown to be inappropriate for the following reasons:

(i) The presence of complexing agents.

(ii) The formation of sulfur/selenium compounds. Little is known about the solution chemistry of these species, for example the pH dependence of their equilibria.

(iii) The pH independence of the E° value associated with the reduction of $SeSO_3^{2-}$.

Figure 2.40 illustrates is a more useful form of representation

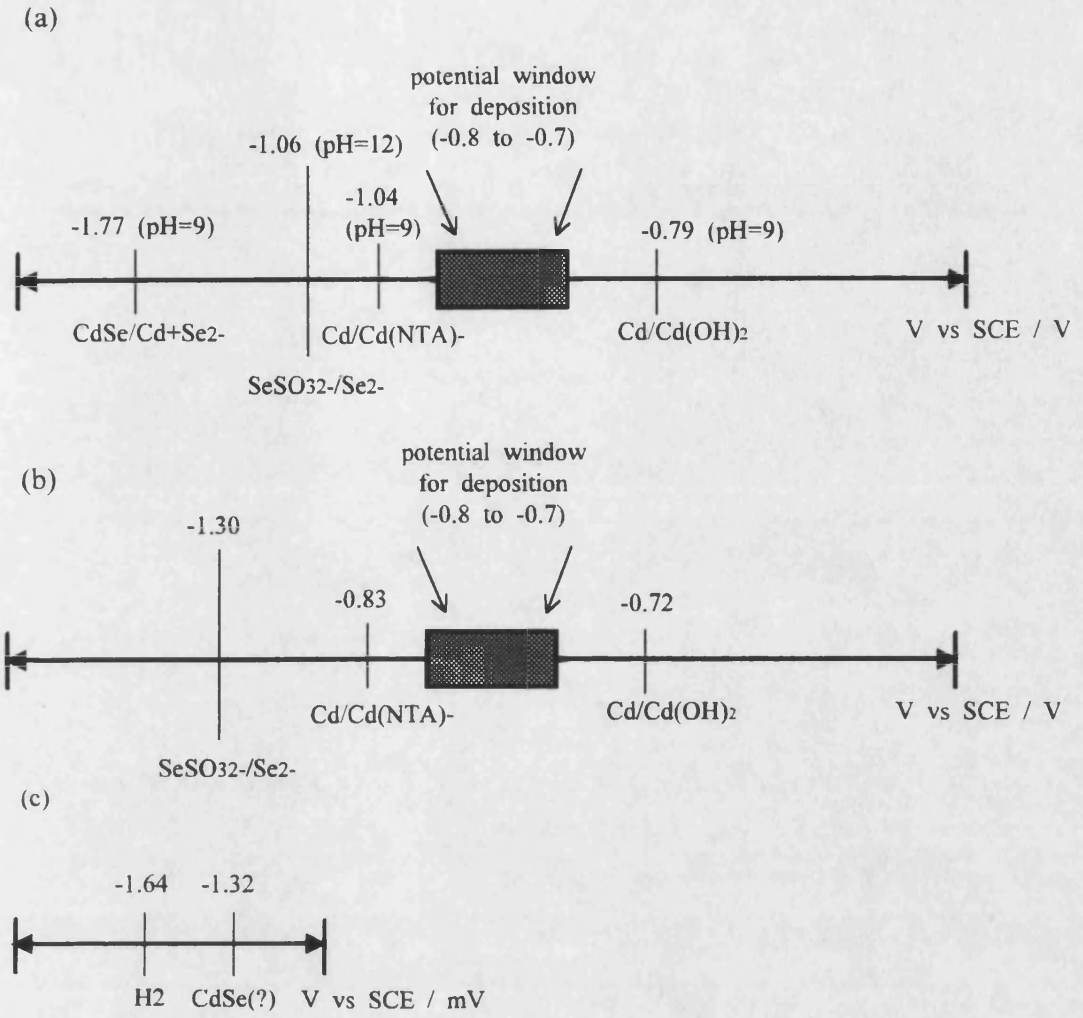

Figure 2.40. Potential scale diagram for the CdSe system. (a) Calculated reduction potentials for all species at pH≈9 (Cd^{2+}=0.05 mol dm^{-3}, $SeSO_3^{2-}$=0.1 mol dm^{-3}, NTA=0.1 mol dm^{-3}). (b) Experimental reduction peak potentials for individual species measured at a glassy carbon electrode at pH≈9 and 70°C. (c) As (b) but with *both* $Cd(NTA)^-$ and $SeSO_3^{2-}$ present.

The top potential scale, (i), shows the equilibrium reduction potentials calculated for the species involved in the electrodeposition of CdSe at pH=9. The value given for $SeSO_3^{2-}$ reduction has been calculated from free energy data as no reference to the standard reduction potential of this species could be identified. The potentials listed in the second scale, (ii), were determined by linear sweep voltammetry and correspond to the reduction of individual species at the surface of a glassy carbon electrode. In scale (iii), the two values were obtained using the same electrode, but immersed in a deposition bath containing all the precursors necessary for the growth of CdSe. The shaded box

illustrated in the top pair of scales represents the potential range over which films with optimum properties could be obtained. The uncertainty in the mechanism of CdSe deposition is immediately obvious. According to equation 2.74, deposition would be expected to occur close to -1.0 V (i.e. between -1.06 V and -1.04 V). However, in fact poor quality, amorphous films were obtained in this region. The best deposition conditions were found to be 300 to 400mV positive of this region. This anomalous behaviour will be discussed in Chapter 4.

2.11 Chemical Bath Deposition

Chemical bath or solution deposition (CBD) is used for the deposition of layers of metal sufides and selenides and occurs by a controlled chemical precipitation reaction[116,117]. Film formation takes place through the reaction of dissolved precursors (ions or decomposable molecules) either in solution or at a substrate by means of a nucleation and growth mechanism. CBD may be considered as the liquid phase counterpart to the gas phase chemical vapour deposition (CVD) method [118]. For CVD, the condensed phase forms a gaseous (liquid) phase containing voltatile compounds (ions) in a metastable condition.

Kitaev *et al* [119,120] and Chopra *et al* [121] have developed the basic method for the deposition of metal chalcogenides by the homogeneous precipitation method. The original mechanism involves thiourea decomposition in basic solution to form sulfide ions, which in the presence of complexed metals, such as amine complexed cadmium, induces formation if the CdS by precipitation. As a prelude to the growth of CdS on a solid support we should consider the basic chemical precipitation reaction for insoluble materials. Insoluble sulfide may be obtained by bubbling H_2S through an aqueous solution of the metal salt [122,123]. The H_2S / HS^- equilibria is given by

$$H_2S + OH^- \leftrightarrow HS^- + H_2O \quad (2.105)$$

The solubility of a salt MX may be described in terms of the equilibrium

$$MX(s) \leftrightarrow M^+(aq) + X^-(aq) \quad (2.106)$$

The solubility product of the solid is given by

$$K_{sp} = \{a_m^+ a_m^-\}_{eqbm} \quad (2.107)$$

where a_m and a_x are the activities of the dissociated cations and anions, respectively. Formation of the metal sulfide occurs when the ionic product (IP) of the two ions exceeds their solubility product (SP) so that the solution contains more ions than are required for saturation. When the IP is more than the SP, precipitation occurs.

In order to form a thin film by a controlled ion-by-ion reaction, it is necessary to eliminate spontaneous precipitation. This is achieved by having a stable complex of the metal ion, which provides a controlled number of the free ions according to the equilibrium

$$M(A)^{2+} \leftrightarrow M^{2+} + A \quad (2.108)$$

The concentration of the free metal ions at a particular temperature is given by

$$K = \frac{[M^{2+}][A]}{[M(A)^{2+}]} \qquad (2.109)$$

where K is the complex dissociation constant. The concentration of the metal ions is controlled by the concentration of the complexing agent and the solution temperature. Here we shall consider cadmium complexed by ammonia forming the tetraamine species $[Cd(NH_3)_4^{2+}]$.

2.11.1 Kinetics of Growth

CdS films are deposited on a substrate by the reaction between $CdSO_4$, NH_4Ac, NH_3, and $CS(NH_3)_2$ in an aqueous solution. Ammonia is a complexing agent, thiourea furnishes S^{2-}, and the NH_4Ac acts as a buffer. The various reactions involved and their equilibrium constants at room temperature are as follows [117,124,125].

Reaction	Rate Constant, K
$NH_3+H_2O \leftrightarrow NH_4^+ + OH^-$	1.8×10^{-5}
$Cd^{2+} + 2OH^- \leftrightarrow Cd(OH)_2$	1.88×10^{14}
$Cd^{2+} + 4NH_3 \leftrightarrow Cd(NH_3)_4^{2+}$	3.6×10^{6}
$CS(NH_2)_2 + 2OH^- \leftrightarrow S^{2-} + H_2O + H_2CN_2$	3.8×10^{-3} *
$Cd^{2+} + S^{2-} \leftrightarrow CdS(s)$	7.1×10^{28}

* The rate constant for the hydrolysis of thiourea at room temperature is negligible. The value given here is appropriate to the typical conditions for CBD of CdS (at 80°C and pH=13)

Table 2.3. Rate constants for the important reactions involved in the solution formation of CdS thin films

When the concentration product of Cd^{2+} and S^{2-} exceeds the solubility product of CdS ($K_{sp}=1.4x10^{29}$), CdS precipitates. The rate of formation of CdS is determined by the concentration of Cd^{2+} provided by $Cd(NH_3)_4^{2+}$ and S^{2-} from the hydrolysis of thiourea. The optimum deposition conditions for CdS have been determined on the basis of a diagram which correspond to the graphical solution of equations representing the equilibria for (i)cadmium hydroxide formation and (ii) cadmium ion formation from the tetraamine species. By considering the solubility product of $Cd(OH)_2$ and the dissociation constant for $Cd(NH_3)_4^{2+}$, Chopra *et al* [116,121] have derived two relationships given by equations 2.110 and 2.111 which when plotted give the hydroxide and complex lines, respectively. This is illustrated in figure 2.41.

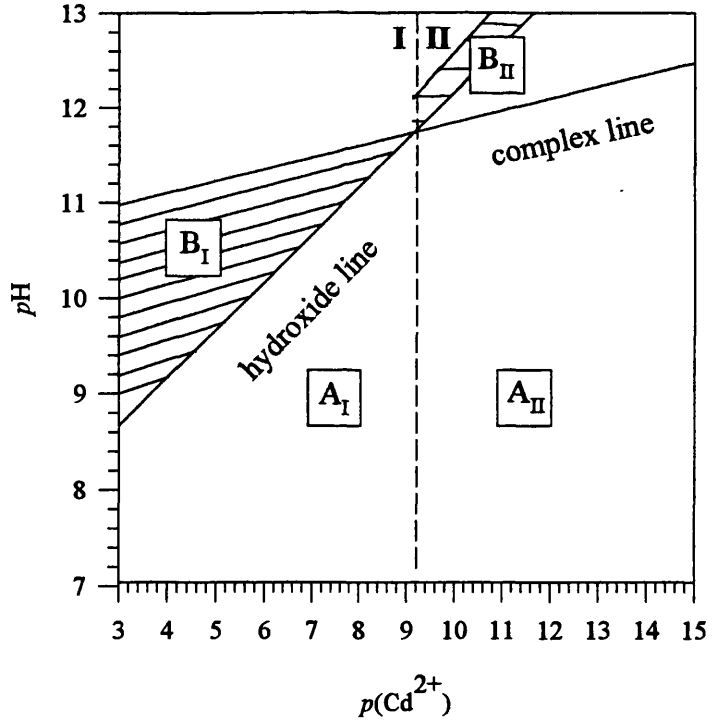

Figure 2.41 Plot of equations 2.110 and 2.111 showing the hydroxide and complex formation lines

$$pH = 0.5\, p[Cd^{2+}] + 7.17 \quad (2.110)$$

$$pH = 1/8\, p[Cd^{2+}] + 10.6 \quad (2.111)$$

where p[Cd2+] is the concentration of free Cd^{2+} ions in solution. Cadmium hydroxide is formed in the solution only for pH values above the hydroxide line, and the complex $Cd(NH_3)_4^{2+}$ is stable only for pH values below the complex line. For pH values above the complex line, the complex is hydrolysed to $Cd(OH)_2$. We can therefore see that the bath composition is very much pH dependent. It has been found that the relative proportion of the hydroxide and tetraamine species strongly determine the type of CdS film obtained. From figure 2.41 we can divide the plot into two regions, I and I, separated by a dotted line. In the shaded region that lies above the hydroxide line, $Cd(OH)_2$ is present. In these regions adherent and specularly reflecting films of CdS in the hexagonal orientation are obtained. In regions A_I and A_{II} where no hydroxide exists in solution, powdery films with the cubic modification are obtained. It is interesting to note that for conditions corresponding to points on the complex line in region II, film formation only takes place at elevated temperatures (>50°C), since the ionic product does not exceed the saturation product for CdS. As the temperature rises the IP eventually exceeds the SP. Such films have the same properties as those which lie above the hydroxide line, but are polymorphic, i.e. they contain both hexagonal and cubic phases [126]. We shall refer to the high quality films (adherent, hexagonal) type(A), the poor quality films (powdery, cubic) as type(B), and mixed hexagonal/cubic films as type(C). Controversy has existed as to whether $Cd(OH)_2$ is necessary for the formation of high quality films. Chopra *et al* [121] found that CdS could be deposited in the absence of the hydroxide whereas Kitaev *et al* [119] suggest that the presence of hydroxide precipitate is a necessity for film formation of CdS. However the former authors only

considered a limited number of equilibrium conditions, i.e. the formation of the complexes $Cd(OH)_2$ and $Cd(NH_3)_4^{2+}$. In fact under the typical conditions of CBD there are six cadmium tetraamine and six hydroxide species, each with different pH dependent dissociation constants. It is likely therefore that $Cd(OH)_x$ was present where x=1 to 4, but not as $Cd(OH)_2$.

2.11.2 Mechanisms of Growth

The precipitation process between Cd^{2+} and S^- can take place either homogeneously in the solution or heterogeneously at a substrate surface, as for example on tin oxide coated glass. The heterogeneous process may be subdivided into a growth mechanism involving [127]:

(i) reaction of ionic species at the surface, known as ion-by-ion condensation. Type (A) or (C) films are obtained in this way.
(ii) aggregation of colloids formed in the homogeneous solution reaction, known as cluster-by-cluster growth leading to the formation of powdery films. Here Type (B) films are formed.

In the case of CdS the high quality films are formed by the ion-by-ion condensation process. Based on this, Lincot *et al* [127] have proposed the following model for CdS film growth which is illustrated in figure 2.42.

$$Cd(NH_3)_4^{2+} + 2OH^- + SITE \leftrightarrow Cd(OH)_{2\ ads} + 4NH_3 \qquad (2.112)$$

$$Cd(OH)_{2\ ads} + S{=}C(NH_2)_2 \leftrightarrow [Cd(S{=}C(NH_2)_2(OH)_2]_{ads} \qquad (2.113)$$

$$[Cd(S{=}C(NH_2)_2(OH)_2]_{ads} \leftrightarrow CdS + CH_2N_2 + 2H_2O + SITE \qquad (2.114)$$

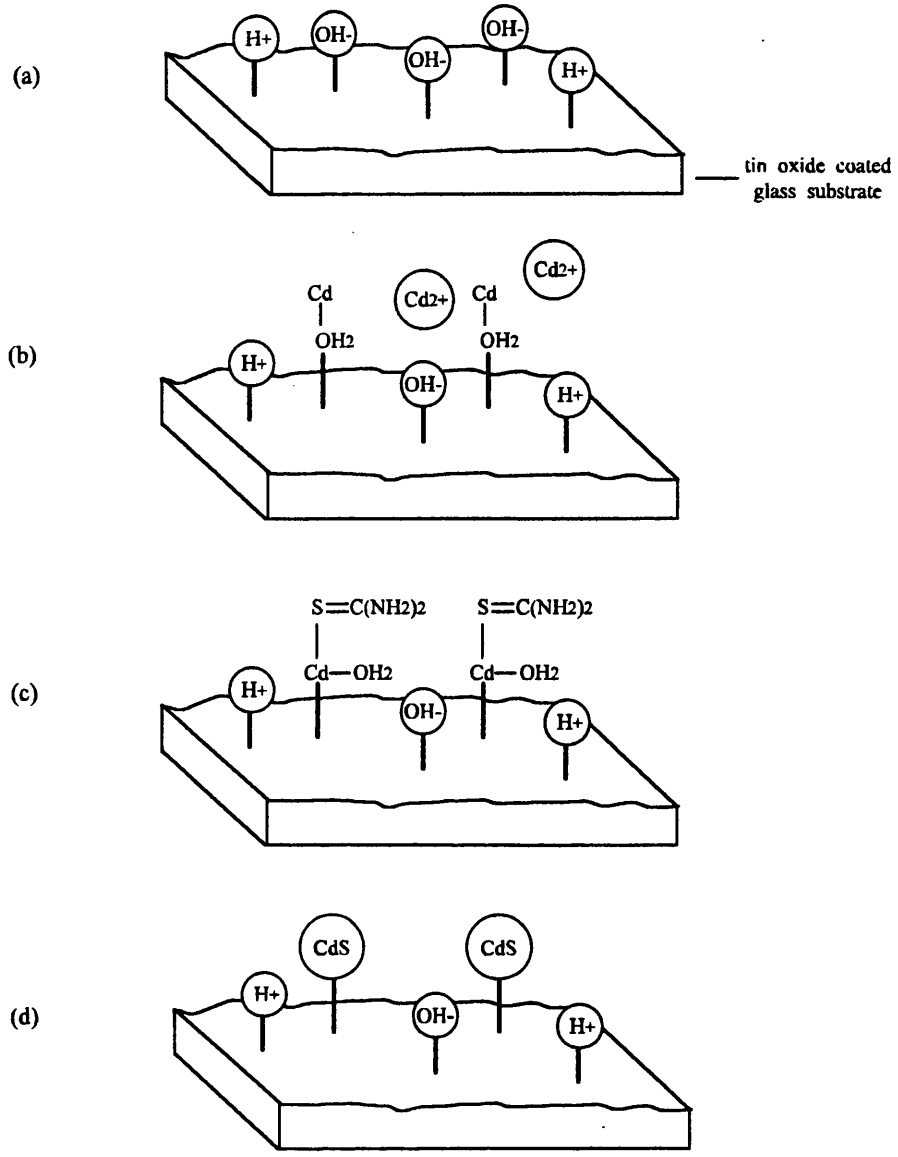

Figure 2.42. Schematic representation of the heterogeneous growth mechanism for CdS. (a) hydroxide terminated conducting glass surface (b) site specific reaction of Cd^{2+} with adbsorbed OH^- (c) decomposition of thiourea (d) formation of CdS

The adsorption of $Cd(OH)_2$ plays an important role in the deposition mechanism. This may either present in solution or at the substrate surface Pre-treatment of substrates such as tin oxide coated glass prior to deposition render its surface hydrophillic. It will therefore contain a high surface coverage of H+ and OH- species. Free Cd^{2+} ions can combine with OH^- forming catalytic hydroxide growth sites for the subsequent formation of CdS via S^{2-}. Colloidal cluster growth is also represented by reactions 2.112 to 2.114,

except that no surface adsorption site is involved. Instead all reactions take place in solution.

Films formed by the ion-by-ion process would be expected would be expected to be of higher crystallinity and uniformity compared to those formed by aggregation. In fact films with highly oriented crystallites with gain sizes of the order of a few nanomteres strongly support atom-by atom growth. Further evidence for this mechanism is the possibility of LPALE (Liquid Phase Atomic Phase Epitaxy) on certain substrates [128]. No cluster growth process would be expected to give such highly oriented films. In cluster growth CdS is present in the cubic modification, as is the homogeneously precipitated CdS in solution. Crystallites are typically 10 nm in diameter. No evidence for incorporation of clusters of CdS have been found in films deposited by ion-by-ion growth [126]. We shall now briefly consider the mechanism of the formation of well defined CdS particles that comprise the bulk of CdS thin films.

2.11.3 Nucleation and the LaMer Theory

The original concepts used to describe the formation of nuclei in a homogeneous environment and their subsequent growth to particles of larger size was described by LaMer [129,130]. In terms of the formation of CdS the model states that particles form when the process of Cd^{2+} release from the tetraamine complex takes place in a kinetically controlled manor, so that the concentration of constituent species reach critical supersaturation, resulting in a short burst of CdS nuclei. These can then grow to produce larger nuclei. A schematic representation of the LaMer theory is given in figure 2.43. This was originally devised for the growth of molecularly dissolved sulfur in aqueous solution.

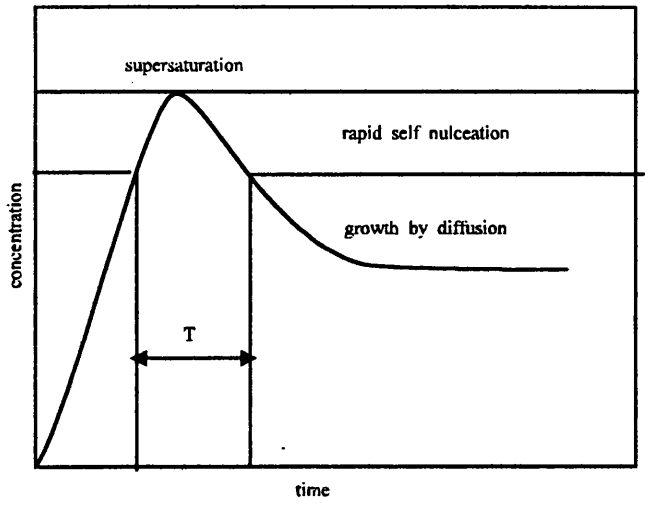

Figure 2.43. Growth of nuclei before and after nucleation as a function of time

During the initial stages of reaction the concentration of sulfide ions (produced via the catalytic decomposition of thiourea by cadmium hydroxide) in the reaction mixture increases to a point, the critical supersaturation. We would expect Cd^{2+} and S^{2-} to precipitate as CdS nuclei once the solution becomes saturated with these ions. However as the system moves from a liquid to a solid phase, interfaces are created which are thermodynamically unfavourable. The additional driving force to overcome this energy barrier is supersaturating the solution with S^{2-} ions. The close proximity and high repulsion energies between ions provides the driving force for the more favourable nucleation process. As nuclei of CdS start to grow the concentration the concentration profile falls as S^{2-} ions are consumed. The nuclei continue to grow, growth eventually being diffusion controlled. Highly monodisperse systems are obtained where the time scale τ for self-nucleation is short. For a more detailed discussion of nucleation processes work by A. Van Blaardeen *et al* [131] and D. H. Everett [132] should be consulted.

References

1 B. Ray, II-VI Compounds, p. 12-14, Pergamon, London (1969)

2 M. L. Cohen and T. K. Bergstresser, *Phys. Rev.*, **141**, 789 (1967)

3 P. A. Cox, The Electronic Structure and Chemistry of Soilds, Chapter 1, Oxford University Press, Oxford, 1987

4 R. H. Bube, Photoelectronic Properties of Semiconductors, Chapter 2, Cambridge University Press, Cambridge, 1992

5 Yu. V. Pleskov and Yu. Ya. Gurevich, Semiconductor Photoelectrochemistry, Consultants Bureau, New York, 1986

6 L. M. Peter, *Chem. Rev.*, **90**, 753 (1990)

7 S. R. Morrison, Electrochemistry at Semiconductor and Oxidisd Metal Electrodes, Chapter 3, Plenum Press, New York, 1987

8 H. O. Finklea, Semiconductor Electrodes, Chapter 1, in Studies in Theoretical and Physical Chemistry, Vol. 55, H. O. Finklea, Editor, Elsevier, New York, 1988

9 P. Allongue and H. Cachet, *J. Electrochem. Soc.*, **132**, 45 (1985)

10 D. Vanmaekelgergh and F. Cardon, *Electrochim. Acta*, **37**, 837 (1992)

11 M. J. Furlong, M.Phil/Ph.D Transfer Report, University of Bath, 1993

12 L. M. Peter *et al*, Instrumental Methods in Electrochemistry, Chapter 8, Ellis Harwood, London (1990)

13 A. Goosens, *J. Electroanal. Chem.*, **317**, 27 (1991)

14 J. F. Dewald, *Bell System Tech.*, **34**, 615 (1960)

15 L. M. Peter, M. J. Furlong, G. G. Goodlet, A. A. Shingleton, M. Bailes, E. Özsan, *J. Mat. Sci.:Electronic Mat.* (in press)

16 C. Kittel, Introduction to Solid State Physics, 6th Edition, Wiley, New York, 1986

17 R. A. Batchelor, D. Phil Thesis, University of Oxford, 1991

18 A. Etchberry, M. Etman, B. Fotouhi, J. Gautron, J. L. Sculfort, P. Lemasson, *J. Appl. Phys.*, **53**, 8867 (1982)

19 W. W. Gärtner, *Phys. Rev.*, **116**, 84 (1959)

20 L. M. Peter in, "Specialist Periodical Reports in Electrochemistry", Volume 9, Chapter. 2, Royal Society, London (1984)

[21] M. A. Butler, *J. Appl. Phys.*, **48**, 1914 (1977)

[22] M. Metikos-Hukovic, *Electrochim. Acta*, **26**, 989 (1981)

[23] P. Lemasson, A. Etchberry, and G. Gautron, *Electrochim. Acta*, **27**, 607 (1982)

[24] J. Reichmann, *Appl. Phys. Lett.*, **30**, 574 (1980)

[25] F. El Guibaly and K. Colbow, *J. Appl. Phys.*, **53**, 1737 (1982)

[26] J. Reichmann and M. A. Russak, "Photoeffects at the Semiconductor Electrolyte Interface", ACS Symposium 146, Ed. A. J. Nozik, Washington DC (1980)

[27] D. Hanemann and J. F. Mcann, *Phys. Rev. B. Condens. Matter*, **25**, 1241 (1982)

[28] W. J. Albery *et al, J. Electrochem. Soc.*, **128**, 1492 (1981)

[29] L. M. Peter, L. Li, and R. Peat, *J. Electroanal. Chem.*, **165**, 29 (1984)

[30] L. M. Peter and L. Li, *J. Electroanal. Chem.*, **193**, 27 (1985)

[31] M. Cardona, A. G. Thompson, E. Matatagui, *Phys. Rev.*, **176**(3), 450 (1968)

[32] G. W. Gobeli and E. O. Kane, *Phys. Rev. Lett.*, **15**, 142 (1965)

[33] D. E. Aspnes, *Surface Science*, **37**, 418 (1973)

[34] D. E. Aspnes in, M. Balanski (ed.), Handbook on Semiconductors, Vol. 2, North Holand, New York, 1980, p. 109

[35] D. F. Blossey and P. H. Handler in, R. K. Wilardson and A. C. Beer (Eds.), "Semiconductors and Semimetals", Vol. 9, Academic Press, New York, p. 257 (1972)

[36] F. H. Pollak and H. Shen, *Superlattices and Microstructures*, **6**(2), 203 (1989)

[37] M. Cardona, "Modulation Spectroscopy", Academic Press, New York (1969)

[38] P. M. Raccah, J. W. Garland, Z. Zhang, U. Lee, S. Ugur, S. Mioc, S. K. Ghandi, and I. Bhat, *J. Appl. Phys.*, **57**, 2014, (1985)

[39] F. H. Pollak and H. Shen, *Mat. Sci. Eng. Reports*, **R10**, 275 (1993)

[40] B. O. Seraphin and N. Bottka, *Phys. Rev.*, **145**, 628 (1966)

[41] F. H. Pollak in, M. Balanski (ed.), Handbook on Semiconductors, Vol. 2, North Holland, New York, 1993, p. 335

[42] D. E. Aspnes and A. A. Studna, *Phys. Rev. B*, **7**, 4605 (1973)

[43] D. E. Aspnes, *Phys. Rev. B*, **10**, 4228 (1974)

[44] D. E. Aspnes and J. E. Rowe, *Phys. Rev. B*, **5**, 4022 (1972)

[45] D. E. Aspnes and A. Frova, *Solid State Commun.*, **7**, 155 (1969)

[46] A. Hamnett, R. Lane, P. Trevellick, and S. Dennison in, Electrolyte Electroabsortion at Semiconductors, R. G. Compton (ed.), New Techniques for the Study of Electrodes and their Reactions, Vol. 29, Chapter 9, Elsevier, Oxford (1989)

[47] H. Shen and F. H. Pollak, *Phys. Rev.* B, **42**, 7097 (1990)

[48] P. L. Jackson and E. G. Seebauer, *J. Appl. Phys.*, **60**, 943 (1991)

[49] U. Behn and H. Röppisher, *J. Phys. C: Solid State Phys.*, **21**, 5507 (1988)

[50] P. M. Raccah, J. W. Garland, U. Lee, Da Zhong Xue, L. L. Abels, S. Ugus, and W. Wilinsky, *Phys. Rev. Lett.*, **55**, 1323 (1985)

[51] P. E. Vanier, F. H. Pollak, P. M. Raccah, *Appl. Optics*, 16, 2858 (1977)

[52] P. Salvador, A. M. Chaparro, B. Coll, and M. Gonzalez, *Surface Sci.*, **293**, 160 (1993)

[53] J. L. Birman, *Phys. Rev.*, **114**(3), 1490 (1959)

[54] B. B. Snavely, *Phys. Rev.*, **167**(3), 730 (1968)

[55] M. Chester and L. Fritsche, *Phys. Rev. A*, **139**, 518 (1965)

[56] B. B. Snavely, *Solid State Comm.*, **4**, 561 (1966)

[57] N. Hase and M. Onuki, *J. Phys. Soc. Japan*, **28**(4), 1965 (1970)

[58] P. I. Perov, L. A. Avdeeva, and M. I. Elinson, *Soviet Phys.-Solid State*, **11**, 438 (1969)

[59] D. G. Thomas and J. J. Hopfield, *Phys. Rev.*, **116**, 573, (1959)

[60] G. Hodes, Y. Golan, L. Margulis, and I. Rubenstein, *Langmuir*, **8**(3), 749 (1992)

[61] M. Tomkiewicz, I. Ling, W. S. Parsons, *J. Electrochem. Soc.*, **129**(9), 2016 (1982)

[62] G. A. Ozin, *Adv. Mater.*, **4**(10), 612 (1992)

[63] G. Hodes, *Nature*, **285**, 29 (1980)

[64] W. M. Yim and E. J. Stofko, *J. Electrochem. Soc.*, **121**, 965 (1974)

[65] C. Liu and J. H. Wang, *Appl. Phys. Lett.*, **36**, 852 (1980)

[66] T. M. Ratcheva-Stambolieva, Yu. D. Tchistyakov, G. A. Krasulin, H. D. Djoglev, *Phys. Status Solidi a*, **16**, 315 (1973)

[67] G. Hodes, D. Cahen, J. Manassen and M. David, *J. Electrochem. Soc.*, **127**, 2252 (1980)

[68] M. Hyugaji and T. Miura, *Jpn. J. Appl. Phys.*, **24**, 1575 (1985)

[69] C. D. Lokhande and S. H. Pawar, *phys. stat. sol. (a)*, **111**, 17 (1989)

[70] K. Rajeshwar, *Adv. Mater.*, **4**(1), 23 (1992)

[71] M. E. Özsan *et al*, *Int. Jnl. Solar Energy*, **12**, 79 (1992)

[72] B. M. Basol, *Solar Cells*, **23**, 69 (1988)

[73] M. P. R. Panicker, M. Knaster, and F. A. Kroger, J. *Electrochem. Soc.*, **125**, 566 (1978)

[74] As Reference 12, Chapter 9.

[75] M. Volmer and G. Thomfor, *Ann. Phys.*, **33**, 109 (1939)

[76] A. R. Despic in, *Comprehensive Treatise of Electrochemistry*, eds., B. E. Conway, J. O'M Bockris, E. Yeager, S. U. M. Khan, and R. E. White, Vol. 7, p.451, New York, Plenum (1983)

[77] R. Kaishew, *Bull. Acad. Bulg. Sci. (Phys.)*, **1**, 1220 (1950)

[78] G. F. Fulop and R. M. Taylor, *Ann. Rev. Mater. Sci.*, **15**, 197 (1985)

[79] F. A. Kröger, *J. Electrochem. Soc.*, **125**, 2028 (1978)

[80] B. W. Gregory, M. L. Norton, and J. L. Stickney, *J. Electronanal. Chem.*, **300**, 543 (1990)

[81] H. Gerisher, D. M. Kolb, and K. Saas, *Adv. in Physics*, **27**(3), 437 (1978)

[82] P. N. Ross Jr., *Surf. Sci.*, **102**, 463 (1980)

[83] J. L. Stickney and D. W. Suggs, *J. Phys. Chem.*, **95**(24), 10056 (1991)

[84] J. L. Stickney *et al*, *J. Electrochem. Soc.*, **127**(10), 2023 (1995)

[85] L. F. Kozin, *Amalgam Metallurgy*, **3**, 1351 (1967)

[86] C. C. Lai and Y. Ku, *The Chem. Eng. Jnl.*, **153**, 183 (1994)

[87] M. Pourbaix, "Lectures on Electrochemical Corrosion", Ed. W. Roger Stachie, Plenum, New-York (1973)

[88] A. von Hippel and M. C. Bloom, *J. Chem. Phys.*, **18**, 1243 (1950)

[89] A. Baranski, W. R. Fawcett, A. C. McDonald, and R. M. de Nobriga, *J. Electrochem. Soc.*, **128**(5), 963 (1981)

[90] U. Stimming, Electrochim. Acta, 31(4), 415 (1986)

[91] N. F. Mott and E. A. Davies, Electronic Processes in Non-Crystalline Solids, Clarendon Press, Oxford, 1979

[92] M. Fleishmann and H. R. Thirsk, Adv. *Electrochem. Electrochem. Eng.*, **3**, 123 (1963)

[93] G. J. Hills and D. J. G. Ives, *J. Chem. Soc.*, **311** (1951)

[94] B. Miller and A. Heller, *Nature*, **262**, 680 (1976)

[95] N. Cabrera and N. F Mott, *Rep. Prog. Phys.*, **12**, 163 (1949)

[96] E. J. W. Verwey, *Physica*, **2**, 1059 (1935)

[97] L. M. Peter, *Electrochim. Acta*, **23**, 165 (1978)

[98] J. W. Diggle, T. C. Downe, and C. W. Goulding, *Chem. Rev.*, **69**, 365 (1969)

[99] R. Kaishew, *Acta. Phys. Acad. Sci. Hung.*, **8**, 75 (1957)

[100] E. B. Budevski, *Comprehensive Treatise of Electrochemistry*, eds., B. E. Conway, J. O'M Bockris, E. Yeager, S. U. M. Khan, and R. E. White, Vol. 7, p.399, New York, Plenum (1983)

[101] E. Budevski, V. Bostanov, T. Vitanov, Z. Stoynov, A. Kotzeva, and R. Kaischew, *Phys. Stat. Solidi*, **13**, 577 (1966)

[102] K. J. Vetter, Electrochemical Kinetics, p. 283, Academic Press, New York, (1967)

[103] G. A. Gunawardena, G. J. Hills, and I. Montenegro, *Electrochim. Acta*, **23**, 693 (1981)

[104] B. R. Scharifker and G. J. Hills, *Electrochim. Acta*, **28**, 879 (1983)

[105] N. A. Pangarov, *Electrochim. Acta*, **9**, 721 (1964)

[106] F. C. Frank and J. H. Van der Merve, *Proc. R. Soc. Lond. Ser. A.*, **198**, 205 (1949)

[107] J. B. Zeldovich, *Acta. Phys. USSR*, **18**, 1 (1943)

[108] As reference 12, Chapter 9

[109] D. Pletcher, "A first course in electrode processes", Chapter 4, Electrochemical Consultancy, Romsey (1991)

[110] D. Pletcher, Industrial Electrochemistry, Chapter 5, Electrochemical Consultancy, Romsey (199?)

[111] B. Levich, Physicochemical hydrodynamics, Prentice Hall, 1962

[112] F. Decker, J. R. Moro, J. L. S. Ferreira, and M. Vazi, *Ber Bunsenges. Phys. Chem.*, **91**, 412 (1987)

[113] M. Cocivera, A. Darkowski, and B. Love, *J. Electrochem. Soc.*, **131**, 2514 (1984)

[114] M. Skylas Kazakos and B. Miller, *J. Electrochem. Soc.*, **127**, 378 (1980)

[115] V. F. Toropova, *Russian Jnl. Anal. Chem.*, **11**, 594 (1953)

[116] K. L. Chopra, R. C. Kainthla, D. K. Pandya, A. P. Kapoor, *Physics of Thin Films*, **12**, 167 (1982)

[117] T. L. Chu and S. S. Chu, *Solid-State Electronics*, **38**(3), 533 (1995)

[118] J. H. Fendler and F. C. Meldrum, *Adv. Mater.*, **7**(7), 607 (1995)

[119] G. A. Kitaev, S. G. Mokrushin and A. A. Uritskaya, *Colloid J. USSR*, **27**, 38 (1965)

[120] G. A. Kitaev and T. S. Terekhova, *Russian J. Inorganic Chemistry*, **15**, 25 (1970)

[121] K. L. Chopra, D. K. Pandya, I. Kaur, *J. Electrochem. Soc.*, **127**(4), 943

[122] J. M. Dona and J. Herrero, *J. Electrochem. Soc.*, **139**(10), 2810 (1992)

[123] F. A. Cotton and G. A. Wilkinson, Advanced Inorganic Chemistry, 5th ed., Wiley, New York (1986)

[124] P. C. Rieke and S. B. Bentjen, *Chem. Mater.*, **5**, 43 (1993)

[125] J. A. Dean, Ed., Lange's Handbook of Chemistry, McGraw Hill, New York (1985)

[126] D. Lincot, R. Ortega-Borges and M. Froment, *Philisophical Magazine B*, **68**(2), 185 (1993)

[127] D. L. Lincot and M. Froment, *Electrochima Acta*, **40**(10), 1293 (1995)

[128] S. Lindroos, T. Kanniainen and M. Leskelä, *Appl. Surface Sci.*, **75**, 70 (1994)

[129] E. Matijevic, Chem. Mater., **5**, 412 (1993)

[130] V. K. LaMer, *Ind. Eng. Chem.*, **44**, 1270 (1952)

[131] A. Van Blaardeen, J. Van Geest, and A. Vrij, *J. Colloids and Interface Sci.*, **154**, 481 (1992)

[132] D. H. Everett, Colloid Chemistry and Interface Science, Royal Society, London

Chapter 3

Experimental

3.1. Reagents and Solutions

All solutions were prepared from analytical grade reagents and high purity Milli-Q water which contains very low levels of ionic, organic, and particulate contamination. This was provided by a Milli-RO 6 Plus (ZFRO 050 06) reverse osmosis (RO) filtration system and Milli-Q 185 Plus (ZFMQ 050 UV) unit where the prepurified feedwater was exposed to ultraviolet light (UV) of low wavelength (185nm and 254nm) which photooxidises any organic and bacterial traces present. The UV treated water is then passed through a final RO pack which removes the ionic compounds plus the by products of photooxidation. The resistivity of the water was typically 18.2MΩ. Unless otherwise stated, oxygen free nitrogen was used to remove dissolved oxygen from electrolytes and was performed in all depositions and characterisation.

For the electrodeposition of CdSe the precursor Na_2SeSO_3 was prepared by refluxing selenium (0.1 mol dm^{-3}) (Aldrich) with an excess of Na_2SO_3 (0.25 mol dm^{-3}) (Aldrich) at 60-70°C for 8 hours. To aid dissolution of the selenium the mixture was bubbled with oxygen free nitrogen.

All experiments were made at room temperature and pressure in screened Faraday cages.

3.2 Glassware

3.2.1. Cells for Characterisation

Two types of three compartment glass cells utilising a Luggin capillary and fritted counter electrode side-arm were used. The first was a single window quartz cell used for current-voltage, capacitance voltage, photocurrent and electrolyte electroreflectance measurements of thin film electrodes. A simple rectangular cell was also used in photoelectrochemical measurements. This was constructed from 4

microscope slides (Chance Propper) held together with silicone rubber (Elastosil E41, Wacker) with a fifth side sealing one end. This cell design enabled the photodiode to be placed right up against the cell wall maximising the amount of light throughput. The cell cap was constructed from polypropylene (see figure 3.1) and was designed for easy and straightforward mounting of thin film electrodes.

The second major cell was a more elaborate 3 window design used for single crystal studies (see figure 3.2). This design enables reflection measurements to be made with two quartz windows placed such that incident light strikes the electrode and is reflected at a 60° angle. The third central quartz window provides a 0° incident angle for the incoming light necessary for photocurrent measurements. The electrode positions in the cell corresponding to these two cases are shown in figure 3.3. The working electrode entered the side of the cell via a precision bore Young's glass joint. The Luggin was also prepared from a similar but smaller diameter tube with two recessed O-Ring seals (PTFE and Elastomer) for sealing. The cell was also equipped with N_2 de-gassing inputs for the main cell body and counter electrode compartment

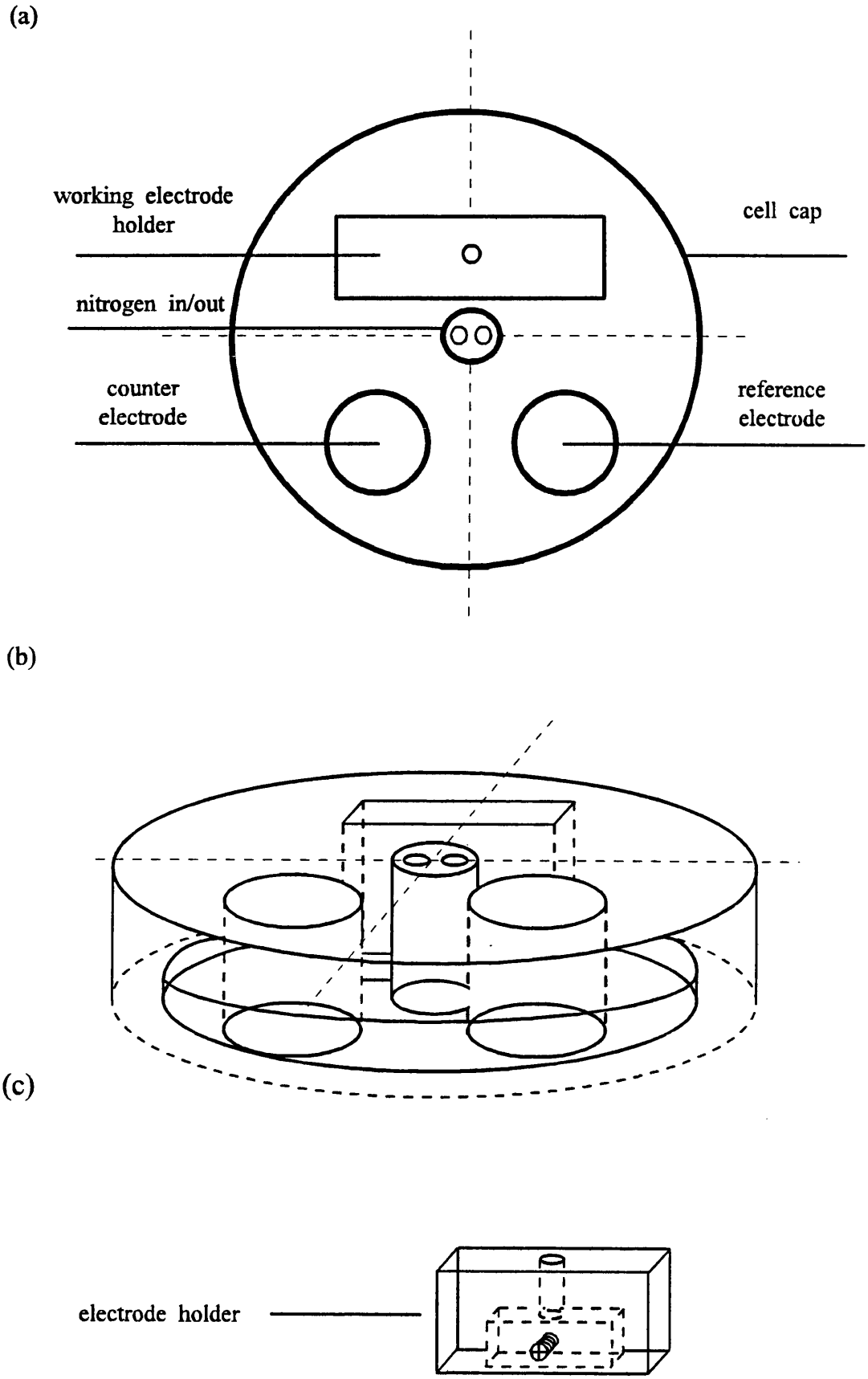

Figure 3.1 (a) Plan view of cell cap used with rectangular glass cell. (b) 3D view of 3.1 (a). (c) thin film electrode holder

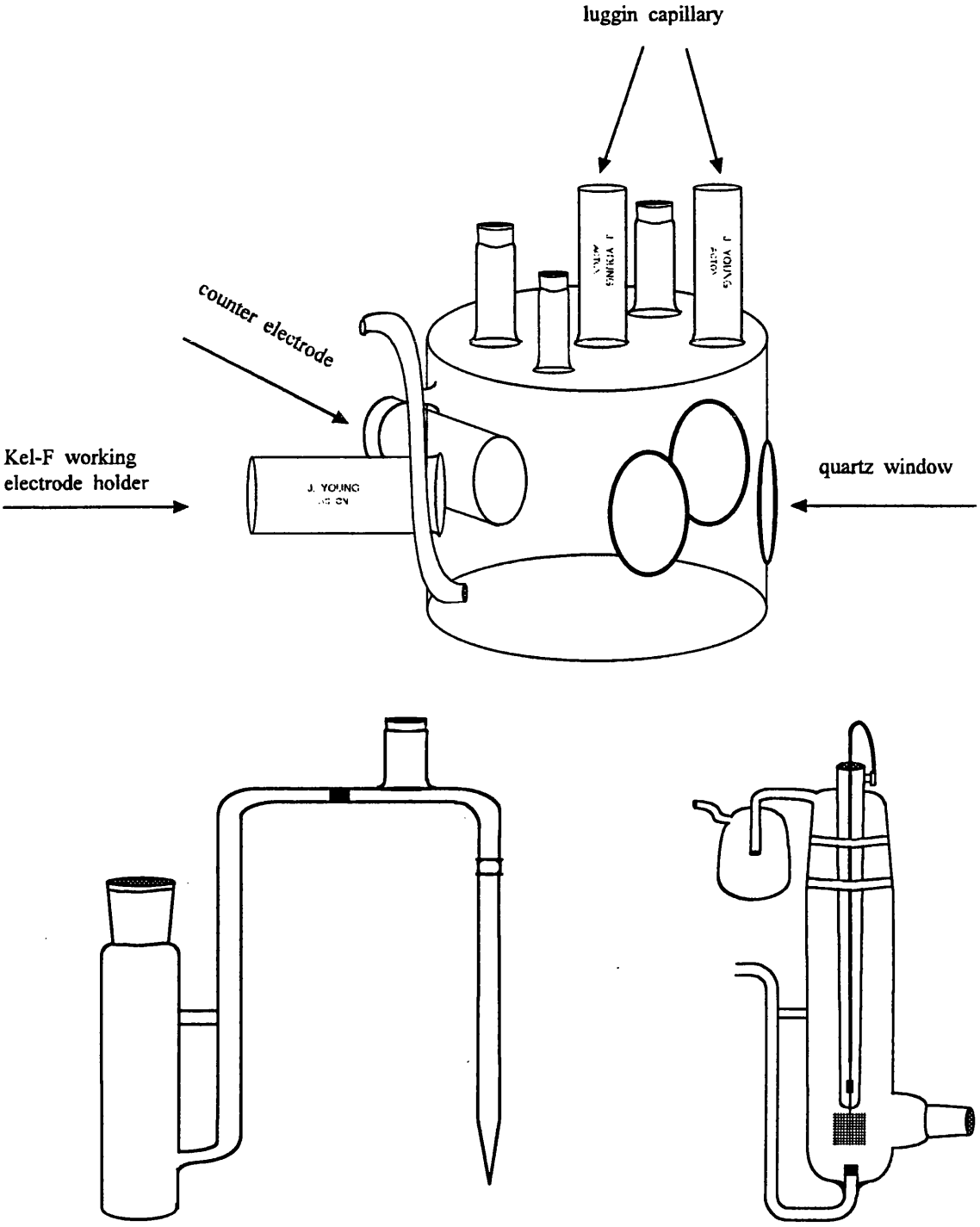

Figure 3.2 (a). Three electrode glass cell for reflection/absorption measurements. (b) Luggin capillary fabricated from a Young's glass joint. (c) Counter electrode with nitrogen bubbler.

3.2.2. Cells for Deposition

A variety of cells were used for electro- and electroless deposition. These were all designed for versatile use and to ensure the maximum reproducibility for the deposited films.

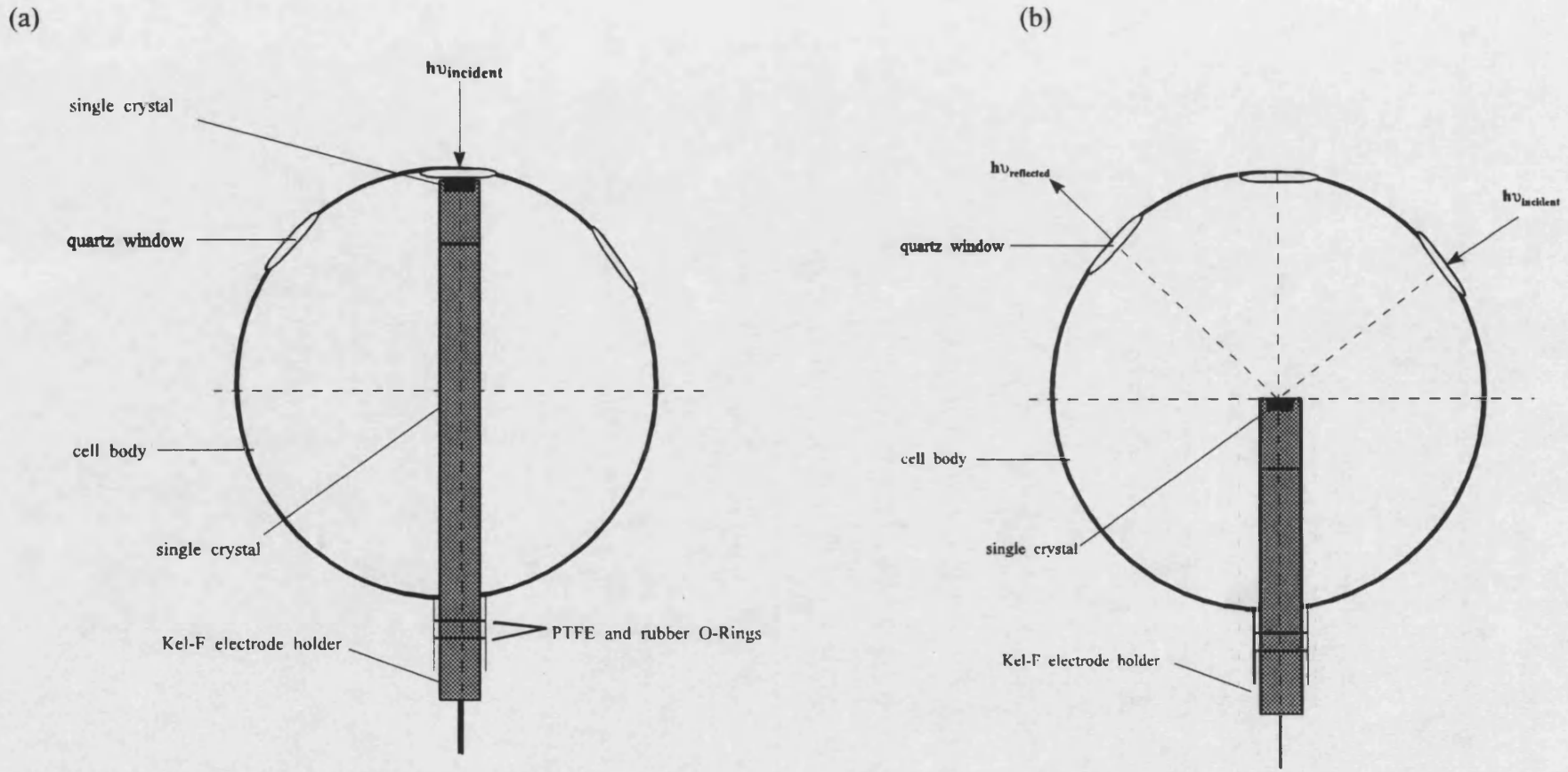

Figure 3.3. Plan view of the three electrode glass cell used for photoelectrochemical characterisation of single crystal CdS and CdSe. (a) and (b) correspond to the electrode positions for absorption and reflection, respectively.

Shown in figure 3.4 is the cell used for the cathodic electrodeposition (ED) of CdSe and CdS.

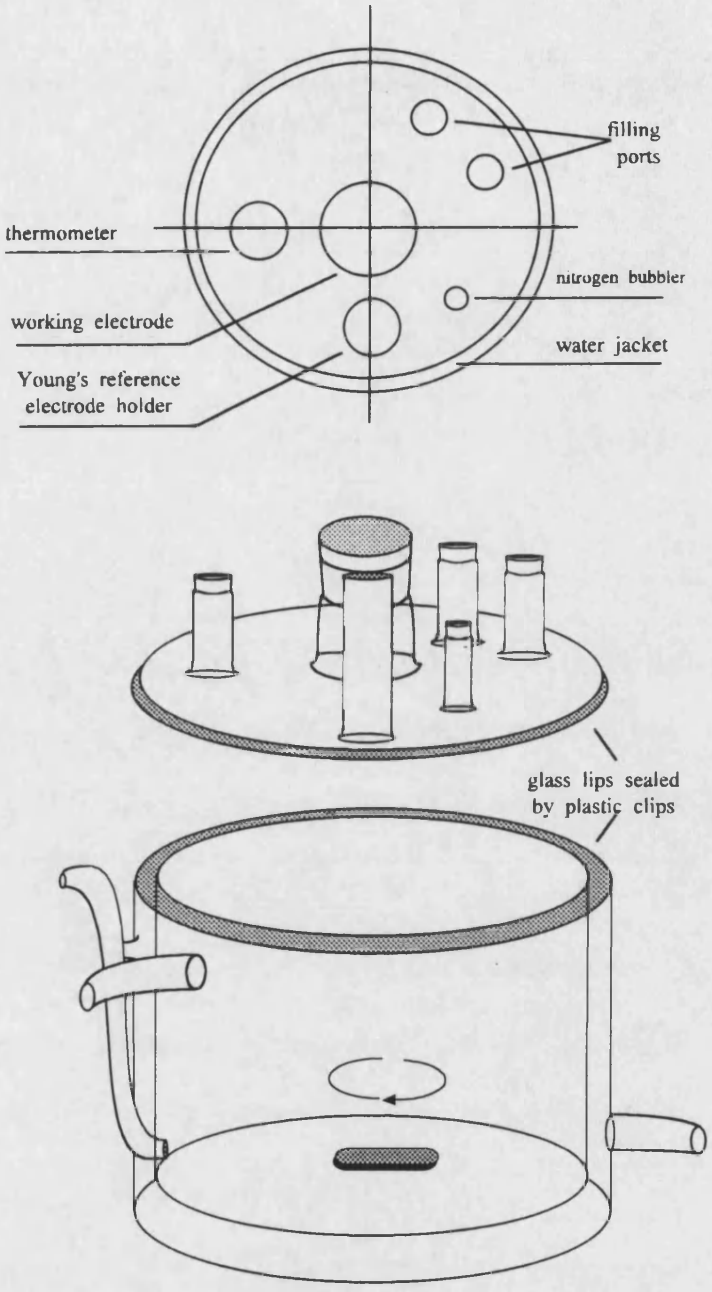

Figure 3.4 Cell lid and body used for the cathodic electrodepositon of CdSe.

This cell was constructed to allow rotating disk electrode (RDE) studies and so it had a larger cell lid designed to accommodate the RDE feature. The total cell volume was 230cm^3. The main cell body was jacketed for temperature controlled work and possessed a side arm counter electrode compartment plus N_2 de-gassing input. The cell

lid comprised a gas bubbler, three Quickfit joints for cell filling, a single precision Young's joint for the reference electrode compartment, and a Quickfit working electrode joint. The lid and cell body both possessed an outer glass lip for precise fitting. The two were held in place with plastic clips and further sealed by PTFE tape. So as to maximise the ease of use of the entire electrodeposition apparatus, the cell jacket was linked to the heated circulator bath via automatic shut-off quick connectors (Aldrich). This enabled cells to be exchanged quickly without having to wait for the bath water to cool to room temperature.

A simple jacketed cell was used for the chemical bath deposition (CBD) of CdS as is shown in figure 3.5(b). The cell lid illustrated in figure 3.5(a) incorporates ports for suspending the tin oxide glass electrode holder, pH and temperature probes, and two filling holes. This was attached tightly to the cell by wrapping PTFE tape around the lip of the glass cell. Electrodes were arranged back-to-back in pairs and placed in slots cut in the electrode holder shown in figure 3.5(c). For any single deposition four electrodes could be coated at once. A magnetic stirring bar was used to agitate the solution. Cell connection to the water bath was as for the ED cell.

3.3. Cells used in Photoelectrochemical Imaging

These are described in a separate section owing to the more specialised nature of the cells employed

3.3.1. Scanning Microscopy for Semiconductor Characterisation (SMSC)

The cell used for the SMSC was designed by Dr. A. M. Martinez Chaparro at the C.S.I.C, Madrid and is shown in figure 3.6(a). This consists of a central glass body with two Quickfit joints for placing the reference and counter electrodes and one central screw threaded glass joint for the working electrode holder. The base of the cell was

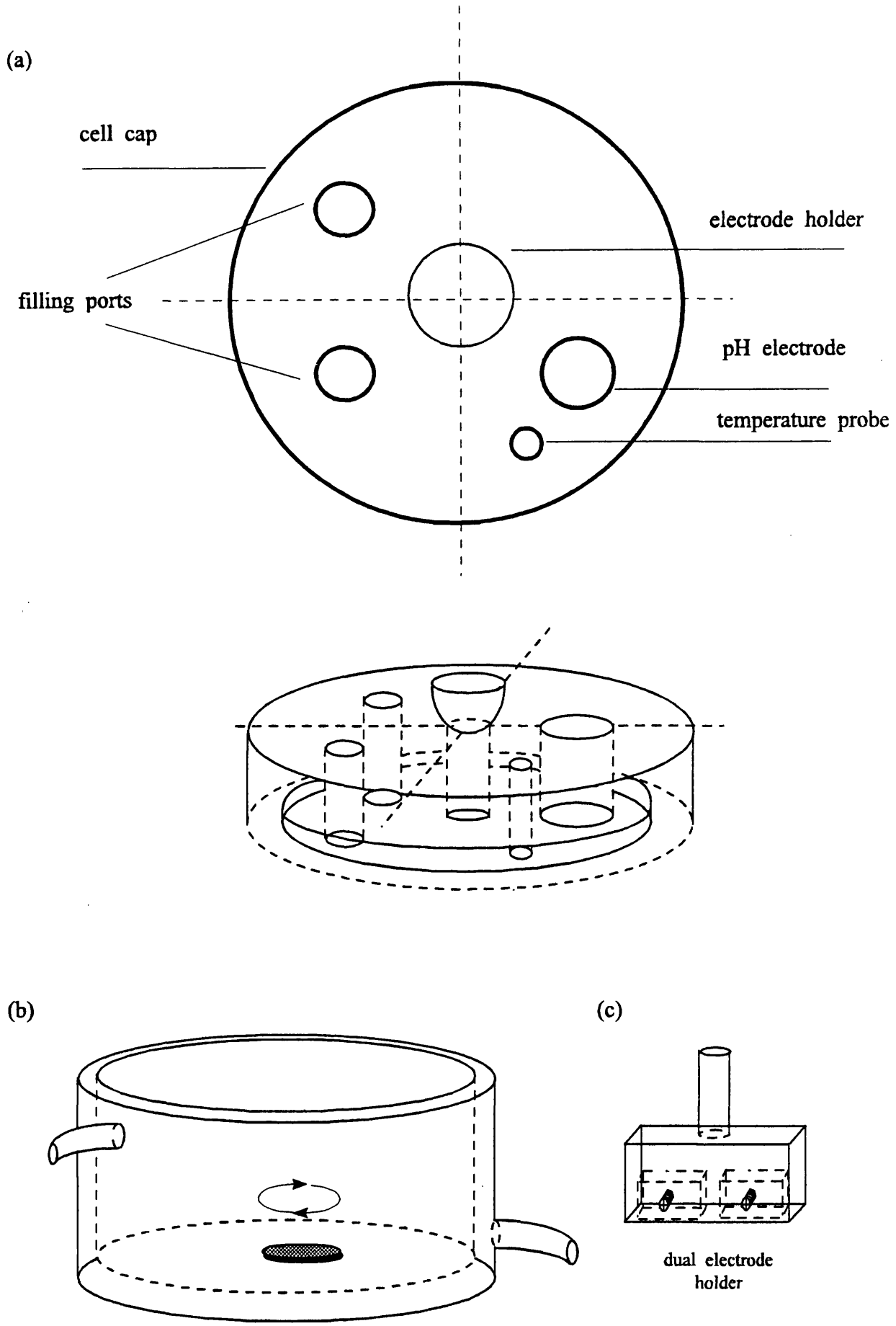

Figure 3.5. (a) Plan view of cell cap used in CBD cell (b) 3D view of figure 3.5(a). (b) jacketed cell with magnetic stirring bar. (c) thin film electrode holder

constructed around a circular glass plate with a central aperture of 2.5cm in diameter covered by a thin glass cover slip (Chance Propper) through which the working electrode was illuminated. This was made leak proof by applying silicone rubber between the body and slip. The cell was held in place on the travelling microscope stage by means of three screw connectors.

3.3.2. Photoelectrochemical Microscopy (PEM)

The cell employed in the PEM measurements was constructed from a block of PTFE (4cm square) with a central working and reference compartment. The counter electrode chamber was connected to this via a drilled bore through which electrolyte could flow. Due to the very narrow diameter (<1mm) of the connection, electrolyte was displaced through the cell using a teat pipette to ensure all bubbles escaped. The working electrode holder was held firmly in the cell by means of a single PTFE O-Ring. A diagram of the cell is given in figure 3.6(b). Attachment of the cell to the fixed microscope stage was via two sprung clips. This cell was designed and constructed at University College, London by Dr. R. S. Hutton.

3.4. Electrodes

3.4.1. Counter Electrodes

Either Pt flag or Pt gauze counter electrodes were used. In all cases their surface area was considerably larger than the working electrode so polarisation effects are minimised. After all experiments the Pt electrodes were cleaned in triply distilled water and frequently flamed to remove any organic impurities.

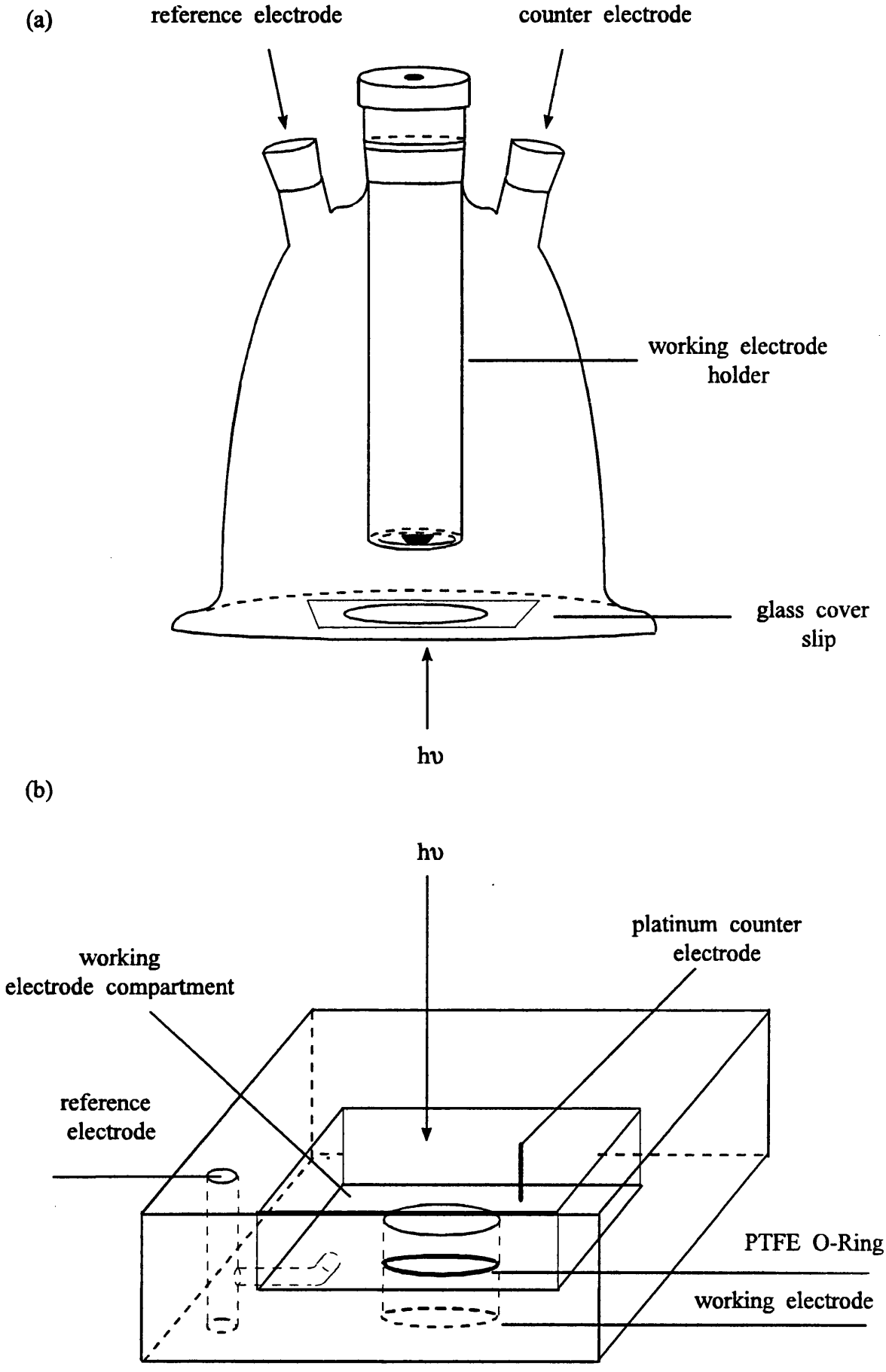

Figure 3.6 (a) Glass and (b) PTFE cells used with SMSC and PEM photoelectrochemical imaging techniques, respectively

3.4.2. Reference Electrodes

For all experiments involving semiconductor deposition and characterisation a $Hg/HgCl_2/KCl_{(satd)}$ (saturated calomel) reference electrode (SCE) (Radiometer) was used. For the initial studies on cathodic CdSe electrodeposition a Cd reference electrode was prepared consisting of 2cm of 0.5mm Cd wire (Aldrich) suspended in a saturated solution of $CdSO_4$ (Aldrich). This was contained in a fritted glass tube constructed from a broken SCE and sealed at the top with PTFE tape. In an indifferent electrolyte this electrode had a reference potential of -0.625V vs SCE. However when immersed in the selenosulfite bath diffusion of Se^{2-} through the frit resulted in CdSe formation on the Cd wire giving an unstable reference potential. Subsequent depositions were made using a SCE electrode placed in a length of precision Young's tubing adapted at the end to form a Luggin probe.

3.4.3. Thin Film Working Electrodes

The substrate used for all cathodically electrodeposited thin films was tin oxide coated glass (TOG) (Nippon Sheet Glass). For consistency all electrodes were sourced from the same batch of TOG. Samples were cut to approximately 2cm x 1cm using a diamond scribe from a 30cm x 30cm sheet. Prior to deposition they were vapour degreased in a Soxhlet column using propan-2-ol (Sigma-Aldrich B.Pt. = 82.4°C) for 2 hours, dried under a N_2 stream, and stored in Petri dishes. Electrodes were subsequently mounted either as pairs placed back to back and held by a crocodile clip sealed with PTFE tape or for the CBD experiments by the holder shown in figure 3.5(c). Care was be taken when sealing the electrodes with PTFE tape to prevent any short circuit paths for electrolyte contact to the crocodile clip contact. Tightly stretching the tape around the TOG provided a leak free seal. After deposition, coated TOG electrodes

were de-mounted, placed in Milli-Q water in an ultrasonic bath to remove any loosely adherent deposits, and finally rinsed prior to drying under an N_2 stream. Figure 3.7(a) shows a coated TOG plate prepared for subsequent characterisation. Contact is made to the top of the plate by a crocodile clip (RS) and silver paint (RS) with further sealing using wrapped PTFE tape.

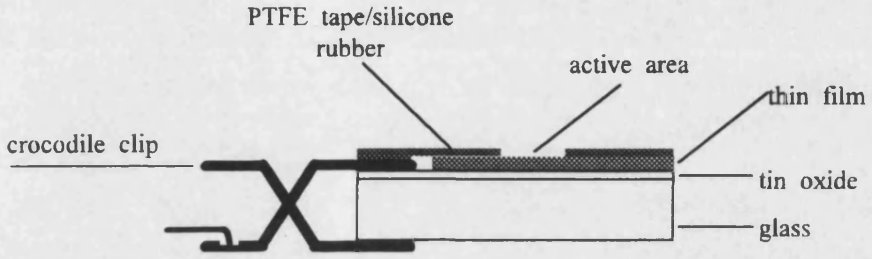

Figure 3.7. Diagram of a thin film working electrode

As the contact must be made to the tin oxide, no thin film must be present at the top of the electrode. In electrodeposition this area does not make contact with the electrolyte as it is covered, however in the CBD of CdS entire TOG coating may take place and so a small portion of film must be removed by partial insertion of the plate in concentrated H_2SO_4 (BDH, Analar) for 1 second followed by thorough rinsing with triply distilled water. An active area of the electrode was then defined by painting the entire plate with an insulating varnish (RS 188-611) leaving a central square area typically $1cm^2$ exposed on both sides of the electrode. Two coats were applied, each being allowed to dry for 24 hours at room temperature (18-28°C). To further minimise the chances of the electrode leaking, the edges of the glass plate were sealed with silicone rubber.

3.4.4. Single Crystal Electrodes

Single crystal studies were made with samples mounted in Kel-F (PCTFE) and polypropylene electrode holders using epoxy (Araldite) as an adhesive. Care was taken not to cover other than the edges of the crystal with the adhesive. The holders were threaded to accept the larger O-ring sealed Kel-F barrels which fit in the precision Young's joint of the glass cell shown in figure 3.2. The entire single crystal electrode is shown in figure 3.8.

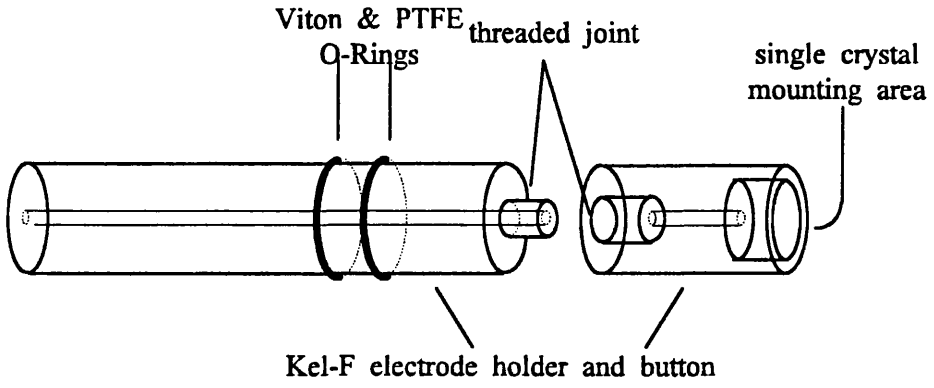

Figure 3.8. Diagram showing a Kel-F single crystal electrode holder

Four 5mm x 5mm CdS single crystals (Clevland Crystals) were cut from a waxed 1cm square using a diamond saw (Prepared by A. Dutton, Phillips (IR Devices), Southampton). Subsequent vapour degreasing for 2 hours in a Soxhlet column using propan-2-ol ensured a thoroughly clean electrode surface. One face of each sample was polished using alumina lapping film from 3 μm down to 0.03 μm (3M) using water as a lubricant. During polishing the crystal was held between plastic tweezers wrapped in PTFE tape to prevent damage of the crystal sides. To identify the crystal surface the polished side was etched in 0.1 mol dm^{-3} HCl for 5 seconds followed by copious rinsing

with Milli-Q water to quench the etch reaction. Identification of the face was made using an Olympus CH series optical microscope (x500), and characteristic hexagonal etch pits corresponding to the hexagonal (wurtzite) Cd (0001) face and powdery layer corresponding to the S (0001) face were observed. In figure 3.9(a) and (b) optical microscope images of the Cd surface at (x100) and (x500) magnification, respectively are shown.

Figure 3.9(a) Optical microscope images of the (0001) crystal surface of CdS after etching in 0.1 mol dm^{-3} HCl for 5 seconds at room temperature. Sharply defined etched pits are developed on the cadmium surface (x100).

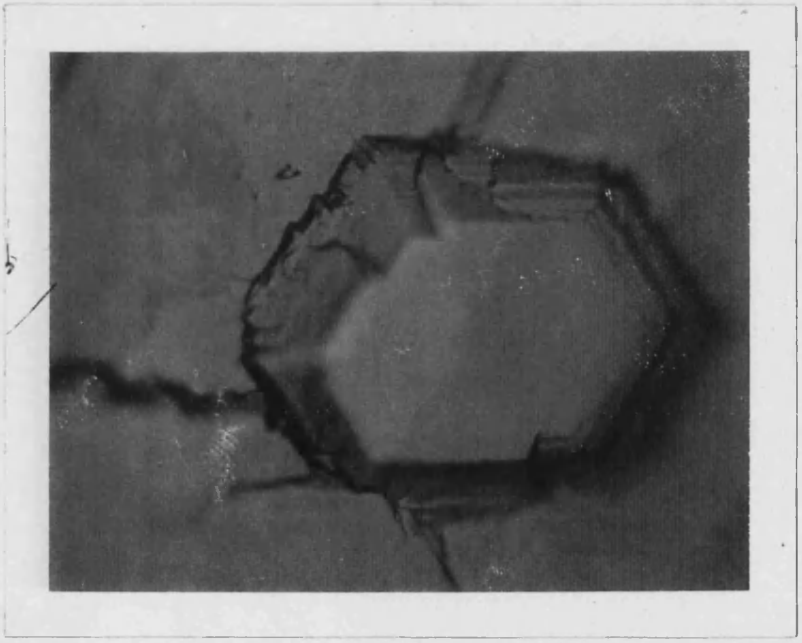

(b) single etch pit (x500)

Electrical contact was made to the Cd and S faces by lightly scratching Ga-In (Aldrich, 7:3) eutectic into one surface leaving a border of approximately 1.5mm from the outside. In the case of the S-face though a powdery sulfur layer remained from the etch. This was again removed by a saturated Na_2S dip. The surface was subsequently contacted with silver epoxy (RS) and a short length of Pt wire (Goodfellow) soldered to PTFE coated copper wire (RS). Contact to thin film electrodes has been described in section 3.4.3.

After electrical contact had been made to the crystal, it was mounted in the Kel-F holder and the crystal faces prepared. Both electrodes were initially polished with 3μm lapping film to remove any excess epoxy from the surface and polished to a mirror finish with alumina paste (Leco) from 1 micron down to 0.05 micron on a flocked twill cloth (Leco). Finally, polishing damage was removed by chemical etching in a mixture of acetic acid (Aldrich), nitric acid (Aldrich), and water (6:6:1) for one minute. According to Gatos *et al* [1] this gives a surface virtually free of any defects. The appearance of the post etch faces were quite different though. The Cd-face retained its mirror like appearance though the S-face was coated in a powdery sulfur layer. This was removed by washing the face in saturated Na_2S (Fluka) followed by Milli-Q water.

For measurements made on single crystal CdSe (Materials Research) an electrode already mounted was used. However, no information was available on the orientation of the sample. The electrode was polished in the same way as for single crystal CdS, then etched in HCl and HNO_3 (4:1) followed by 1 second in concentrated HCl [2] . The electrode was dipped in saturated Na_2S to remove the Se rich layer remaining from the etch reaction. Each of these steps was followed by rinsing with Milli-Q water. A highly reflecting black crystal surface was obtained.

3.4.5. Electrodes used in Photoelectrochemical Imaging

SMSC electrodes were constructed around a cylindrical rubber holder with a moveable inner brass rod mounted within in a plastic electrode holder. A central stainless steel tube made the external electrical connection. This is illustrated in figure 3.10.

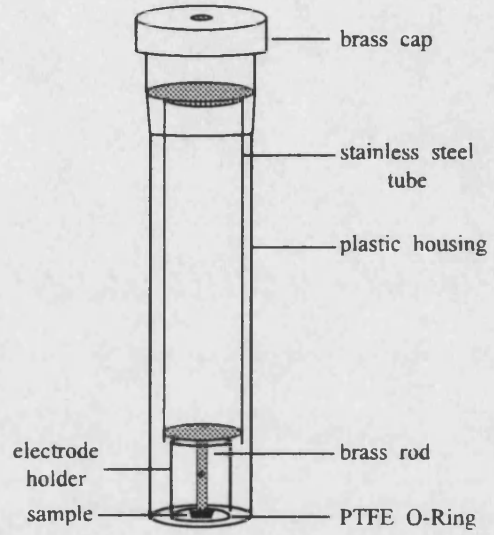

Figure 3.10. Diagram showing a SMSC electrode holder

These electrodes were used to study the anodic growth of CdS and Cd. Anodes were prepared according to the method of Peter *et al* [3]. Foils, 5mm x 5mm were cut from a 0.5mm thick Cd sheet (Aldrich) and attached to brass buttons using silver paint. Layers of epoxy (Araldite) were then built up around the electrode edges and over all areas of exposed brass to prevent electrolyte penetration to the underlying electrical contact. Electrodes were chemically etched in 50% HNO_3 (Sigma) for 2 seconds, rinsed in Milli-RO water, and then chemically polished for 5 seconds in a mixture of glacial acetic acid (Fluka) and hydrogen peroxide (110 vols., 33%)(Aldrich) (1:1) [3]. Finally, the

crystallite morphology of the metal was revealed by etching in Hcl (0.1M) for 2s. Rinsing in Milli-RO water gave a slightly rough but highly reflecting finish to the anodes. Previous workers have used an initial mechanical polish using alumina powders [4]. However this was found to give an irreproducible surface and so was not adopted.

For PEM, Cd foil anodes were prepared in an identical way to those used for SMSC measurements. The electrode holders differed though and are shown in figure 3.11. Cd foils were mounted onto brass buttons and placed within Kel-F buttons and sealed with epoxy. Electrical contact to the rear of the brass button was made by PTFE coated copper wire.

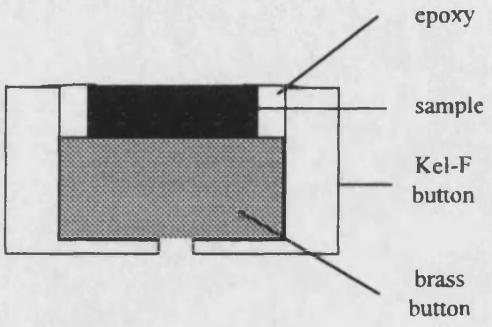

Figure 3.11. Diagram of a PEM button electrode holder

3.4.6. Annealing of Thin Film Electrodes

Thin film CdSe samples were annealed in air using a home built furnace. Temperature control was via a Eurotherm thermocouple (Pt.13%Rh.Pt) and Variac power supply. Samples were annealed in a ceramic boat placed within a quartz tube around which the heating coil (Kanthal, $11\Omega m^{-1}$, (RS) was wound and fixed using fire cement). The entire furnace was located in an insulated metal box. Typical annealing temperatures and times were 450 °C and 30 minutes, respectively.

3.5. Experimental techniques

3.5.1. Current Voltage

The current voltage plots characteristic semiconductor electrode was determined via a standard three electrode potentiostatic configuration. Potential ramps were generated by a waveform generator (Hi-Tek Instruments, PPR1) and applied to the semiconductor using a potentiostat (Hi-Tek Instruments). Either i-v, i-t, or v-t variations were recorded using a chart recorder (Phillips PM 8271). The experimental setup was similar to that shown in section 3.5.2 except that the phase sensitive detector and sine wave oscillator were omitted.

3.5.2. Capacitance Voltage Measurements

Capacitance voltage measurements for Mott Schottky plots were made using a phase sensitive detection technique. The experimental set-up is shown in figure 3.12.

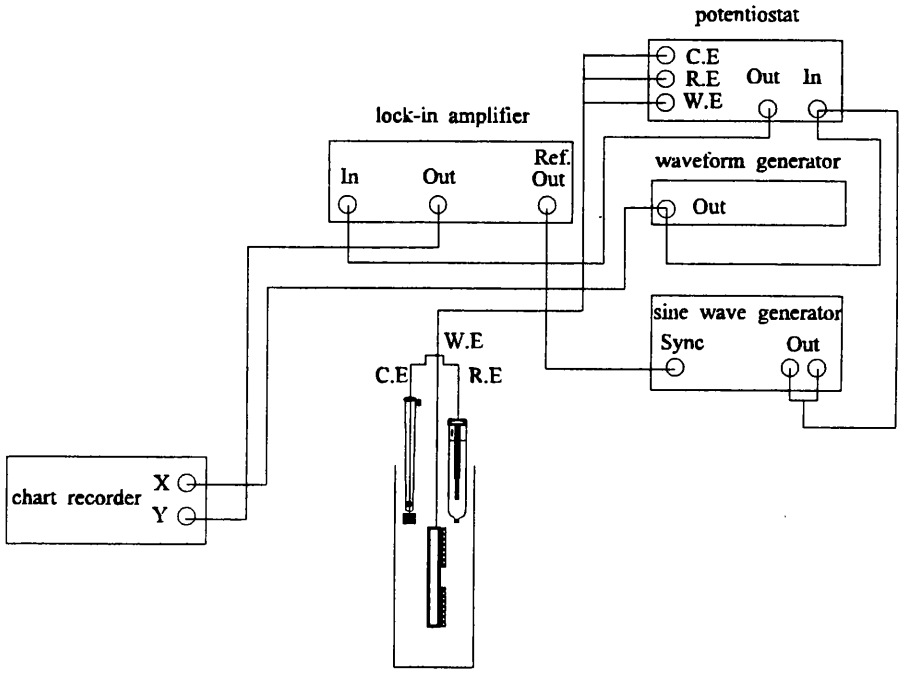

Figure 3.12. Diagram of the experimental setup used for capacitance voltage measurements.

Measurements were made under potentiostatic control. The dc potential was applied using a waveform generator (Hi-Tek Instruments, PPR1). A sinusoidally modulated ac voltage was superimposed on the dc potential using a sine wave generator (Farnell LF1). The current flowing through the electrode was detected using a lock-in amplifier (Stanford Research SRS830). The capacitance was derived from the 90° component of the ac current assuming a parallel equivalent circuit (i.e. series resistance effects were neglected). A chart recorder (Phillips PM8271) was used to record all results. The system was calibrated using precision capacitance (Time Electronics, 9000) and resistance boxes (RS 255-575) both with accuracies of 1%.

3.5.3. Photocurrent Spectroscopy and Voltammetry

The experimental arrangement for photocurrent spectroscopy is illustrated in figure 3.13.

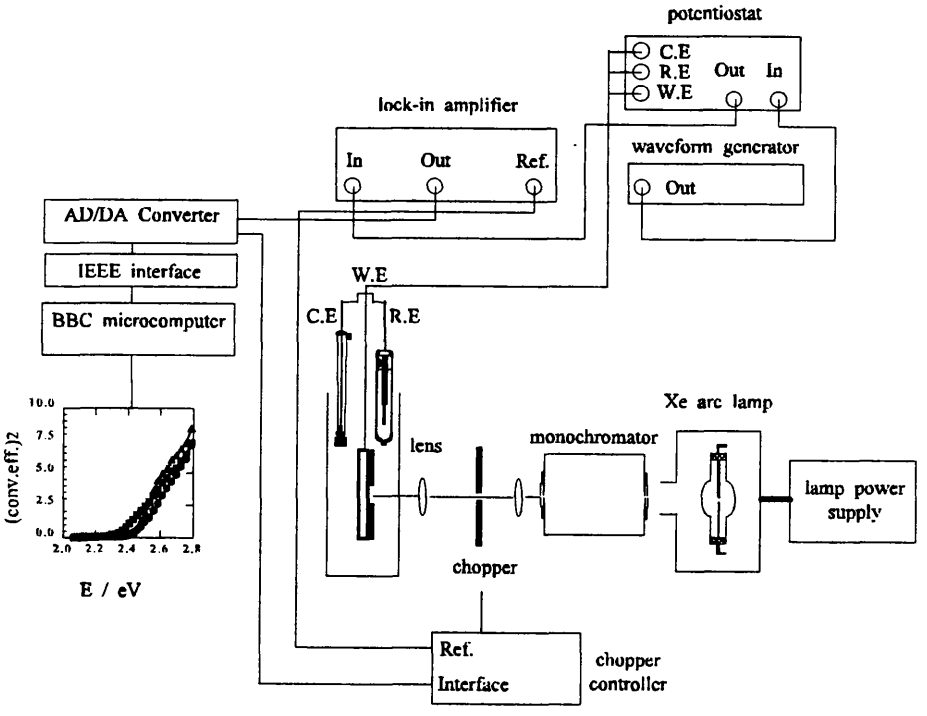

Figure 3.13. Diagram of the experimental setup used for photocurrent spectroscopy.

Light from a 150 W Xenon arc lamp (Osram XBO OFR, Applied Photophysics) passed through a computer controlled monochromator (Applied Photophysics, f/3.4) interfaced to a stepper motor/driver (Applied Photophysics, 7602) and was focused onto the working electrode using two quartz lenses (f=50 mm). The beam was modulated using a mechanical chopper (Bentham 218). To eliminate the $\lambda/2$ component in the incident beam (particularly for measurements made on CdSe in the range 650-850 nm) selected Schott OG series filters were used. The output of the potentiostat was fed to the lock-in amplifier (Stanford Research SRS830) synchronised to the frequency of the chopper. This possessed an auto phase function that locked into the maximum in-phase photocurrent measured on each occasion. For photocurrent voltammetry the output of the lock-in amplifier was fed directly to the chart recorder (Farnell RW 11) bypassing the BBC, with the voltage drive provided by a waveform generator (Hi-Tek Instruments, PPR1).

In order to determine the absolute photocurrent conversion efficiency for the samples measured, it was necessary to measure the output power of the of the illumination source using a calibrated Si photodiode (Macam Photometrics, SD112-UV). The photocurrent conversion efficiency of the photodiode (Φ_{DIODE}) may be calculated using equation 3.1.

$$\Phi_{DIODE} = \frac{i_{DIODE}}{P_{DIODE}} x \frac{hc}{\lambda e} \qquad (3.1)$$

where i_{DIODE} current measured from the photodiode (Am^{-2})

P_{DIODE} the power of the incident radiation (Wm^{-2})

h Planck constant (6.63×10^{-34} Js)

c velocity of light (2.99×10^8 ms^{-1})

e electronic charge (1.902×10^{-19} C)

λ wavelength of incident light (m)

The photocurrent conversion efficiency of the sample (Φ_{SAMPLE}) is given by

$$\Phi_{SAMPLE} = \frac{i_{SAMPLE}}{i_{DIODE}} x \Phi_{DIODE} \qquad (3.2)$$

The photodiode spectrum and thus photocurrent conversion efficiency were always measured for each set of photocurrent data.

For photocurrent spectroscopy all data acquisition was made using a BBC 128K microcomputer with IEEE interface. This was linked to the monochromator stepper motor for automated wavelength scans. For measurements made on samples with very low photocurrents (few nA) signal averaging was also employed. Data recorded on the BBC was transferred to PC by a file transfer program (KERMIT) for analysis and plotting.

3.5.4. Electrolyte Electroabsorption and Reflectance

Figure 3.14 shows a schematic diagram of the experimental set-up for electrolyte electroabsorption measurements. Description of the cell types and geometries used in absorption and reflection configurations are given in section 3.2.1.

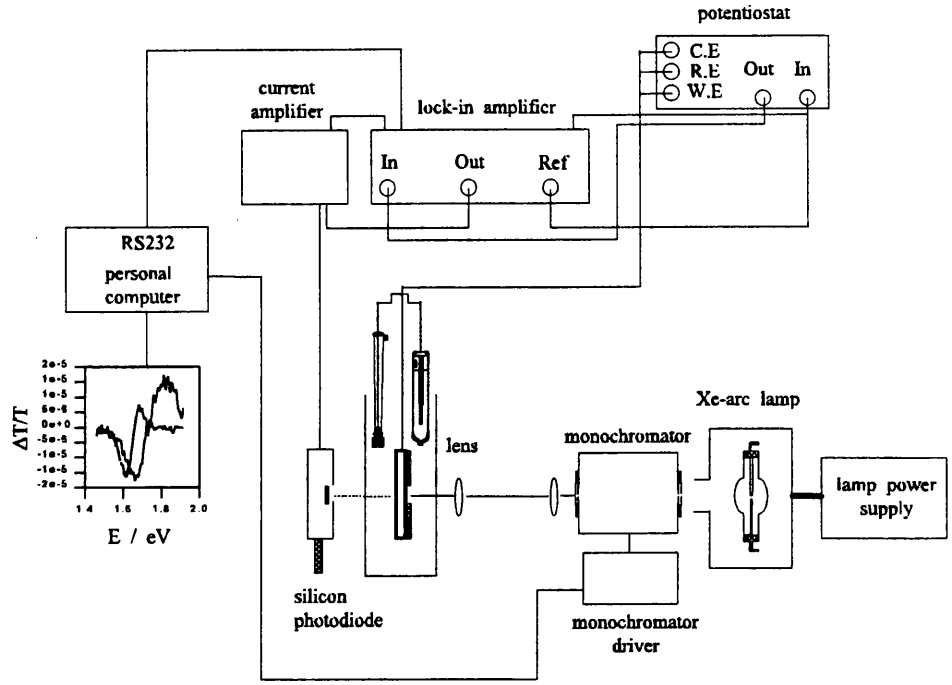

Figure 3.14. Diagram of the experimental setup used for electrolyte electroabsorption spectroscopy

For electroabsorption measurements, the working electrode was illuminated by a monochromatic light beam at an angle of incidence of 90°. Either a 120 W tungsten (Bentham IL1) or 150 Xe arc lamp (Osram XBO OFR, Applied Photophysics) in combination with a computer controlled diffraction grating monochromator (Bentham M300) and driver (Bentham SMD 3B/IEEE) were used to provide illumination. Stray $\lambda/2$ light was removed using suitable Schott OG series filters for the desired wavelength range. The beam was focused onto the working electrode using a lens (f=50mm). The modulated beam, after passing through the sample, was detected by either a Si-photodiode (Macam Photometrics) or side window photomultiplier tube (Bentham 231 and EMI 97556 Tube) powered by a high voltage power supply (750 V, Bentham 216) connected to a current amplifier (Bentham 265HF). The output of either of these was fed to a lock-in amplifier (Stanford SRS-830) interfaced to a microcomputer (Opus PC 486). Interfacing between the monochromator motor driver and PC was via the IEEE

interface and programmable inputs/outputs of the lock-in amplifier. Dedicated software written by Dr. M. Bailes enabled data acquisition, signal averaging, and ratioing to be performed through a series of simple on screen menus. Extensive data manipulation and plotting options were also available. The electrode potential was applied by a potentiostat (Hi-Tek Instruments) connected to a home built auto-ranging current amplifier (designed and constructed by Dr. M. Bailes). This unit also contained a dummy cell comprising of a pair of resistors. Prior to all measurements the system performed a self-test based on applying known dc and ac potentials to these resistors and subsequently measuring the magnitude and phase of the resulting current. Providing all system connections were correct values for these parameters equalled the calculated values written into the program. However, due to the close proximity of the dummy cell and current amplifier in the same unit, stray coupling between the potentiostat output and dummy cell led to cross talk effects. This was overcome by including the dummy circuit in the measuring system, then by-passing this section of the circuit for spectral measurements. The electrode potential was modulated with a sine wave using the in-built sine wave oscillator of the lock-in amplifier. Typical frequencies and amplitudes of modulation were 270 Hz and 100 mV rms., respectively. The dc bias was applied using one of the programmable outputs of the lock-in amplifier set by the user in the EER software. Detection of ΔT and T was made by splitting the signal and sending it to the phase sensitive detected and dc inputs, respectively. $\Delta T/T$ was calculated by the EER program.

3.5.5 Photoelectrochemical Imaging

Localised photoelectrochemical measurements were made on the anodic growth of CdS on Cd using two systems. The first, Scanning Microscopy for Semiconductor

Characterisation (SMSC)[5,6] was developed by Professor P Salvador and Dr A. M. Martinez Chaparro at the Instituto de Catálisis y Petrolequímica (C.S.I.C), Madrid. The second system, Photoelectrochemical Microscopy (PEM)[7,8], was developed by Professor D. E. Williams and Dr. R. S. Hutton at University College, London.

(i) SMSC

Shown in figure 3.15 is a diagram of the SMSC setup. This technique is based on an inverted microscope (Nikon Epiphot-MTE) with a choice of objectives in the range x 2.5, 5, 10, 20 and 40 and computer controlled *xy* stage of 1μm resolution which allowed automatic scanning of the light spot on the electrode surface. The sample was illuminated through the base of the cell using a choice of either a halogen lamp (Oriel, 50W) and monochromator (Oriel, 77250, 1/8m) with entrance and exits slits set at 1nm resolution, or an Ar-ion laser (Ion Laser Technology, 100 mW, λ=514 nm). In the former case using the x40 objective the minimum light spot diameter that could be obtained was 32 μm. For higher resolution illumination by laser was necessary. Using a beam collimator and spatial filter (SF) (Newport, M-910B), a spot radius in the order of 1μm was obtained. The spatial filter was found to appreciably improve image contrast, although a number of hours had to be invested in its alignment to ensure the optimum resolution. A schematic diagram of its operation is shown in figure 3.16.

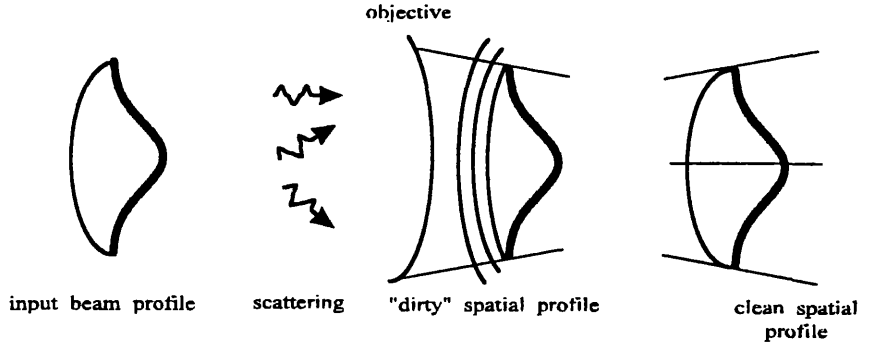

Figure 3.16. Diagram showing the mode of operation of a spatial filter

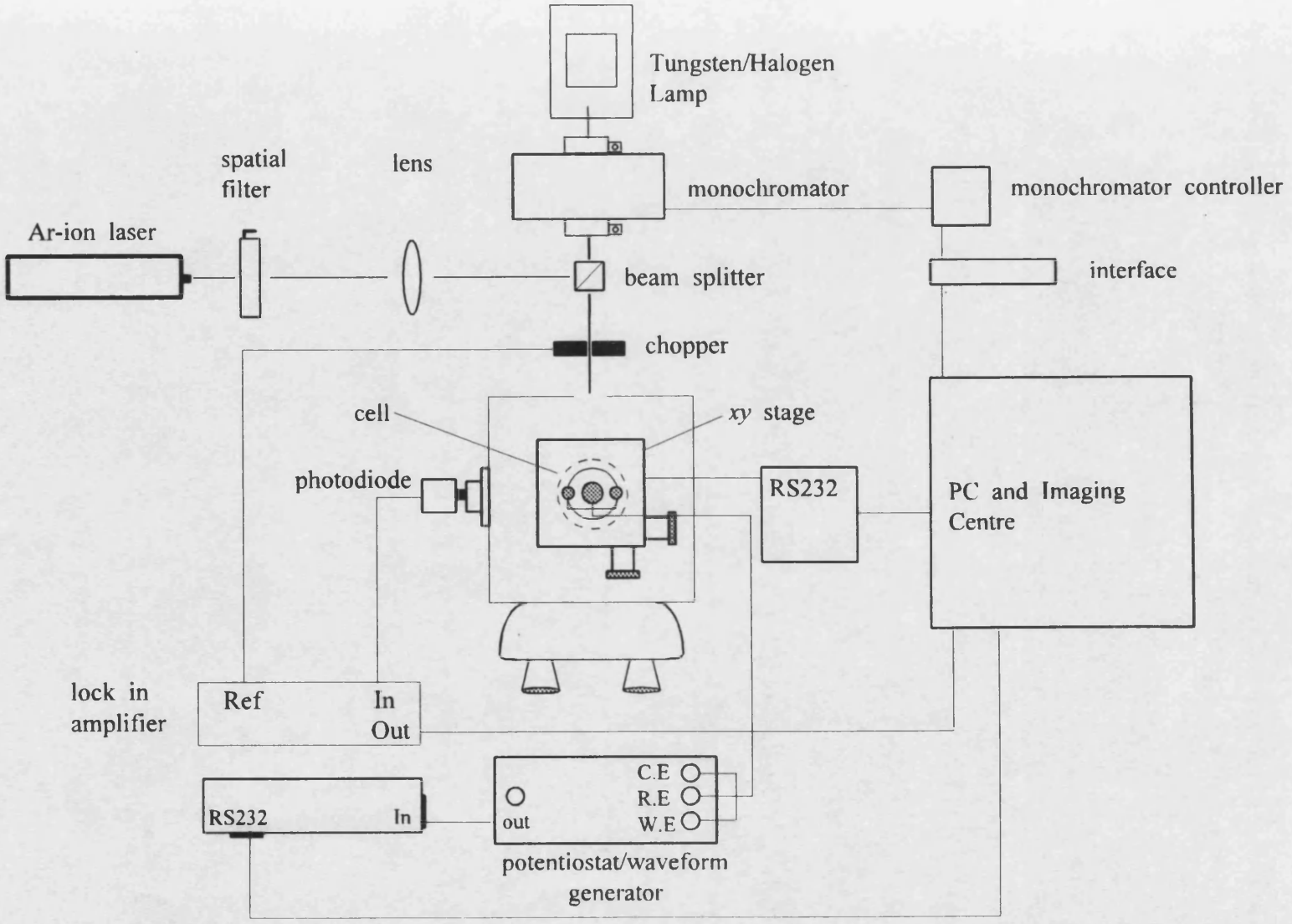

Figure 3.15. Schematic diagram of the "Scanning Microscopy for Semiconductor Characterisation" (SMSC) technique

As a result of airborne particulates and optical defects in other components of the system the intensity of the beam diminishes and fluctuations are introduced away from the normal gaussian distribution in light intensity. To produce a "clean" distribution in light intensity the beam is focused at the filter to produce an image of the source. All imperfections in the optical path are defocused in an annulus. A 25 μm diameter pinhole blocks most of the noise. Further focusing of the beam on to the sample surface was achieved by a combination of adjusting the position of the lens situated between the SF and beam splitter and movement the *xy* stage in the ±*z*-direction. Optimum focus was obtained when a sharp pin-point spot with no observable scattering was observed. As the illumination source was viewed by eye directly through the objective care had to be take when using the laser source. The laser intensity was cut using two 1% transmission neutral density filters (Schott) to ensure low enough light levels for safe viewing. Illumination levels were still sufficient for measuring photoelectrochemical effects. To improve the optical image contrast, the microscope incorporated "Normarski" prisms with all objectives used here. These produce increased contrast by enhancing surface features in the *z*-direction and are based on the differential interference (DIC) effect. A simplified diagram of the optical setup used in the microscope is given in figure 3.17.

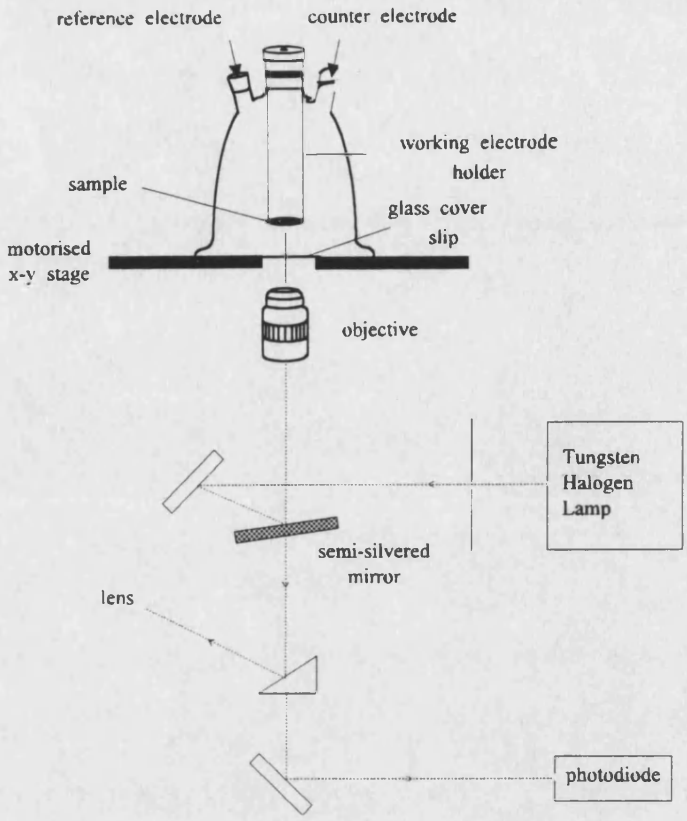

Figure 3.17. Optical setup used in the SMSC system

The three electrode glass cell shown in figure 3.6(a). was mounted on the *xy* stage and held in place via two polypropylene screws. The sample was moved into the field of view by adjusting the stage position by a joystick control. The dc potential was applied to the sample using a potentiostat (Wenking POS 73). A lock-in amplifier (EG&G 5120) synchronised to the chopping frequency was used to detect the in-phase photocurrent collected by the objective and sent to the Si photodiode. Light was modulated using a chopper (Rofin 7505) placed between the beam splitter and microscope. The chopping frequency was typically 20 Hz. A more detailed description of the principle of photocurrent measurements is given in section 2.8

The recording of photoelectrochemical data and subsequent image processing was made by PC (286, 16 MHz) and serial interface (RS232) connected to the lock-in

amplifier via a 12 bit AD card (Lab-PC, National Instruments). Control of the *xy* stage was also made via the serial interface.

Image processing software was written by Dr. A. M. Martinez Chaparro for a commercial video digitising card (Professional Image Board, Atronics International Inc.) enabling images to be displayed in either 32 grey scales or 16 colours. Video images of the surface were recorded using a charge coupled device (CCD) camera (Hitachi KPC-501) and video grabber (Sony SLV-474). Images were displayed on a monitor (Sony PVM-1440QM). Image quality was improved by filtering according to an anisotropic diffusion method [9] and further functional segmentation [10]. In all cases though as little further image manipulation was made as possible so as to minimise distortion of the original image.

(ii) PEM

Figure 3.18 shows the confocal laser microscope configuration based on a scanning laser microscope (MRC 600, Bio-Rad Microsciences). Light from an Ar-ion laser (25 mW, λ=415 nm) (Ion Laser Technology No. 5425) passes through the microscope, impinging on the electrode surface via the microscope objective (x10) and is rastered across its surface via two servo driven mirrors mounted on orthogonal axis. This is illustrated in figure 3.18 (a) and (b). The specularly reflected light passes back up through the microscope objective and is detected by a photomultiplier tube (Bio Rad). As the beam is rastered across the surface, the relative position of the mirrors corresponding to the localised change in current for a each position is recorded. The data was accumulated and saved in a framestore to obtain a grey scale image (0-256).

Experiments were made in the PTFE cell with the electrode holder shown in figures 3.6(b) and 3.11, respectively. The dc bias was applied to the sample using a

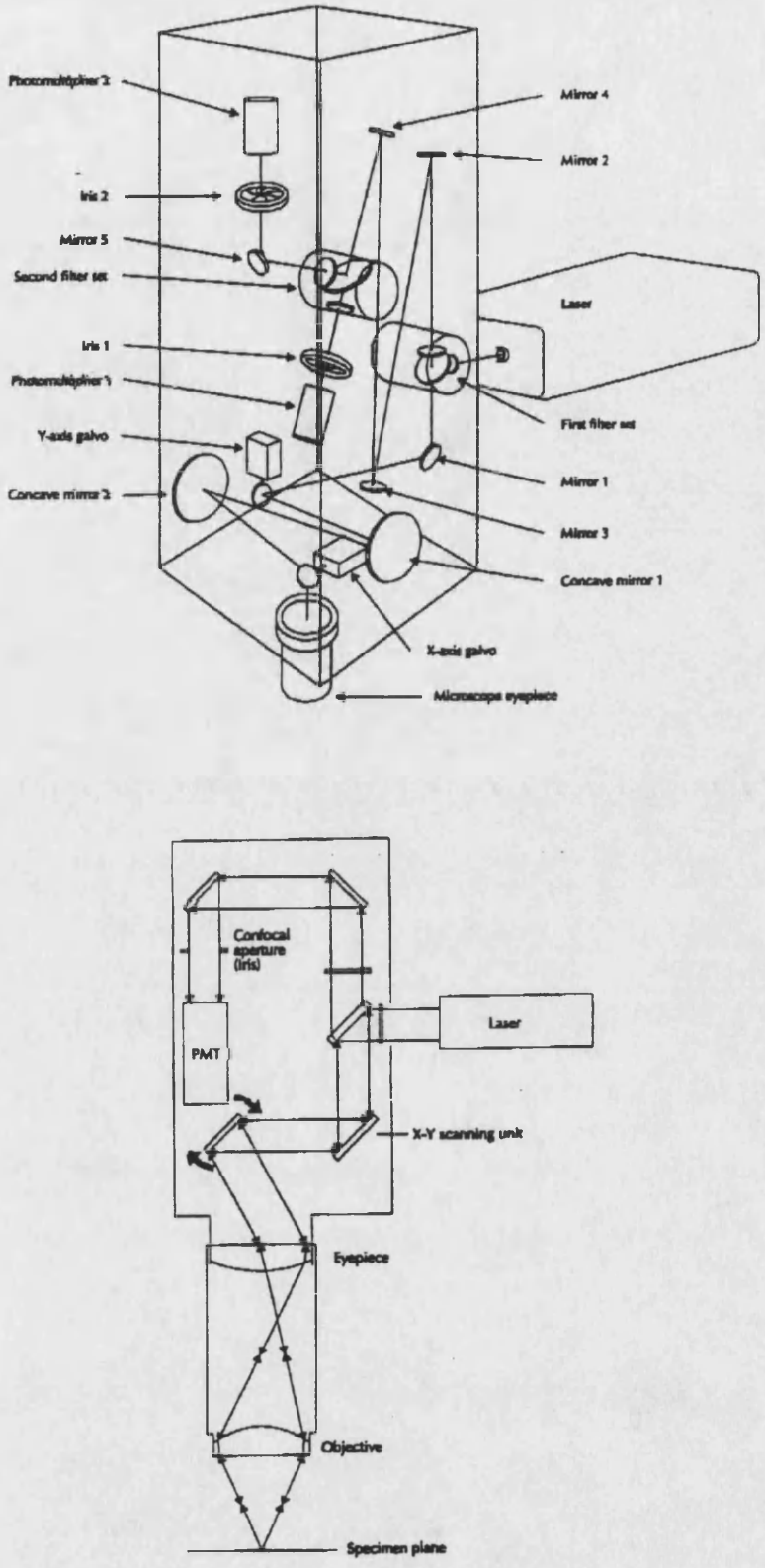

Figure 3.18. Confocal microscope. (a) Beam scan head and (b) beam rastering in specimen plane

potentiostat (home built) and waveform generator (PPR1, Hi-Tek Instruments). So as not to overload the input of the framestore for high illumination levels, the output of the potentiostat was coupled through a pre-amplifier and offset to match the input range of the framestore. In this way image contrast corresponds to changes in current due to the movement of the laser spot across the surface.

Image manipulation was made using a comprehensive imaging centre (Bio-Rad). This had extensive image manipulation facilities, but generally the only enhancements that were made were removal of noise, sharpening and contrast adjustment.

It will be seen in chapter 6 that the PEM technique gave images with far more detail than those obtained by SMSC, although the later does provide useful information. The principal reason for obtaining far sharper images of greater resolution by PEM is the use of confocal optics. In normal optical microscopy virtually all light reflected from the illuminated sample is detected, whereas in confocal mode the presence of a pinhole and focusing optics does not allow light scattered from regions out of the focal plane to retrace the path of the illuminated beam and so will not reach the photodetector [11]. This is illustrated in figure 3.19 (a) and (b).

(a)

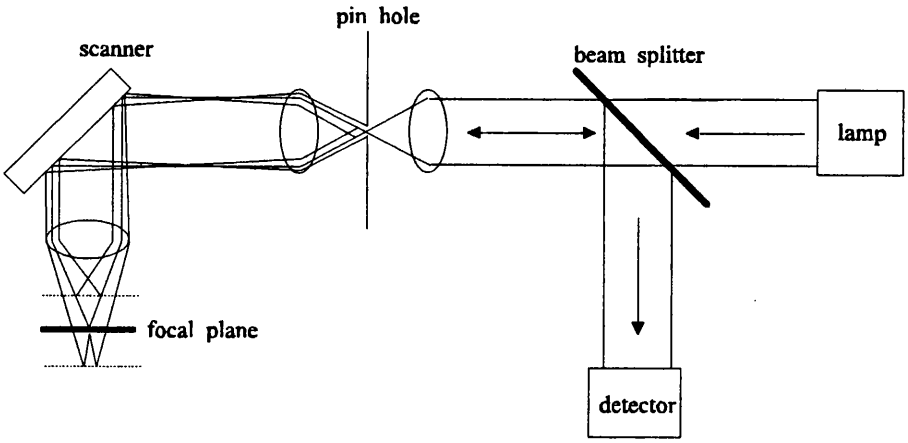

(b)

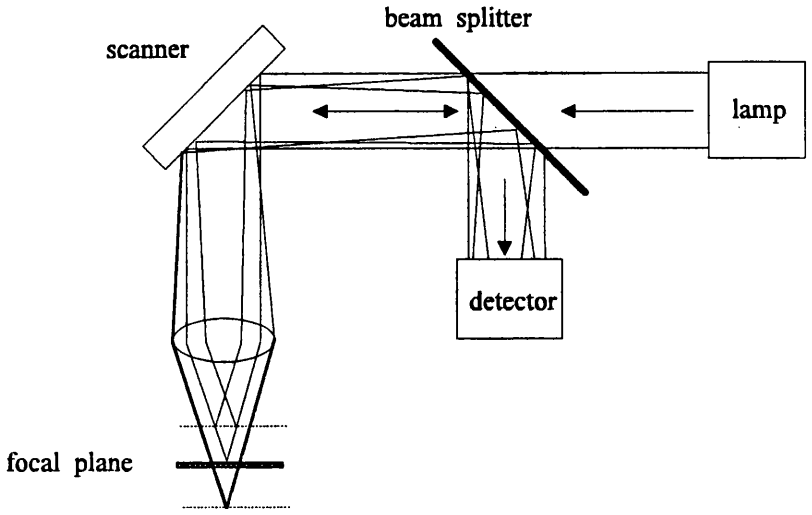

Figure 3.19. Diagram showing the effect of (a) confocal optics resulting in the refection of light from objects out of the focal plane (b) The absence of the pinhole and focussing optics leads to poor image resolution.

3.5.6 Surface Analytical Techniques

Table 3.1 lists details of the surface analytical techniques that were used to characterise CdSe and CdS thin films.

Acronym	Full description	Model	Measurement
SEM	Scanning electron microscopy	Jeol T330 and 6310	Surface morphology
AFM	Atomic force microscopy	Topometrix 2010 Discoverer	High resolution surface morphology
WDX	Wavelength dispersive x-ray analysis	Jeol Mircoprobe X-Ray analyser	Deposit composition
XRD	X-ray diffraction	Phillips Diffractometer	Structural analysis

Table 3.1. Summary of the surface analytical techniques used to characterise thin film CdS and CdSe.

References

1 H. Gatos, E. P. Warekois, M. C. Lavine, and A. Mariano, *J. Appl. Phys.*, **33**(2), 960 (1962); and subsequent erratum **34**, 2203 (1962)

2 R. Tenne and G. Hodes, *Appl. Phys. Lett.*, **37**(4), 428 (1980)

3 L. M. Peter, *Electrochima Acta*, **23**, 165 (1978)

4 M. W. Breiter, and W. Vedder, *Electrochim. Acta*, **13**, 1405 (1968)

5 P. Salvador, A. M. Martinez Chapparro, B. Coll, and M. Gonzalez, *Surf. Sci..*, **293**, 160 (1993)

6 P. Salvador, F. Decker, M. Pujadas, G. Razzin, L. P. Bicelli, and B. Scrosati, *J. Electrochem. Soc.*, **135**, 1934 (1988)

7 R. S. Hutton, D. E. Williams, *Electrochim. Acta*, **39**(5), 701 (1994)

8 L. M. Peter, R. Peat, A. Riley, and D. E. Williams, *J. Electrochem. Soc.*, **136**(11), 3352 (1989)

9 L. Alvarez, P. L. Lions, and J. M. Morel, *J. Numer. Anal.*, **29**, 845 (1992)

10 G. Koepfler, J. M. Morel, and S. Solimini, *Cachier du CEREMADE*, **9022** (1990)

11 A. R. J. Kucernak, Ph. D. Thesis, University of Southampton, 1991

Chapter 4

Results

Growth and Characterisation of CdSe thin films

4.1. Introduction

CdSe in an n-type semiconductor which can show either hexagonal (wurtzite) or cubic (zinc blende) structures. Table 4.1 lists some of its physical and chemical properties [1,2,3]. CdSe has reportedly been electrodeposited as a p-type material, although with limited success, by thallium[4] or indium doping[5].

Molar Mass / g	Density / gcm^{-3}	Melting Point / °C	ΔH°_f / $kJmol^{-1}$	ΔG°_f / $kJmol^{-1}$	ε	E_g / eV	E_{VB} / eV	E_{CB} / eV
191.36	5.9	1239	145.2	-141.5	9.25 $E \parallel c$ 8.75 $E \perp c$	1.74	6.62	4.95

Table 4.1. Physical and chemical properties of single crystal CdSe

The major driving force the study of CdSe is the promise it has shown as a semiconducting material for photoelectrochemical cells [6]. In aqueous polysulfide electrolytes (1 M Na_2S: 1M S: 1 M NaOH), solar conversion efficiencies of 8.4% and 6.5% have been reported for single crystal [7] and vacuum deposited [8] CdSe, respectively. CdSe photoelectrodes have been prepared in a wide variety of ways with a corresponding wide variation in performance in liquid junction solar cells (LJSC). Table 4.2 gives details of the various preparative routes and the solar-to electrical conversion efficiencies obtained. More comprehensive details of the fabrication procedures can be found in the relevant references. Earlier uses of CdSe relied on its high photoactivity. CdSe has been employed in photoconductivity cells to detect radiation in the spectral region extending from the near infra-red to gamma radiation. Its other uses include lasing platelets in $Ga(P_xAs_{1-x})$ laser diodes [9], ultrasonic amplifiers [10], and image intensifiers [11].

Method of Preparation	Experimental Procedure	Maximum Efficiency (%) / Light Intensity (mW/cm^2)	Reference
Cathodic Electrodeposition	Electrolyte contains Cd^{2+} and SeO_2 which are reduced at the cathode precipitating CdSe.	6.7 / 80	37, 42, 76
Cathodic Electrodeposition	Excess Se incorporation is avoided by use of $SeSO_3^{2-}$. $[Cd^{2+}]$ is by complexed to prevent bulk Cd deposition.	No efficiency data available	12, 71
Anodisation	Anodisation of Cd rod or sheet in 1M K_2Se/1mol dm^{-3} KOH	0.6 / 75	13, 14, 15
Pressure Sintered	CdSe powder is held under a P=10kPa and T=1000°C for 2hrs. CdSe disks were annealed in Cd to increase conductivity	5.1 / 71	16,15
Slurry Painted	CdSe powder + fluxing agent ($ZnCl_2$) is painted onto Ti and sintered at 650-670°C for 40 minutes in Ar.	3.9 / 84	17
Vacuum Evaporation	Evaporation of CdSe or co-evaporation of Cd and Se at 10^{-6} Torr onto Ti or SnO_2/glass substrates.	6.5 / 75	18,19
Spray Pyrolysis	Solution of Cd^{2+} and selenourea is sprayed onto heated substrate. HSe^- ions formed by hydrolysis react with Cd^{2+} ions.	6.4 / 68	20, 21
Electrophoretic	CdSe powder is introduced ultrasonically into propylene carbonate as a suspension. Particles deposited by applying a dc voltage	2 / AM1.5 equivalent	22
Chemical Deposition	Growth proceeds by $Cd(NH_3)_4^{2+}$ and Se^{2-} or $SeSO_3^{2-}$ ions. Precipitation is controlled by the release rate of Cd^{2+} from the complex.	6.3 / 80	23,24

Table 4.2 Preparation and performance of CdSe photoelectrodes

During the early studies on the growth and properties of CdSe thin films, interest was still strong in the photovoltaic action [25] and photoconductive action [26] shown by elemental selenium. For this reason Se was widely employed in the production of photocells and exposure meters for photographic use. However, the use of Se as a photoactive material has been widely superseded by compounds which had better defined properties and superior photoelectrochemical performance such as CdSe and ZnSe.

More recent and exciting areas CdSe has found application are:

(i) CdSe quantum dots [27]: Epitaxially oriented CdSe quantum dots (≈5nm in diameter) have been electrochemically deposited onto Au(111) surfaces.

(ii) Electroluminescent devices [28,29]: Hybrid organic/inorganic light emitting diodes (LED's) have been constructed by embedding CdSe particles prepared by controlled precipitation in a layer of semiconducting *p*-paraphenylene vinylene (PPV).

(iii) Coupled Semiconductor Systems [30]: CdSe thin films with improved photocurrent stability and efficiency have been obtained when electrodeposited onto TiO_2 particulate supports.

Electrodeposition is a simple and versatile method for preparing thin film CdSe. However, contamination of the target material with side products, e.g. Se, is often a problem with the technique. This is the case when selenious acid, which appears to be the most favoured precursor, is used as the Se source. The co-deposition of excess Se necessitates the need for a final annealing stage. In this work, films with good stoichiometries have been grown by electrodeposition from selenosulfite solutions. The various aspects of the solution chemistry involved with the acid and alkaline based plating baths are discussed in the following section

In solution, selenium exists electrochemical activity in two different valent states: Se^{2-}, and Se^{4+}. The polarographic behaviour of Se has been studied in great

detail where it has been found that the composition of the solution and pH value exert a considerable influence on the number and shape of the reduction waves as well as on the half-wave potential values. Species that have been identified include[31] H_2Se, HSe^-, Se^{2-}, SeO_3^{2-}, $HSeO_2^-$, and H_2SeO_3.

(i) Selenious acid

H_2SeO_3 can undergo either a $4e^-$ or $6e^-$ reduction according to equations 4.1 and 4.2.

$$H_2SeO_3 + 4H^+ + 4e^- \rightarrow Se + 3H_2O \qquad E^\circ = +0.50 \text{ V vs SCE} \qquad (4.1)$$

$$H_2SeO_3 + 6H^+ + 6e^- \rightarrow H_2Se + 3H_2O \qquad E^\circ = +0.12 \text{ V vs SCE} \qquad (4.2)$$

Schawer and Suchy [32] were the first to measure the polarograms of tetravalent Se in selenious acid (1 mol dm^{-3} HCl) where three reduction waves were observed. A comparison of the limiting currents obtained showed that selenious acid is subjected to a four or six electron reduction stages. However there was some uncertainty in assigning the origin of the third wave. The explanation for this lies in the formation of a Hg-Se intermetallic compound via the $4e^-$ reaction.

$$H_2SeO_3 + 4e^- + 4H^+ + Hg \rightarrow HgSe + 3H_2O \quad E^\circ = -0.49 \text{ V vs SCE} \qquad (4.3)$$

In early studies made using mercury drop electrodes, the polarographic waves of Se(IV) were found to change with standing, although the formation of HgSe was overlooked. More recent investigations by Skyllas Kazakos [33] and Wei [34] have studied the solution chemistry of Se(IV) at gold electrodes and it has been suggested that certain peaks in the voltammogram correspond to the reduction of intermetallic Au-Se compounds. On this

basis, Rajeshwar [35] tentatively assigned an anodic peak measured in the voltammogram of selenious acid at an Au electrode to the following reaction

$$H_2SeO_3 + 4H^+ + 4e^- \rightarrow Se\ (Au) + 3H_2O \qquad (4.4)$$

Andrews and Johnson [36] have reported two waves for the reduction of Se(IV) at Au, suggesting that the peak at more positive potentials may be due to a under potential deposition of Se(0) as a result of strong Au-Se bond interactions.

Of particular importance to the electrodeposition of CdSe films is the chemical conproportionation reaction given in equation 4.5

$$H_2SeO_3 + 2H_2Se \rightarrow 3Se + 3H_2O \qquad (4.5)$$

The rate of this chemical reaction is dependent on the concentration of H_2SeO_3, so if this concentration is large enough, reaction 4.4 is fast and the overall reduction process appears to be

$$H_2SeO_3 + 4H^+ + 4e^- \rightarrow Se + 3H_2O \qquad E^\circ = -0.98\ V\ vs\ SCE \qquad (4.6)$$

Skyllas Kazacos and Miller [33] observed a rapid electrode passivation when H_2SeO_3 solution concentrations were above $2x10^{-3}$ mol dm^{-3}, attributed to the formation of an insulating Se layer. On the basis of these reactions the authors proposed two mechanisms for the cathodic reduction of H_2SeO_3 depending on the nature of the metal substrate used. For group I substrates (Au, Pt, and C), a competition exists between formation of H_2Se and of Se which passivates the electrode (reactions 4.1, 4.2, and

4.5). Group II substrates are "active" metals like AuHg, Ag, and Cu, and for these metals the mechanism follows the reaction given in equation 4.3. However Rajeshwar [35] has incorrectly placed Au in group I as it has been shown by Andrews *et al* [36] that Au also constitutes an active metal though Au-Se formation.

(ii) CdSe formation from selenious acid

The earliest reported studies on the cathodic electrodeposition of CdSe were made by Pacanskas [37] and Gobrecht [38]. Thin layers of CdSe were prepared on Pt or Cu cathodes by electrolysis of $CdSO_4$ and SeO_2 acidified in H_2SO_4. Hodes *et al* [39] carried out the first photoelectrochemical studies of polycrystalline CdSe films produced by this technique using a polysulfide redox couple. The mechanism for CdSe formation has received considerable attention in an attempt to understand why CdSe films deposited from an acidic bath always contained an excess Se.

Two mechanisms have been proposed for CdSe formation

(i) Direct $6e^-$ co-reduction,

$$H_2SeO_3 + Cd^{2+} + 6e^- + 4H^+ \rightarrow CdSe + 3H_2O \qquad (4.7)$$

(ii) $6e^-$ Reduction to H_2Se, followed by

$$H_2Se + Cd^{2+} \rightarrow CdSe + 2H^+ \qquad (4.8)$$

In the case of solutions of Cd^{2+} and SeO_2 (equation 4.7), it is commonly supposed that the deposition involves the reduction of Se(IV) to Se^{2-}, which then reacts chemically with Cd^{2+} at the electrode surface. However, Mishra and Rajeshwar [40] have argued that the mechanism for CdSe deposition is a direct $6e^-$ reduction via equation 4.6, although

presumably reactions 4.1 and 4.2 operate in competition with this process. For either mechanism, the net reaction is that represented by equation 4.7.

(iii) CdSe formation from selenosulfite

Annealing treatments to remove selenium would be unnecessary if co-deposition of selenium, via the conproportionation reaction (equation 4.5) could be avoided. In order to achieve this Skyllas Kazacos and Miller [33] started with the selenosulfite ion, $SeSO_3^{2-}$ (where Se occurs in oxidation state -2, compared with +4 in selenious acid). The authors postulated that free selenide ions, for subsequent reaction with Cd^{2+} ions, are formed electrochemically by the reaction

$$SeSO_3^{2-} + 2e^- \rightarrow Se^{2-} + SO_3^{2-} \qquad E° = -1.0V \text{ vs SCE} \qquad (4.9)$$

Elementary Cd would be formed unless the activity of free Cd^{2+} ions is kept low by means of complexation with NTA. Film formation in the alkaline selenosulfite bath takes place according to

$$SeSO_3^{2-} + Cd^{2+} + 2e^- \rightarrow CdSe + SO_3^{2-} \qquad (4.10)$$

The reaction mechanism appears to depend very much on the complexant; when EDTA is employed, the reduction of $SeSO_3^{2-}$ to Se^{2-} and SO_3^{2-} has been proposed [76]; however when NTA is used it seems that first Cd^{2+} is reduced to Cd which then chemically reacts with $SeSO_3^{2-}$ to give CdSe [76].

However, relatively few studies have been made on the voltammetry of $SeSO_3^{2-}$ and its use in the cathodic electrodeposition of CdSe, so that uncertainty exists about the mechanism by which CdSe is formed. A mechanism for the growth of CdSe is

proposed in section 4.2.1 based upon a voltammetric study of the individual species present in the electroplating bath.

An alternative strategy to avoid excess Se incorporation when depositing films from selenious acid has been given by Kresin *et al* [41]. Stoichiometric CdSe was obtained by sequential monolayer deposition. This method involves the electrodeposition of sequential layers of CdSe by sweeping the potential of the cathode (Ti or Ni) between two cathodic limits in a solution containing $CdCl_2$ (0.1 mol dm^{-3}) and SeO_2 ($3x10^{-3}$ mol dm^{-3}). The Se concentration is low enough that only submonolayer amounts of Se are reduced for each cycle, while a large excess of Cd is deposited and subsequently stripped. The CdSe films that result were found by electron microprobe analysis to have ≈1:1 stoichiometries.

Pandey *et al* [42] have reported the cathodic electrodeposition of CdSe from an acidic SeO_2 based bath containing 10^{-2} mol dm^{-3} EDTA, supposedly to prevent the co-deposition of metallic impurities. Band gaps derived from photocurrent spectra were close to those obtained for single crystal CdSe (E_g = 1.74 eV), although doping densities were rather low (≈ 10^{16} cm^{-3}). However no information on the stoichiometries of the films were given to indicate the success of combining the complexation strategy usually associated with the selenosulfite route for growing CdSe films with a method which is well known to produce deposits with an excess of Se.

4.2. Results and Discussion

4.2.1 Linear sweep voltammetry

(i) $CdCl_2$

Figure 4.1 shows the cyclic voltammogram obtained for the reduction of Cd at a glassy carbon electrode from $CdCl_2$ (0.08 mol dm^{-3}, pH 9).

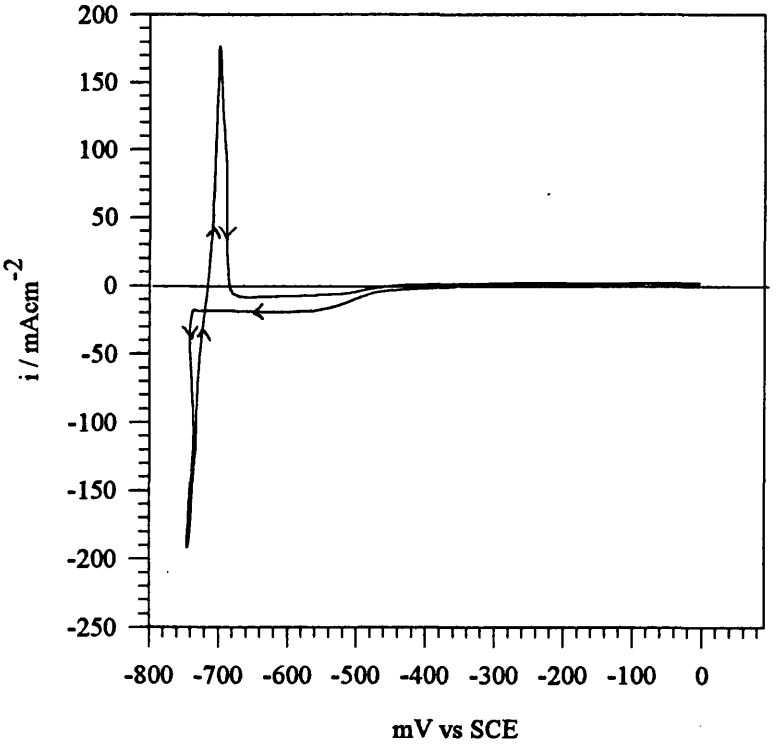

Figure 4.1. Cyclic voltammogram of $CdCl_2$ (0.08 mol dm^{-3}) at a glassy carbon electrode (pH 9), ν=100 mVs^{-1})

The sharp rise in the cathodic current at -740 mV indicates the deposition of bulk cadmium. The shape of the voltammogram is characteristic of a metal deposition reaction exhibiting a nucleation overpotential, i.e. in this case the potential has to be more negative to deposit Cd on glassy carbon than on bulk Cd ($\eta \approx 70$ mV). The equilibrium potential has been taken as the point at which the voltammogram crosses the potential axis on the reverse (anodic going) scan. At potentials close to the cathodic limit of the scan, the electrode surface became covered in loosely adherent, dendritic cadmium. This is characteristic of mass transfer controlled growth observed at high current densities.

(ii) $SeSO_3^{2-}$

In the same manner, pure selenium can be deposited from freshly prepared Na_2SeSO_3 (0.05 mol dm^{-3}, pH 12). The cyclic voltammogram for this system is shown in figure 4.2.

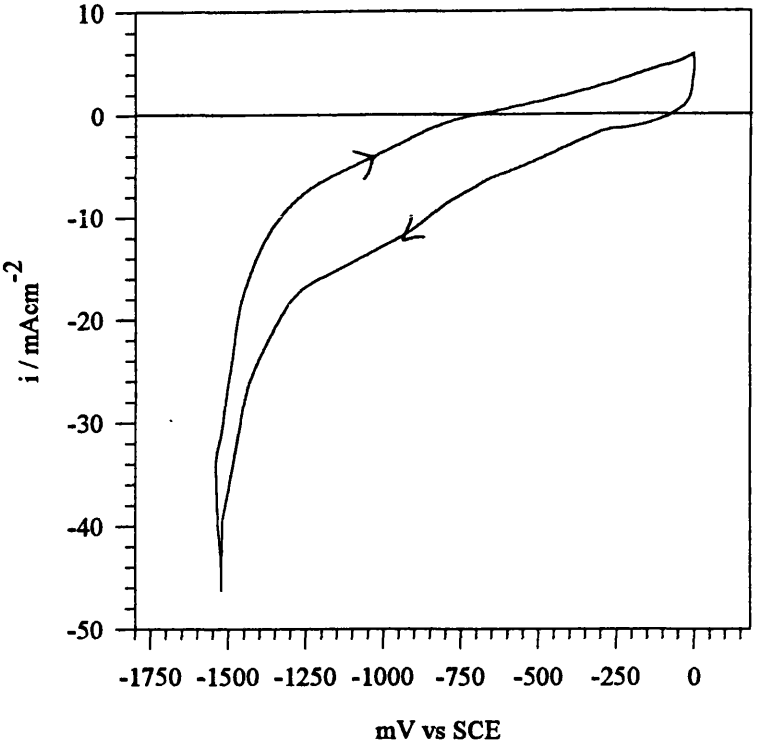

Figure 4.2. Cyclic voltammogram of Na_2SeSO_3 (0.1 mol dm^{-3}) at a glassy carbon electrode (pH 12, v=100 mVs^{-1})

The theoretical equilibrium potential for the $SeSO_3^{2-}$/Se couple is ≈ -1.0 V. As the i-V curve is poorly defined, extracting a potential for the reduction of the selenosulfite ion is difficult. The increasing current before and beyond E° suggests that deposition occurs over a much wider region, and the slow increase in cathodic current rises implies a sluggish rate of nucleation and growth of the Se layer. As current flow commences at potentials far more positive that the E° for $SeSO_3^{2-}$, a mass transfer controlled UPD process is possible.

The electrode was removed from the electrolyte at -400, -800, and -1000 mV to ascertain whether film growth had occurred on the glassy carbon surface. Only at

-1000 mV had a deep red film had formed at the electrode surface. For growth at more positive potentials, characterisation of the composition and morphology of the electrode by surface analytical techniques would reveal whether Se deposition proceeds via a UPD route. Lozios *et al* [43] found that under mildly acidic conditions the electrodeposited selenium consists of the red insulating phase, mixed with a small amount of the grey metallic phase. By using very acidic electrolytes (pH<1), the conducting grey phase is favoured. If an insulating layer of Se were formed on the electrode surface, some form of plateau behaviour would be expected. It could be anticipated that the cathodic current would decrease to a plateau by scanning the potential further negative. However, under such conditions the simultaneous process of hydrogen evolution could mask these effects. The significant difference between the forward and reverse scan and the absence of a well defined stripping peak are characteristic of an electrode surface covered by a passivating layer. Jarzabek and Kublik [44] have observed well defined waves of Se(IV) reduction at soft graphite electrodes, but poorly defined voltammetric features at glassy carbon. They attributed this to the favourable surface glassy carbon presents for forming absorbed layers with species such as Se. In this case an absorbed layer containing Se is stripped at a sluggish rate from the electrode surface. The situation is further complicated by the presence of polyselenides (Se_x) which may also undergo reduction to form elemental Se. However no assessment of their redox chemistry has been made in solutions containing selenosulfite. From studies made by Müller *et al* [45] on the cathodic dissolution of selenium, it was found that in strongly alkaline electrolytes such as 0.1 mol dm^{-3} KOH, there is a shift from the formation of an insulating layer of red Se on the cathode surface to the formation of polyselenides in the solution. The authors supposed that selenide ions formed initially by the reduction of

$SeSO_3^{2-}$, subsequently dissolve selenium to yield polyselenides. These are responsible for the light yellow tint of selenosulfite solutions.

During the forward potential scan in figure 4.2, the increase in the cathodic current is not constant but shows subtle changes associated with the reduction of distinct selenosulfite and polyselenide species. The difficulty is in assigning identities to the reduction peaks with confidence. As the passivating layer of red selenium restrict the flow of electrons between the substrate and the solution, the currents associated with these small "fluctuations" are superimposed on a broad background and are of the order of less than μA. Topopova[46] has shown that a diffuse poorly defined reduction wave at -1.0 V corresponding to the $2e^-$ reduction of $SeSO_3^{2-}$ on the dropping mercury electrode has been found to be identical for selenosulfide (Se_2S^{2-}) and polyselenide (Se_x) species. The authors put forward the hypothesis that the selenium containing anions react in all cases with mercury, and that the HgSe formed as result of this interaction undergoes reduction. In this work it could be postulated that chemisorbed selenosulfite and polyselenide species are reduced at the glassy carbon surface. Only in acidic electrolytes are the reduction steps associated with selenite, selenide, and selenium clearly visible. The electrode only becomes passivated at potentials close to the hydrogen evolution region where the selenide ions interact with selenite ions to yield elemental Se.

(iii) Cd^{2+} + NTA

Figure 4.3 illustrates the effect of the chelating agent, nitrilotriacetic acid (NTA) (0.1 mol dm^{-3}) (pH 9), on the reduction behaviour of Cd^{2+} between 0 mV and -1000 mV

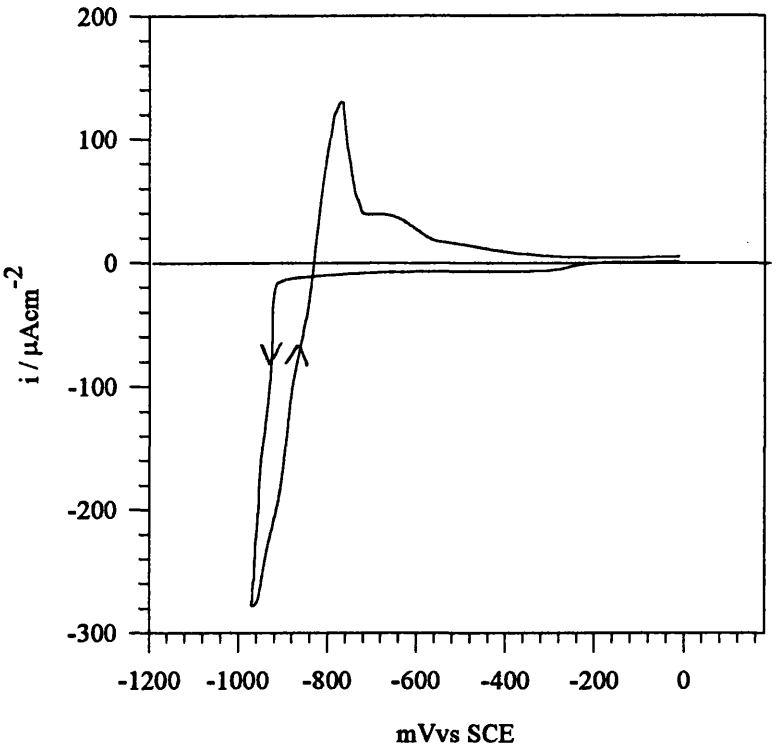

Figure 4.3. Cyclic voltammogram of $CdCl_2$ (0.08 mol dm^{-3}) and NTA (0.01 mol dm^{-3}) at a glassy carbon electrode (pH 9, v=100 mVs^{-1})

The presence of the chelating agent clearly shifts the reduction of Cd^{2+} ions to more negative potentials (compare with figure 4.1). The corresponding stripping region seems to be composed of two peaks: one that is sharp and centred at ≈ -770 mV and the second which appears as a broader shoulder on the first peak at ≈ -640 mV. This suggests that stripping involves the oxidation of two types of Cd species, although only a single reduction wave is observed. Lai *et al* [47] found that for solution pH values between 2.0 and 7.0, a ≈200 mV difference separated the reduction of free and chelated cadmium species that co-exist in solution. However, at pH 9, Cd^{2+} is likely to only exist in the bound form. This work suggests that oxidation of Cd is responsible for the

1st stripping peak, whereas the shoulder at more positive potentials corresponds to a pre-peak associated with the *electrochemical* oxidation of a *chemically* absorbed layer of Cd/NTA at the electrode surface. It is well known that NTA is adsorbed at metal surfaces as it is used as a surface leveller in the electroplating of metals [48]. The complexing agent modifies the kinetics of nucleation and growth of the metal layer via adsorption at the electrode surface.

(iv) Na_2SeSO_3 and NTA

The degree of interaction, if any, between $SeSO_3^{2-}$ (0.05 mol dm^{-3}) and the complexing agent, NTA (0.1 mol dm^{-3}) (pH 12), can be assessed in the voltammogram plotted in figure 4.4.

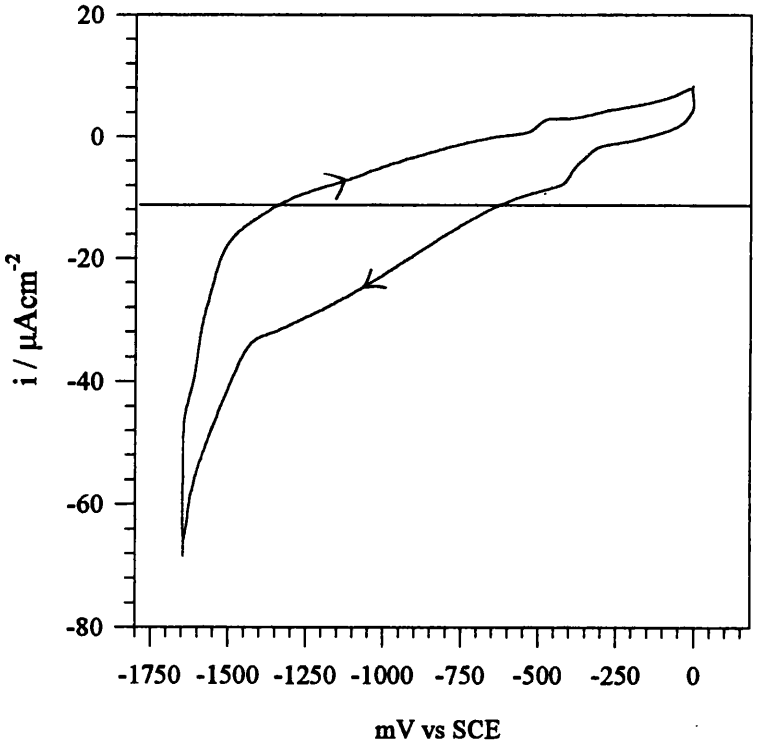

Figure 4.4. Cyclic voltammogram of Na_2SeSO_3 (0.05 mol dm^{-3}) and NTA (0.1 mol dm^{-3}) at a glassy carbon electrode (pH 12, ν=100 mVs^{-1})

Comparison of the above voltammogram with that obtained for $SeSO_3^{2-}$ alone reveals a great similarity in shape and magnitude. However, in the presence of NTA, additional structure is evident in the forward scan, in particular a wave at ≈ -480 mV and a sharp increase in current at ≈ -1400 mV corresponding to the onset of hydrogen evolution. In figure 4.2, the first case was assigned to the slow reduction of selenosulfite ions. The role of the NTA can be ascertained from the Cd/NTA system, where additional "routes" for electron transfer are provided via NTA species bound by adsorption at the glassy carbon surface. The wave at ≈-480 mV may therefore be due to selenosulfite reduction at a glassy carbon surface covered by NTA. As the potential is made more negative, further reduction of $SeSO_3^{2-}$ occurs at a Se covered surface. At these potentials the influence the NTA layer on the reduction of the selenosulfite ion is no longer important and the reduction follows a route similar to $SeSO_3^{2-}$ alone.

It can be concluded, principally from the great similarity between $SeSO_3^{2-}$ and $SeSO_3^{2-}$ /NTA voltammograms, that complexation between the two species does not occur. NTA is a metal complexing agent and so is unlikely to combine with anions such as selenosulfite.

(v) Cd^{2+}, NTA, and $SeSO_3^{2-}$

Figure 4.5 shows the cyclic voltammogram for a plating bath containing Cd^{2+}, NTA, and $SeSO_3^{2-}$ at pH 9. The potential was ramped between 0 mV and -1650 mV at 100 mVs^{-1}.

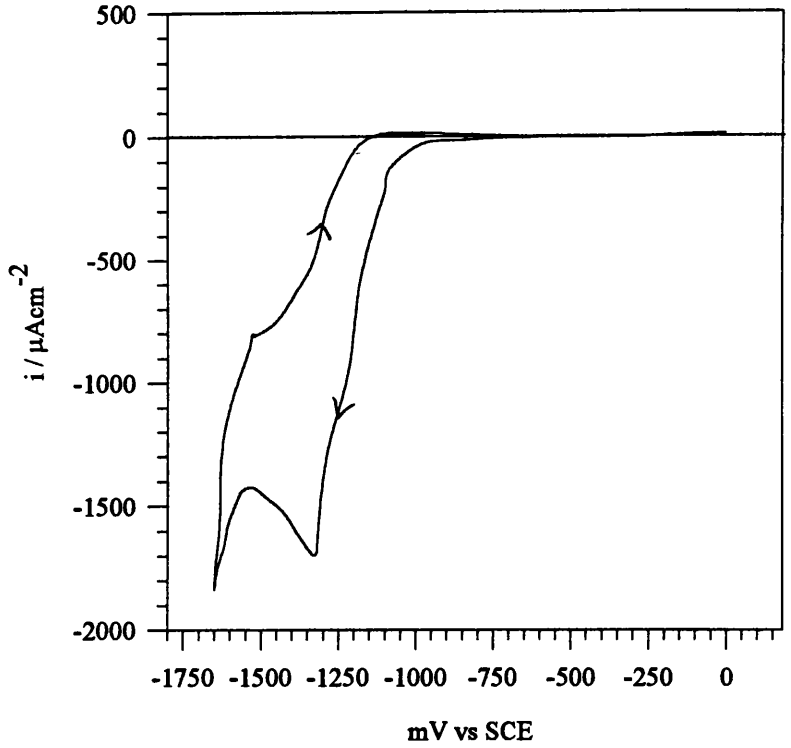

Figure 4.5. Cyclic voltammogram of $CdCl_2$ (0.08 mol dm^{-3}), $Na_2SeSO_3^{2-}$ (0.05 mol dm^{-3}) and NTA (0.1 mol dm^{-3}) at a glassy carbon electrode (pH 9), v=100 mVs^{-1})

The most noticeable change in the voltammogram is that considerably higher currents are obtained compared to figures 4.1 to 4.4. As the potential in swept in a negative direction from 0mV, the cathodic current increases in the same way as for $SeSO_3^{2-}$ alone. However, the increase in the current is not smooth but follows a slightly undulating path. As these reduction waves are poorly defined, it is impossible to assign identities to the individual regions. This is no doubt complicated by NTA absorption at the electrode surface. To determine whether a layer of CdSe had been deposited, the electrode was removed from the electrolyte at -1200 mV and -1000 mV. In the first case a dark orange, rough layer covered the glassy carbon surface, and in the second case a far more compact and homogeneous layer was obtained. Both layers appeared quite

different from the deep red Se layer grown from Se-only containing electrolytes, suggesting CdSe had been formed. The most negative peak in the voltammogram corresponds to the reduction of CdSe ($E^\circ = -1.77$ V) and the onset of hydrogen evolution. The sharp increase in current observed on scan reversal is associated with stripping of Cd and Se^{2-} from CdSe layer. Not until ≈ -700 mV is the electrode surface completely stripped of the electrodeposited layer, as indicated by the near zero oxidation current.

(vi) CdSe formation from selenosulfite on tin oxide coated glass

Figure 4.6 shows the i-V curve obtained at a SnO_2 coated glass electrode immersed in a plating solution containing $SeSO_3^{2-}$, Cd^{2+}, and NTA at 80°C and pH 9.

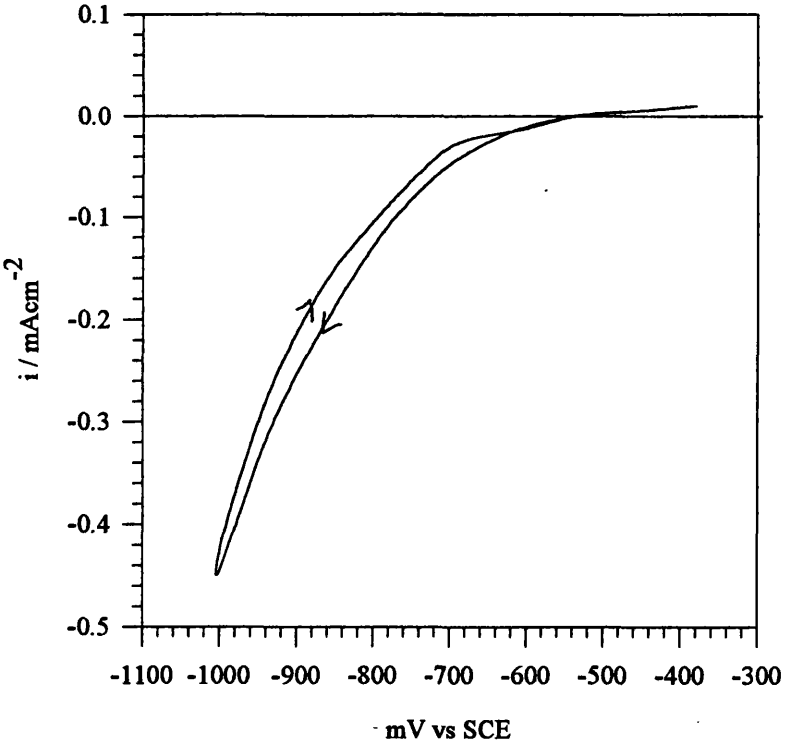

Figure 4.6. Cyclic voltammogram of $CdCl_2$ (0.08 mol dm^{-3}), $Na_2SeSO_3^{2-}$ (0.05 mol dm^{-3}) and NTA (0.1 mol dm^{-3}) at a SnO_2/glass electrode (pH 9), v=100 mVs^{-1})

The most striking feature of the voltammogram is the lack of any obvious features associated with the growth of CdSe, for example, reduction half waves or stripping peaks. Following analysis of the results obtained on glassy carbon, a layer was grown for fifteen minutes by pulsing the potential of the cathode from open circuit to -1000mV vs SCE. During this period an extremely rough and poorly adherent layer formed on the electrode surface. On rinsing in water this film was displaced to reveal a compact and homogeneous dark brown layer underneath. The procedure was repeated but for 30 minutes at -850 mV. On this occasion only the compact and more transparent layer had formed. The optical absorption spectrum recorded for this sample is plotted in figure 4.7.

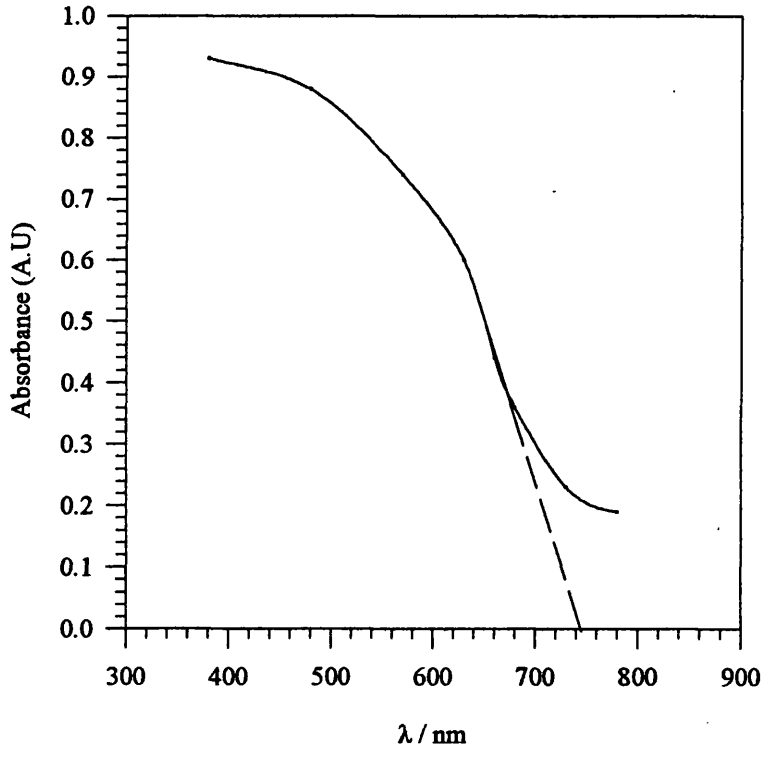

Figure 4.7. Optical absorption spectrum for as-deposited CdSe grown on SnO_2/glass at -850 mV vs SCE (pH 9, 80°C)

Extrapolation of the absorption edge gave a band-gap of 1.63 eV.

Growth of CdSe was initially investigated over the range -400 mV to -800 mV from which a potential window of -700 mV to -800 mV was identified where films could be grown that had a useful thickness and band gaps closer 1.74 eV. The potentials at which films were grown are listed in table 4.3. At each potential, CdSe was deposited onto four pieces of SnO_2/glass ≈1x2 cm in area which were subsequently characterised by photoelectrochemical and surface analytical techniques.

Sample Number	Deposition Potential (mV vs SCE)
1	-698
2	-713
3	-740
4	-759
5	-776
6	-788

Table 4.3. Potentials at which CdSe was deposited for the sample series 1 to 6

(vii) Mechanism for CdSe growth

The major obstacles in determining a mechanism for film growth are (i) the lack of well defined reduction waves for the formation of CdSe on either glassy carbon or SnO_2/glass substrates and (ii) films with the optimum composition and structure are grown at potentials considerably more positive than the reduction potentials of either $Cd(NTA)^-$ or $SeSO_3^{2-}$ species.

From the total charge passed during each deposition cycle, the film thickness was calculated for samples 1 to 6. In figure 4.8 these values have been compared with physical thickness measurements made using a Rank Taylor Hobson "Tallysurf" profilometer

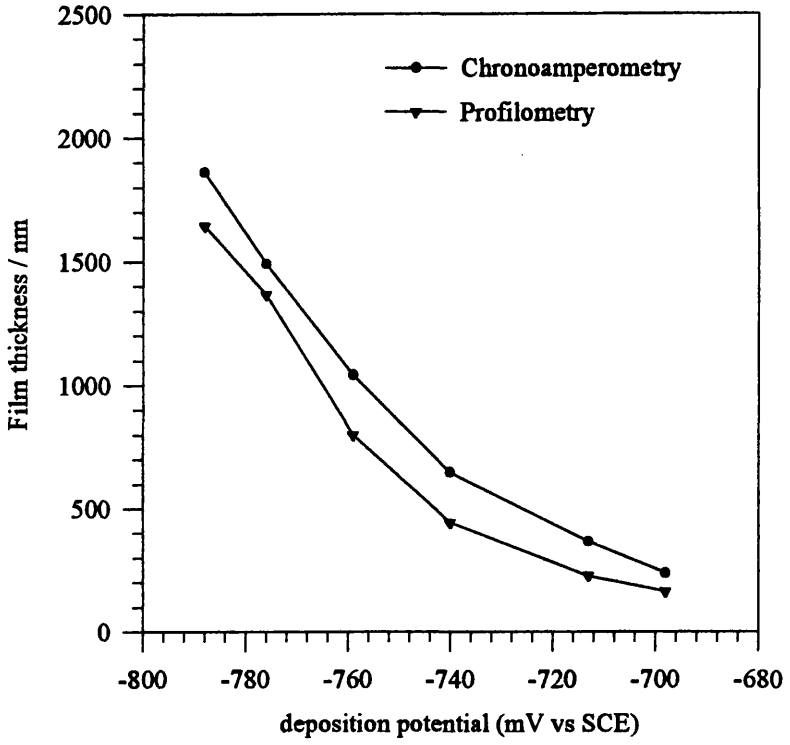

Figure 4.8. Variation in film thickness with deposition potential determined by chronoamperometry (filled circles) and profilometry (filled triangles) (Deposition time = 90 minutes)

Within the error of the profilometry measurement (±0.025 μm) and the assumptions made in equation 3.30, the similarity in film thickness determined by the two methods confirms CdSe formation proceeds by a $2e^-$ reduction with a current efficiency approaching ≈80%.

The cyclic voltammograms suggests that the following processes may be considered

Scheme A (4.12)

(i) Critical nucleus formation

$Se \rightarrow Se_{ads}$

$$[Cd(NTA)]^- \leftrightarrow NTA^{3-} + Cd^{2+}$$

$$Cd^{2+} + 2e^- \rightarrow Cd$$

$$Cd + Se_{ads} \rightarrow CdSe$$

(ii) At Se centre

$$[Cd(NTA)]^- \leftrightarrow NTA^{3-} + Cd^{2+}$$

$$Cd^{2+} + 2e^- + Se \rightarrow CdSe$$

(iii) At Cd centre

$$SeSO_3^{2-} + 2e^- \rightarrow Se^{2-} + SO_3^{2-}$$

$$Cd + Se^{2-} \rightarrow CdSe$$

Scheme B (4.13)

$$[Cd(NTA)]^- \leftrightarrow NTA^{3-} + Cd^{2+}$$

$$Cd^{2+} + SeSO_3^{2-} \leftrightarrow Cd(SeSO_3)^{2-}$$

$$Cd(SeSO_3)^{2-} + 2e^- \rightarrow CdSe + SO_3^{2-}$$

Scheme A is based on the direct electrodeposition of a stoichiometric layer of CdSe. Based on the reduction potentials recorded for $Cd(NTA)^-$ and $SeSO_3^{2-}$ species, deposition of CdSe would not be expected to occur over the potential range where samples 1 to 6 were grown (-698 to -788 mV vs SCE). This strongly suggests that an underpotential deposition process is operative. The underpotential deposition of Cd onto Se seems possible due to the strong interaction between Cd and Se. In scheme A is it proposed that grown is initiated by the adsorption of an atom of Se at the electrode surface, followed by the UPD deposition of Cd at the same Se site (reaction (i)). This leads to the formation of a critical nucleus of CdSe from which bulk growth can proceed To maintain stoichiometry in the growing deposit it is assumed that the two electron

reduction of Cd^{2+} ions takes place only at those lattice sites on the electrode surface where Se is exposed (reaction (ii)), whereas the reduction of $SeSO_3^{2-}$ takes place at those sites where Cd is exposed (reaction (iii)). This mechanism is compatible with the observation that over a potential range of ≈ 90 mV the deviations in film stoichiometry determined by wavelength dispersive x-ray analysis were very small.

Scheme B has been devised to illustrate the possibility of $SeSO_3^{2-}$ forming a complex with Cd^{2+} which subsequently undergoes reduction to yield CdSe. Although a survey of the literature revealed no kinetic or thermodynamic information on the formation of these complexes, Dean and Head [49] have identified Cd complexes involving coordination by Se in low temperature NMR studies.

The growth of CdSe can be summarised by the simple reaction

$$Cd^{2+} + SeSO_3^{2-} \rightarrow CdSe + SO_3^{2-} \qquad (4.14)$$

Cd-selenosulfite complexes may also be involved in the reduction, although no evidence has been reported for their presence in solution. The substantial shifts in the deposition potential for CdSe on SnO_2 suggests that the reaction mechanism is based on the UPD growth of Cd on Se. This is the process on which the ECALE method developed by Stickney *et al* [65] is based.

4.2.2. Capacitance Voltage Measurements

Plotted in figure 4.9 is a Mott-Schottky plot obtained for sample 3. The inset shows the Mott-Schottky plot obtained for single crystal CdSe where V_{fb}= -0.83 V and N_D= 9.5x10^{17} cm^{-3}. Both measurements were made in 0.1 mol dm^{-3} Na_2SO_3.

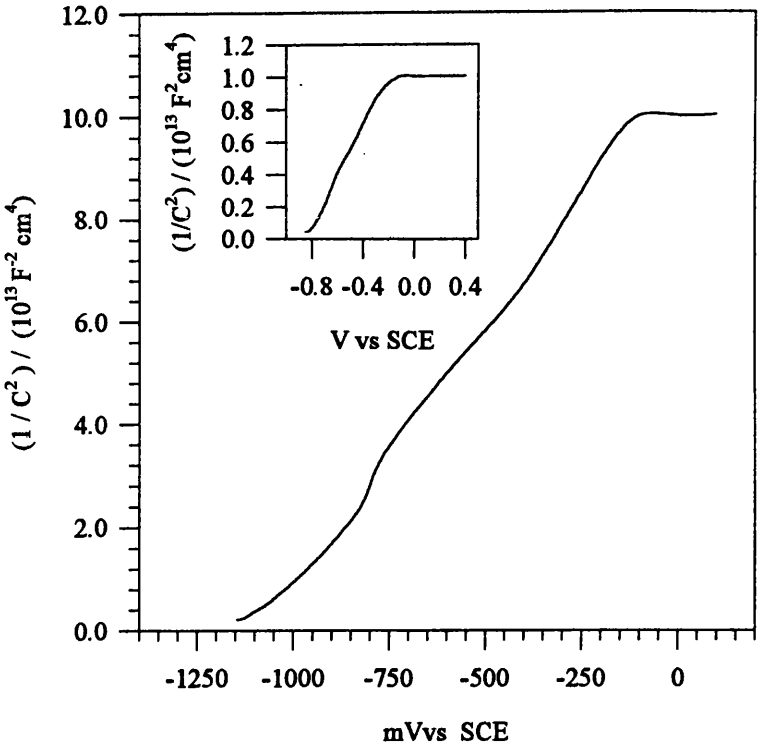

Figure 4.9. Mott-Schottky plot for electrodeposited CdSe (sample 3) in 0.1 mol dm^{-3} Na_2SO_3 (V_{ac}=10mV pk-pk, f=1.2kHz, v=5 mVs^{-1}). The inset shows the Mott-Schottky plot for single crystal CdSe.

Following annealing of the sample at 300°C for 30 minutes in air, Mott Schottky analysis for the heat-treated CdSe film gave V_{fb}= -0.82 V and N_D= 5.1x10^{17} cm^{-3}. The $1/C^2$ versus V plot for this sample is given in figure 4.10.

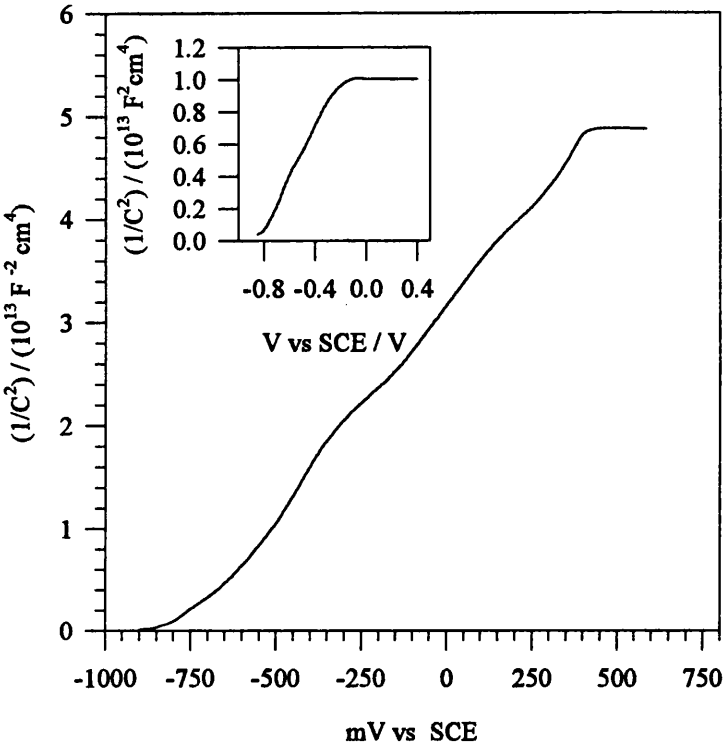

Figure 4.10. Mott-Schottky plot for CdSe annealed in air at 300°C for 30 minutes (sample 3) in 0.1 mol dm^{-3} Na_2SO_3 (V_{ac}=10 mV pk-pk, f=1.2 kHz, v=5 mVs^{-1}). The inset shows the same representation for single crystal CdSe.

Table 4.4 shows the flatband potentials (V_{fb}) and donor densities (N_D) determined from Mott-Schottky plots of $1/C^2$ versus V for samples 1 to 6.

Sample	V_{fb} / V	N_D x10^{17} / cm^3
1	-1.10	2.7
2	-1.11	0.6
3	-1.12	1.5
4	-1.06	0.2
5	-1.11	0.4
6	-1.07	0.2

Table 4.4. Values of V_{fb} and N_D determined from Mott-Schottky plots for samples 1 to 6 in 0.1 mol dm^{-3} Na_2SO_3 (V_{ac}=10 mV pk-pk, f=1.2 kHz, v=5 mVs^{-1})

Although much of the work reported in the literature on the cathodic electrodeposition of CdSe has been made on samples deposited from the acidic SeO_2 based bath, very few

assessments have been made of the donor densities or flatband potentials of these films by capacitance voltage measurements. For films electrodeposited from selenosulfite solution, there have been no reported capacitance-voltage studies, or for that matter, no extensive characterisation by electrochemical or photoelectrochemical techniques. Therefore, in this work the main comparisons that can be drawn are with single crystal CdSe.

Table 4.4 shows that the donor density decreases, as the deposition potential is made more negative. In figure 4.11 the variation in N_D with deposition potential is fitted by a first order linear regression routine. Of particular importance is that all the points lie in a similar range to the donor density obtained for single crystal CdSe, suggesting that both structure and composition of the thin films are similar to those of the single crystal form. To determine whether differences in N_D were due to experimental variability, donor densities were determined for four samples deposited during the same deposition cycle. The error in N_D was calculated to be $\pm 2.3 \times 10^{16}$ cm^{-3}. For samples deposited under identical conditions, but with a fresh deposition solution, the error is N_D was $\pm 3.6 \times 10^{16}$ cm^{-3}. This suggests that within these levels of accuracy, the changes in the donor density between samples grown at different potentials are small.

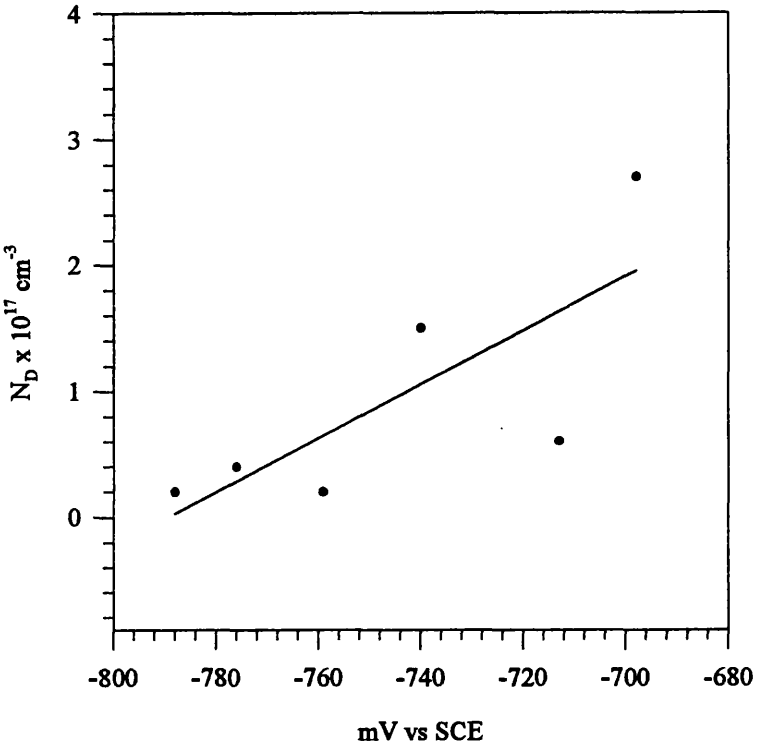

Figure 4.11. Variation of donor density with applied potential (points) fitted to a first order linear regression (line)

Mott Schottky plots for the as-deposited films were found to have a poorer linearity than those determined for single crystal CdSe, probably reflecting the less well defined structure and higher impurity levels in the films. In all the capacitance voltage plots, a slight "bump" characteristic of an inhomogeneously doped region within the film was observed at ≈ -800 mV. As this occurs close to flatband, the space charge region extends only a short distance away from the front of the film towards the bulk suggesting the bump is associated with a region close to the electrode surface. Following annealing in air the linearity of the plot was far closer to the response obtained for single crystal CdSe. Associated with this is a slight increase in the donor density compared to as-deposited samples. This suggests that the origin of the "bump" in the capacitance

voltage plots is a thin defective layer which extends into the bulk of the film. This is likely to be a residual layer remaining from the deposition process with the composition Se/SeO_2. Tenne *et al* [50] found that for SeO_2 derived films, the electrical properties of as-deposited samples were so poor that the donor densities were impossible to measure. Only after annealing or photoelectrochemical etching could reliable values of N_D be determined. The role of heat treatment in films grown from SeO_2 based baths is to vaporise excess Se from the film and recrystallisation to give a less defective structure.

Cocivera *et al* [51] found that annealing CdSe films in oxygen containing atmospheres substantially improved the photocurrent conversion efficiency of as-deposited films. Films annealed in an inert atmospheres, gave power conversion efficiencies of only 2.6%, whereas in the presence of as little as 2% O_2 during the heat treatment, efficiencies of 7% were obtained. The authors also monitored changes in the minority carrier diffusion length (L_p) and doping density (N_D) for different annealing conditions. In oxygen containing atmospheres, diffusion lengths were 35 times greater than similar films heat treated under vacuum. Several explanations were presented for the role oxygen may have in the thermally induced reduction of grain boundary recombination centres within the film. Comparison with as-deposited films revealed doping densities decreased to $4.6x10^{17}$ cm^{-3} after annealing in air at 500°C for 15 minutes. This compares well with the films annealed here where $N_D=5.1x10^{17}$ cm^{-3}. However, the authors found that heat treatment reduced the doping density. The increase in N_D observed in this work in consistent with thermal activation of Se vacancies or Cd interstitials which act as donor states in CdSe films. At higher temperatures, the formation of CdO at grain boundaries by the incorporation of oxygen may explain the reduction in N_D observed by Cocivera *et al* [51].

It is interesting to note that the Cd:Se ratios obtained by Cocivera *et al* [51] for as-deposited and annealed films were 1.12 and 1.04, respectively. In this work values close to 1:1 were obtained for *both* samples. Comparison of the method followed here and that used by Cocivera [70] revealed no obvious differences that would account for the discrepancies observed in the stoichiometries.

Excellent consistency was found for the values of V_{fb} which were all close to -1.1V. In the same electrolyte, the flatband potential for the heat treated sample was -0.81V. This compares well with values of V_{fb} for single crystal CdSe determined both in this work (-0.83V) and reported in the literature (-0.85V) [52]. In capacitance voltage measurements made by Meissner *et al* [53] on single crystal CdS, flat band potentials considerably more negative for the Cd-face (≈ -1.75V vs SCE) than the S-face (-0.9V vs SCE) were obtained. The authors found that contamination of the S-face by a thin layer of elemental sulfur remaining from the acidic etch treatment was responsible for the anodic shift. Similar behaviour has been observed by Gomes *et al* [54] for single crystal CdSe. Shifts in the flat band potential were attributed to a thin layer of Se at the electrode surface. Dielectric relaxation in this layer was also suggested as the origin of "Type A behaviour" in frequency dependent Mott-Schottky plots (see section 2.7). The surface etch treatments of single crystal CdSe produces a Se rich layer on the electrode surface which is removed by soaking the crystal face in saturated Na_2S or NaCN. In this work soaking CdSe thin films electrodes in Na_2S prior to characterisation was found to have no effect on the capacitance voltage behaviour. However, in the case of single crystal CdSe, capacitance voltage plots showed a distinct "bump" at ≈ -300 mV which was considerably suppressed after treatment with Na_2S. So far it has been suggested that prior to annealing, the surface of the electrode is covered in a layer of Se/SeO_2. As soaking in sulfide media has no effect on the capacitance voltage response, it is unlikely

this Se is a located at the electrode surface. The position of the "bump" in the capacitance voltage plots suggests that this defective region may be located in the bulk of the film, just below the film surface.

4.2.3 Photocurrent Spectroscopy

Figure 4.12 compares the photocurrent spectra for thin film and single crystal (inset) CdSe. For the latter a band gap of 1.73 eV was obtained which compares well with the literature value of 1.74 eV [52]. All measurements were made at 0 mV vs SCE in 0.1 mol dm^{-3} Na_2SO_3.

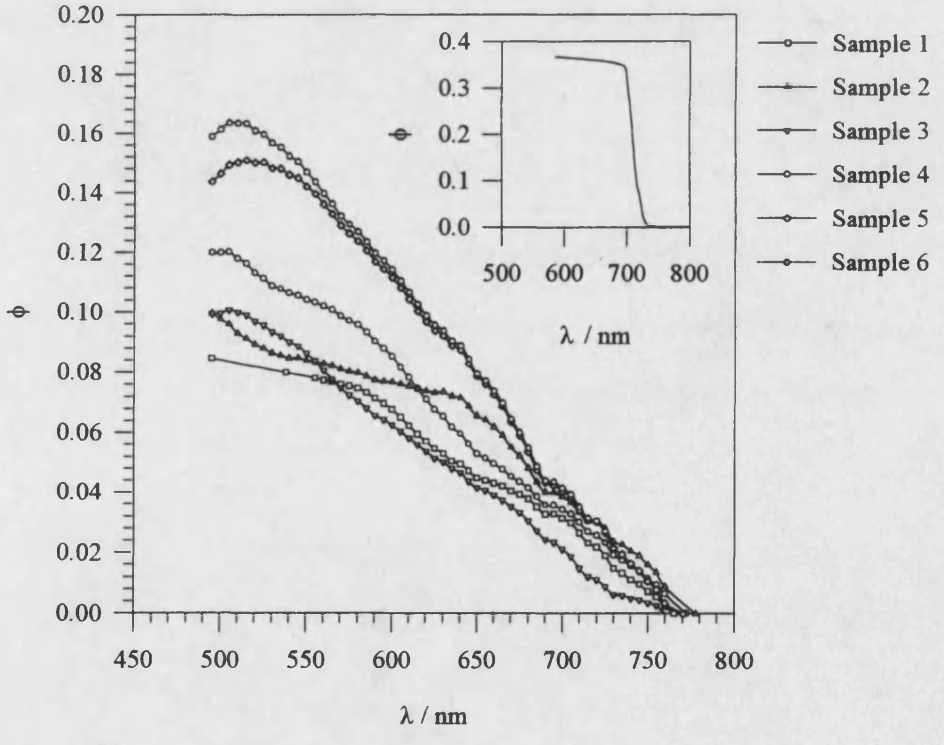

Figure 4.12. Photocurrent spectra recorded for samples 1 to 6. The inset shows the photocurrent response for single crystal CdSe. Both measurements were made at 0mV vs SCE in 0.1 mol dm^{-3} Na_2SO_3 (chopping frequency = 27 Hz)

Table 4.5 shows values of the band gap (E_g) determined from plots of the square of the photocurrent conversion efficiency (Φ) versus wavelength for samples 1 to 6.

Sample	E_g / eV
1	1.60
2	1.60
3	1.63
4	1.61
5	1.62
6	1.63

Table 4.5. Values of E_g determined from photocurrent spectra recorded for samples 1 to 6 in 0.1 mol dm^{-3} Na_2SO_3 (chopping frequency = 27 Hz)

The values of E_g obtained for the films are rather low compared to the single crystal reference, but are in a similar range to those obtained by other authors [51,43]. As values for the band gaps were quite close, an assessment was made of the variation in E_g for samples deposited (i) during the same deposition cycle and (ii) under identical conditions to (i), but from a fresh deposition solution. This gave the errors in $E_g = \pm 0.02$ and ± 0.03 eV, respectively, suggesting the band gaps of films deposited in the range -698 mV to -799 mV are quite similar.

For thicker samples deposited at more negative potentials, higher photocurrent conversion efficiencies were obtained, whereas for thinner films, efficiencies of only a few percent were observed. Low values of ϕ are often associated with incomplete absorption of light within a film. However, in certain cases if the film thickness is comparable to the penetration depth of the light ($1/\alpha$), some light is reflected at the film/substrate interface and can pass through the film for a second time, thus further increasing the photocurrent. Given the absorption coefficient of CdSe (6.4×10^6 m^{-1} at 644 nm)[51], incomplete absorption of light will occur in films with a thickness less than 0.39 μm, which includes samples 1 to 3. However, as the photocurrent conversion

efficiency increases further in samples 4 to 6, recombination effects are also likely to influence the measured photoresponse. Often associated with film growth is the incorporation of impurities from the electrolyte or substrate into the growing deposit. Also, for growth on foreign substrates, an initially defective layer is formed to accommodate the lattice mismatch between the substrate and growing film. Both of these phenomena will lower the photocurrent conversion efficiency by promoting recombination. This will be particularly predominant in the thinner electrodeposits. Under illumination, recombination within these regions will lead to deviations in the photocurrent response from the sharp onset observed for single crystal samples in plots of Φ vs. λ. If changes in the film structure or composition occur at distinct regions within the film, local variations in the photoelectrochemical properties of the deposit will also occur. The position and energy of these states may be estimated by varying the width of the space charge layer and the region of the film sampled by the incident light. The steps in the photocurrent response will occur in areas where for example, large deviations in the charge carrier recombination rate occur. The effect of recombination dominating the bulk response of the film is illustrated in samples 1 and 2. Saturation in the photocurrent occurs at ≈650 nm and ≈590 nm, respectively, even though CdSe continues to absorb in these regions and so should give a rising photocurrent. As the potential applied to the electrode is far away from flatband, it is unlikely that saturation is limited by the extent of the space charge region within the film. In which case the width of the space charge layer approaches the thickness of the film.

Non-linearity in the photocurrent response may be associated with an impure or defective form of CdSe. In a study by Szabo *et al* [51] on the photocurrent and absorption response of CdSe films electrodeposited from selenosulfite solutions, a series of plateaus or steps were obtained that were reproducible for films of various thickness. These were

observed at energies right across the band gap, but were far greater in magnitude and better defined than the features observed here. Parsons *et al* [55] have observed similar states in single CdSe but at energies corresponding to transitions from a subband of the valence band to the conduction band. In a study made by Gore *et al* [42] on the energy and density of trapping centres in CdSe deposited from SeO_2 based solutions, a high density of shallow traps was observed at 0.20 eV below the conduction band. This trap has also been observed in single crystal CdSe but with a far lower trap density. Interestingly, for films deposited from a bath with the addition of EDTA, the energy of the trap was decreased to 0.17 eV. From figure 4.12, the poorly defined steps in the photocurrent curves appear to occur between 2.3 eV and 1.6 eV which would include the energy of the traps identified by Parsons *et al* [55]. However, it is impossible to assess the effect of the 0.20 eV (≈867 nm) state as photocurrent spectra were only measured up to 775 nm. As this state has been found in both single crystal and thin film CdSe (from SeO_2 solution), it is also likely to be present in the films grown here. These observations strongly suggests that the presence of trapping centres is due to some inherent native defect or defect-impurity complex in CdSe.

Figure 4.13 illustrates the photocurrent spectrum for sample 3 after annealing in air at 300°C for 30 minutes.

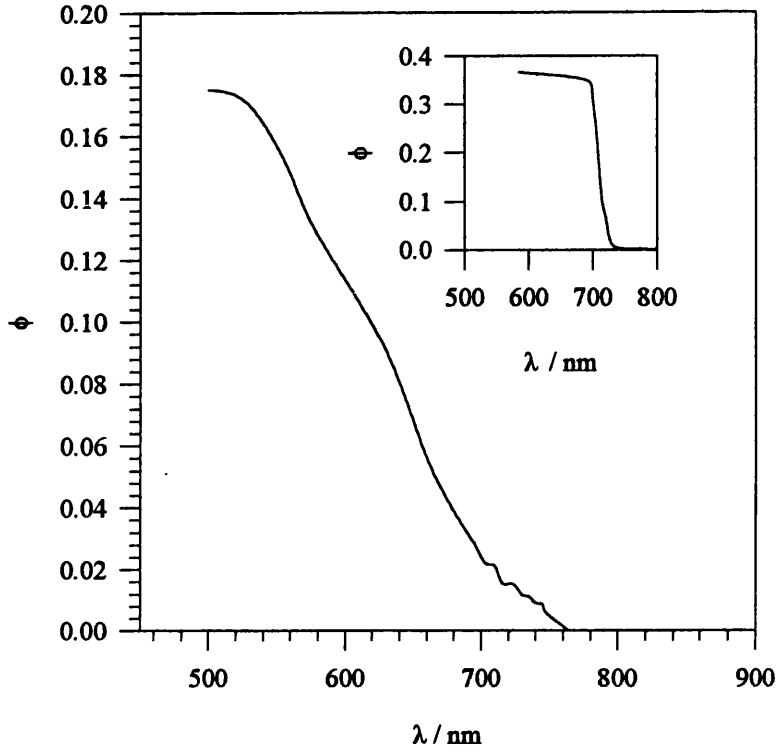

Figure 4.13. Photocurrent spectra recorded for sample 3 after annealing in air at 300°C for 30 minutes. The inset shows the photocurrent response for single crystal CdSe. Both measurements were made at 0mV vs SCE in 0.1 mol dm^{-3} Na_2SO_3 (chopping frequency = 27 Hz)

The inset shows the photocurrent response measured for single crystal CdSe (E_g=1.73 eV). Both spectra were obtained under conditions identical to those adopted in figure 4.10. Comparison with figure 4.12 reveals a higher maximum photoconversion efficiency and improved band gap of 1.71 eV. This compares well with the value of 1.74eV obtained by Cocivera *et al* [70]. However, the same authors obtained a far sharper threshold for absorption at the band edge. The slight stepping in the spectrum observed for as-deposited samples is also diminished, suggesting that if subband trap states are present, their density has been reduced by the heat treatment.

Figure 4.14 illustrates the variation in photocurrent conversion efficiency with voltage at 600 nm for samples 1 to 6.

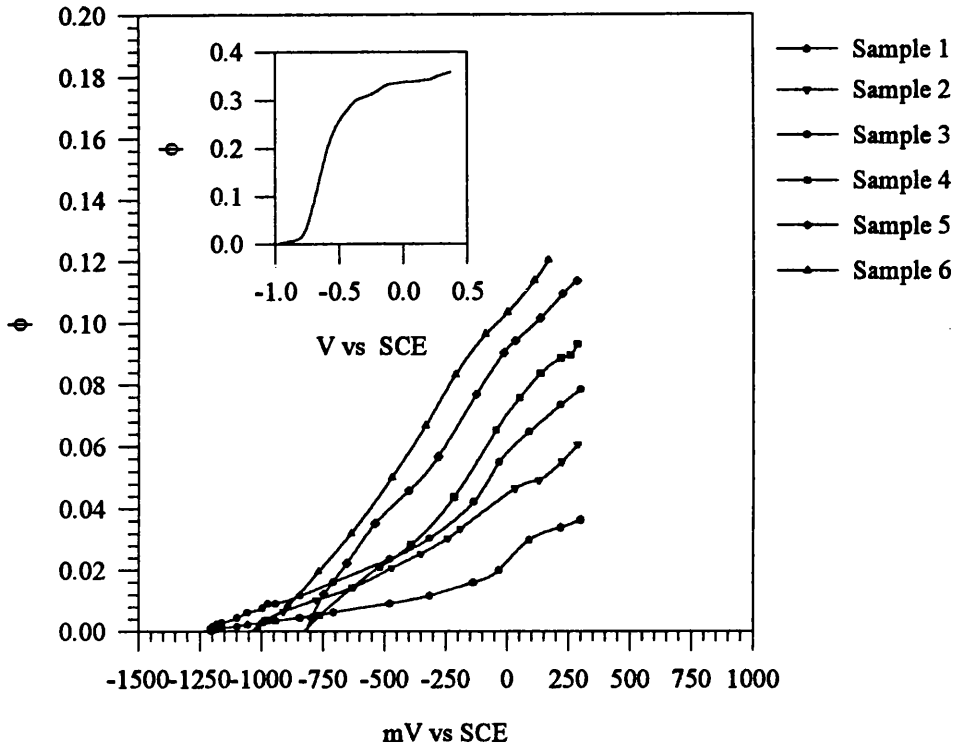

Figure 4.14. Photocurrent voltage plots recorded for samples 1 to 6. The inset shows the photocurrent voltage response for single crystal CdSe. Both measurements were made at 600 nm in 0.1 mol dm^{-3} Na_2SO_3 (chopping frequency = 27 Hz)

The inset shows the photocurrent voltage response obtained for single crystal CdSe (V_{fb} = -0.80 V vs SCE), showing the well developed anodic saturation limit expected for a single crystal sample. Both measurements were made in 0.1 mol dm^{-3} Na_2SO_3. In the previous discussion, the steps in the photocurrent spectra were attributed to the location of defective regions at a given energy within the film. This is complemented by photocurrent voltage measurements which provide not only values of the flatband potential but also a qualitative estimate of the location of defective regions within the film.

Table 4.6 lists values of the flatband potential determined by extrapolation of the photocurrent voltages curves plotted in figure 4.14.

Sample	V_{fb} vs SCE / mV
1	-0.95
2	-0.95
3	-0.88
4	-0.85
5	-0.93
6	-0.88

Table 4.6. Values of V_{fb} determined from photocurrent voltage spectra recorded for samples 1 to 6.

The non-linearity of the photocurrent voltage plots makes the estimation of a reliable value of V_{fb} uncertain. The flatband potential was determined by linear extrapolation of the rising linear portion of curves 1 to 6. The photocurrent voltage response was also assessed for each sample at 500, 700, and 800 nm. For each wavelength, the photocurrent voltage curves converged to the same point on the potential axis. The standard deviation in the V_{fb} for three sets of samples deposited (i) during the same deposition cycle and (ii) under identical conditions, but from a fresh solution were ±0.01 V and ±0.02 V, respectively.

Figure 4.14 shows that the increase in photocurrent conversion efficiency for samples deposited at more negative potentials follows the same trend as the photocurrent spectra recorded in figure 4.12. The photocurrent voltage curves for samples 1 to 3 are also characterised by a "bump" in the range 0 to +250mV vs SCE which gradually diminishes as the film thickens. If this is associated with a defective region within the film, it appears that its influence on the photoresponse becomes less important for the thicker samples. Estimation of the position this region corresponds to in the film is uncertain as saturation in the capacitance is not observed. However, as this feature

occurs over a potential range far from flatband, it is likely to be associated with a region located within the bulk of the film.

Unlike values of the flatband potential determined from capacitance voltage measurements, there is a lack of any trend observed in the values of V_{fb} determined from photocurrent voltage measurements. The differences suggest that photocorrosion at the electrode surface may be responsible for the observed shifts. The more positive values of V_{fb} obtained under illumination are likely to reflect absorption of Se produced by photocorrosion at the electrode surface. Depending upon the nature of the interaction between the adsorbed species and the electrode surface, either an anodic or cathodic shifts in the flatband potential can occur [53].

A second possibility is the presence of some contaminating layer on the electrode surface which is not removed after the initial cathodic going scan. It has been suggested that electrode behaviour can be improved by repetitively cycling between pre-set potential limits. Meissner *et al* [53] have reported that "clean" S free single crystal CdS surfaces (Cd 0001 face) are obtained by repetitively cycling the potential of the electrode in O_2-saturated K_2PO_4. However, the work of Meissner *et al* has been widely criticised as flat band potentials recorded for the Cd face were ≈ 1 V more negative than the accepted value of ≈ -0.8 V vs SCE [56]. The authors suggested that the cathodic shift was associated with the oxidation of surface S to SO_4^{2-} which dissolves in the electrolyte. It is more likely though that this shift is due to contamination of the electrode surface by cycling in the phosphate electrolyte. It has been pointed out by Salvador that the surface obtained by Meissner may well be free of a S layer, but the origin of the shift in flatband potential lies in the poor quality of the single crystal surface. If a similar study was to be made on electrodeposited CdSe thin films, it would be vital that during potential cycling the the surface composition and morphology were monitored at regular intervals.

Plotted in figure 4.15 the photocurrent voltage response at 600 nm for sample 3 annealed in air at 300°C for 30 minutes.

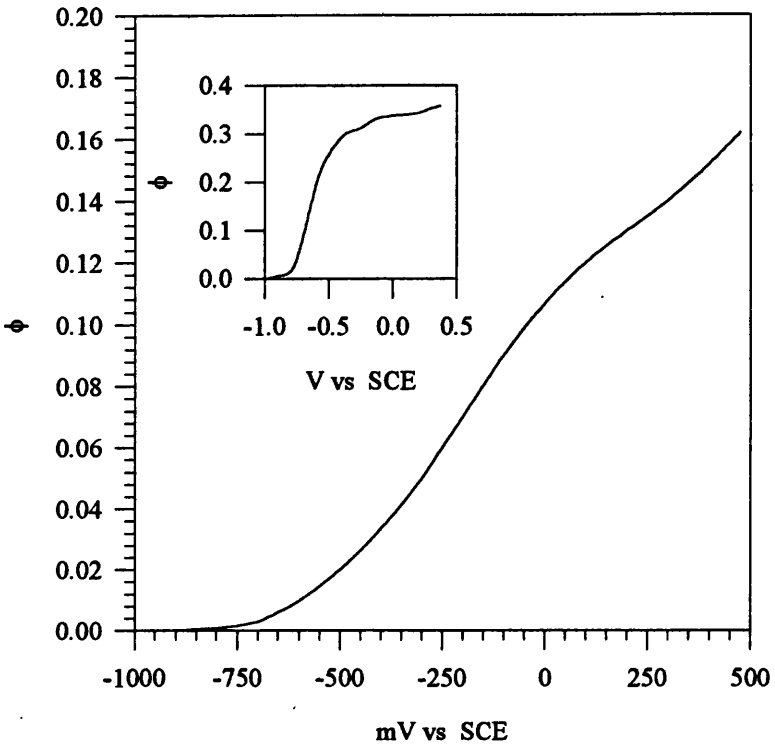

Figure 4.15. Photocurrent voltage plot recorded for sample 3 after annealing in air at 300°C for 30 minutes. The inset shows the photocurrent response for single crystal CdSe. Both measurements were made at 600 nm in 0.1 mol dm^{-3} Na_2SO_3 (chopping frequency = 27 Hz).

In comparison with the as-deposited sample, the photocurrent conversion efficiency has increased from ≈0.08 to ≈0.14 at +250 mV. However the flatband potential has shifted further positive to -650 mV vs SCE.

Salvador *et al* [56] have pointed out that the SO_3^{2-} ion used in many photoelectrochemical studies retards photocorrosion by acting as an efficient hole acceptor. When single crystal CdS is illuminated with high intensity radiation, photocorrosion results in the formation of a powdery sulfur layer on the electrode surface. Sulfite ions encourage dissolution of S^0 according to: $S(s) + SO_3^{2-} \rightarrow S_2O_3^{2-}$

(aq). In the same way $Se_2O_3^{2-}$ (aq) may be formed when CdSe is illuminated in the presence of sulfite containing electrolytes. In aqueous solution, Se species are well known to preferentially adsorb on electrode surfaces. The formation of such species may be one contributing factor to the positive shift in flatband potential observed under illumination. Szabo *et al* [51] have recorded photocurrent voltage curves for air annealed CdSe (500°C, 10 minutes) in contact with 1 mol dm^{-3} Na_2S + 1 mol dm^{-3} NaOH using a 1 mW HeNe laser. However, the combination of high light intensity and a sulfide containing electrolyte is likely to result in extensive formation of a CdS_xSe_{1-x} layer at the electrode surface [57]. This will have a strong influence on the flatband potential measured. However, as no comparisons were drawn with the same measurement made in an inert electrolyte, the effect of photocorrosion on the flatband potential can only be unclear. Unfortunately, Szabo *et al* [51] are the only authors who have reported a value for the flatband potential of CdSe electrodeposited from selenosulfite solution.

Photocurrent and photocurrent voltage measurements have revealed deviations in the photoresponse are associated with defective regions which occur at distinct energies and positions within the film. These features become attenuated for deposits that are thicker and those which are annealed. In studies made by other workers[55, 42, 51], evidence for similar states has been found.

Analysis of the flatband potentials measured reveals a some interesting trends:

(i) Values of V_{fb} determined by photocurrent voltage spectroscopy are systematically more positive than those obtained from capacitance voltage plots.

(ii) More positive values of V_{fb} are obtained for annealed films compared with those which are as-deposited.

In both cases shifts towards (or even beyond) the value of V_{fb} for single crystal CdSe are observed. This suggests that photocorrosion has the same beneficial effect on film properties as annealing by removing any contaminants on the electrode surface.

4.2.4. Electrolyte Electroabsorption Spectroscopy

(i) CdSe/SnO_2/Glass electrodes

Table 4.7 lists values of the band gap (E_g) and broadening parameter (Γ) derived by applying Aspnes [58] third derivative fitting function (TDFF) (n=5/2) to spectra recorded for samples 1 to 6. The validity of applying the low field fitting routine was confirmed by the low value calculated for the electrooptic function (24 meV).

Sample	E_g / eV	Γ / meV
1	1.73	175
2	1.72	170
3	1.77	179
4	1.76	201
5	1.78	174
6	1.70	170

Table 4.7. Values of the band gap and broadening parameter determined by Apnes [58] third derivative fitting routine (V_{dc} = 0 mV vs SCE, V_{ac} = 100 mV p-p, f = 270 Hz)

The standard deviation in E_g and Γ calculated according to the same described in section 4.2.3, gave values of E_g= ±0.03eV and Γ= ±10meV for cases (i) and (ii). From table 4.7 it could be argued that a slight increase in the band gap occurs for films grown at more negative deposition potentials. However, comparison of the largest difference between values of E_g (samples 2 and 5) and their standard deviation (±0.03 eV), suggests that over the potential window for deposition, values of E_g are very similar. A similar trend was observed between values of E_g determined by photocurrent spectroscopy. Figure 4.16 illustrates the EER response of single crystal CdSe in 0.1 mol

dm^{-3} Na_2SO_3 before and after etching in 5% Br_2/MeOH. Following the etch treatment the electrode was soaked in a saturated solution of Na_2S to dissolve the selenium layer remaining from the etch reaction. Prior to etching, values of E_g = 1.72 eV and Γ = 150 meV were obtained from analysis of the EER spectra. After etching, the band gap remained more or less unchanged at 1.71 eV, but the broadening parameter was substantially reduced to 50meV.

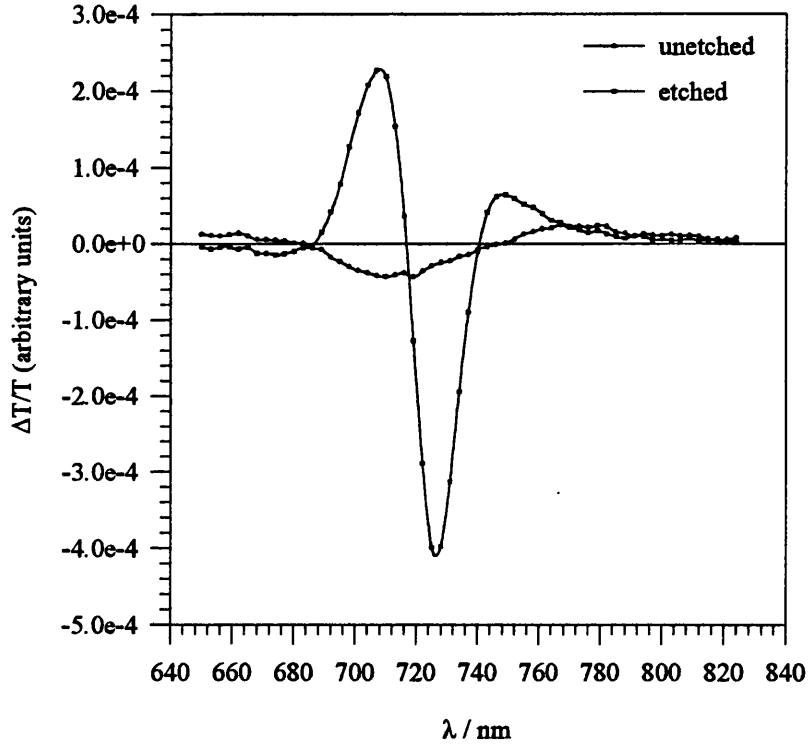

Figure 4.16. Electrolyte electroabsorption spectra for single crystal CdSe in 0.1mol dm^{-3} Na_2SO_3 before (filled circles) and after etching in 5% Br_2/MeOH (5s) (filled squares) (V_{dc} = 0 mV vs SCE, V_{ac} = 100 mV p-p, f = 270 Hz)

Values of the band gap determined for samples 1 to 6 compare well with data for the single crystal although, as expected, the considerably larger broadening parameter reflects the defective nature of as-deposited films. Similar trends have been observed between single crystal and polycrystalline CdS [59] and $HgCd_xTe_{1-x}$ [60]. Apart from sample

4, values for Γ are all within the range 170 - 180 meV. The slightly higher value of Γ obtained for sample 4 is likely to reflect the effect of a process such as photocorrosion resulting from prolonged illumination of the electrode surface.

Values of E_g determined by EEA appear to be ≈0.1 eV greater than those determined by photocurrent spectroscopy. Bhattarcharya *et al* [61] have determined the band gap of amorphous MoS_3 prepared under different conditions using both EER and transmission measurements and found that band gaps evaluated by the modulation technique were ≈0.1 eV higher than those determined from transmission data. Values of the band gap determined by transmission and reflection measurements at liquid He temperatures are often quoted as "exciton absorption energies", and for Group II-VI semiconductors these are usually ≈0.1 eV greater than band gaps derived from room temperature absorption measurements. This shift may reflect the influence of excitons on band to band excitations at the fundamental edge. Room temperature optical absorption spectra of semiconductors are relatively featureless though taking derivatives of the reflectance response reveals highly structured spectra. As excitons alter the spectral line shape from which values of E_g are determined, excitonic influences may be responsible for the observed shifts.

Salvador *et al* [62] have determined values of E_g=1.77 eV and Γ=57 meV from EEA spectra measured for O_2 annealed CdSe deposited from selenosulfite solution. In the present work a broadening parameter of 63 meV was obtained for a similarly heat treated film, suggesting annealing renders the electrodeposited layer relatively defect free. However the band gap is red shifted to 1.63 eV. Figure 4.17 compares the EEA spectrum for as-deposited and annealed CdSe (sample 3).

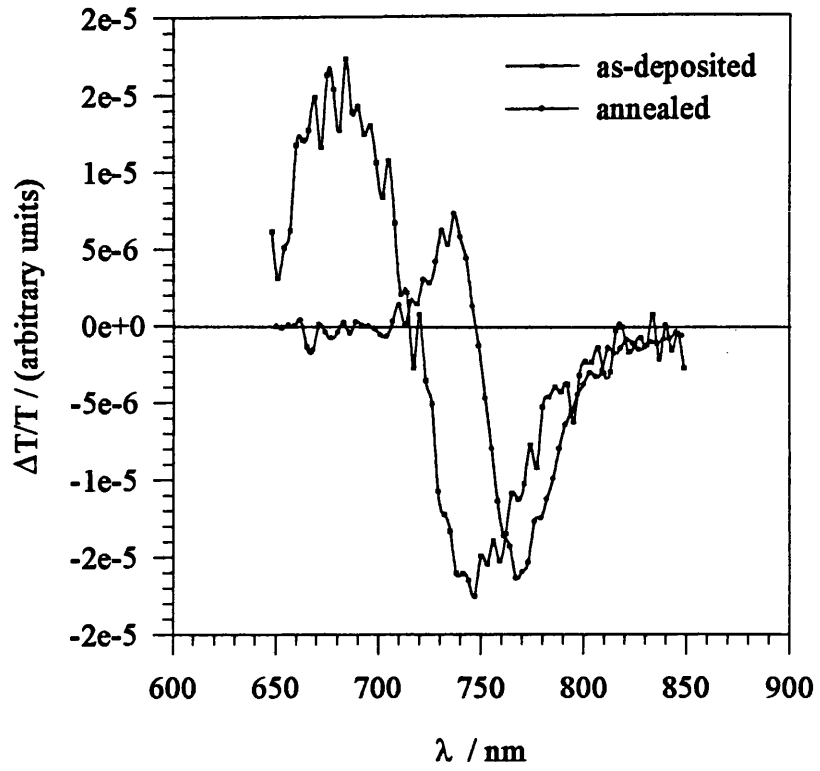

Figure 4.17. Electrolyte electroabsorption spectra for as-deposited (filled squares) and annealed (filled circles) CdSe thin films in 0.1mol dm^{-3} Na_2SO_3 (V_{dc} = 0 mV vs SCE, V_{ac} = 100mV p-p, f = 270 Hz)

A similar change has been observed in E_g by transmission, photocurrent and EEA measurements for air annealed CdS films grown by the chemical bath route[59]. These differences may reflect a change in composition and structure of the film during heat treatment. In section 4.2.2 annealing was found to increase the doping density of CdSe films through "activation" of Se centres. The concurrent change in film properties associated with this lead to alterations in the value of E_g. Silberstein *et al* [63] have measured the EER response of CdSe films electrodeposited onto Ti substrates from a SeO_2 based bath. Even though the samples were subjected to a series of anodisation and annealing procedures, poorly defined EER spectra showing no characteristic third derivative lineshape were presented. As a line shape fitting function could not be used to

determine a value of E_g, the authors estimated the band gap from the peak maxima (1.68 eV). A full width half maximum (FWHM) of ≈50 meV was quoted rather than the broadening parameter. The authors found that the annealing stage was necessary to seal off pin holes present within the films, suggesting the deposits were initially highly defective. In a second study by Silberstein *et al* [64] comparing the EER response of electrodeposited CdSe to the single crystal form. In the later, poorly defined EER spectra barely approaching a third derivative form prevented an accurate determination of E_g and Γ by Aspnes [58] TDFF. The gap was estimated from the peak maxima as 1.74 eV. Curiously, the FWHM was inferior (≈100 meV) to that obtained for electrodeposited CdSe. As no details were given for pre-treatment of the single crystal surface, the origin of the poor electroreflectance response is unknown.

(ii) Monitoring changes in CdSe and CdTe film structure from variations in the broadening parameter

The variation observed in the broadening parameter has been used to monitor the crystallinity of (a) CdSe electrodeposited onto CdS/SnO_2/Glass and (b) CdTe electrodeposited onto the $CdSe/CdS/SnO_2$/Glass configuration as grown in (a).

In the formation of a metal or semiconductor layer on a foreign substrate, the morphology of the underlying layer strongly determines the nature of the growing deposit. This is particularly important in the field of epitaxy where the aim is to grow high quality, defect free films. As a guide, the similarity in the lattice parameter (a_o) is used to determine whether an epitaxial relationship between two materials is possible. According to Stickney *et al* [65], to observe epitaxy, the mismatch in a_o should be less than 10%. The lattice match between CdS (hexagonal, a_o=4.13 Å) and CdSe

(hexagonal, a_o=0.429 Å) is only 3.7% whereas for CdTe (cubic, a_o=6.5 Å) the difference in a_o for CdS and CdSe is 36% and 34%, respectively.

(a) CdSe/CdS/SnO_2/Glass

The CdSe/CdS/SnO_2/Glass heterostructure was fabricated by electrodepositing a thin layer of CdSe (≈100 nm) at -750 mV vs SCE for 15 minutes (80°C) onto a sample of CdS/SnO_2/Glass supplied by BP Solar. From an EEA spectrum recorded of the sample, Aspnes [58] TDFF gave values of the bandgap similar to those recorded for CdSe electrodeposited onto SnO_2/Glass (table 4.7) but Γ decreased considerably to 115 meV.

(b) CdTe/CdSe/CdS/SnO_2/Glass

A 0.5 μm layer of CdTe was electrodeposited onto CdSe/CdS/SnO_2/Glass (see (a)) according to the method of Lincot *et al* [66] at +5 mV (vs Cd reference electrode) for 181 minutes (85°C). In figure 4.18 the EEA spectrum for the CdTe/CdSe/CdS/SnO_2/Glass structure is plotted. Using Aspnes[58] TDFF, values for the band gap and broadening parameter of 1.55eV and 92meV, respectively were obtained. The band gap agrees well with values determined by another worker for similar films grown on CdS and sensitized SnO_2 [67], although compared with the same samples, the broadening parameter has increased by 41meV.

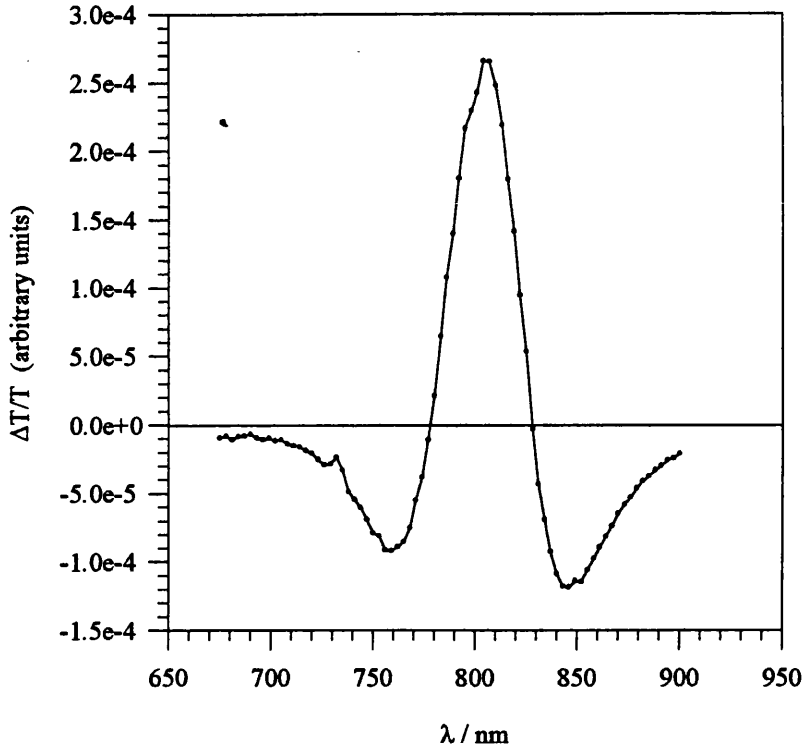

Figure 4.18. Electrolyte electroabsorption spectra for CdTe/CdSe/CdS/SnO_2/Glass in 0.1mol dm^{-3} Na_2SO_3 (V_{dc} = 0 mV vs SCE, V_{ac} = 100 mV p-p, f = 270 Hz)

Immediately it can be seen that in case (a) compared with films grown on SnO_2/Glass, the reduction in the broadening parameter suggests CdS promotes the growth of a less defective layer of CdSe. This correlates well with the close agreement between the lattice parameters for CdS and CdSe. In case (b), the substantial increase in the broadending parameter for CdTe compared with films grown on CdS and sensitised SnO_2 suggests the underlying CdSe layer promotes the growth of poorly crystalline form of CdTe. However, based on the similarity in lattice mismatch between CdTe with CdS and CdSe, similar values of Γ would be expected for CdTe/CdSe and CdTe/CdS heterostructures. In fact, in the latter case considerably lower values for the broadening parameter have been reported [67]. This casts doubt over using values of a_o to predict

epitaxial relationships suggesting factors other than the relationship between atomic spacings must influence the nature of a growing layer. The presence of surface oxides, defects and impurities may all be equally important as the lattice parameter in the formation of a deposit. Further analaysis by XRD could reveal the precise relationship between the orientation of the substrate and electrodeposited layer.

Froment *et al* [68] have suggested that the effects of a large lattice mismatch are diminished where there is chemical affinity between substrates and deposits which both contain Cd. However, this appears not to apply to CdTe/CdSe. Lincot *et al* [66] have investigated the approach of using an intermediate or buffer layer in the formation of epitaxial CdTe layers. In spite of the relatively small lattice match of ≈9.5% between CdTe and InP (111 polar face) (cubic, a_o=5.87Å), the authors found that epitaxial films of CdTe could not be deposited unless a CdS buffer layer was initially grown on the InP substrate. Similar attempts to grow epitaxial CdTe on InSb (cubic, a_o=6.47Å) have failed, even though the lattice parameters are near equal.

EEA is an important technique for characterising thin film and single crystal semiconductors. In addition to providing values of the band gap which can be compared with other determinations by photocurrent and absorption spectroscopies, it also enables changes in the crystallinity or defect structure to be followed by monitoring changes in the broadening parameter. In this study it is emphasised that the absolute values of E_g and Γ are not the most important quantities. More useful is the relative difference between values of E_g and Γ derived from EEA spectra for samples grown or treated in different ways.

4.2.5. Compositional Analysis

The ratio of Cd to Se in the films deposited have been assessed using the X-Ray analyser in wavelength-dispersive mode (WDX). However, to ensure the electron beam penetrated the entire sample, the energy dispersive mode of the instrument was used to monitor the point at which x-rays with energies characteristic of the SnO_2 substrate were emitted. For the thickest film the gun energy necessary to probe the entire film was ≈6keV. This ensured the composition quoted corresponded to the bulk value of Cd:Se within the film. All compositions have been determined using a freshly etched CdSe single crystal as a reference sample. In order to test the accuracy of the WDX technique, single crystal CdSe was analysed. This is gave a Cd:Se ratio to within 2% of the expected ratio of 1:1. For samples 1 to 6, the composition was determined at five different points across the electrode surface. The variation in Cd to Se was also assessed for samples grown under identical deposition conditions but from a second deposition solution. The resulting compositions of the films grown are listed in table 4.8. The terms x(Cd) and x(Se) refer to the average Cd and Se compositions, respectively. The standard deviation in the atomic percent of Cd and Se between (i) different points across the surface and (ii) different samples deposited at the same potential are given as σ_{Area} and σ_{Sample}, respectively. x(CdSe) gives the average ratio of Cd:Se.

Sample	x(Cd)	x(Se)	σ_{Area}	σ_{Sample}	x(CdSe)
1	50.33	49.67	0.90	0.95	1.01
2	49.76	50.24	0.93	0.88	0.99
3	50.36	49.64	1.01	0.89	1.01
4	50.32	49.68	0.91	0.97	1.01
5	50.39	50.33	0.96	0.97	1.00
6	50.60	49.60	0.90	0.98	1.02
Annealed	50.67	49.33	0.88	0.95	1.03

Table 4.8. Ratio of Cd:Se found in as-deposited and annealed CdSe films by wavelength dispersive x-ray analysis

Table 4.8 shows that films with excellent stoichiometries have been deposited from the selenosulfite based bath. The standard deviation in the Cd:Se ratios within the film is about the same as the standard deviation amongst deposits. This suggests that there is no significant difference in the Cd:Se ratios among these films, even though the conditions of growth differ. No reports of values for Cd:Se approaching the almost ideal values obtained here have been presented for films electrodeposited from acidic SeO_2 solutions. Films grown by this route typically contain Se in excess of 50%. In assessing the variation in composition of Cd and Se across the surface of films grown by the same route, Tomkiewicz *et al* [69] found that at different structural features, the Cd:Se ratios varied from 0.6 to 0.05.

The composition of sample 3 shows no significant change after annealing in air at 300°C for 30 minutes. The absence of any change in composition has also been observed for films annealed under vacuum. However, it could be that post deposition treatments such as annealing significantly increase the oxygen content in films and reduce the level of volatile species. These are important factors as they will influence the photoelectrochemical properties of thin films.

Cocivera *et al* [70] have used polarography and Rutherford backscattering (RBS) to assess the effect of varying deposition conditions on the stoichiometries of films electrodeposited from selenosulfite solution. RBS analysis yielded a Cd:Se ratio which agreed to within 4% of the polarographic ratio for each film. Films deposited over a potential window of -950 to -1200 mV vs SCE were found to have composition of ≈ 0.95 with a standard deviation of 0.05 which suggests deposits have a slight excess of Se. However at potentials more negative than -1150 mV, the authors found increasing levels of Se incorporation in the films until at -1300 mV a 50% excess of Se was detected.

Based upon the mechanism proposed in section 4.2.2, it is likely the presence of excess Se results from the reduction of selenosulfite ($E_c \approx -1.30$ V vs SCE) at the film surface. As discussed in section 4.2.2, although conditions identical to those described by Cocivera *et al* [70] have been followed for the electrodeposition of CdSe, the anodic shift in the deposition potential of ≈150 mV suggests the origin of this difference lies in substrate used. In this work films were grown on SnO_2 coated glass whereas the other authors used etched Ti [70,75]. The separation in deposition potential is likely to reflect the differing influence these two different substrates exert on the mechanism of film growth.

The influence of photoetching on the stoichiometry of single crystal CdSe has been investigated by Marcu *et al* [71]. A series of energy dispersive X-Ray measurements showed that the surface of the crystal is enriched with Se after photoetching (Cd:Se = 0.4:0.6). However, by varying the electron energy, the authors showed that only a thin layer of elemental Se covered the electrode surface. Values of 1:1 for Cd:Se were obtained after removal of the Se overlayer by rinsing the electrode surface in KCN. In the present work the same procedure was adopted, but using saturated Na_2S.

4.2.6. X-Ray Diffraction

Figure 4.19 presents the x-ray diffraction spectra for samples 1 to 6 (Cu K_α radiation, $\lambda = 1.54 \times 10^{-10}$ m) (for peak assignments see figure 4.20). Tables 4.9 and 4.10 list the major X-Ray diffraction lines found in a powdered polycrystalline sample of CdSe (wurtzite)[72] and a tetragonal (cassiterite) SnO_2 layer[73], respectively. In both cases the line intensities and *hkl* assignments are given.

d / Å	2θ / degrees	Intensity	*hkl*
3.72	23.90	100	100
3.51	25.35	70	002
3.29	27.03	75	101
2.55	35.11	35	110
2.15	41.97	85	103
1.98	45.79	70	200
1.86	48.84	12	112
1.83	49.67	50	201

Table 4.9. X-ray diffraction lines for a CdSe powder. 2θ values have been calculated for $\lambda = 1.54 \times 10^{-10}$ m.

d / Å	2θ / degrees	Intensity	*hkl*
3.35	26.63	100	110
2.64	33.93	75	101
2.37	37.98	21	200
1.76	51.83	57	211
1.68	54.81	14	220
1.49	61.93	11	310
1.44	64.78	12	112
1.42	66.00	14	301

Table 4.10. X-ray diffraction lines of a tetragonal (cassiterite) SnO_2 film on a glass support. 2θ values have been calculated for $\lambda = 1.54 \times 10^{-10}$ m.

The x-ray diffraction pattern of the as-deposited CdSe films exhibits peaks corresponding to the (002) and (103) reflections. The broad XRD peak centred at around 25 degrees may also include the (100) reflection from the film. In both cases, CdSe reflections are easily distinguishable from the far sharper peak arising from the SnO_2 substrate. The absence of any diffraction peaks associated with elemental Se (hexagonal, rhombohedral, and monoclinic) confirms the near 1:1 stoichiometries obtained by WDX for the same CdSe films.The effect of annealing on the diffraction pattern of as-deposited and annealed CdSe has been investigated in figure 4.20 (a) and (b), respectively. Comparing the (002) and (103) peaks in each case reveals heat treatment sharpens both

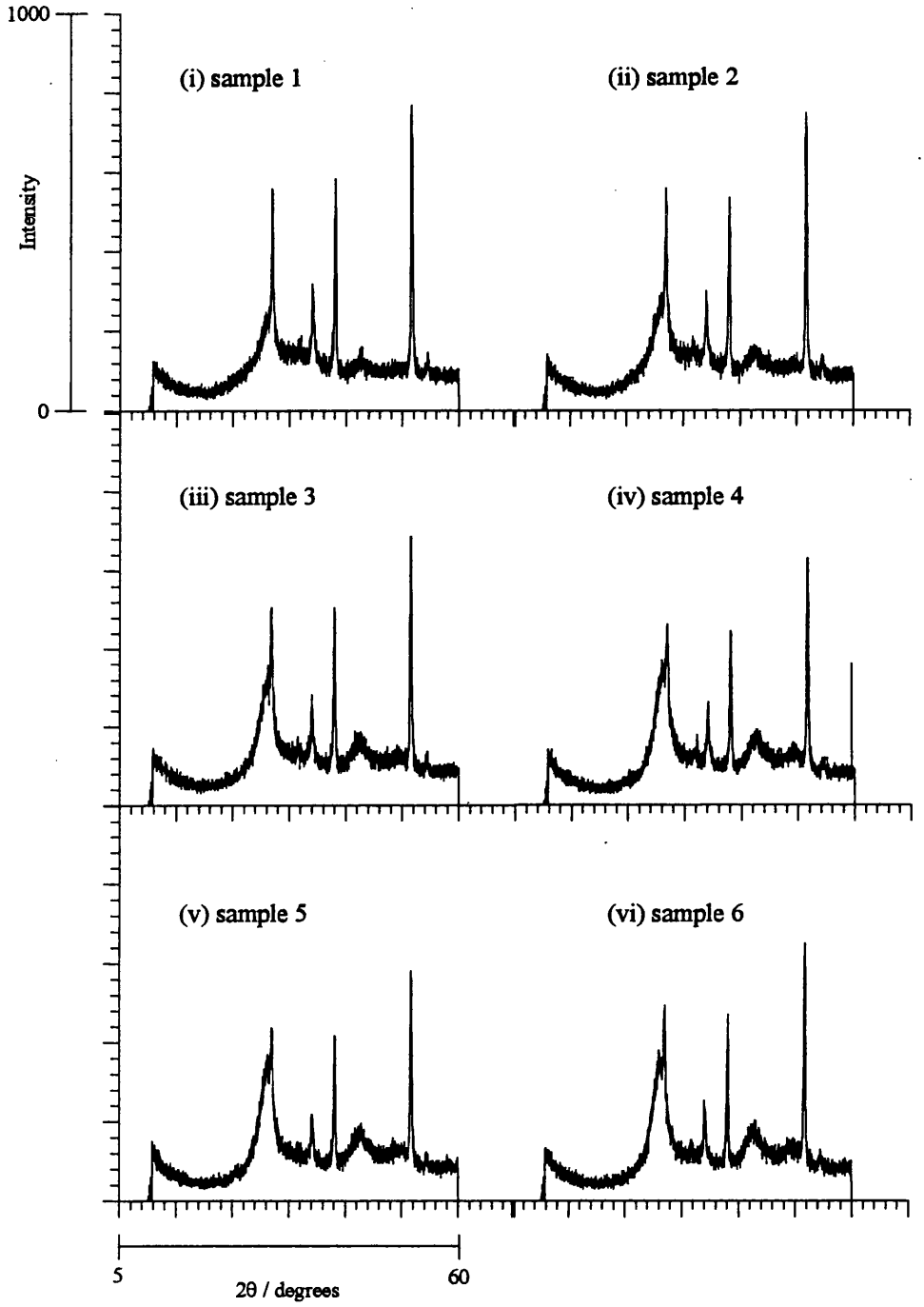

Figure 4.19. X-ray diffraction patterns measured for CdSe samples 1 to 6 using CuK radiation

peaks which is consistent with a thermally induced rearrangement of the semiconductor lattice. Like the as-deposited film, the heat treated layer is composed of polycrystalline CdSe of wurtzite structure and exhibits noticeable (002) preferential orientation.

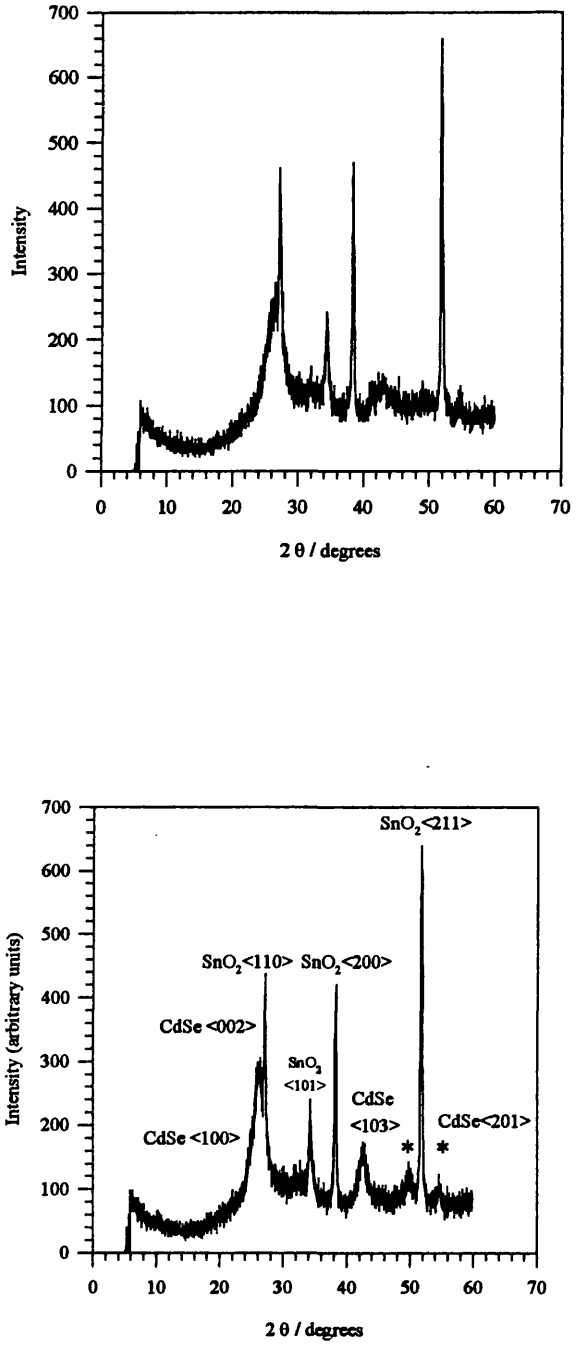

Figure 4.20. X-Ray diffraction patterns for (a) as-deposited (sample 3) and (b) annealed (sample 3) CdSe.

In tables 4.11 (i) and (ii) the change in the peak intensity and full width at half maximum (FWMH) for the (002) and (103) reflections are compared for as-deposited and annealed CdSe films.

(a) As-deposited

hkl	Intensity / A.U	FWHM / degrees
002	189	2.8
103	67	4.4

(b) Annealed

hkl	Intensity / A.U	FWHM / degrees
002	222	1.6
103	106	1.6

Table 4.11. Changes in the intensity and width at half maximum (FWHM) for (002) and (103) reflections in (a) as-deposited and (b) annealed CdSe

Annealing results in a significant reduction of the width of the XRD peaks, implying the film crystallinity has improved. However these are some way from the sharp reflections expected, suggesting that only partial re-crystallisation of the film has taken place. Heat treatment also reveals orientation in the deposit in the (201) direction. In similar films grown by Cocivera et al onto etched Ti foils [70], X-Ray data indicated that the films were amorphous when deposited. Even after annealing at 300°C, no evidence for any crystallinity was found. Only following annealing temperatures of 480°C did the films exhibit peaks characteristic of polycrystalline CdSe, the highest intensity peak corresponding to the (002) reflection. The same result has been reported by Pal *et al* [72] for films grown by physical vapour deposition onto glass substrates. The photoelectrochemical performance of the annealed films has been assessed in terms of their light to electrical power conversion efficiencies in a polysulfide electrolyte [70]. Prior to annealing, efficiencies of only 2.8% were obtained for films less than 0.5 μm in thickness. After heat treatment this was increased to 5% reflecting the improved

structure and lower recombination losses within the films. The same improvements in crystallinity have been found for CdSe films grown via the SeO_2 based route, where films are essentially amorphous upto annealing temperatures of 500°C. Loizos *et al* [43] have grown cubic CdSe films on SnO_2/glass substrates and found that the films exhibited a marked (111) preferred orientation after annealing. The crystalline quality and therefore the intensity of the main (111) diffraction peak was found to be very sensitive to the deposition potential. A difference in deposition potential of only 50 mV increased the intensity of the (111) peak from ≈200 to ≈2300. The intensity of the (230) and (311) peaks remained unchanged. In figure 4.19 the peak intensities also increase with a more negative deposition potential for the (002) and (103) reflections. Although this increase partly reflects an improvement in film crystallinity, the largest change in intensity is probably due to the variation of x-ray emission intensity with film thickness. For films grown at more positive potentials, the emission level will be low, whereas higher intensities will be obtained for the same peaks in thicker films.

The results given by Cocivera [70] it appears to suggest that films grown in this work should have been annealed at temperatures close to 500°C to gain large improvements in crystallinity. However a preliminary annealing study found that at these temperatures, films grown on SnO_2/Glass substrates were extensively cracked due to thermal stresses within the film. This made it impossible to measure the photorepsonse of the treated samples because of the significant leakage currents towards the SnO_2 substrate. The difference between the thermal expansion coefficient of the substrate and electrodeposited layer is responsible for cracking in films. However, for heat treated films grown on titanium the metal substrate is able to accommodate stresses and strains within the film preventing cracking. It is clear that CdSe films grown on SnO_2/Glass are far less resilient to heat treatment than those deposited on Ti.

Although annealing at 300°C may seem over-cautious, a noticeable improvement was obtained in the band gap and photocurrent conversion efficiency with heat treatment. Further investigations should aim to control and optimise the annealing treatment more carefully to suppress crack formation and improve the structural and photoelectrochemical characteristics of the films.

4.2.7. Film Morphology

The deposition of CdSe onto SnO_2/glass substrates produces highly reflecting and homogeneous films that adhere well to the underlying substrate.

(i) Scanning electron microscopy (SEM)

Figure 4.21 reveals the films are composed of CdSe aggregates of average size 0.18 ±0.05 μm.

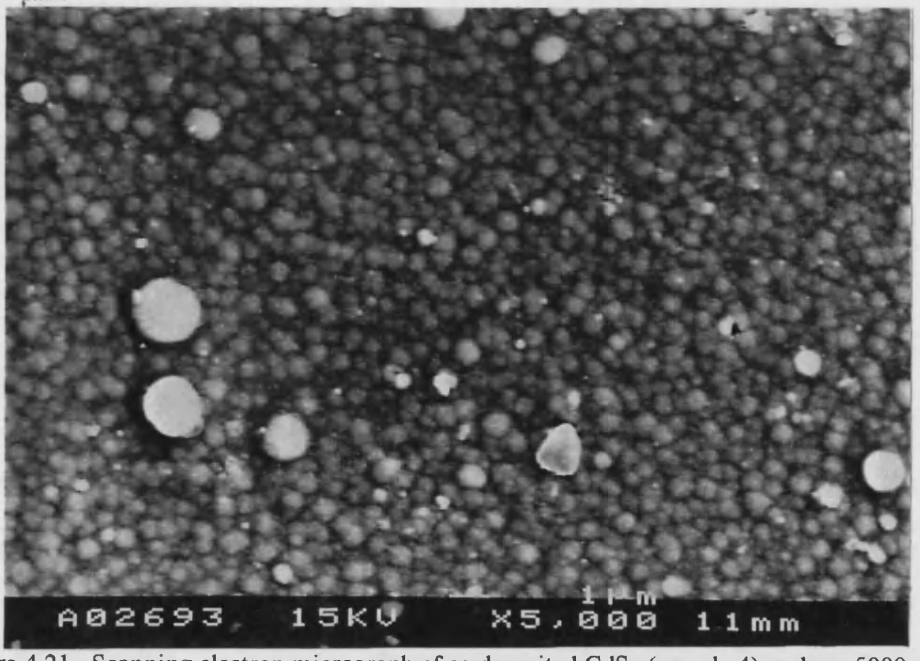

Figure 4.21. Scanning electron micrograph of as-deposited CdSe (sample 4) under x 5000 magnification

In all samples, small nodules (0.1 - 0.15 μm) of what appear to be CdSe structures protruding from the electrode surface were found to be sparsely distributed across the electrodeposit. WDX analysis revealed these had stoichiometries identical to that of the bulk film. These are shown as the bright centres in the SEM image in figure 4.22.

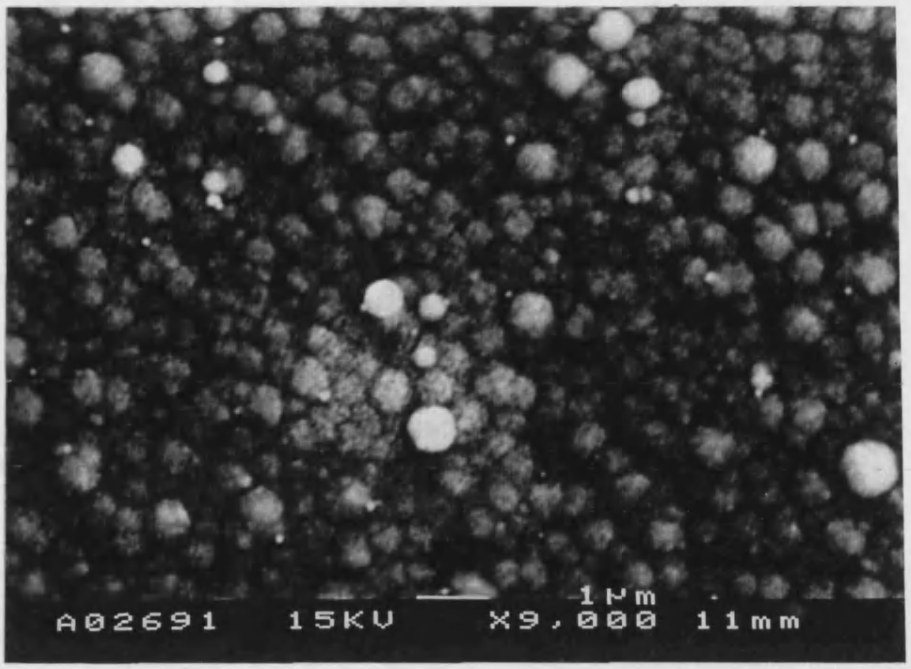

Figure 4.22. Scanning electron micrograph of as-deposited CdSe (sample 4) under x 9000 magnification

Comparison with similar films grown on Ti substrates reveals [70] deposits grown on metallic substrates are considerably rougher than those formed on SnO_2/glass. However after annealing, films deposited onto metals are very similar in appearance to the as-deposited films grown here, although the grain sizes appear to be lower for CdSe grown on SnO_2/glass compared to Ti or Ni substrates [64]. Murali *et al* [74] have reported grain sizes in excess of 1.5 μm for layers grown on stainless steel whereas this decreases to less than 0.8 μm for SnO_2./glass. Cocivera *et al* [70] have noted grain sizes ranging from 0.5-2 μm for as-deposited film grown on Ti. In this work, as the grain size of CdSe is similar to that of the SnO_2 substrate (0.16 ± 0.05 μm), the electrodeposited film appears to replicate the metal oxide microstructure.

The nodules visible in figure 4.22 have also been observed by other authors, especially for CdSe grown on metallic substrates. Kressin *et al* [41] found that the density of the centres was considerably less in films deposited on polished Ni substrates in comparison with Ti foils. Energy dispersive X-Ray analysis confirmed the presence of

Se and Cd in these growths but no stoichiometries were given. The high surface roughness of films grown by this route has been attributed to a high number density of nodular CdSe. These are responsible for the characteristic "cauliflower" morphology of the deposit. Decker *et al* [75] have compared the morphology of CdSe films grown on Si from SeO_2 and $SeSO_3^{2-}$ solutions. In the SeO_2 bath it was shown that the CdSe deposited after 25 s consists mainly of isolated nuclei with a hemispherical shape. After approximately 1 minute these centres coalesce to give larger irregular centres (≈5 μm) which were responsible for the rough deposits obtained. For films grown from selenosulfite solution small and large irregularly shaped nuclei were initially formed on the electrode surface. As the film thickened, the clusters increased in size (≈0.1-0.15 μm) and became rounder in shape. An interesting possibility is that the bright centres formed during the early stages of growth are Cd metal. According to the mechanism presented in section 4.2.2 these would be able to undergo chemical reaction with selenosulfite ions to give CdSe. The SEM image given by the authors is very similar to micrograph shown in figure 4.21, suggesting the mechanism of film growth and the resulting morphology of CdSe films grown on Si and SnO_2/glass are very similar.

Tomkiewicz *et al* [69] have used an Auger structure probe with a resolution of 3μm to determine the composition of different structural features on the surface of a CdSe layer grown on Ti from an SeO_2 solution. For as-deposited films the Cd:Se ratio varied from 0.67 for the smooth bulk deposit to 0.02 for dendritic structures growing away from the electrode surface. After heat treatment it was found that all structural features were composed of Cd:Se in a ratio between 1.2 and 1.3.

(ii) Atomic force microscopy (AFM)

AFM has been used in contact mode to study the morphology of electrodeposited CdSe films. In this configuration the tip is held at a constant force as it scans across the

substrate surface yielding information on the height and topography of the electrodeposited layer. A contact mode AFM image for as-deposited CdSe is shown in figure 4.23. The film surface contains a wide array of crystallite sizes and interfaces. However, the presence of what appear to be cauliflower like structures must not be confused with the growths which protrude from the surface of films deposited from SeO_2 solutions. The principal means of distinguishing these two forms of nodular growth is their elevation from the bulk film surface. Comparison with SEM images of SeO_2 derived films reveals heights for the individual cauliflowers of ≈ 5 μm [75] whereas figure 4.23 shows the "hillock" like structures have heights closer to ≈100 nm. Figure 4.24 illustrates an AFM image of the same surface showing grain sizes similar to those determined from figures 4.21 and 4.22. However, closer inspection reveals smaller grains can be found located on and between larger grains covering the electrode surface. The fact they are of a similar shape and morphology to the larger grains suggests they are associated with the later stages of grain growth. Alternatively they may correspond to the aggregation of much smaller crystallites. The image shown at much higher magnification in figure 4.25 clearly shows the presence of these smaller grains. If the suggestion that smaller grains form at longer deposition times is true, the microroughness of the surface should increase as the film thickens.

Figure 4.26 is the AFM image of sample 4 after annealing in air at 300° for 30 minutes. Across the entire film surface it was found that heat treatment totally suppressed the presence of smaller grains, revealing a smoother and more homogeneous electrode surface. No overall change in bulk grain structure was visible. The small change in film structure accompanying annealing confirms the suggestion made in section 4.2.6 (XRD analysis) that only partial recrystallisation of the electrodeposited layer has taken place. Rearrangement of the film surface by recrystallisation of the smaller grains

may represent the initial stages of reorganisation within the electrodeposited layer. At higher temperatures further coalescence between larger grains is expected, lowering the grain boundary density and improving the structure of the deposit.

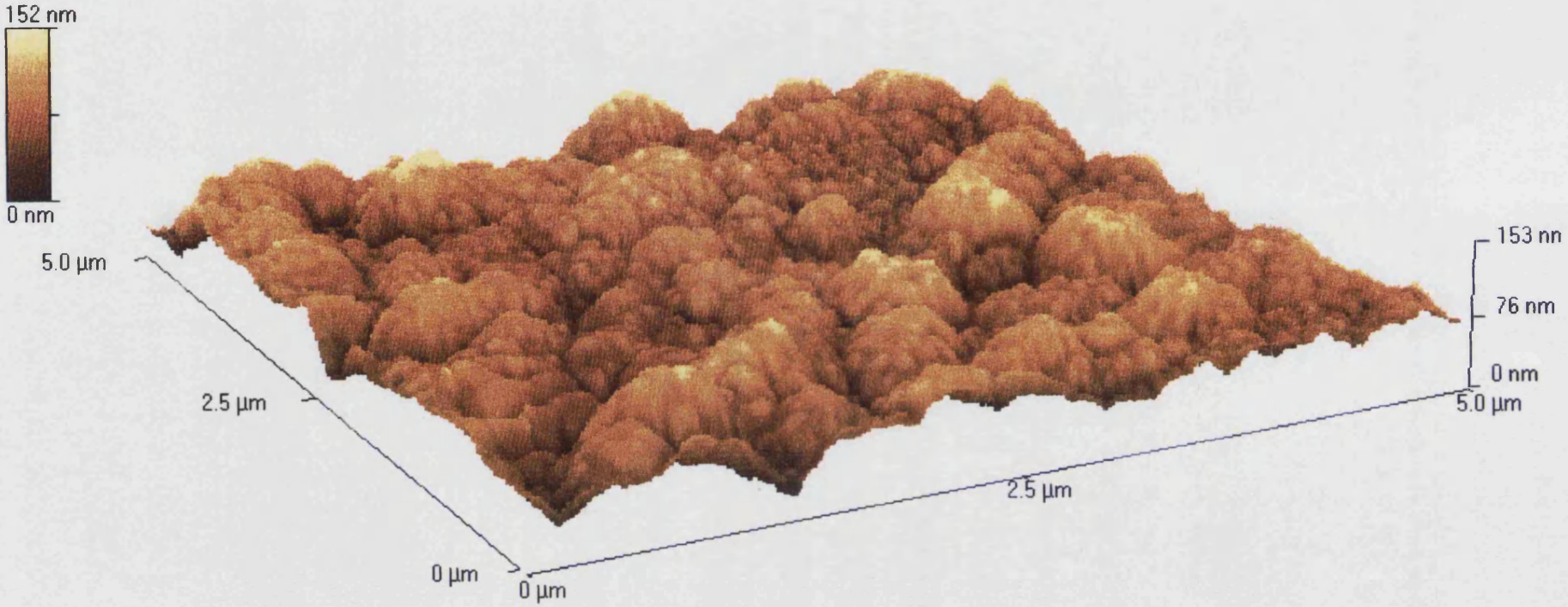

Figure 4.23. Atomic force microscopy image of electrodeposited CdSe on SnO_2 coated glass

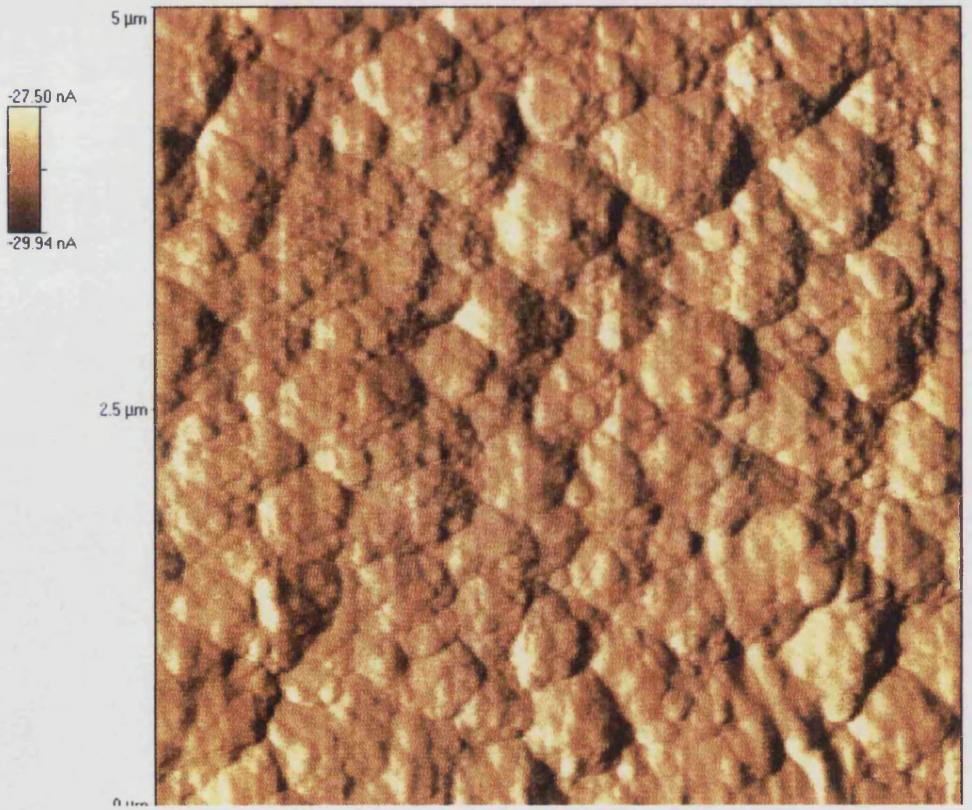

Figure 4.24. Atomic force microscopy image of electrodeposited CdSe on SnO_2 coated glass

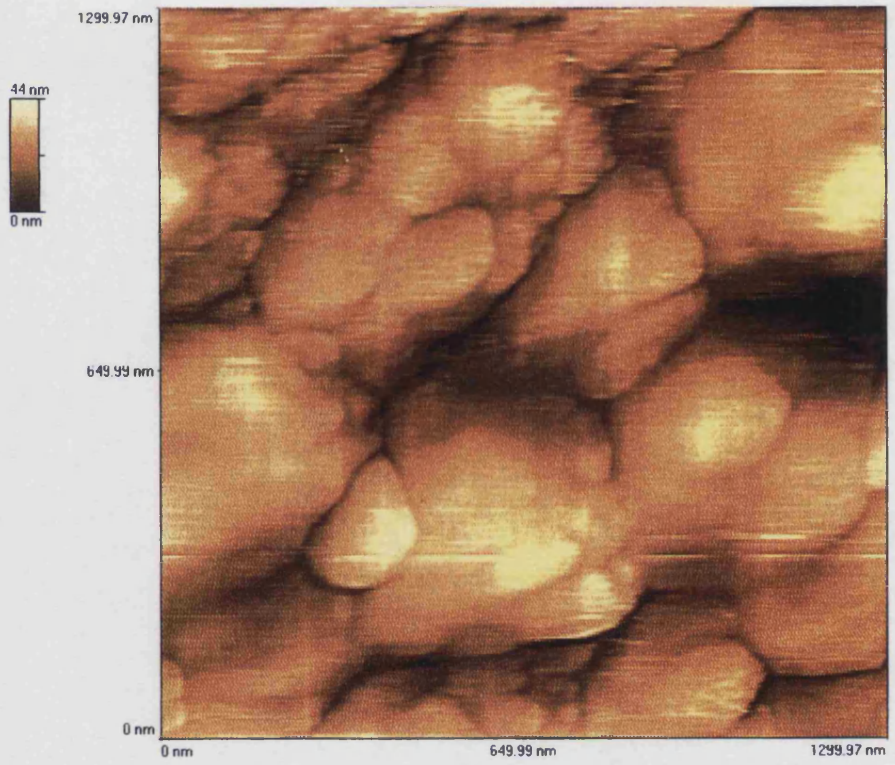

Figure 4.25. Atomic force microscopy image of electrodeposited CdSe on SnO_2 coated glass

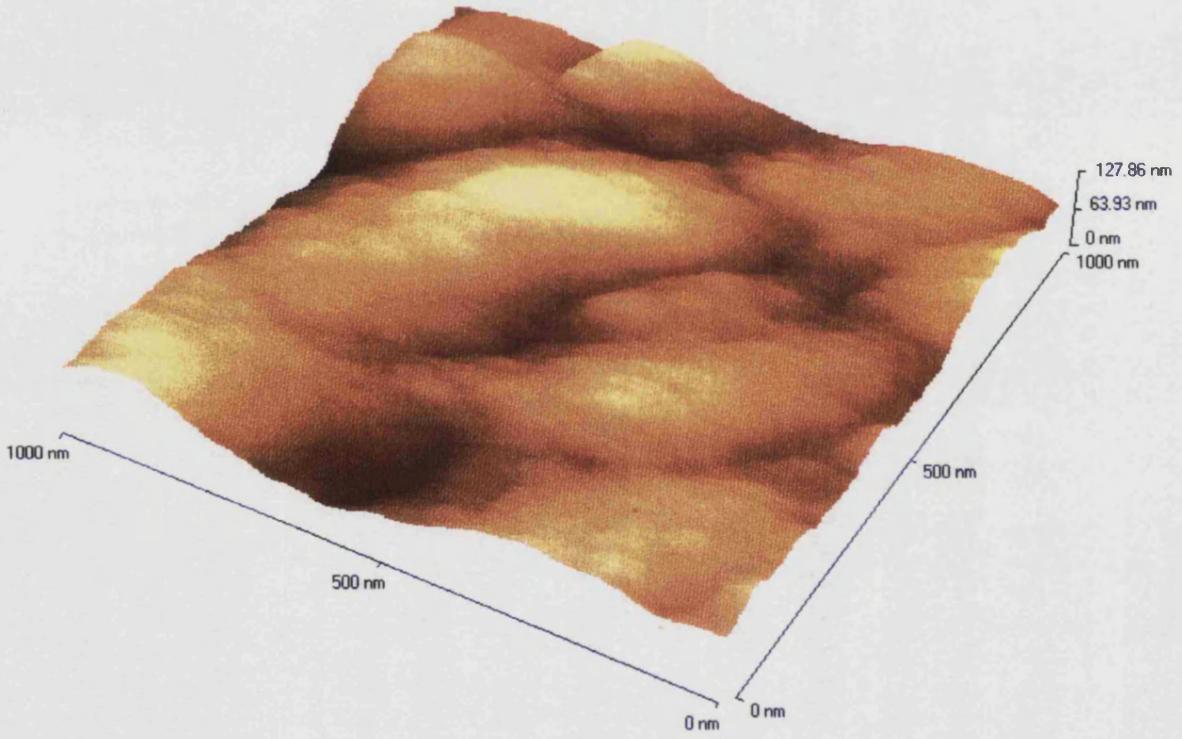

Figure 4.26. Atomic force microscopy image of electrodeposited CdSe on SnO_2 coated glass following annealing in air at 300 degrees C for 30 minutes

4.3. Conclusion

In this chapter it has been shown that the electrodeposition of CdSe from selenosulfite solution is a viable alternative to films grown by the more common seleneous acid route. Unlike the later, homogeneous polycrystalline films of CdSe were grown with ≈1:1 stoichiometries and good photoelectrochemical performance. Heat treatment was been found to improved the photocurrent conversion efficiency and crystallinity of the deposit, but to a lesser extent than annealed films grown from SeO_2 solutions. A low annealing temperature was identified as the reason for the small increase in photocurrent conversion efficiency due to partial recrystallisation of the electrodeposited layer. Further improvements are expected by careful choice of the annealing conditions. So far solar conversion efficiencies of ≈7% under AM 1.5 illumination have been obtained for annealed films electrodeposited from seleneous acid solutions. Based on the superior properties of the as-deposited CdSe grown here, this suggests that by annealing under optimised conditions deposits with improved solar energy conversion efficiencies could be realised.

Photocurrent, photocurrent voltage, and capacitance voltage measurements have revealed that inhomogeneous regions of dopant density or defect structure are present within as-deposited films. From the improvements observed in the capacitance voltage and photoresponse, annealing appears to have significantly reduced the density of these centres within the film. The improved crystallinity of heat treated CdSe was confirmed by the sharper (002) and (103) XRD peaks and AFM images which showed smaller grains had recrystallised into the bulk grain structure of the deposit

In section 4.2.3 it was suggested that the presence of trapping centres were likely to influence the observed photoelectrochemical response. Several authors have confirmed the presence of trapping centres in thin film and single crystal CdSe suggesting

they are associated with some form of inherent native defect within the semiconductor [43,52,56]. As traps are associated with impurities or defects, a considerable reduction in the density is expected after annealing.

Over the wide potential range where films were grown, the absence of any change in the stoichiometry of the deposits is consistent with reaction schemes A and B presented. The possibility of complex formation between Cd^{2+} and $SeSO_3^{2-}$ participating in the reduction has been proposed. To clarify the mechanism further, the early stages of film formation should be studied, particularly the likelihood of $SeSO_3^{2-}$ reduction at electrodeposited Cd centres on the electrode surface. Monitoring the early stages of CdSe growth would provide a challenging SPM study. Further investigations are also required to develop an understanding of how the substrate influences the reduction of Cd^{2+} and $SeSO_3^{2-}$, in particular whether electrode kinetics are modified by surface adsorbed agents. It has been proposed that NTA modifies the kinetics of nucleation and growth of CdSe via absorption at the electrode surface.

References

1 B. Ray, II-VI Compounds, Chapter 3, Pergamon, London, 1969

2 A. Najar and M. Shamsuddin, *J. Less Common Metals*, **158**, 131 (1990)

3 R. K. Swank, *Phys. Rev.*, **153**(3), 814 (1967)

4 J. P. Rai, *J. Mat. Sci. Lett.*, **12**, 1479 (1993)

5 K. Tsvetkova and K. Kochev, *Solar Energy Mat. and Solar Cells*, **31**, 423 (1993)

6 G. Hodes, L. M. Peter, I. D. J. Howell, *J. Electrochem. Soc.*, 139(11), 3136 (1992)

7 A. Heller, K. C. Chang, and B. Miller, *J. Electrochem. Soc.*, **124**, 697 (1977)

8 M. Russak, J. Reichmann, and J. DeCarlo, paper 488 presented at the Electrochemical Society Meeting, Denver, Colorado, Oct. 11-16, 1981

9 N. Holonyak *et al*, *Proc. I.E.E.E.*, **54**, 1068 (1966)

10 T. A. Midford, *J. Appl. Phys*, **35**, 3423 (1964)

11 F. H. Nicoll, Photoelectronic Materials and Devices, pp. 313-373, Van Nostrand Pubs., New Jersey, 1965

12 F. Cerdeiva, I. Torriani, P. Motisuke, V. Lemos, and F. Decker, *Appl. Phys. A.*, *46*, 107 (1988)

13 B. Miller and A. Heller, *Nature*, **262**, 680 (1976)

14 L. Ham, K. Mishra, and K> Rajeshwar. *J. Electrochem. Soc.*, **138**(1), 100 (1991)

15 B. Miller, A. H. Heller, M. Robbins, S. Menzes, K. C. Chang, and J. J. Thompson, *J. Electrochem. Soc.*, **124**, 1019 (1977)

16 K. Jackowska and H. Ti Tien, *J. Appl. Electrochem.*, **18**, 357 (1988)

17 G. Hodes, D. Cahen, J. Manassen, and M. David, *J. Electrochem. Soc.*, **127**, 2252 (1980)

18 M. A. Russak, J. Reichmann, H. Wittzke, S. K. Deb, and S. N. Chen, *J. Electrochem. Soc.*, **127**, 725 (1980)

19 M. A. Russak, J. Reichmann, *J. Electrochem. Soc.*, **129**, 542 (1982)

20 M. Tsuiki, H. Minoura, T. Nakamura, and Y. Ueno, *J. Appl. Electrochem.*, **8**, 523 (1978)

[21] C. J. Liu and J. H. Wang, *J. Electrochem. Soc.*, **129**, 719 (1982)

[22] Y. Ueno, H. Minoura, T. Nishikawa, and M. Tsuiki, *J. Electrochem. Soc.*, **130**, 43 (1983)

[23] R. A. Boudrea and D. R. Rauh, *J. Electrochem. Soc.*, **130**, 519 (1983)

[24] G. Hodes, A. Albu-Yaron, F. Decker, and P. Motisuke, *Phys. Rev. B*, **30**(8), 4215 (1987)

[25] J. S. Curran, N. Du, R. Phillipe, G. Stremsdoerfer, *Thin Solid Films*, **144**, 117 (1986)

[26] R. W. Pittman, *J. Chem. Soc.*, p. 855 (1953)

[27] S. I. Khobinov in, Encyclopedia of Electrochemistry of the Elements, Volume 4, ed. A. J. Bard, Marcell Decker Inc., New York, 1991

[28] Y. Golan, L. Margulis, G. Hodes, I. Rubinstein, J. L. Hutchinson, *Surf. Sci.*, 311, l633 (1964)

[29] V. L. Colvin, M. C. Schlamp, and A. P. Alivisatos, *Nature*, *370*, 354 (1994)

[30] B. O. Dabbousi, M. G. Bawendi, O. Onitsuka, and M. F. Rubner, *Appl. Phys. Lett.*, 66(11), 1316 (1995)

[31] A. J. Bard, R. Parsons, and J. Jordan, Standard Potentials in Aqueous Solution, Marcell Decker Inc., New York (1985)

[32] L. Schwarer and K. Suchy, Coll. *Czechoslov. Chem. Commun.*, **7**, 25 (1935)

[33] M. Skyllas Kazacos and B. Miller, *J. Electrochem. Soc.*, **127**, 869 (1980)

[34] C. Wei, C. S. C. Bose, and K. Rajeshwar, *J. Electroanal. Chem.*, **327**, 331 (1992)

[35] K. Rajeshwar, C. Wei, and N. Myung, *J. Electroanal. Chem.*, **375**, 109 (1994)

[36] R. W. Andrews and D. C. Johnson, *Anal. Chem.*, **47**(2), 294 (1994)

[37] E. I. Patsauskas, I. V. Yanitski, and A. I. Saudargaite, Proc. 10th Lithuanian Conf. on Electrochemistry, Vilnius, 143 (1968) (Eng. Trans., U.S. Dept. Commerce)

[38] H. Gobrecht, H. D. Leiss, and A. Tausend, *Ber. Bunsenges. Phys. Chem.*, **67**, 930 (1963)

[39] G. Hodes, J. Manassen, and D. Cahen, *Nature*, **261**, 403 (1976)

[40] K. K. Mishra and K. Rajeshwar, *J. Electroanal. Chem.*, **273**, 109 (1989)

[41] A. M. Kressin, V. V. Doan, J. D. Klien, and M. J. Sailor, *Chem. Mater.*, **3**, 1015 (1991)

[42] R. B. Gore, R. K. Pandey, and A. J. N. Rooz, *J. Phys. D: Appl. Phys.*, **20**, 1059 (1987)

[43] Z. Loizos, N. Spyrellis, and G. Maurin, *Thin Solid Films*, **204**, 139 (1991)

[44] G. Jarzabek and Z. Kublik, *J. Electroanal. Chem.*, **114**, 165 (1980)

[45] E. Müller and R. Navakowski, *Ber. Bunsenges. Phys. Chem.*, **11**, 931 (1985)

[46] V. F. Toropova, *Zh. Anal. Khim.*, **11**, 599 (1956)

[47] C. C. Lai and Y. Ku, *Chem. Eng. Jnl.*, **53**, 183 (1994)

[48] D. Pletcher, Inductrial Electrochemistry, Chapter 5, Electrocheical Consultancy, Romsey U.K., 1991

[49] P. A. Dean and M. K. Head, *Can. J. Chem.*, **58**, 180 (1980)

[50] R. Tenner, H. Flaisher, R. Jäger-Waldu, N. Stückeli, M. Braun, M. Lux Steiner, E. Bucher, W. Kelfin, R. Braun, and W. Koschel, *J. Appl. Phys.* **64**(5), 2601 (1988)

[51] M. Cocivera and J. P. Szabo, *J. Appl. Phys.*, **61**(10), 4820 (1987)

[52] D. Rauh in, Semiconductor Electrodes in Theoretical and Physical Chemistry, Chap. 7, Vol. 55, Elsevier, New York (1988)

[53] D. Meissner, R. Memming, and B. Kastenig, *J. Phys. Chem.*, **92**, 3476 (1988)

[54] W. P. Gomes, E. C. Dutoit, R. C. VanMeirhaege, and F. Cardon, *Ber. Bunsenges. Phys. Chem.*, **79**(12), 1206 (1975)

[55] R. B. Parsons, W. Wardzynski, and D. Yoffe, *Proc. Roy. Soc.*, **262**, 120 (1961)

[56] P. Salvador, I. J. Ferrer, J. G. Velasco, *J. Electroanal. Chem.*, **189**, 363 (1985)

[57] G. Hodes and B. Miller, *J. Electrochem. Soc.*, **133**(10), 2177 (1986)

[58] D. E. Apnes, *Surf. Sci.*, **37**, 418 (1973)

[59] M. E. Özsan, D. R. Johnson, M. Sadeghi, D. Sivapathasundaram, G. Goodlet, M. J. Furlong, L. M. Peter, and A. A. Shingleton, *J. Mat. Sci: Electronic. Mat.* (in press)

[60] P. M. Raccah, J. W. Garland, Z. Zhang, U. Lee, S. Ugur, S. Mioc, S. K. Ghandi, and I. Bhat, *J. Appl. Phys.*, **57**(6), 2014 (1985)

[61] R. Bhattacharya, C. Y. Lee, F. H. Pollak, and D. M. Schleich, *J. Non. Cryst. Solids.*, **91**, 235 (1987)

[62] P. Salvador, M. Pujadas, J. Gandi, and F. Decker, *J. Electroanal. Chem.*, **218**, 347 (1987)

[63] R. P. Silberstein, F. H. Pollak, J. K. Lyden, and M. Tomkiewicz, *Phys. Rev. B.*, **24**(12), 7397 (1981)

[64] R. P. Silberstein, J. K. Lyden, M. Tomkiewicz, and F. H. Pollak, *J. Vac. Sci. Technol.*, **19**(3), 466 (1981)

[65] J. L. Stickney and D. Wayne Suggs, *J. Phys. Chem.*, **95**, 10056 (1991)

[66] D. Lincot, A. Kampmann, P. Cowache, and J. Vedel, *J. Electroanal. Chem.*, **387**, 53 (1995)

[67] Communication with Dr. G. Goodlet, University of Bath

[68] M. Froment, D. Lincot, B. Mokili, M. Claude Bernard, and R. Cortes, *J. Electrochem., Soc., 142*(8), 2642 (1995)

[69] M. Tomkiewicz, I Ling, and W. S. Parsons, *J. Electrochem. Soc.*, **129**(9), 2016 (1982)

[70] M. Cocivera and J. P. Szabo, *J. Electrochem. Soc.*, **133**(6), 1247 (1986)

[71] V. Marcu, R. Tenne, and I. Rubenstein, *J. Electrochem. Soc.*, **133**(6), 1143 (1986)

[72] U. Pal, D. Samanta, S. Ghorai, B. K. Samantaray, and A. K. Chaudhuri, *J. Phys. D: Appl. Phys.*, **25**, 1488 (1992)

[73] Phillips x-ray diffraction file standard No.

[74] K. R. Murali, I. Radhakrishna, K. Nagaraja Rao, And V. K. Venkatesan, *J. Mat. Sci.*, **25**, 3512 (1990)

[75] F. Decker, J. R. Moro, J. L. S. Ferreira, and M. Vanzi, *Ber. Bunsenges. Phys. Chem.*, **91**, 408 (1987)

Chapter 5

Results

Optical and electrical characterisation of CdS thin films

5.1. Introduction

Cadmium sulfide (CdS) is a II-VI n-type semiconductor that can show either a wurtzite or zinc blende structure Table 5.1 lists some of its physical and chemical properties. CdS is important in a wide variety of electronic and optoelectronic applications ranging from solar cells to IR windows and more recently quantum dot structures [1,2]. It exists in a variety of forms (single crystal, polycrystalline, and colloidal). The most important technically are thin films which can be obtained by vacuum evaporation, sputtering, spray pyrolysis, and chemical deposition techniques [3,4].

Molar. Mass / g	Density / gcm^{-3}	Melting Point / °C	ΔH°_f / $kJmol^{-1}$	ΔG°_f / $kJmol^{-1}$	ε	E_g / eV	E_{VB} / eV	E_{CB} / eV
144.46	4.82	1475	167	-164.6	8.64 E∥c 8.28 E⊥c	2.42	7.26	4.87

Table 5.1. Physical and chemical properties of single crystal CdS.

One major use of polycrystalline CdS is in thin film photovoltaic devices. CdS is a suitable window material for the CdS/CdTe solar cell. Efficiencies of 15.8% under AM 1.5 illumination have been achieved with such cells [5].

The CBD process has been shown to be a low cost effective route to the production of uniform adherent films for large area (30 cm x 30 cm) electrodeposited solar cells, such as in BP Solar's commercial *Apollo*™ solar cell [6]. This heterojunction device is based upon the growth of CBD CdS (<1000 Å) on commercially available SnO_2/glass substrates followed by electrodeposition of the CdTe absorber layer (<2 μm) is deposited (see chapter 1)

Considerations of simplicity, economics, and energy requirements have dictated the deposition of thin films by the solution grown route to be an important area. The

technique was first developed for the growth of PbS thin films in pioneering work by Mokrushin [7], Lundin [8], and Kitaev [9]. Bode *et al* [10] subsequently optimised conditions to grow high quality PbS and PbSe films for infra-red detectors. The first report of the growth of CdS thin films by the chemical bath route was made by Kitaev *et al* [11], and the method has subsequently been pursued by many workers.

Although work on chemically deposited CdS films has been established for more than 3 decades, until recently, the technique was less widely used than vacuum deposition and spray pyrolysis as far as technological application were concerned. The reason for lies in the fact that the technique appeared to be recipe oriented and difficult to control. Subtle changes in deposition temperature, reagent concentration, and substrate type were found to alter the morphology and electrical properties of the deposit. These uncertainties led to more wide spread use of vacuum techniques to deposit films in a more consistent and reliable manner. However, a greater understanding of the mechanisms of film growth has now been achieved and films with a structure and photoelectrochemical performance equalling those deposited by more traditional routes can now be grown reproducibly. A related growth technique is spray pyrolysis (SP) which involves spraying a mixture similar to that used for the CBD of CdS on a heated substrate [41]. Spray droplets reaching the hot substrate surface undergo thermal decomposition to form a cluster of crystallites leading to film formation. Banerjee *et al* [12] have deposited CdS films by the SP route. However for films such as CdS, the special containment requirements for the toxic sprays used in SP suggests the future of solution growth films lies in the far simpler CBD route.

One particularly interesting area to emerge from the renewed interest in chemical bath deposition is the growth of epitaxial layers of CdS. Froment *et al* [13] have recently deposited epitaxial layers of CdS on single crystal InP (111, polar face). The

characteristics of the heterostructures grown in this way suggests the implementation of this technology in photovoltaic devices. Saito *et al* [14], for example have reported an efficiency of 17.8% for a InP/(CBD)CdS/In_2O_3 device. Epitaxial films of CdS have also been grown by a solution growth technique known as "successive ionic layer adsorption and reaction process" or Liquid Phase Atomic Layer Epitaxy (LPALE) [15]. This method is based on the successive adsorption of chalcogenide anions with metal cations in separated baths, and is the electroless analogue of the ECALE process developed by Stickney *et al* [16] to electrodeposit epitaxial CdTe.

A survey of the literature of the methods employed to characterise CBD CdS films shows that surface sensitive techniques seem predominant. In addition to more common means of analysis such as SEM, TEM, and XRD, the use of techniques such as PIXE [17] (proton induced X-Ray emission - qualitative analysis of composition ratio and impurities) and RBS [18] (Rutherford back scattering - composition and structural information) has also been reported. However less emphasis has been placed on the electrochemical and photoelectrochemical characterisation of these films. Techniques such as photocurrent spectroscopy are useful as they provide information on processes directly related to charge carrier generation in the films [19]. Of particular importance is the recombination of charge carriers at defective regions with the film structure. The photocurrent response allows simple identification of deposits with the optimum quantum efficiencies for implementation in CdS/CdTe solar cells. This chapter describes the application of capacitance voltage, and electrolyte electroabsorption spectroscopy for the characterisation of CBD CdS thin films grown in this work and supplied by BP Solar[20].

Capacitance voltage measurements made with electrolyte contacts have been used to evaluate the doping density of CBD CdS films. Deposits with high donor

densities are desirable as this increases the conductivity of the film, therefore improving the collection of charge carriers generated in the p-type (CdTe) absorber layer (see chapter 1). Earlier and unsuccessful attempts to increase the donor density of films by doping with group I metals have been superseded by carefully controlled heat treatments. Annealing of CBD films under a wide variety of atmospheres and conditions has been reported. These include H_2, N_2, vacuum, H_2/In, and H_2/Cd [21]. In all cases significant increases in the donor density over as-deposited films were obtained. Heat treatment also induces a number of changes in the film morphology and structure. Of particular importance is the reduction in defect density and improved crystallinity that accompany recrystallisation of the deposit. However excessive annealing temperatures can lead to deformation and cracking of the deposit due contraction or expansion at the substrate surface. These films are highly defective and unsuitable for photovoltaic applications. It is therefore important that changes in structure are also monitored so films with the optimum structure/conductivity balance are obtained. In this work an emphasis has been placed on relating changes in CdS properties to differences in film morphologies following heat treatment in different atmospheres.

Relatively few studies have been made on the characterisation of CdS films by capacitance voltage analysis and most that have been reported have been based on the solid state or Schottky configuration using a metallic top contact layer [22]. The use of an electrolyte offers a number of advantages over the metallic contacts for the non-destructive characterisation of semiconductor materials. Firstly, transparent blocking contacts are easily formed and secondly the absence of any lattice mismatch leads in many cases to ideal junction behaviour. In the second case the use of wet contacts also avoids the risk of modifying the properties of the sample surface during the formation of contact layer. In section 5.2.2 capacitance voltage data have been treated by a modified

form of the Mott-Schottky plot to determine the surface roughness ($\Re$) of CdS films before and after heat treatment. The transition (V_{TR}) from Mott-Schottky behaviour to geometric capacitance has been compared to calculated values of V_{TR} to demonstrates the internal consistency of the approach taken to deal with the problem of surface roughness. It has also been used to identify poorly compact deposits where electrolyte penetration between the uppermost grains in the film influences the calculated value of $\Re$.

Electrolyte electroabsorption (EEA) and reflectance (EER) spectroscopy have been used extensively to characterise single crystal and thin film semiconductors. The first studies on the EEA/EER effect in CdS were published over 30 years ago by Snavely [38] for vacuum deposited films. Since then few publications have appeared on the modulation spectroscopy of CdS. Experimental and theoretical studies of EEA and EER appear to be confined primarily to elemental and group III-V semiconductors. Materials such as Si , GaAs, and $HgCd_xTe_{1-x}$ seem to dominate reviews on the subject [23,24,25]. The reason for this lies in the complex modifications which must be made to existing EEA theories to account for the presence of excitons in CdS. However, in the absence of a reliable theoretical model to deconvolute the excitonic effects, the simple lineshape function of Aspnes [52] used to determine values of the band gap (E_g) and broadening parameter (Γ) has been found to give satisfactory fits.

The use of EEA for characterisation of as-deposited and air annealed films forms part of an emerging trend to use modulation spectroscopy to follow the effects of process or growth induced effects or annealing in semiconductors. Of particular importance is the broadening parameter which provides information on film heterogeneity and defect structure. Some examples of where changes in Γ have been monitored during surface treatment of semiconductors are (i) H_2 annealing of GaAs

<100> wafers [26] and (ii) chemical etching (Br_2/MeOH) of $HgCd_xTe_{1-x}$ wafers [46]. In both cases the reduction in the broadening parameter correlated with the improved crystallinity of the samples. Monitoring of film properties by changes in EEA/EER spectra has recently been extended to the *in-situ* control of semiconductor fabrication conditions, although at present this has only been applied to the growth of semiconductors such as GaAlAs by vacuum deposition routes [27].

In this chapter differences in the broadening parameter have been related to changes in the film morphology following annealing under different atmospheres. Values of the band gap derived from EEA spectra have enabled changes in the transmission of the CdS films to be assessed. The CdS window layer in currently fabricated CdTe based photovoltaic cells absorbs 10-15% of the incident radiation. The aim has therefore been to increase the band gap of the CdS layer so that a greater proportion of light reaches the p-type absorbed layer. Alternative approaches have used different semiconducting materials with higher band gaps such as ZnS [28] (3.6eV) and $CdZn_xS_{1-x}$ [29]. However these have been shown to form a poor heterojunction with CdTe where the gains in transmission are offset by charge carrier recombination within interfacial layer. Attention has therefore focused on improving the transmission of the existing CdS window layer though various post deposition annealing treatments.

5.2. Results and Discussion

5.2.1. Structure of CdS thin films

The macrostructure of the CBD CdS films has been studies by SEM, FSEM, and HRTEM/TEM. Figures given for the previous three techniques were supplied by BP Solar. As-deposited CdS films grown in this work and supplied by BP Solar were referred to as samples 1 and 2, respectively. The air annealed deposits were dark orange in colour whereas as-deposited and $CdCl_2$ flux annealed films were light yellow.

The SEM image of an as-deposited CdS film in figure 5.1(a) shows the aggregate structure typical of films grown from the solution phase with an average grain size of $0.19 \pm 0.06\mu m$ (sample 1a, deposition time = 15 minutes). In figure 5.1 (b) the SEM image shows the film surface after a deposition time of 1 minute. This shows that during the early stages of film formation, the layer is not continuous and uncovered areas of the substrate remain.

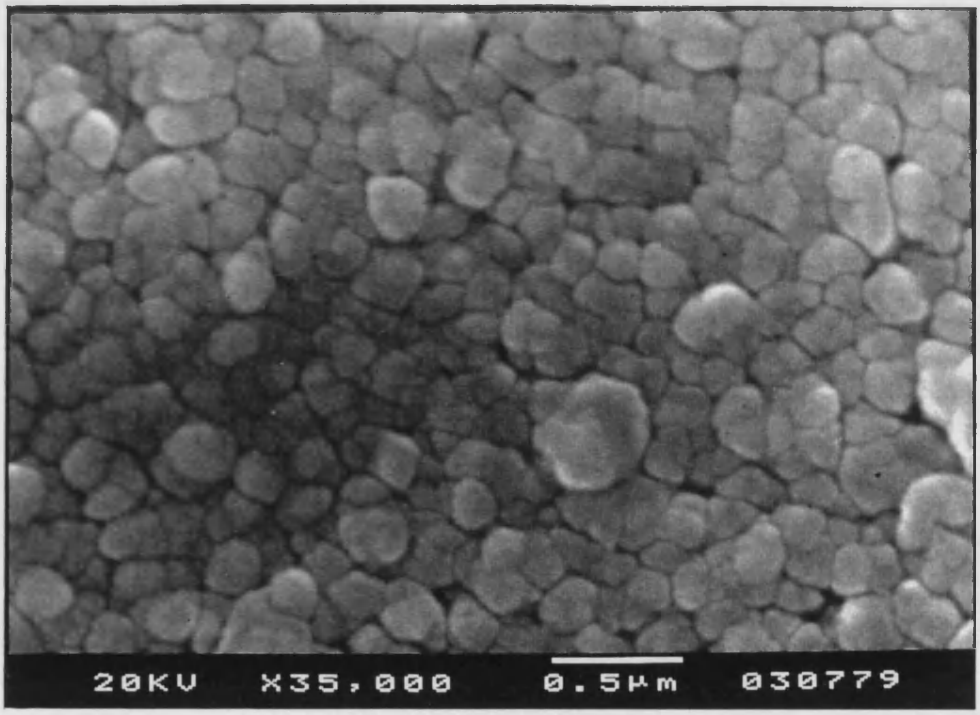

Figure 5.1(a). Scanning electron micrograph of as-deposited CdS after a deposition time of 15 minutes (x35,000) (sample 1)

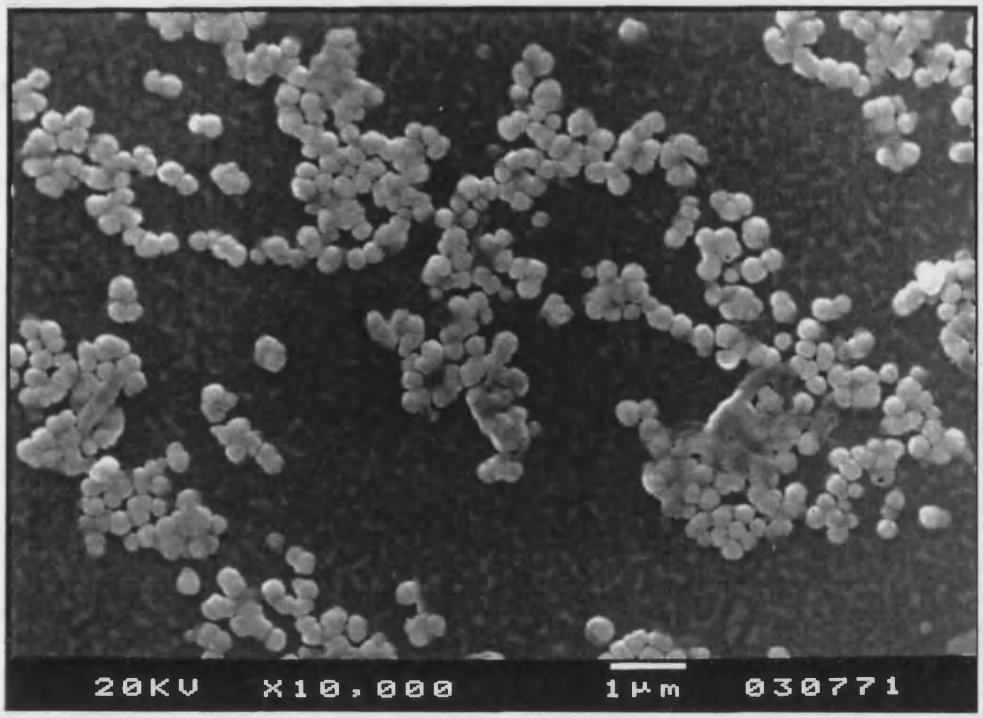

Figure 5.1(b). Scanning electron micrograph of as-deposited CdS after a deposition time of 1 minute (x10,000) (sample 1)

Shown in figure 5.2. an FSEM micrograph of an as-deposited CdS film with a grain size of 0.22 ±0.06μm (sample 2). This compares well with the grain size in sample 1.

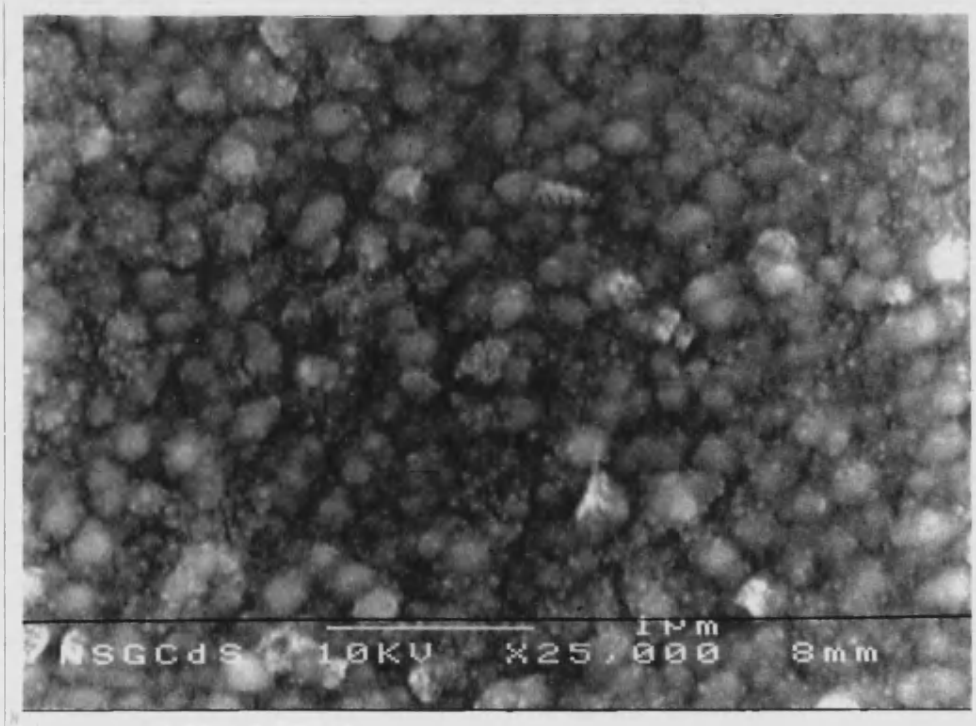

Figure 5.2. Scanning electron micrograph of as-deposited CdS (450°C, 15 minutes) (x35,000) (BP Solar)

Following heat treatment of sample 2 in air (450°C, 15 minutes) little change in substrate morphology from the as-deposited film was noticed. In contrast, CdS films annealed under a $CdCl_2$ flux for 10 minutes at 400°C show a much larger grain size of $0.35 \pm 0.1\mu m$, as shown in the TEM image in figure 5.3.

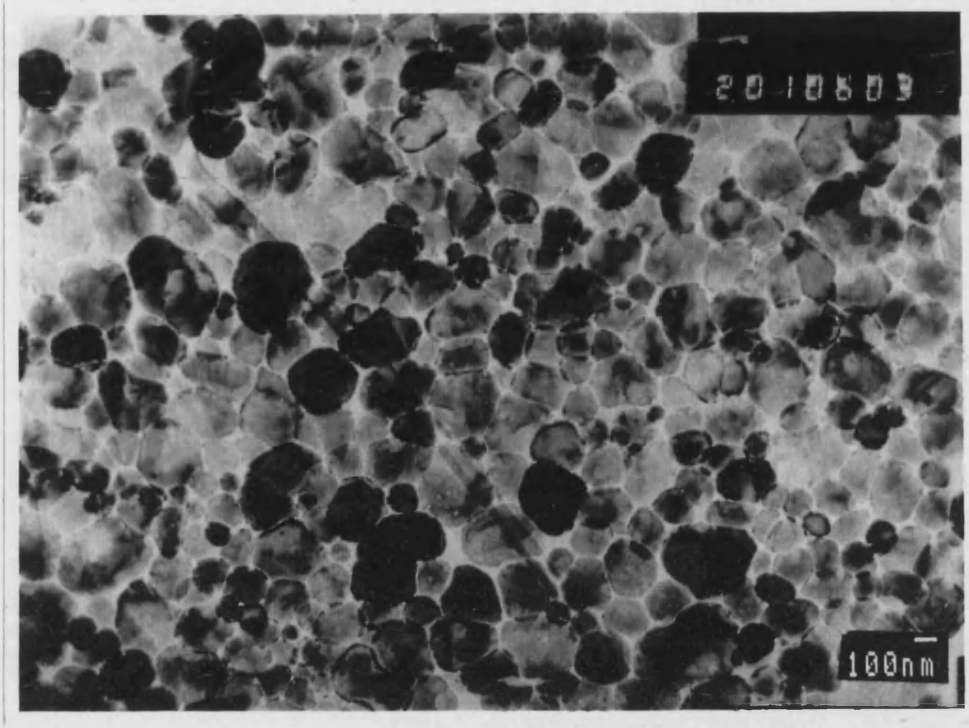

Figure 5.3. Transmission electron micrograph of $CdCl_2$ annealed (400°C, 10 minutes) CdS film

From analysis of the microstructure of the CdS films by XRD, as-deposited films (sample 2) were found to produce no significant reflections whereas following heat treatment in air, reflections corresponding to the hexagonal (greenockite) and cubic phase were identified. After annealing under a $CdCl_2$ flux, the films were entirely of the hexagonal phase.

5.2.2. Capacitance Voltage Measurements

Figure 5.4 shows the capacitance voltage response for a typical CBD CdS thin film grown on SnO_2 coated glass (Nippon Sheet Glass, NSG) (sample 1). The film was deposited at 60°C from a solution containing NH_3 [1.7 mol dm^{-3}], Cd^{2+} [0.01 mol dm^{-3}]

introduced as the chloride salt, and $SC(NH_2)_2$ [0.01M]. Deposition times were typically 15 minutes corresponding to a layer thickness of ≈100nm [31].

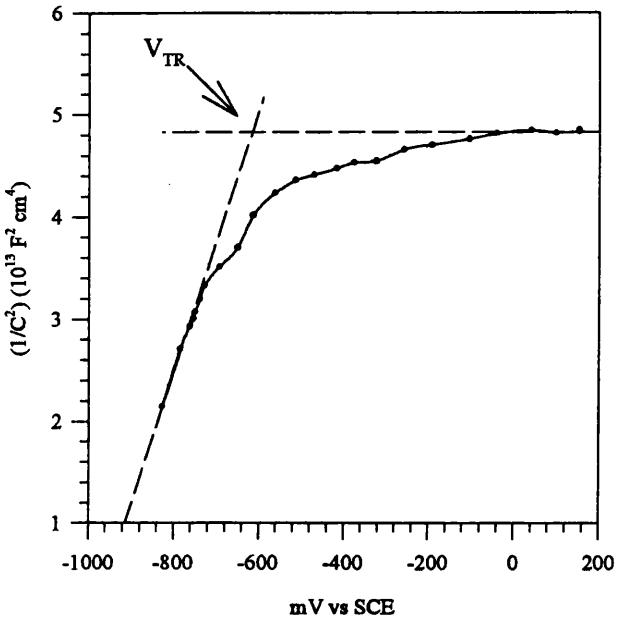

Figure 5.4. Capacitance voltage plot obtained for CBD CdS (sample 1) in 0.1 mol dm^{-3} Na_2S and 0.1 mol dm^{-3} NaOH (V_{ac} = 5 mV pk-pk, f = 1 kHz, ν = 50 mVs^{-1})

Figure 5.5 illustrates the capacitance voltage behaviour recorded for an as-deposited CBD CdS thin film supplied by BP Solar (sample 2)

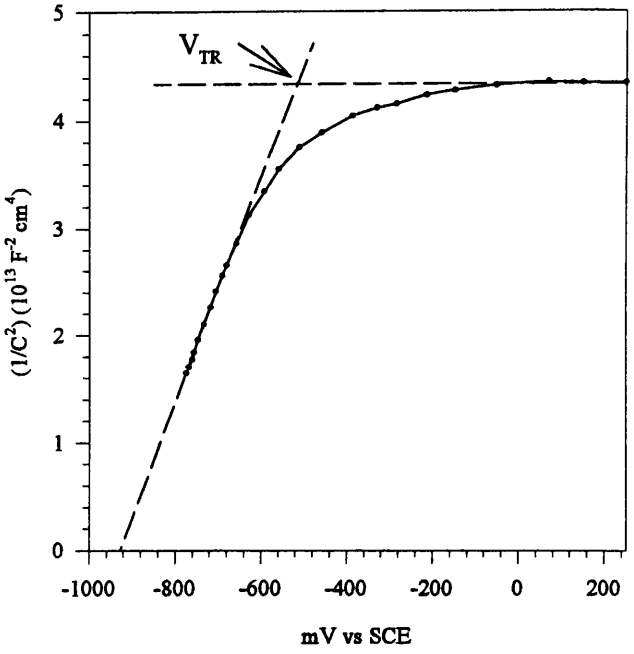

Figure 5.5. Capacitance voltage plot obtained for CBD CdS grown on NSG SnO_2/glass (sample 2) in 0.1 mol dm^{-3} Na_2S and 0.1 mol dm^{-3} NaOH (V_{ac} = 5 mV pk-pk, f = 1 kHz, ν = 50 mVs^{-1})

According to the method described in 2.7, capacitance voltage data was treated using a modified form of the Mott-Schottky relationship (equation 2.30) which takes the interfacial surface roughness ($\Re$) into account. The saturation voltage (V_{TR}) which corresponds to the potential at which the width of the space charge layer equals the thickness of the film has been calculated using equation 2.32. Table 5.2 lists values for these parameters along with of the flatband potential (E_{fb}) and donor density (N_D) determined from each of the capacitance voltage plots.

Sample Details	E_{fb} vs SCE / V	Donor Density, N_D / 10^{16} cm^{-3}	Surface Roughness, $\Re$	V_{TR} / Experiment / V	V_{TR} / Theory / V
As-deposited (sample 1)	-0.89	7.1	2.0	0.54	0.14
As-deposited (sample 2)*	-0.92	3.2	1.6	0.23	0.25
Air annealed*	-0.81	4.4	1.7	0.30	0.42
$CdCl_2$ annealed*	-1.29	11	1.9	1.24	1.15

Table 5.2. Data obtained from capacitance-voltage plots for CdS films (samples marked with an asterix were supplied by BP Solar)

In figure 5.4 the deviations observed from the expected capacitance voltage behaviour in the Mott-Schottky and geometric capacitance regimes suggest the sample contains regions of inhomogeneous doping usually associated with a defective film structure. For films supplied by BP Solar, the absence of these variations implies the structure of the deposit is far more homogeneous. To determine the relationship between capacitance behaviour and CdS morphology, the mechanism of film formation must be considered. According to Froment *et al* [30], growth of CdS by the chemical bath route proceeds initially by an ion-by-ion process forming a compact inner layer on the substrate surface (see chapter 2.11). As CdS is deposited, the composition of the bath changes and a porous outer layer forms as the mechanism switches to colloidal growth. During both these processes homogeneous precipitation of colloidal CdS in the solution phase may also occur. Depending on the composition and pH of the deposition bath, each of these three processes may be responsible for film growth. Lincot *et al* [31] found that film morphology is strongly dependent on the ratio of thiourea [Tu] to cadmium ions

$[Cd^{2+}]$ in the bath . Based upon this relationship, three principal film morphologies can be identified.

(i) For [Tu] >> $[Cd^{2+}]$: Smooth compact layers with fine grain structure are formed.

(ii) For [Tu] ≈ $[Cd^{2+}]$: Inner layer appears smooth but the outer layer is significantly rougher.

(iii) For [Tu] < $[Cd^{2+}]$: Layer is no longer homogeneous and uncovered areas of the substrate remain.

According to the concentration of [Tu] and $[Cd^{2+}]$ used in the deposition of sample 1, growth should proceed to give an initially compact layer with a rougher outer surface. If the inhomogeneity in the film structure deduced from the capacitance voltage results in figure 5.4 is associated with disorder at the deposit surface, the value of 2 for the surface roughness compared with 1.6 for sample 2 would seem acceptable. However, although excellent agreement between the experimental and theoretical values of V_{TR} determined for sample 2 demonstrate the internal consistency of the approach taken to deal with surface roughness, the corresponding values determined for sample 1 are nearly 40 mV apart. In calculating $\Re$ and V_{TR}, it is assumed that penetration of the electrolyte between the uppermost crystallites in the film is negligible. However, an increase in capacitance is likely to be associated with electrolyte leakage in a film which has a porous upper layer. This will lead to overestimates in the calculated values of $\Re$ and V_{TR}. In an earlier study [32], a 6.6% increase in the capacitance was measured over 280 minutes for a similar CdS film supplied by BP Solar. As the time of measurement was typically 2-3 minutes, it was concluded that electrolyte penetration into the film was

limited. Therefore, for sample 1, a far larger increase in the capacitance would be expected over a shorter period of time leading to the observed difference in V_{TR}.

Even though the morphologies of samples 1 and 2 appear to be quite different, the values of their flatband potential are very similar, suggesting the surface composition of the two samples are alike. However, both values differ significantly from the flatband potential of single crystal CdS (Cd 0001 face) in the same electrolyte (-1.3V vs SCE). The origin of the ≈50mV shift may lie in the presence of a $Cd(OH)_2$ overlayer remaining on the CBD electrode surface after deposition. From the FSEM image of sample 2 (figure 5.2), the most striking feature is the scattering of small well defined white centres over the electrode surface. According to Lincot *et al*[33] , these are crystallites of $Cd(OH)_2$ formed at the air/solution interface as the film is removed from the deposition bath. At this point evaporation of NH_3 from the film surface decreases the ionic concentration of $[Cd^{2+}]$ $[OH^-]^2$ into the precipitation range forming $Cd(OH)_2$ crystallites with sizes ranging from a few nm upto 1μm. A similar process has been found to be responsible for the growth of $Cd(OH)_2$ on the surface of Langmuir Blodgett films [34].

Doping densities for samples 1 and 2 are in good agreement with the value determined for a single crystal CdS sample in the same electrolyte ($5x10^{16}$ cm^{-3}) suggesting that the bulk compositions are quite similar. A survey of the literature reveals that doping densities of as-deposited CBD CdS films are typically in the range low 10^{15} - high 10^{16}. Attempts have been made to increase the donor density of CBD CdS films through the addition of metal salts to the deposition bath. Shikalgar *et al* [35] and Saur *et al* [36] have reported donor densities that were not only extremely low but were also unchanged for films grown from lithium containing deposition baths Saur *et al* [36] have reported donor densities for CBD CdS films of ≈10^{14} cm^{-3}. As lithium (or any other

Group I metals) do not form insoluble chalcogenides or any related compounds, the reported approach of doping CdS by Li seems questionable.

Based upon capacitance voltage study published by Lincot *et al* [31] for CBD CdS films, the suitability of applying the modified form of the Mott-Schottky relationship to the authors data was assessed. Surface roughness values of 1.59 (d = 0.085μm) and 1.15 (d = 0.13μm) were calculated for films grown on SnO_2 glass at 60°C for 400 and 900s, respectively. However, based upon the concentration regime followed for growth, [Tu] ≈ [Cd^{2+}], an increase in $\Re$ would be expected at longer deposition times. For the thinner film, the calculated value of V_{TR} was shifted 47 mV from the experimental value whereas for the thicker film the difference was only 22 mV. Based upon this difference, electrolyte penetration effects are likely to be operative in the same way as discussed for sample 1. From the SEM image shown of the film surface, the presence of poorly compact and rough grains across the film surface appears to confirm this.

After heat treating the as-deposited films in air at 450°C for 15 minutes, the capacitance voltage behaviour was found to be very similar to the as-deposited film but the doping density has increased slightly. More significant is the even further positive shift in V_{fb} from the values determined for samples 1 and 2 and single crystal CdS. These differences appear to reflect large changes in surface composition after heat treatment. Although the slight increase in N_D may be associated with an increase in the density of S vacancies in the lattice, the more drastic changes in the surface properties are likely to result from oxygen adsorption at the film surface. For similar CdS deposits grown by the CBD route, Danaher *et al* [21] have found that air annealing increases the surface oxide coverage and incorporation of chemisorbed oxygen at film grain boundaries. The origin of this may lie in the thermally induced transformation of $Cd(OH)_2$ crystallites on the film

surface into CdO by the loss of water. In this case the film surface would be composed of a CdO/CdS layer with quite different electrical characteristics to the surface of a CdS single crystal. The slight increase in surface roughness is consistent with the partial recrystallisation of the as-deposited layer following heat treatment in air.

The most drastic change in film properties was brought about by annealing as-deposited CdS films under a $CdCl_2$ flux at 400°C for 10 minutes. Following heat treatment, the flat band potential almost coincides with the value for single crystal CdS, suggesting both forms of CdS have a similar surface composition. However, in comparison with air annealed CdS where the film is likely to be covered in a CdO over layer, the $CdCl_2$ flux appears to promote the removal of oxides/hydroxides or impurities from the deposit creating a "clean", surface more comparable to that of the single crystal.

Accompanying the large negative shift in flatband potential is an increase in the donor density for $CdCl_2$ annealed films to values in the range $\approx 10^{17}$ cm^{-3}. Uda *et al* [37] have found that the donor density of CBD CdS films is strongly dependent on the concentration of chloride ions incorporated into the film from the deposition bath during growth. Auger analysis has shown the presence of significant amounts of chloride within films deposited from $CdCl_2$ baths [38]. The large increase in N_D after annealing under $CdCl_2$ is due to the creation of an increased number of S vacancies which are occupied by chloride ions. For ZnO films grown by spray pyrolysis, chloride incorporated into the deposit derived from the deposition solution has been shown to act as donor impurity centre [39]. However, Bube *et al* [39] have found that the effect of chlorine doping is negligible in heat treatment samples compared with the increase in donor density due to oxygen desorption from grain boundaries. The authors concluded that the presence of Cl^- becomes harmful in terms of features that limit the transmission by acting as optical

scattering centres. To establish whether changes in the electrical properties of $CdCl_2$ annealed films correlate with variations in chloride concentration, techniques such as SIMS or Auger spectroscopy must be used to probe the composition of heat treated deposits.

For the annealed samples the difference between experimental and theoretical values of V_{TR} are likely to reflect increased penetration of the electrolyte into the uppermost value of the deposit. From the TEM image of the flux annealed sample in figure 5.3, the compactness of the surface appears to be considerably lower than either the as-deposited or air annealed films. It appears contraction or expansion of the film on the underlying substrate surface accompanies extensive recrystallisation of the deposit. The high interfacial surface area is probably created by the overlap of crystallites with a wide range of sizes and textures.

The correspondence between surface roughness values and changes in film morphology after annealing demonstrates the validity of the approach used to treat capacitance voltage data. However for less compact deposits, electrolyte penetration leads to an increase in the capacitance and over-estimate of the surface roughness.

5.2.3. Electrolyte Electroabsorption Spectroscopy (EEA)

Figure 5.6 and 5.7 illustrate EEA spectra recorded for CdS thin film samples 1 and 2, respectively.

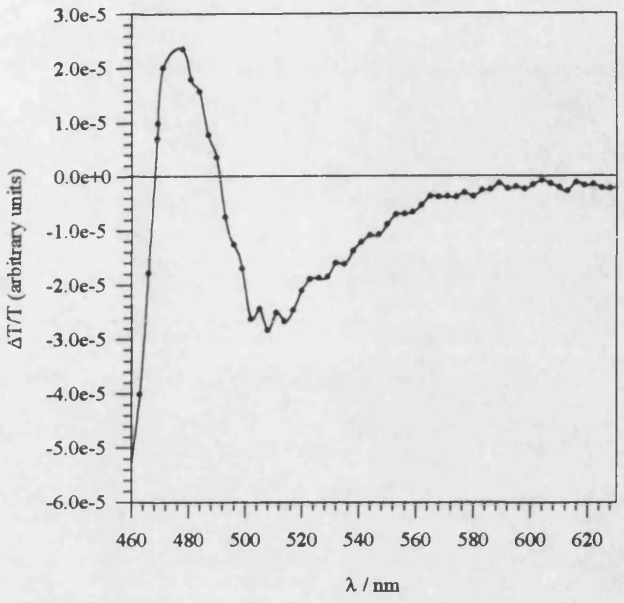

Figure 5.6 Electrolyte electroabsorption spectra for as-deposited CdS (sample 1) in 0.1 mol dm^{-3} Na_2S and 0.1 mol dm^{-3} NaOH. (V_{ac} = 100 mV rms, f = 270 Hz, Vdc = 0 mV vs SCE)

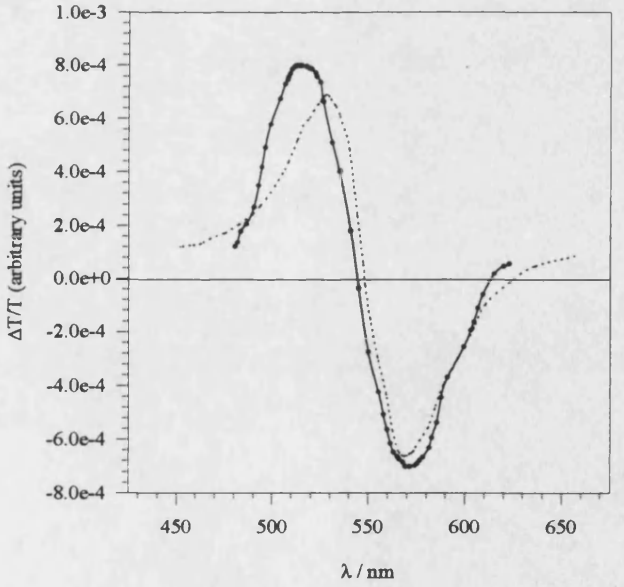

Figure 5.7 Electrolyte electroabsorption spectra for as-deposited CdS (sample 2) in 0.1 mol dm^{-3} Na_2S and 0.1 mol dm^{-3} NaOH. The dotted line shows the fit of the generalised lineshape function to the experimental data. (V_{ac} = 100 mV rms, f = 270 Hz, Vdc = 0 mV vs SCE)

Table 5.3 lists values of the band gap and broadening parameter derived from the Aspnes [52] third derivative fitting function.

Sample	E_G / eV	Γ / meV
As-deposited (sample 1)	2.50	164
As-deposited (sample 2)*	2.47	175
Air annealed*	2.32	213
$CdCl_2$ annealed*	2.46	74

Table 5.3. Bandgap and broadening parameters for CdS films (samples marked with a * were supplied by BP Solar)

To assess the accuracy of the fitting routine and sample measurement, values of $E_g \pm 0.02$eV and $\Gamma \pm 9$ meV were determined from three spectra recorded from the same CdS thin film. The effect of heat treatment on the EEA response was determined for CdS thin films following annealing in air at 400°C for 15 minutes and under a $CdCl_2$ flux at 400°C for 10 minutes. These are plotted in figures 5.8 and 5.9, respectively.

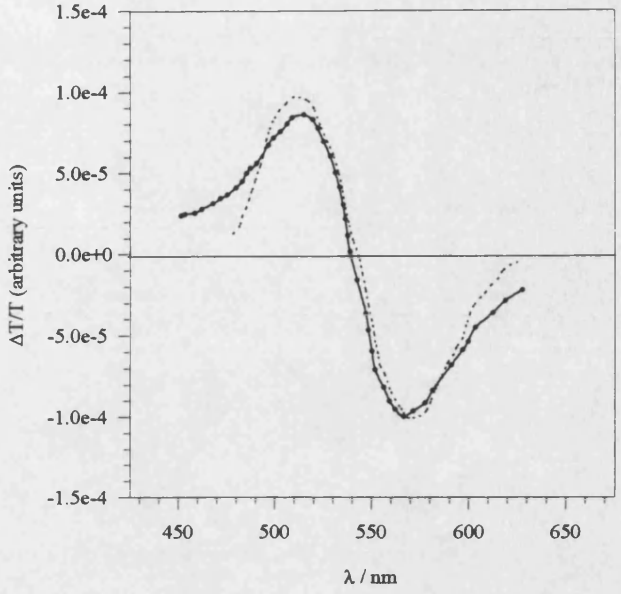

Figure 5.8 Electrolyte electroabsorption spectra for air annealed CdS in 0.1 mol dm^{-3} Na_2S and 0.1 mol dm^{-3} NaOH. The dotted line shows the fit of the generalised lineshape function to the experimental data. (V_{ac} = 100 mV rms, f = 270 Hz, Vdc = 0 mV vs SCE)

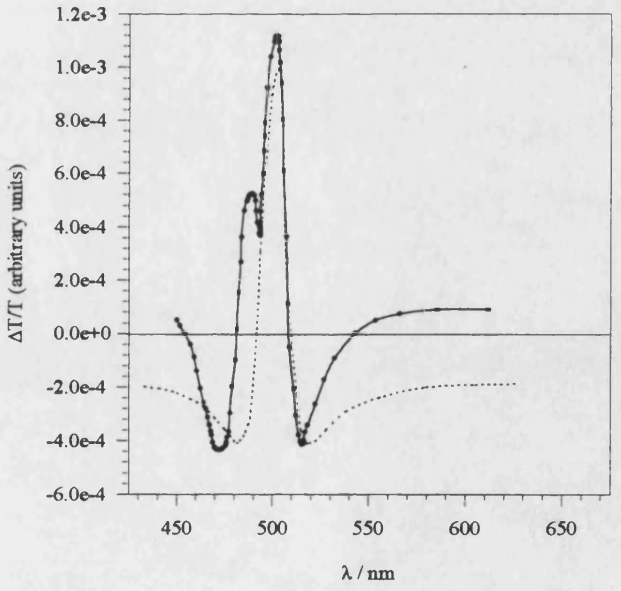

Figure 5.9 Electrolyte electroabsorption spectra for $CdCl_2$ annealed CdS in 0.1 mol dm^{-3} Na_2S and 0.1 mol dm^{-3} NaOH. The dotted line shows the fit of the generalised lineshape function to the experimental data. (V_{ac} = 100 mV rms, f = 270 Hz, Vdc = 0 mV vs SCE)

In the case of as-deposited and air annealed CdS films, broad derivative structures with two main extrema were observed. The overall shape resembled room temperature electroabsorption spectra reported for evaporated CdS films by Snavely [40] and for thin monocrystalline films by Hase and Onuki [41]. In contrast, the $CdCl_2$ annealed sample exhibits a narrower line-shape and increased number of crossing points. These spectra may be compared with the sharp response obtained for single crystal CdS (Cd 0001 Face) in figure 5.10.

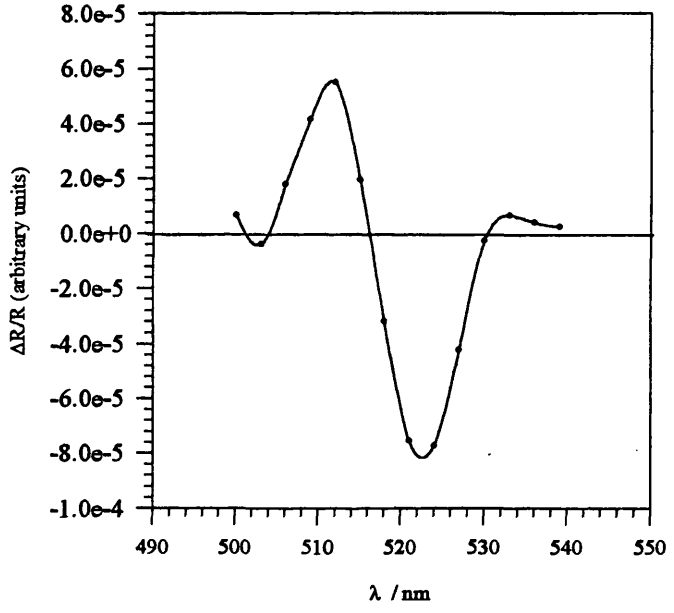

Figure 5.10 Electrolyte electroabsorption spectra for single crystal CdS (Cd 0001 face) in 0.1 mol dm^{-3} Na_2S and 0.1 mol dm^{-3} NaOH (V_{ac} = 100 mV rms, f = 270 Hz, Vdc = 0 mV vs SCE)

Although this is the first report on the modulation spectroscopy of CBD CdS films, Dulak *et al* [42] have reported a similar study on films grown by spray pyrolysis. However, in their study EEA spectra were obtained with no characteristic third derivative line shape or features close to the E_o transition of CdS (514 nm). In comparison with SP CdS films grown by Chopra *et al* [43], the use of considerably lower substrate

temperatures was necessary to achieve stoichiometric CdS films. As films were deposited on borosilicate glass maintained at 435°C, the decomposition reaction at higher temperatures is likely to lead to films with quite differing stoichiometry. Attention has also be drawn to the unsuitability of borosilicate glass as a heated substrate in the spray pyrolysis of thin films [44]. In the SP of In doped SnO_2 films, Manifacier *et al* [44] found Sn/In ratios differed significantly from films grown on substrates such as Si. The authors suggested at high temperatures (>400°C), impurities such as B, Na, Al, K, Si, and oxides from the glass surface transfer into the growing deposit. In the case of SnO_2, this was thought to strongly influence the pyrolytic reactions responsible for film formation. These observations suggest strongly that the composition and morphology of the films grown by Dulak *et al* [42] differ substantially from the CdS films described in this work.

It is important to relate changes in the broadening parameter to differences in film structure. As discussed in 2.9, there are several processes that are responsible for changes in the third derivative line shape. Of particular importance is the effect of field inhomogeneity due to defects or impurity centres within the film. Owing to the dependence of the complex dielectric function on the electric field, coupling with the field leads to changes in the lineshape function. Shen [45], Pollak [46], and Raccah [47] and have all shown that variations in the width of band spectral functions occur when the field interacts with defects or polarisable impurities. For this reason EEA can be used to detect the presence of defects that can act as coupling centres by following changes in the lineshape of these transitions.

The most striking feature of the EEA spectra of the as-deposited and air annealed films is the very large values of the broadening parameter that reflect the broad spectra obtained. The similar values of the broadening parameter obtained for samples 1 and 2

suggest that their defect structure is quite similar even though sample 1 has been found to be prone to electrolyte leakage effects through having a less compact structure. However, air annealing increases the broadening parameter by nearly 40 meV, suggesting that heat treatment serves to increase the defect density in the film. However, based on the large change in surface composition deduced from the positive shift in the flatband potential (section 5.2.2), it is likely that the increased broadening also includes a contribution from coupling between the electric field and defects in the film oxide layer. During heat treatment, volatile impurities diffuse out of the film into the annealing atmosphere. If the oxide layer traps these species, the impurity content of the film will rise leading to further field-impurity coupling. In contrast, after annealing under a $CdCl_2$ flux, the broadening parameter is substantially reduced to 74 meV which is close to the value obtained to single crystal CdS (see figure 5.10). Figure 5.9 illustrates the EEA spectrum recorded for the $CdCl_2$ annealed sample. HRTEM studies have shown that the large density of stacking faults which predominate in as-deposited and air annealed films are considerably reduced in flux-annealed deposits. Chao *et al* [48] and Raccah *et al* [47] have reported that the broadening parameter is primarily sensitive to this type of extended two-dimensional defect. Therefore it seems reasonable to correlate the changes in the broadening parameter with the presence of stacking faults within the film. In the HRTEM image shown in figure 5.11, the arrows show the location of stacking faults. These features arise by the incorporation of 3 to 4 atomic layers of cubic CdS into the basal plane of the hexagonal CdS structure. This suggests that during the growth process, grain formation alternates between hexagonal and cubic modifications of CdS which may explain the polymorphism often reported for CBD CdS films. Zelaya-Angel[49] has recently reported the possibility of growing cubic films by the CBD route.

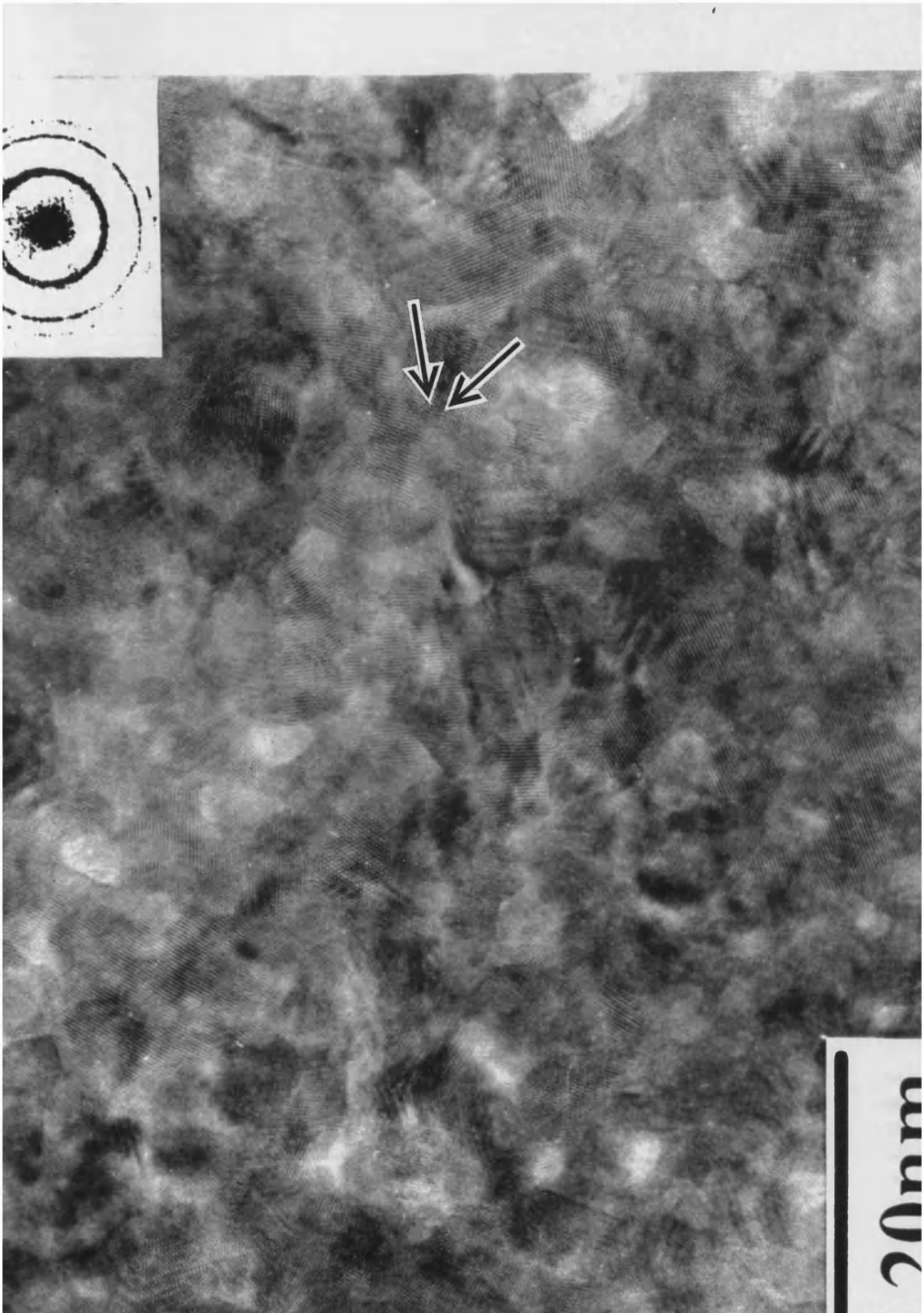

Figure 5.11 HRTEM image of an as-deposited CdS thin film. Arrows point to the presence of stacking faults.

According to Froment *et al* [50] the minimum density of stacking faults is comparable to the best CdS films grown by MOCVD or pulsed laser ablation.

However, other broadening mechanisms are likely to contribute to the observed differences between spectral lineshapes in figures 5.6 to 5.9. The variation of potential within the space charge region is particularly important in films which are inhomogeneously doped. From values of the broadening parameter it was previously suggested that samples 1 and 2 had a similar defect structure, although capacitance voltage results show sample 1 is inhomogeneously doped. If broadening due to field inhomogeneity could be deconvoluted from that resulting from the variation of potential within the space charge layer, changes in the broadening parameter could be used to characterise variations in defect structure. However, in the case of CdS, broadening effects are further complicated by the influence of excitonic transitions on the lineshape. This can lead to an increases in the spectral width, although as discussed in 2.9, attempts to determine the exact role of excitons in electroabsorption spectra have been met with limited success. In the spectra recorded here it is impossible to isolate the contributions from the various effects responsible for broadening, although it is important to consider all the mechanisms that may be involved.

An unusual feature in the EEA spectrum recorded for the $CdCl_2$ annealed sample was the shoulder on the high energy side of the positive going peak. As this has not been observed in any other EEA or EER spectra reported for thin film or single crystal CdS, it was presumed to be derived from the post deposition treatment. However, in an EEA study made by Raccah *et al* [47] on the reactive ion etching of n-Si in CHF_3/Ar, a similar effect was observed. From mathematical treatment of the results it was suggested that the "splitting" was associated with lattice strain induced by the damage caused by the etching treatment. The origin of this was sought in the electric field concentration within

these highly strained regions. The difference in the magnitude of coupling the electric field with strained and unstained regions was so great that two transitions effectively occurred. This was equivalent to the valence band splitting into two levels giving rise to an additional transition close in energy to the main peak. Although the exact details of this are outside the scope of this work, a similar situation may exists in CdS. A particularly strained film will be formed during recrystallisation if substantial film expansion or contraction occurs. Comparison of the film morphology obtained for as-deposited and air annealed CdS reveals that grains are far less compact and overlap extensively in the $CdCl_2$ treated deposit. This strongly suggests that film expansion has occurred. Alternative explanations may be considered for the observed shoulder, in particular those involving a bound chloride-exciton complex. As excitons are known to form bound impurity complexes [51], this feature may represent a transition resulting from a complex formed between an exciton in CdS and a chloride centre. The presence of chloride in the film acting as a donor has been discussed in section 5.2.2.

Figure 5.12 illustrates the potential dependence of the EEA spectra recorded for as-deposited CdS (sample 2). The most striking feature is the collapse of the third derivative lineshape to a homopolar band as the electrode is polarised from depletion to accumulation. An immediate consequence of this is that at more negative potentials Aspnes [52] fitting routine can no longer be applied to EEA spectra.

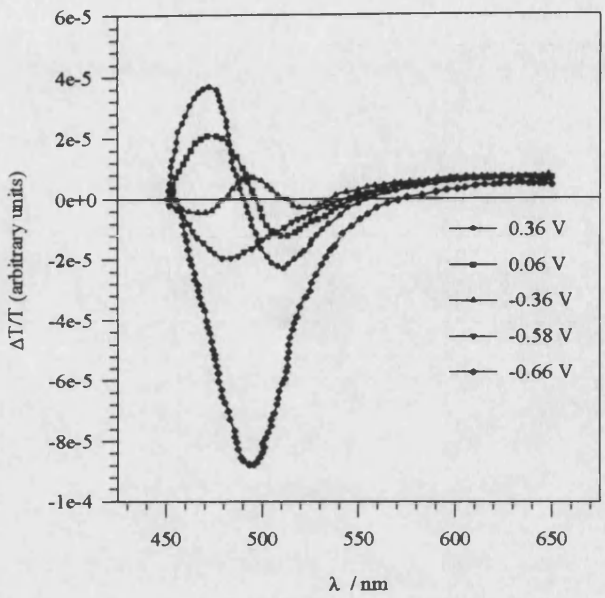

Figure 5.12 Electrolyte electroabsorption spectra for as-deposited CdS recorded over a series of potentials in 0.1 mol dm^{-3} Na_2S and 0.1 mol dm^{-3} NaOH. (V_{ac} = 100 mV rms, f = 270 Hz, Vdc = 0 mV vs SCE)

Iliev *et al* [53] have reported a similar effect in EER spectra recorded for single crystal CdS. Interestingly the authors noted that the same negative peak was absent in spectra produced using a freshly cleaved crystal under unchanged experimental conditions. Based on the similarity of the spectra, it may be that certain features in the EEA spectrum originate at the surface of the film. A simple qualitative model that may explain this is as follows. If we consider the electrode biased far away from flat-band where third derivative spectra are obtained, the space charge region extends throughout the entire sample (i.e. the saturation region). Upon illumination the modulated electric field will sample optical transitions in both the surface and bulk regions. If the electrode is then biased towards accumulation, contributions from the surface will become more important and from the bulk less so (assuming the intensities of the transitions in the two regions are the same). Based on the low temperature EEA spectrum reproduced in

figure 2.19 (chapter 2.9), peaks A and C could be assigned to optical transitions predominantly in the bulk. Peak B corresponds to the homopolar band and represents an optical transition in the surface layer. As the origin of this effect has been sought at the film surface, two possibilities arise. The most tempting is that this transition is associated with photocorrosion sites on the film surface as a result of illumination. However, the same features are observed in measurements made using non-electrolyte contacts. Alternatively the origin of this effect may lie in an inhomogeneous surface layer which is often present on the surface of single crystal and polycrystalline semiconductors. If the surface layer is particularly defective and impure, an extreme case of field inhomogeneity may be responsible for the large spectral changes. This is expected to be the case for CBD CdS as the films are particularly rough and prone to surface incorporation of by-products from the deposition bath. The absence of the homopolar band in the EEA spectrum of freshly cleaved single crystal CdS supports this as a homogeneous field would be expected at a single crystal surface.

Lineshape inversion can also be caused by the effect of excitons on band-to-band transitions. In chapter 2.9 it was shown that the third derivative nature of electromodulation is a consequence of the fact that the electric field can destroy the transitional symmetry of the crystal and accelerate electrons and holes. However, this is not the case for excitons as they are localised in space. Because of this confinement, the exciton energy is discrete and appears as a first derivative response. The effect of the electric field strength on exciton dissociation may provide an alternative explanation for the origin of the homopolar band. For example, at potentials close to flatband, the optical response is dominated by excitonic transitions as the applied field strength is insufficient to overcome the binding energy of the electron-hole pair. However, as the electrode is polarised towards depletion, exciton dissociation is more probable as the

field strength increases. Therefore, in the first case a pseudo first order derivative response is expected whereas in the second, although the optical response is still influenced by excitonic transitions, band-to-band transitions can also occur giving rise to a third derivative lineshape.

This makes the issue of lineshape inversion in CdS a very complicated problem. Even at low temperature where excitonic effects can be partially deconvoluted, the distinction between broadening effects due to excitonic and field inhomogeneity is by no means clear.

The "lineshape" rotation discussed above has also been used to determine the flatband potential of semiconductors such as TiO_2 and $CuInSe_2$ [54]. Hamakawa *et al* [55] and Salvador *et al* [54] have reported that the signal amplitude falls to zero and EEA/EER spectra invert when the dc potential applied equals the flatband potential. In the method of Hamakawa, individual spectra were recorded over a wide potential range to accurately determine the point of inversion. The less tedious approach of Salvador *et al* [54] involves monitoring the change in phase of the signal with potential. At the flatband the signal inverts by 180°. Values of the flatband potential were in excellent agreement with capacitance voltage measurements. However, this method is not valid for the case of EEA or EER signal with excitonic structure such as CdS, because excitons cannot distinguish between sign changes in the electric field. This is confirmed in figure 5.12 as a flatband potential between -0.36 to -0.56 V vs SCE is estimated from the point of inversion. This differs significantly from -0.92 V vs SCE determined for the same sample from capacitance voltage data.

The band gap values derived from the three point fit of the EEA spectra are compared in table 5.3. Under the same conditions a value of $E_g = 2.42$ eV was determined for single crystal CdS (figure 5.10). Variations in the concentration and type

of impurities between the CdS films are likely to be mainly responsible for the observed shifts in the band gap. For the two as-deposited films, a blue shift in the band gap from the single crystal value was observed. This increase may be related to quantum size effects, as found in colloids or particulate films. Calculations made by Yang *et al* [56] showed that this effect is relevant for CdS particle sizes less than 10 nm. From the HRTEM image shown in figure 5.11, this size is comparable with *some* of the grains present. However, as the larger grains present will counteract this effect, it is likely size quantization only makes a small contribution to the observed shift in the band gap. Following heat treatment in air at 400°C for 15 minutes the bandgap is reduced by 0.1 eV. This is likely to reflect the formation of an oxide layer at the film surface which alters the stoichiometry of the film. Annealing under a $CdCl_2$ flux leads to a bandgap similar to that obtained for the as-deposited films. Optical transmission spectra recorded for similar films has revealed that $CdCl_2$ annealing results in a sharpening of the absorption edge. The low value determined for the broadening parameter and the sharpening of the absorption edge provide evidence for recrystallisation of the flux annealed layer. Unlike films heat treated in air which are orange, those annealed under a $CdCl_2$ flux are a light yellow colour similar to as-deposited CdS. Although no satisfactory explanation of the colour change has been given, the orange colour in the air annealed sample is thought to be due to presence of oxygen centres within the film which red shift the bandgap.

The use of EEA spectroscopy has demonstrated that differences in the bandgap and broadening parameter may be correlated with changes in the properties of CdS thin films. However, in order to use Aspnes fitting function it is important that spectra are recorded at potentials where the third derivative lineshape is obtained.

5.3 Conclusion

Capacitance voltage and electrolyte electroabsorption measurements have been used to relate changes in film structure to the electrochemical and photoelectrochemical properties of CdS films grown by the chemical bath deposition route. The properties of the films characterised are summarised as follows

(i) As deposited. Intermediate behaviour between two heat treated samples. Most compact deposit formed. By products of deposition process ($Cd(OH)_2$) cover areas of the films surface. Films deposited in this work have a greater surface roughness and are less homogeneous than samples supplied by BP Solar.

(ii) Air annealed. Poor crystallinity and surface composition following heat treatment in air. A oxide layer is likely to be present at the film surface.

(iii) $CdCl_2$ flux annealed. Large improvement in crystallinity. Surface composition very similar to single crystal CdS. Less compact film structure formed following extensive recrystallisation. The increase in donor density is likely to arise from an increased number of S vacancies associated with chloride incorporation in the film.

This chapter has highlighted the unsuitability of $CdCl_2$ annealed CdS films for use in CdS/CdTe based heterojunction solar cells. Although the crystallinity of the deposit is high, the high surface roughness revealed by capacitance voltage measurements and poorly compact and pinholed grain structure observed in FSEM suggests that the flux annealed deposit offers a poor surface for the subsequent electrodeposition of CdTe. In

commercial CdS/CdTe solar cells the most promising treatment has been to air anneal CdS but *following* electrodeposition of the CdTe absorber layer. The CdS heat treated under CdTe has been found to have a similar crystallinity to $CdCl_2$ flux-annealed layers, but without the detrimental effects of a poorly compact and inhomogeneous grain structure [57]. Annealing also creates a range of solid solutions between CdTe and CdS which improve the quality of the heterojunction. This introduces the interesting possibility of using electrolyte electroabsorption spectroscopy to asses the crystallinity of the CdS underlayer following removal of CdTe by carefully controlled etching.

From these initial results the most promising post deposition treatment of CBD CdS appears to be heat treatment under air . However the uncertainties described above suggest extensive optimisation of the heat treatment is still necessary. Particular attention should be directed towards the formation of more compact deposits. In this way high quality window layers with low recombination losses may be realised

For as-deposited and $CdCl_2$ annealed films little difference was observed between their bandgaps. To substantially reduce the absorption losses in CdS, post deposition treatments are required that increase the bandgap of CdS. An alternative approach is the fabrication of nanocrystalline CBD CdS window layers. By preparing films with grain sizes in the order of a few nm, an improvement in the transmission will occur as quantum confinement within the individual crystallites shifts the band edge towards the UV. However although this is an intensive area of research, Q-Particle window layers are still far from developed

Lineshape inversion has highlighted the complexity of the EEA response in CdS. Lineshape changes due to field inhomogeneity are further complicated by the rich excitonic spectra of CdS. However in the absence of complex lineshape models which

take these effects into account, satisfactory fits to Aspnes [52] third derivative fitting function were obtained.

References

1 H. S. Zhou, I. Honma, H. Komiyama, and J. W. Haus, *J. Phys. Chem.*, **97**, 895 (1993)

2 G. A. Ozin, *Adv. Mater.*, **4**(10), 612 (1992)

3 M. E. Ozsan, *Int. Jnl. Solar. En.*, **12**, 79 (1992)

4 A. S. N. Murthy and K. S. Reddy, *J. Power Sources*, **13**, 159 (1984)

5 J. Britt and C. Ferekides, *Appl. Phys. Lett.*, **62**(22), 2851 (1993)

6 J. M. Woodcock, A. K. Yurner, M. E. Özsan, and J. G. Summers, in *Proceedings of the* 22nd IEEE Photovoltaic Solar Energy Conference, Lisbon, Portugal, April 1991, (H. S. Stevens and Associates, Bedford, UK, 1991), p. 931.

7 S. G. Mokrusin and Yu. Tkachev, *Colloid. J*, **23**, 438 (1961)

8 A. B. Lundin and G. A. Kitaev, *Inorg. Mater.*, **1**, 2107 (1965)

9 G. A. Kitaev, S. G. Mokrusin, and A. A. Uritska, *Colloid. J.*, **27**, 38 (1965)

10 D. E. Bode, T. H. Johnson, and B. N. Maclean, *Appl. Opt.*, **4**, 327 (1965)

11 S. G. Mokrusin, G. A. Kitaev, and A. A. Uritskaya, *Russ. J. Phys. Chem.*, **39**, 1101 (1965)

12 A. Banerjee, P. Nath, S. R. Das, and K. L. Chopra, Proc. 7th Int. Solar. Energy. Cong., New Delhi, 1978, p. 698.

13 M. Froment, M. Claude Bernard, R. Cortes, and B. Mokili, and D. Lincot, *J. Electrochem. Soc.*, **142**(8), 2642 (1995)

14 S. Saito, Y. Hashimoto, and K. Ito, First World Conference on Photovoltaic Energy Conversion, Dec. 5-9, 1994, to be published

15 F. Nicolau, M. Dupuy, and M. Brunel, *J. Electrochem. Soc*, **137**(9), 2915 (1990)

16 J. L. Stickney and D. Wayne Suggs, *J. Phys. Chem.*, **95**, 10056 (1991)

17 S. N. Sahu, *J. Mat. Sci: Materials in Electronics*, **6**, 43 (1995)

18 J. Tousková, D. Kindl, and J. Kovanda, *Thin Solid Films*, **214**, 92 (1992)

19 L. M. Peter in, Comprehensive Chemical Kinetics, ed. R. G. Compton, Volume 29, Chapter 8, p. 354

[20] G. Goodlet, M. J. Furlong, L. M. Peter, A. A. Shingleton, M. E. Özsan, D. R. Johnson, M. Sadeghi, and D. Sivapathasundaram, *J. Mat. Sci: Materials in Electronics*, in press

[21] W. J. Danaher, L. E. Lyons, and G. C. Morris, *Solar Energy Mat.*, **12**, 137 (1985)

[22] P. K. Nair, J. Campos, and M. T. S. Nair, *Semicond. Sci. Technol.*, **3**, 134 (1988)

[23] F. H. Pollak and H. Shen, *Mat. Sci. and Eng.*, **R10**(7-8), 275 (1993)

[24] O. J. Glembocki, *SPIE Modulation Spectroscopy*, **128**, 2 (1990)

[25] F. H. Pollak, *Proc. Soc. Photo-Optical Instrum. Eng.*, **276**, 142 (1981)

[26] T. Dittrich, *Phys. Stat. Solidi*, **119(a)**, 479 (1990)

[27] F. H. Pollak and H. Shen, *J. Crystal Growth*, **98**, 53 (1989)

[28] J. M. Dona and J. Herrero, *J. Electrochem. Soc.*, **141**(1), 205 (1994)

[29] N. C. Sharma, R. C. Kainthla, D. K. Pandya, and L. K. Chopra, *Thin Solid Films*, **60**, 55 (1979)

[30] M. Froment and D. Lincot, *Electrochim. Acta*, **40**(10), 1293 (1995)

[31] D. Lincot and R. Ortega-Borges, *J. Electrochem. Soc.*, **139**(7), 1880 (1992)

[32] M. J. Furlong, 1st year M.Phil/Ph.D tansfer report, University of Bath, 1993

[33] D. Lincot, R. Ortega-Borges, and M. Froment, *Philisophical Magazine B*, **68**(2), 185 (1993)

[34] X. K. Zhao, S. Xu, and J. H. Fendler, *Langmuir*, **7**, 520 (1991)

[35] A. G. Shikalgar and S. H. Powar, *Solid State Commun.*, **32**, 361 (1979)

[36] S. N. Sahu and S. Chandra, *Solar Cells*, **22**, 163 (1987)

[37] H. Uda, S. Ikegami, and H. Sonomura, *Jap. J. Appl. Phys.*, **29**(1), 30 (1990)

[38] A. A. Shingleton, M.Phil/Ph.D transfer report, University of Southampton, 1992

[39] R. H. Bube, A. Ortiz, and J. Aranovich, *J. Vac. Sci. Tech.*, **16**, 994 (1979)

[40] B. B. Snavely, *Phys. Rev.* **167**(3), 730 (1968)

[41] N. Hase and M. Onuki, *J. Phys. Soc. Japan.*, **28**(4), 965 (1970)

[42] W. Dulak and H. Meczynska, *Acta Physica Polonika*, **A69**(6), 945 (1968)

[43] K. L. Chopra, R. C. Kainthla, D. K. Pandya, and A. P. Thakoor, *Phys. Thin Films*, **12**, 167 (1982)

[44] J. C. Manifacier, L. Szepessy, J. F. Bresse, M. Perotin, and R. Stuck, *Mater. Res. Bull.*, **14**, 109 (1979)

[45] W. Shen, M. C. A. Fantini, F. H. Pollak, M. Tomkiewicz, H. Leary, and J. P. Gambino, *J. Appl. Phys.*, **66**(4), 1765 (1989)

[46] F. H. Pollak and X. Yin, *Appl. Phys. Lett.*, **59**(18), 1305 (1991)

[47] P. M. Raccah, J. W. Garland, Z. Zhang, U. Lee, S. Ugur, S. Mioc, S. K. Ghandi, and I. Bhat, *J. Appl. Phys.*, **57**(6), 2014 (1985)

[48] S-C Chao and G-J Jan, *J. Mat. Sci Lett.*, **11**, 1504 (1992)

[49] O. Zelaya-Angel, J. J. Alvaro-Gill, R. Lozada-Morales, H. Vargas, and A. Ferreira de Silva, *Appl. Phys. Lett*, **64**, 291 (1994)

[50] M. Froment and D. Lincot, *Electrochimica Acta*, **40**(10), 1293 (1995)

[51] D. F. Blossey and P. Handler, in Semiconductors and Semimetals, eds. R. C. Willardson and A. C. Beer, Vol. 9, Chapter 3, Academic Press, New York, 1972

[52] D. E. Aspnes, *Surf. Sci.*, **37**, 418 (1973)

[53] M. Iliev and I. Assenov, *Physiques des Solides*, **23**(6), 659 (1970)

[54] P. Salvador, J. Gandia, and M. Pujadas, *J. Electroanal. Chem.*, **244**, 69 (1988)

[55] Y. Hamakwa, P. Handler, and F. Germano, *Phys. Rev.*, **167**, 703 (1968)

[56] Y. Wang and N. Herron, *J. Phys. Chem.*, **95**, 525 (1991)

[57] Personal communication, Dr. G. Goodlet, University of Bath.

Chapter 6

Results

Localised photoelectrochemical imaging of anodically grown CdS films on Cd

6.1 Introduction

Much of the interest in electrochemical characterisation and behaviour of cadmium sulfide had primarily been from the point of view of its use in solid state ("dry") and photoelectrochemical ("wet") solar cells. Many early studies were made with well defined single crystal CdS owing to its high photoresponse and quantum efficiency. However the cost of single crystalline materials is far too high for large scale terrestrial applications. Vacuum deposited CdS has been shown to have the characteristics necessary for application in photoelectrochemical cells, but this still appears to be a relatively costly procedure. Electrochemical fabrication could show the way to producing polycrystalline CdS films at considerably lower cost than that involved in the production single crystal or vacuum deposited materials.

The use of CdS as a photoactive material for solar cells was first investigated by Gerischer [1] using single crystal CdS with a ($Fe(CN)_6^{6-/4-}$) redox couple and SnO_2 anode. This photoelectrochemical cell was found to have a solar power efficiency of greater than 5% in spite of the 2.42 eV band gap of CdS which implies that wavelengths greater than 550 nm (the greater part of the solar spectrum) are not absorbed.

In previous work, CdS films have been formed anodically by electrocrystallisation from alkaline sulfide solutions on Cd substrates. Miller and Heller [2] have prepared a semiconductor liquid solar cell based on the *in-situ* anodisation of cadmium in Na_2S. Under illumination, this cell drives a sulphide-polysulfide (S^{2-} / S_x^{2-}) redox couple when connected to a suitable cathode. In this case the S^{2-} / S_x^{2-} couple acts as the medium for film growth *and* as the potential determining redox electrolyte in the electrochemical solar cell. The bulk photoelectrochemical characteristics of these films have also been assessed and

compared to single crystal CdS [3] However, there are a number of disadvantages associated with CdS prepared by this method. Firstly, anodic deposition of materials often result in discontinuous films with many defects that can act as recombination centres, either within the film or at the surface. It is also difficult to form anodic CdS films that are thick enough to be useful. Maximum thicknesses are typically 500nm.

CdS films have also been deposited cathodically [4]. However there are also problems associated with this route. Under the acidic deposition conditions (pH=2), the source of sulfide ions (sodium thiosulfate) is unstable and disproportionates into elemental sulfur which is subsequently be incorporated into the film. This can lead to low photoelectrochemical performance owing to the poor film heterogeneity and stoichiometry. At present, the best CdS films for photovoltaic applications are produced by a chemical bath process. Their quality is good enough for commercial photovoltaic CdS-CdTe devices.

A number of questions still need to be answered in order to understand the poor performance of anodically grown CdS. This provided the stimulus for the present study by two localised photoelectrochemical imaging techniques of the role of the underlying substrate morphology on film growth. These techniques enable spatial mapping of the response to a scanning light spot. Scanning microscopy for semiconductor characterisation (S.M.S.C) [5] and photoelectrochemical microscopy (P.E.M) [6] systems have been used to map the photocurrent response at the illuminated Cd/CdS interface. A survey of the literature shows that most work on localised photoelectrochemical imaging has been made either on single crystal or a metal oxide coated substrate. Some of the systems that have been imaged are given in table 6.1.

System	Contact	Localised Photoeffect
Ti / TiO_2 [7,8]	0.05M H_2SO_4	PC
n-GaAs [9]	0.1M KOH	PC
Fe / FeO_x [6]	0.1M NaOH & 0.1M Na_2SO_4	PC
n-WSe_2 [10]	2.0M KI	EER
HgCdTe [11]	HNO_6/CH_6OH (1:5000)	EER
Au / $Fe(CN)_6^{6-/4-}$ [12]	K_2HPO_4 / KH_2PO_4	PT
GaAs - Si [13]	$NaClO_4$+CpFe/$CpFe^+$ (CH_6CN)	PC,PV EER
n-GaP [14]	0.1M $HClO_4$	PC

Table 6.1. Summary of systems that have been imaged by localised photoelectrochemical techniques. The terms PC, PV, PT, and EER, correspond to photocurrent, photovoltage, photothermal, and electrolyte electroreflectance effects, respectively.

Photoelectrochemical Imaging involves measuring local variations in the photocurrent or photovoltage at a semiconductor electrolyte interface as a function of the position of the illuminating light spot. By perturbing the sample at a microscopic level, changes in the macroscopic response of the system may be measured. As the perturbation is localised, deviations from the background state are attributed to effects within this region. A number of imaging methods have been developed based on this effect which may involve measuring the photocurrent [13], photovoltage [15], photoacoustic [16], or photothermal [12] response of the system. Figure 6.1 (i) showsthe photocurrent or photovoltage effects arising from the excitation of an electron from the valence band to the conduction band. The figure to the right of this, (ii), shows the dissipation of electronic energy gained by electrons during photoexcitation as vibrational (heat) energy. The vibrational energy may alternatively be dissipated in the form of acoustic energy at a frequency *f*. This is illustrated in figure (iii) by the propagating sound waves.

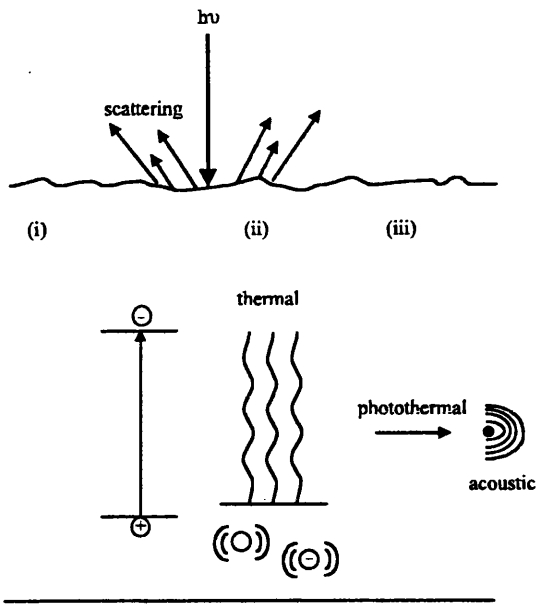

Figure 6.1. Various photoinduced effects that can give rise to image contrast (i) photocurrent and photovoltage, (ii) photothermal and (iii) photoacoustic

In all of the above cases a transparent electrolyte contact is used. The solid state analogue of the photocurrent methods is the light beam induced current (L.B.I.C)[17] technique. This has been used by Yoshida[17] to asses the spatial inhomgeneity of photocurrent efficiency in screen printed CdS / CdTe solar cells.

Early work using localised photoelectrochemical imaging focused on the study of the growth of oxide films on metals, particularly native or electrochemically grown TiO_2 films on Ti [8]. Smyrl *et al* [8] have related the spatial variation in the photocurrent to oxide thickness as a function of the crystallographic orientation of the titanium substrate grains. They also looked at the ordering of the oxide structure using electron diffraction, finding evidence for preferential growth grown on grains of a particular orientation. The understanding of the local structure and electronic properties of thin oxide films is important in the fields of catalysis, optical films, microelectronics and corrosion. In these areas susceptibility to localised chemical attack or electronic breakdown can be influenced by surface properties, which may not be revealed by methods which

probe the material as a whole. Photoelectrochemical microscopy was introduced by Butler [14] to study oxide films and was based on a previous technique developed by Furtak *et al* [18] to image polycrystalline semiconductor materials for liquid junction solar cells.

The early studies made on native oxide layers on metals were extended to characterise electrochemical passivation of metals. The electrochemical behaviour of cadmium in strongly alkaline solutions has been extensively studied in the past, primarily due to the use of the Cd / CdO electrode in nickel-cadmium batteries [19]. The electrochemistry of cadmium in alkaline solutions is complicated by changes in film morphology and composition as the potential is varied. At low potentials, an anodic layer consisting of a complex hydrous $Cd(OH)_2$-CdO mixture forms whereas at intermediate potentials the simultaneous formation of soluble Cd species takes place. Finally, at higher potentials the change of the anodic layer into a passivating film takes place. The major interest of the passivation of cadmium in alkaline sulfide solutions has been in the formation of photoactive layers for use in semiconductor liquid junction solar cells. However the mechanisms of film growth and composition of the anodic films are still uncertain as film formation is accompanied by dissolution. Mechanisms for growth have been proposed by Birss [20], Peter [21], and Arvia [22].

The present work has concentrated on measuring the localised photocurrent response of anodic films on Cd. Factors which give rise to spatial variation of the photocurrent are the optical absorption of the film (determined by film composition and thickness), diffusion length of minority carriers, light scattering, the electric field in the layer and the defect density (this determines the overall quantum yield of charge carrier collection), rate constants for photogeneration or recombination of charge carriers, and the presence of local catalytic centres.

6.2 Theory

Mechanisms for image contrast have been discussed for both the techniques used here (Scanning Microscopy for Semiconductor Characterisation (S.M.S.C) and Photoelectrochemical Microscopy (P.E.M). The two methods use different acquisition processes to obtain localised photocurrent data, and must be considered in developing theories for image contrast mechanisms. The approaches are.

(a) Step scan with lock-in detection [8,10]: This is the method employed in the SMSC system where the sample is moved in small steps in the X-Y plane and the illumination intensity is modulated. The photocurrent or photovoltage signal is then detected by a lock-in technique.

(b) Continuous scan with direct detection [6,9]: In the PEM method (also known as Scanning Laser Photoelectrochemical Microscopy (SCALPEM)), the light beam is rastered rapidly across the surface and the variation in the current flow across the interface measured as a function of spot position using digital data acquisition and framestore.

A brief description will be given of the theory behind image contrast mechanisms. A more quantitative description of photocurrent imaging has been given by Williams *et al* [23].

Image contrast has been described using a photocurrent transfer function developed by Peter *et al* [24] to describe the photocurrent response of a sample to sinusoidally modulated illumination. If the modulation frequency of the incident beam is changed over ranges which include time constants for photocurrent

relaxation processes, then information may be obtained on rate constants for a number of photoinitiated processes. The photocurrent response to an intensity modulation of angular frequency ω is given by

$$i_{ph}(\omega) = H(\omega).Y(\omega) \tag{6.1}$$

where H(ω) represents the excitation function and Y(ω) the photocurrent transfer function. We can conveniently consider the stimulus as the intensity modulated light, the response as the photocurrent and the frequency link between the two, the photocurrent transfer function. The latter was developed from the mechanisms of charge carrier generation and the subsequent fate of photogenerated charge carriers for a variety of electrochemical reactions at the semiconductor electrolyte interface. This is given by

$$Y(\omega) = G_o F(\omega)\left(\frac{g_o + g_1 j\omega\tau_1}{1 + j\tau\omega_1}\right) \tag{6.2}$$

where F(ω) is the attenuation introduced by the cell, G_o is the carrier generation rate, g_o, the steady state photocurrent following illumination, g_1 the maximum photocurrent and τ_1 the time constant associated the recombination of photogenerated carriers. It has been proposed that contrast in a photocurrent image results from a spatial variation of a combination of these parameters.

In the step scan lock-in technique, a lock-in amplifier is used to deconvolute the photocurrent signal from the background dark current. The

incident light is sinusoidally modulated and so may be described by the function $H(\omega)$

$$H(\omega) = I_o[1 + \Delta I_m \sin(\omega t)] \tag{6.6}$$

where I_o is the mean light intensity and ΔI_m the amplitude of modulation. The sensitivity of any of the parameters depends on the frequency of measurement. It is therefore necessary to choose the modulating frequency such that the system has some photocurrent response. This is only achieved when the detection frequency of the lock-in amplifier is matched to the frequency associated with charge carrier generation. We can describe the effects on contrast of varying the modulation frequency using equation (6.4) assuming that the parameters giving rise to contrast vary independently over the surface.

$$\left|i_{ph}\right| = G_o I_o \Delta I_m |F(\omega)|.|Y_o(\omega)| \tag{6.4}$$

The principal difference between the step scan and continuous scan technique is that in the latter the sample is effectively excited by a range of modulation frequencies. We can understand this by considering that the beam is scanned rapidly over the surface and every point within the scanned area sees a "burst" of illumination. In this case the variation of light intensity with time is a complex function of the spatial intensity distribution of light. Hence the "equivalent" modulation frequency of the spot is dependent on the speed and size of the spot as it moves across the surface and extra components due to the complex shape of the spot. We can determine the variation in contrast across the surface of some

parameter (β) of the photocurrent transfer function. The magnitude of the photocurrent at a point *x* is given by

$$\frac{I_{ph}}{vdx} = \int_0^{*} i_{ph}(t, \beta).\, dt \qquad (6.5)$$

where I_{ph} is the photocurrent produced by a point at the surface at a position *vt* behind the current spot position (*v* is the velocity of the scanned spot). Contrast mechanisms also depend on spot shape. Clearly differing intensity profiles will be obtained for different spot geometries. For simplicity, much of the modelling of Williams *et al* [9] assumes a rectangular intensity profile.

This chapter examines the influence of substrate morphology on the photoelectrochemical behaviour of the anodically grown CdS thin films. After characterising the mechanisms of growth by linear sweep voltammetry, preliminary structural-photoeffect relationships are derived from photocurrent measurements made on cadmium substrates pre-treated in a different ways prior to immersion in alkaline sulfide solutions. Localised photoelectrochemical measurements have then been used to asses the effect of microscopic changes in the surface morphology of the cadmium on the formation of CdS layers.

6.3 Results

6.3.1 Voltammetry

A typical i-V curve for polycrystalline Cd in 0.5 mol dm^{-3} Na_2S at a sweep rate of 100 mVs^{-1} is shown in figure 6.2.

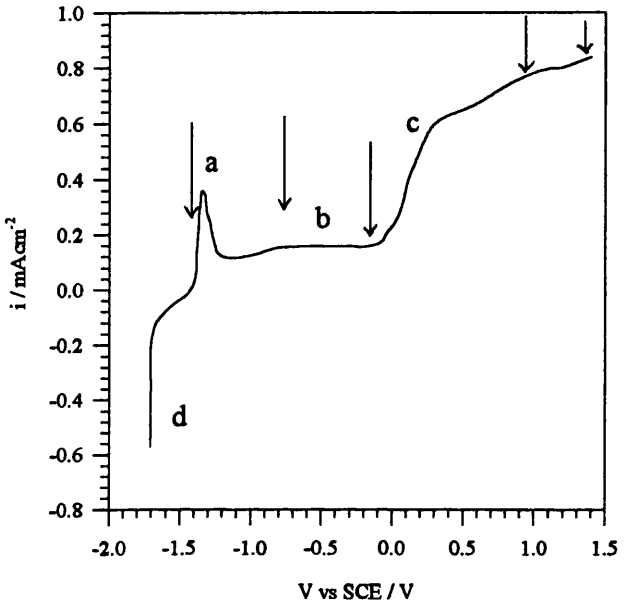

Figure 6.2. Cyclic voltammogram of polycrystalline cadmium foil in 0.5 mol dm^{-3} Na_2S. Sweep rate 100 mVs^{-1}. Illustrated are the (a) monolayer, (b) plateau, (c) transpassive, and (d) reduction regions. The arrows refer to the potentials at which photocurrent action spectra were recorded.

This may be compared with the voltammogram obtained by Arvia *et al* [22] for Cd in 0.01 mol dm^{-3} NaOH. This shows two main anodic peaks (i and ii) attributed to the formation of the anodic layer and soluble Cd species. The cathodic peak (iii) is related to the reduction of the anodic layer.

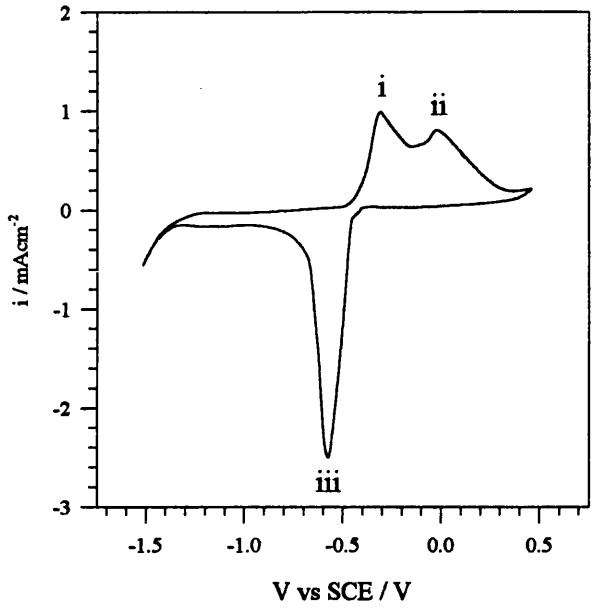

Figure 6.3. Cyclic voltammogram for Cd in 0.01 mol dm^{-3} NaOH at a sweep rate of 100 mVs^{-1} [22]

The presence of sulfide in solution clearly modifies the voltammogram where four main regions may be identified: 3 anodic peaks (a to c) and 1 cathodic peak (d). These are described according to the formalism of Peter [3].

(a) Monolayer region:

Here the initial stages of CdS growth involve nucleation and 2 dimensional growth of a few monolayers. This peak is often asymmetrical and its fine structure is sensitive to pre-treatment of the electrode. We can compare the charge density under this peak to the expected charge density, q, for a single layer of CdS having the density of the bulk material, ρ (4.82 g/cm^3), using equation 6.6

$$q = \left(\frac{\rho \mathrm{d}}{\mathrm{m}}\right)^{2/3} \frac{nF}{N_A} \qquad (6.6)$$

where F is the Faraday constant, N_A is the Avagadro constant, M is the relative molar mass of CdS (144.5 g/mol), and *n* the number of electrons per mole assumed to be 2. Equation 6.6 yields an expected monolayer charge density of 250 $\mu C/m^2$. Integration of the area associated with peak a equals 246 $\mu C/m^2$ corresponding to a single monolayer.

According to the literature, a wide variety of potentials have been quoted for the standard potential for the formation of CdS. These range from -1416 mV to -1470 mV vs SCE. Peak (a) in figure 6.2. occurs at -1659 mV. Such differences are likely to be ascribed to the pre-treatment of the electrode surface and the form of Cd used. A number of mechanisms have been proposed for the monolayer formation of CdS in this region. These have been based on the random absorption of anions from solution on the electrode surface. Birss *et al* [20] suggest that the initial stages of film formation are based upon the deposition of half a monolayer of S^{2-} ions on the Cd surface followed by charge transfer step according to reaction 6.7.

$$2Cd + S^{2-}_{ads} \rightleftharpoons \begin{matrix} Cd \\ Cd \end{matrix} \diagup\!\diagdown S + 2e^- \qquad (6.7)$$

The authors propose that following CdS formation by a simple random 2-dimensional deposition, lateral repulsion between adjacent surface ions induces a place exchange reaction to occur. This turnover occurs by the exchange of positions of the underlying cadmium ions and surface sulfide ions. With increasing anodic charge density, it was found that the stripping peak shifted towards more negative deposition potential. This was attributed to the formation of a more stable and transformed CdS film. Arvia *et al* [22] postulated a similar mechanism based on the competitive adsorption of S^{2-} *and*

OH^- at the Cd surface followed by an electron transfer step. This is illustrated in reactions 6.8 and 6.9.

$$Cd + OH^- \leftrightarrow Cd(OH^-)_{ads} \quad (6.8)$$

$$Cd(OH^-)_{ads} + HS^- \leftrightarrow Cd(S^{2-})_{ads} + OH^- \quad (6.9)$$

Based on the *p*H at which both these studies were made (*p*H 14) it is not clear why Birss *et al* [20] have not considered the role of the complex oxide-hydroxide layer on the electrode surface in devising mechanisms for film growth. Ultimately film formation results from charge transfer between cadmium atoms and adsorbed sulfide ions. However absorbed hydroxide species at the metal surface are also likely to be involved in the steps leading to CdS formation. However, the difficulty is in proving the existence of these species by voltammetric techniques. Breiter and Vedder [25] have used *in-situ* infra-red measurements to determine the potentials at which different forms of $Cd(OH)_2$ grow on a cadmium surface. No attempts have as yet been made to investigate the early stage of anodic CdS growth by *in-situ* spectroscopic methods.

(b) **Plateau region**.

Extending the anodic limit leads into region (b) or the plateau region. Owing to the high electric field strength in the film, it is assumed that thickening of the layer proceeds via a high field growth mechanism. Several theories have been proposed to explain growth in this region. Peter [21] has shown that the well known theories of anodic film growth as studied in for example the growth of oxide films on Fe, Pt, or Au, can be applied successfully to the CdS system. Of particular interest here is the idea of a place exchange mechanism involved in film growth. In the case of oxide films on iron electrodes, Sato and Cohen [26] proposed a model of film thickening that assumes a simultaneous exchange of metal and oxygen atoms takes

place on the electrode surface. This represents a bulk exchange reaction, although Vetter and Schultze [27,28] have considered place exchange for oxides on Pt and Au but only for a few surface layers. Due to the thick native oxide layer present on cadmium, a chemical place exchange reaction may be important during the initial stage of CdS growth on an oxide covered electrode surface

(c) **Transpassive Region.**

In figure 6.2 the transition from (b) to (c) is identified by the sharp rise in current. This corresponds to accelerated growth of CdS due to localised breakdown associated with high field strengths which permit ion movement through the insulating film. After prolonged deposition times, dull orange patches appeared on the highly textured electrode surface. After removal of the electrode from the solution the anodised layer was easily removed from the metal surface under a stream of water. The explanation for these effects lies in the breakdown mechanisms of the film. At high field strengths there becomes a point where film cracking occurs due to dielectric breakdown (see chapter 2.10.5)

Although the processes that lead to the formation of a stable porous film are not well understood, a number of authors have suggested tunnelling may be responsible for pore formation. Peter [21] suggests that under sufficiently high band bending electrons are able to tunnel from the valence band to the bulk leading to the formation of a high density of holes which react as follows.

$$CdS + h^+ \rightarrow Cd^{2+} + S \qquad (6.10)$$

$$Cd^{2+} + HS^- \rightarrow CdS + H^+ \qquad (6.11)$$

If the extent of reactions 6.10 and 6.11 vary across the electrode surface then a local change in the dissolution of CdS and subsequent migration of Cd^{2+} ions will

lead to inhomogeneous film growth. It is likely that the dull orange regions observed on the electrode surface contain sulfur resulting from reaction 6.10.

(d) Reductive Region.

At potentials beyond -1.5 V (region (d)), reduction of the CdS film takes place. For controlled depositions, prior to the anodic going scan, all electrodes were held at this potential for approximately 60 seconds to strip CdS present on the electrode surface. At open circuit potential a light yellow film forms rapidly on the electrode surface due to corrosion of the substrate by oxygen forming CdS. Figure 6.4 shows the second and third potential cycles recorded following the single potentiodynamic trace plotted in figure 6.4. In the second scan (solid line) the anodic limit was extended to +5.6 V examine the effects of film breakdown.

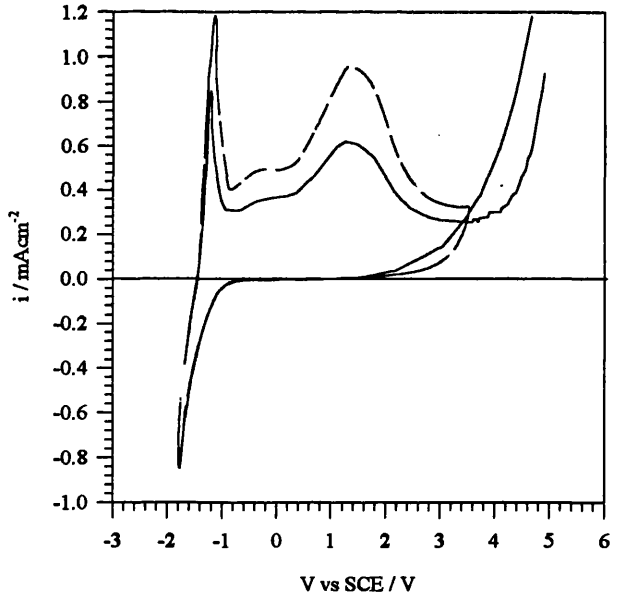

Figure 6.4. Current-voltage behaviour for Cd in 0.5 mol dm^{-3} Na_2S (unbuffered) during a single scan into the oxygen evolution region (solid line) and after a subsequent scan up to the transpassive region (dashed line).

After scanning past the transpassive region the current decreases as film growth ceases (solid line). The onset of an increasing current with small potential

fluctuations beyond 6 V is due to pitting corrosion of the surface leading to fractures in the film structure. The significant hysteresis observed between the anodic going and cathodic going scans suggests the surface has changed considerably during the potential cycle. If the scan is continued and the anodic limit is set within the transpassive region (dashed line), a large increase in the "monolayer" peak is observed for the pitted surface. Integration of the area under the first peak (solid line) gives a charge density of 629μC/m^2, corresponding to a ≈ 65% increase in charge density over the peak recorded in figure 6.2. However, it is important to include the effects of surface roughness associated with the layer of CdS grown following the 1st scan in figure 6.2. Assuming a value of 2 [21], the first monolayer peak (solid line) in figure 6.4 corresponds to just over a monolayer of CdS. However, after potential cycling into the pitting regime, the charge associated with monolayer coverage increases to 692 μC/m^2. From an estimation of the increase in surface roughness due to pitting corrosion, this corresponds to a ≈10% increase in available surface area for growth. Pitting of the electrode surface was clearly evident after the electrode was removed from the deposition cell on the second scan at peak (d), but prior to peak (a). It therefore follows that the anodic growth of CdS has severe limitations in obtaining films of useful thickness. Any film approaching a useful thickness will be porous and prone to cracking.

Figure 6.5 illustrates the various stages involved in the anodic growth of CdS on Cd for a complete voltammetric scan. These are:

(a) Anodisation of cadmium metal yielding Cd^{2+} ions. Electrons move to the back contact and are responsible for the anodic current flow.

(b) Chemical reaction between S^{2-} ions in solution with Cd^{2+} ions at the electrode surface to form a smooth compact film. At higher field strengths nodules of CdS form at the film surface

(c) Reduction of the CdS film giving cadmium and S^{2-} ions

(d) The surface roughness of the electrode increases as Cd atoms do not return to their original sites.

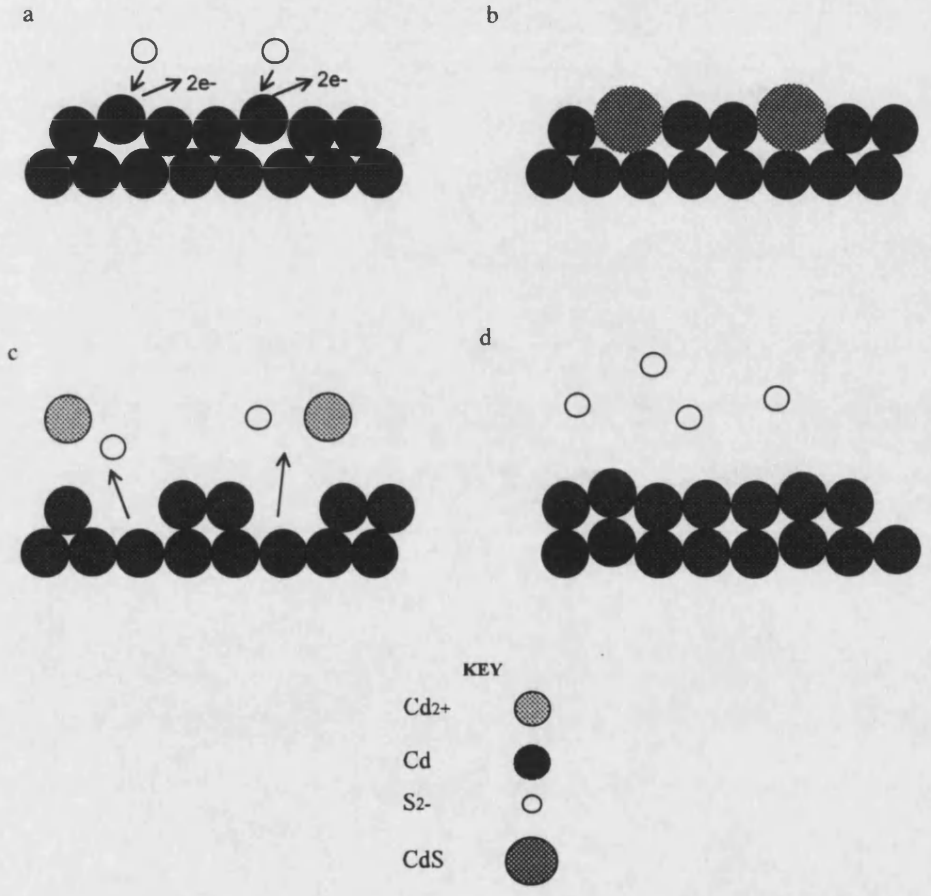

Figure 6.5. Growth mechanism for anodically grown CdS on Cd after a single voltammetric scan

6.3.2. Photocurrent Spectroscopy

Figure 6.6 illustrates the effect of illumination on the anodic growth of CdS.

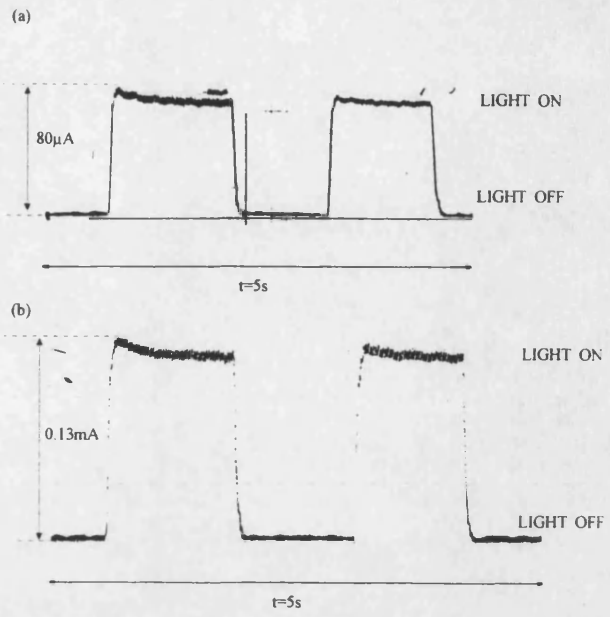

Figure 6.6. Photocurrent-time transients recorded using the SMSC technique. The sample was periodically illuminated at a frequency of 15Hz. The electrode was held at (a) 0.2V and (b) 0.6V.

To examine the photoactivity of the as-grown layer, the photocurrent behaviour of electrode under periodic illumination was determined. The sample was illuminated with a 120W white light source chopped mechanically at 15Hz. Potentials were chosen where appreciable photocurrents could be measured, i.e. at the end of the plateau region (a) and well into the transpassive region (b). The photocurrents measured at 0.2 V and 0.6 V were 80 μA and 0.16 mA, respectively. However, only very small (few nA) and unstable photocurrents could be obtained in the range -1 V to 0 V. The poor signal is likely to reflect the defective nature of the deposit grown during the early stages of anodisation in which the photorepsonse is dominated by recombination effects.

In figure 6.6, the "light off" situation corresponds to the anodisation of Cd in the dark. In the "light on" case, periodic illumination of the CdS film results in an increase the current in both the plateau and transpassive regimes. To understand the origin of this photoeffect we must consider the process of film growth and charge carrier generation within the growing layer. During anodic

growth the dissolution of cadmium ions and subsequent reaction with sulfide ions in solution is a two electron process. This is the dark or growth current measured during film formation. However, upon illumination the chopped response suggests that light modulates the growth process, namely by the creation of electron hole pairs which influence the ionic growth currents associated with electrochemical anodisation of cadmium. Of particular interest are the photogenerated holes. These move to the film electrolyte interface and can participate in the following reactions.

$$HS^- + h^+ \rightarrow S + H^+ \qquad (6.12)$$

$$CdS + h^+ \rightarrow Cd^{2+} + S \qquad (6.13)$$

$$Cd^{2+} + HS^- \rightarrow CdS + H^+ \qquad (6.14)$$

It is therefore important to consider the corrosion of CdS under illumination. In the extreme case, under sufficiently high light intensities, photodecomposition can completely retard film growth.

(i) Photocurrent measurements made on pre-treated Cd foils

The method of Breiter and Vedder [25] was adopted for the preparation of polycrystalline foils prior to anodic CdS deposition. This involves a chemical etch (2s, 50% HNO_3) followed by a chemical polish (5s, H_2O_2: CH_6CH_2COOH, 1:1), and finally a crystallite revealing etch (2s, 0.1 mol dm^{-3} HCl). The photocurrent response for CdS deposited on (a) untreated (b) chemically etched and (c) chemically etched and polished cadmium substrates have been compared along with the response obtained for single crystal CdS (S-face) (E_g=2.42 eV) [29].

Photocurrent spectra were obtained at five different potentials, (-1400, -800, 0, +800, +1400 mV vs SCE). In each case films were grown for 60 seconds. Data acquisition times were typically 45 seconds. The arrows on the graph in figure 6.2 correspond to the regions in the i-V curve where photocurrent action spectra were recorded. Bandgap values for each potential were determined by extrapolation of the band edge to zero photocurrent. However, this method is subject to uncertainties owing to the exponential decay of the band edge towards longer wavelengths. The rising linear portion of the curve was therefore used to estimate E_g. The slope associated with the extrapolation has also been compared with the sharp onset observed in the photocurrent response for single crystal CdS. At potentials close to the monolayer region difficulties were encountered in recording spectra owing to the very low photocurrents produced. In this case values for the band gap have been omitted from tables 6.2 - 6.5.

It is also important to be aware of light scattering effects at the surface of nodular CdS films. If less than 100% of light reaching the electrode surface is involved in charge carrier generation, uncertainties may be introduced into the calculation of the photocurrent conversion efficiency

(a) Untreated.

Cadmium foils were cut from a larger sheet which was dark grey/silver in colour. It is likely a thick native oxide layer is present on the metal surface. Figure 6.7 is a SEM micrograph taken of an untreated cadmium foil surface at x1,500 magnification. Cadmium sheet is formed industrially by cold pressing. During sheet formation, molten cadmium is poured into a press where it is rolled out as a sheet as it cools. This leads to a highly irregular and contaminated surface. The

surface also contains an appreciable density of surface residues which were unremoved by extensive rinsing with water.

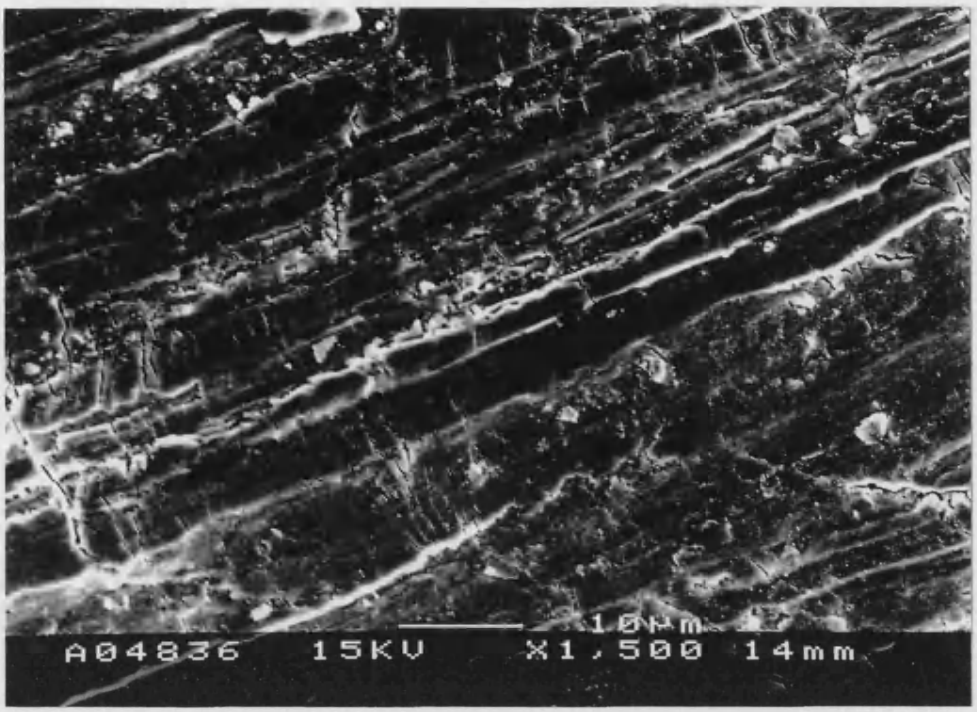

Figure 6.7.Scanning electron micrograph of untreated cadmium foil obtained under x1,500 magnification

Figure 6.8 shows the photocurrent spectra recorded for the same sample. Interestingly the highest photocurrent efficiencies were obtained for CdS grown on untreated foils. This may seem anomalous as the slope is significantly depressed and extensive tailing is found in the red part of the spectrum. An explanation for the high conversion efficiency may lie in the lie in the presence of a thick oxide layer covering the untreated metal surface. In the presence of sulfide ions this may undergo a chemical exchange of O^{2-} by S^{2-} yielding a compact and homogeneous layer of CdS. This will be thermodynamically favourable as the $\Delta G_f°$ value for CdS is more positive than that for CdO.

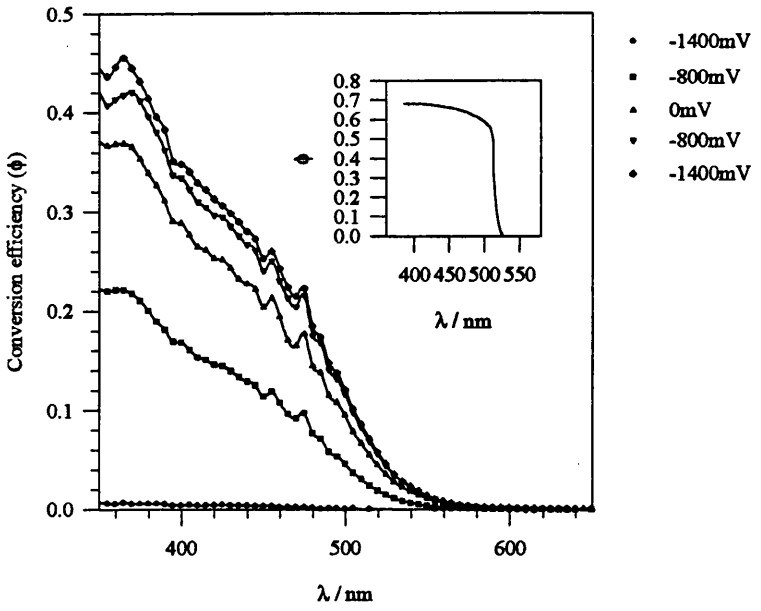

Figure 6.8. Photocurrent spectra recorded over a range of applied dc potentials for anodically grown CdS on untreated Cd foil (Anodisation time = 60 s, Data acquisition time = 45 s). The inset shows the photocurrent response obtained for single crystal CdS (S-face) in 0.5 mol dm^{-3} Na_2SO_3 at V_{dc} = 0mV

To determine whether the thin layer of CdS formed at open circuit potential results from a sulfide exchange reaction involving CdO or, is a result of the corrosion of cadmium by dissolved oxygen in solution, the electrolyte was degassed with nitrogen for 60 minutes. After immersing the cadmium foil in the sulfide solution, a thin yellow film formed on the electrode as was found in the air saturated solution. The most likely mechanism is therefore the exchange of O^{2-} by S^{2-} in CdO. Depending on the thickness of the native oxide layer, it could be speculated that the sulfide exchange reaction is incomplete, i.e. a range of solid solutions are formed consisting of both O and S from the substrate through to the film/electrolyte interface. For a compact film such as that formed at the open circuit potential, the possible graded composition of the layer is illustrated in figure 6.9. This has been illustrated by assigning arbitrary stoichiometries to each

layer. It is possible that charge transfer through this layer is an efficient process due to the lack of recombination centres associated with an abrupt change in phase.

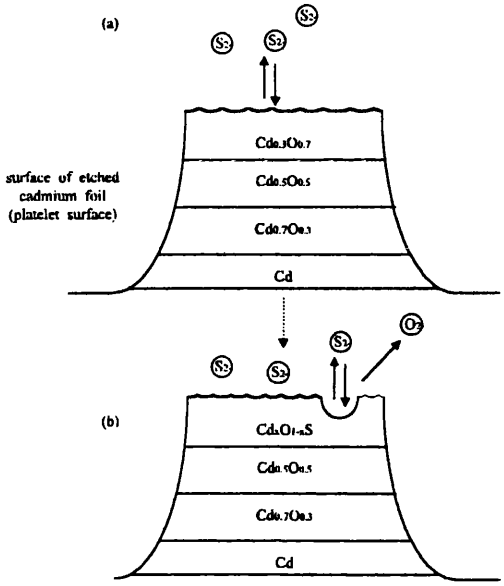

Figure 6.9. Schematic representation of the mechanism for sulfide ion incorporation in the oxide layer on cadmium. The stoichiometries shown are only for the purposes of illustration.

Of all the substrate preparations, the untreated case gives the lowest value for the band gap of CdS. The fact that high photocurrent conversion efficiencies are obtained may therefore seem surprising. If we associate band gap narrowing with the impurities and deviations from stoichiometries of the film, then it appears these properties are not detrimental to the overall quantum efficiency of the deposit. The trend observed in the variation of the maximum photocurrent efficiency with dc potential is the same for CdS grown on all substrates. Bandgap values obtained by extrapolation of the rising portion of the band edge are given in table 6.2.

V_{dc} *vs* SCE / V	E_g / eV
-1.4	-
-0.8	2.66
0	2.28
+0.8	2.27
+1.4	2.27

Table 6.2. Values for the band gap derived from figure 6.8.

(b) **Chemically etched**

The grain structure of cadmium was revealed by a chemical etch. The etch dissolves metal away from the surface in a non-uniform manor revealing crystalline regions of differing orientation. After etching the electrode, the surface was bright and reflecting. An SEM micrograph of the highly textured surface is shown in figure 6.10. The irregular grain morphology results from local variations in the nucleation and growth of the metal phase whilst cooling during sheet formation. Of particular interest here are the darkened regions between adjacent crystallites. These are grain boundaries and arise where two lattices of differing orientation meet. Bragg and Burgers [30] introduced the idea that such boundaries between crystals of the same orientation may be considered as an array of dislocations. However, more complex arrays of dislocations arise where there are large angles or misfits between grains.

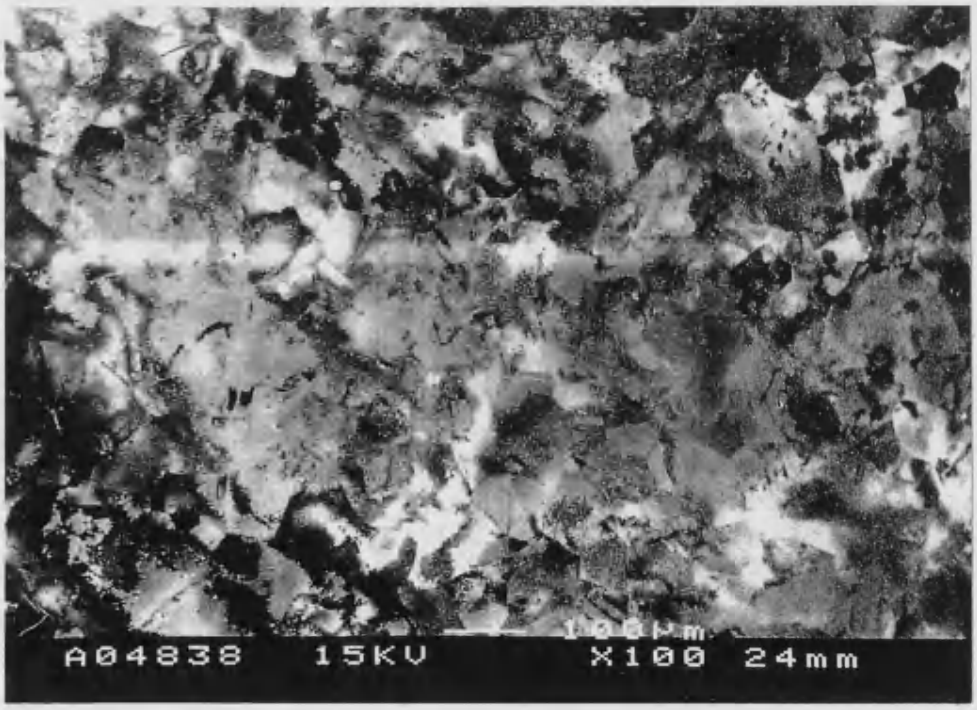

Figure 6.10 SEM micrograph of chemically etched cadmium foil under x100 magnification

The photocurrent spectra given in figure 6.11 shows that etching of the substrate substantially sharpens the band edge and shifts the band gap closer towards the value obtained for single crystal CdS. Photocurrent conversion efficiencies are similar to those grown on untreated Cd foils. Of particular interest is that saturation observed in the photocurrent response occurs at wavelengths below 500nm.

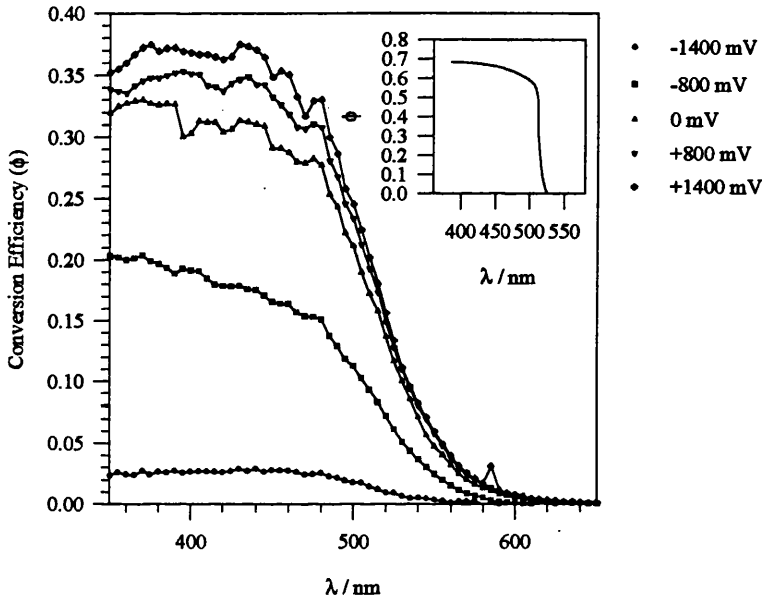

Figure 6.11. Photocurrent spectra recorded over a range of applied dc potentials for anodically grown CdS on chemically etched Cd (Anodisation time = 60 s, Data acquisition time = 45 s). The inset shows the photocurrent response obtained for single crystal CdS (S-face) in 0.5 mol dm^{-3} Na_2SO_3 at V_{dc}=0 mV

According to Peter [3], this behaviour is associated with a highly doped film, where during the early stages of film growth, very high doping densities (up to 10^{24} m^{-3}) result in a decrease in the width of the space charge region until it is smaller than the penetration depth of the incident light. The conversion efficiency therefore decreases as charge carriers generated outside the space charge region recombine. However, for thicker films grown in the transpassive region, more stoichiometric

deposits with lower donor densities are expected. In which case, the space charge region should extend across a significantly larger portion of the film. From figure 6.3, as saturation is independent of film thickness, the quantum yield appears not to be limited by the width of the space charge layer. What is more likely is that recombination is responsible for the observed flattening in the spectral response. Comparing values of the band gap to the saturation wavelength suggests a high density of centres responsible for recombination are located ≈ 0.6 eV above the conduction band. Listed in table 6.6 are values of the bandgap derived from photocurrent spectra recorded for CdS grown on eched Cd foil

V_{dc} *vs* SCE / V	E_g / eV
-1.4	2.20
-0.8	2.60
0	2.24
+0.8	2.24
+1.4	2.24

Table 6.6. Values for the band gap and slope derived from figure 6.11.

(c) Chemical Etch and Polish

Figure 6.12 shows the photocurrent spectrum for CdS grown on a chemically etched and polished Cd substrate.

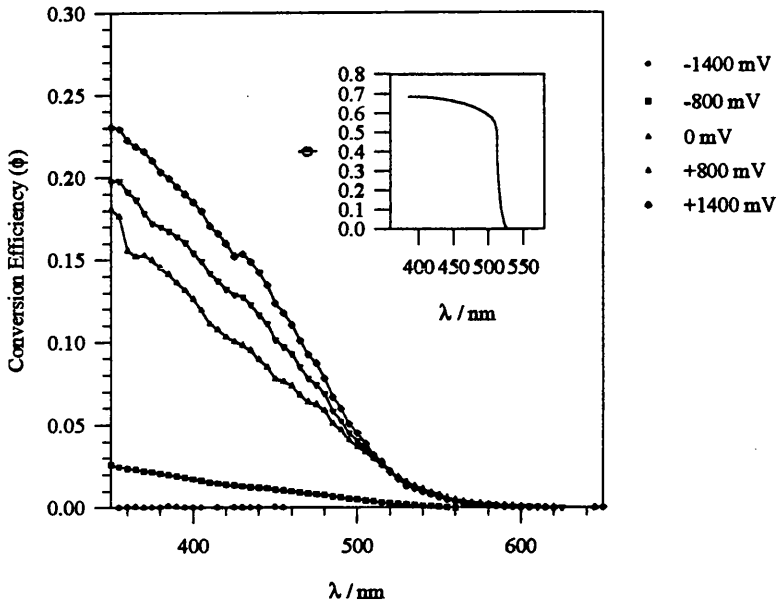

Figure 6.12. Photocurrent spectra recorded over a range of applied dc potentials for anodically grown CdS on chemically etched and polished cadmium. (Anodisation time = 60 s, Data acquisition time = 45 s). The inset shows the photocurrent response obtained for single crystal CdS (S-face) in 0.5 mol dm^{-3} Na_2SO_3 at V_{dc}=0mV

As in the case for anodised films grown on untreated cadmium foils, the photocurrent increases monotonically, and does not appear to saturate at wavelengths down to approximately 650nm. The values for the band-gap further improve towards those obtained for single crystal CdS and are listed in table 6.4.

V_{dc} *vs* SCE / V	E_g / eV
-1.4	-
-0.8	2.16
0	2.26
+0.8	2.41
+1.4	2.62

Table 6.4. Values for the band gap and slope associated with figure 6.12.

Of particular significance is the absence of a well defined photocurrent onset and reduced quantum yield compared with CdS grown on chemically etched foils. This

strongly suggests that enhanced recombination effects dominate the photoresponse. The surface obtained after chemical etch and polish steps is shown in figure 6.13. The most noticeable feature is the emergence of a microcrystalline structure and poorly defined steps or ridges which extend across the electrode surface. If during anodisation the morphology of the growing layer replicates the microcrystalline structure of the underlying substrate, the associated high density of grain boundaries are likely to act as recombination centres for photogenerated charge carriers. Light scattering effects may also be enhanced at films grown in the transpassive region if the Cd microtexture promotes growth of a high density of nodular CdS.

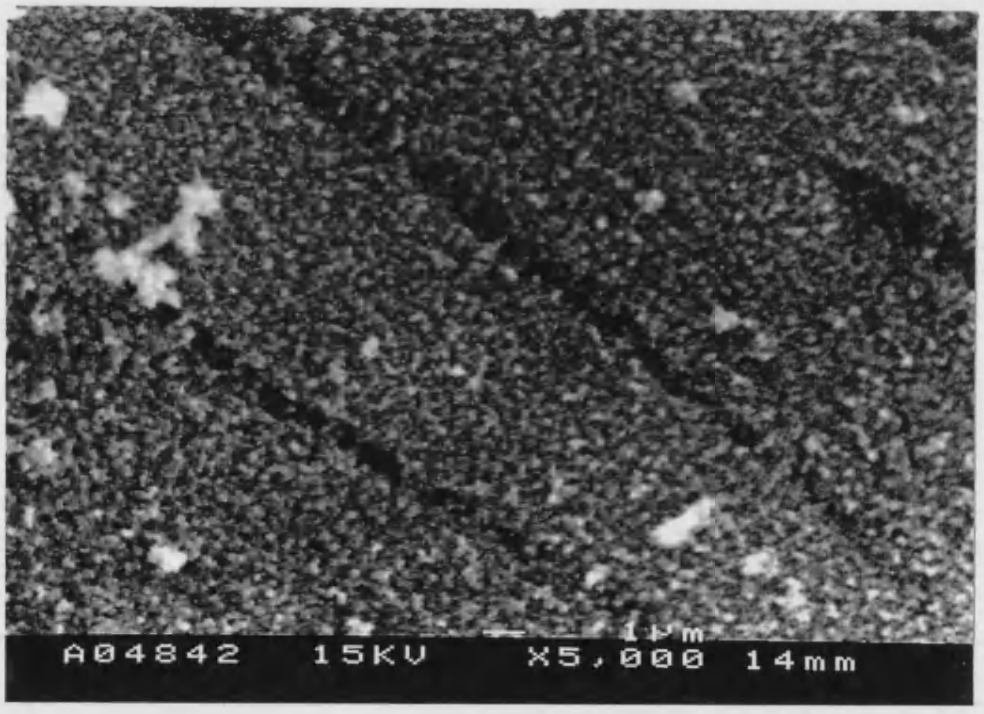

Figure 6.13. SEM micrograph of chemically etched and polished cadmium foil under x5000 magnification

(d) Chemical Etch, Polish, and Reveal

Illustrated in figure 6.14 is the photocurrent response for CdS grown anodically on a chemically etched, polished, and revealed Cd foil

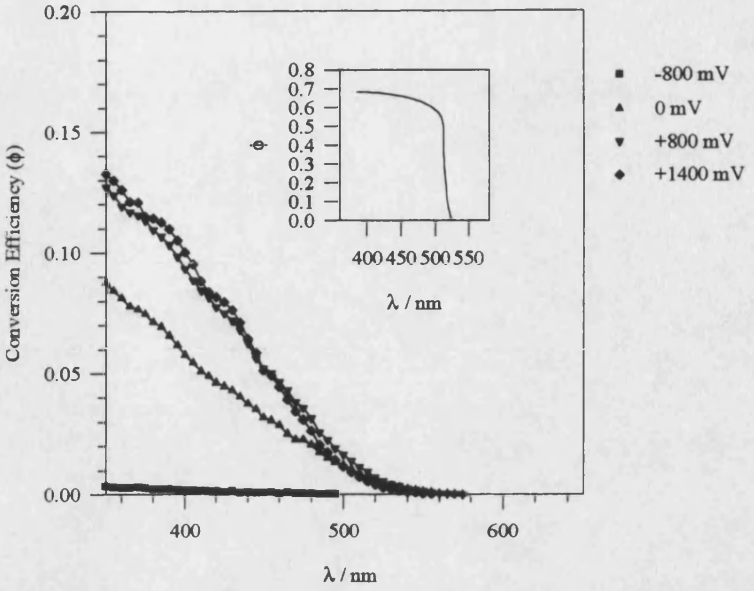

Figure 6.14. Photocurrent spectra recorded over a range of applied dc bias for anodically grown CdS on a chemically etched, polished, and revealed Cd foil. (Anodisation time = 60 s, Data acquisition time = 45 s). The inset shows the photocurrent response obtained for single crystal CdS (S-face) in 0.5 mol dm^{-3} Na_2SO_3 at V_{dc}=0mV

From table 6.5 it can be seen that band gap values are very close to those for single crystal CdS (E_g=2.42 eV), especially for the thicker films grown in the transpassive region.

V_{dc} *vs* SCE / V	E_g / eV
-1.4	-
-0.8	-
0	2.66
+0.8	2.69
+1.4	2.44

Table 6.5. Values for the band gap and slope associated with figure 6.14.

In comparison with films deposited on untreated Cd foil, these appeared less orange in colour. Interestingly for CdS thin films deposited on tin oxide coated glass in the chemical bath process, annealing in air results in a change in change

from light yellow to orange. This has tentatively been attributed to the presence of oxygen sites within the film [35]. Hence in the untreated case O^{2-} remaining from CdO may in part with other impurities be responsible for the orange colour of the film. In comparison with previous treatments, the dilute HCl etch further develops the substrate morphology to reveal an extremely well defined surface composed of a wide variety of crystallographic features.

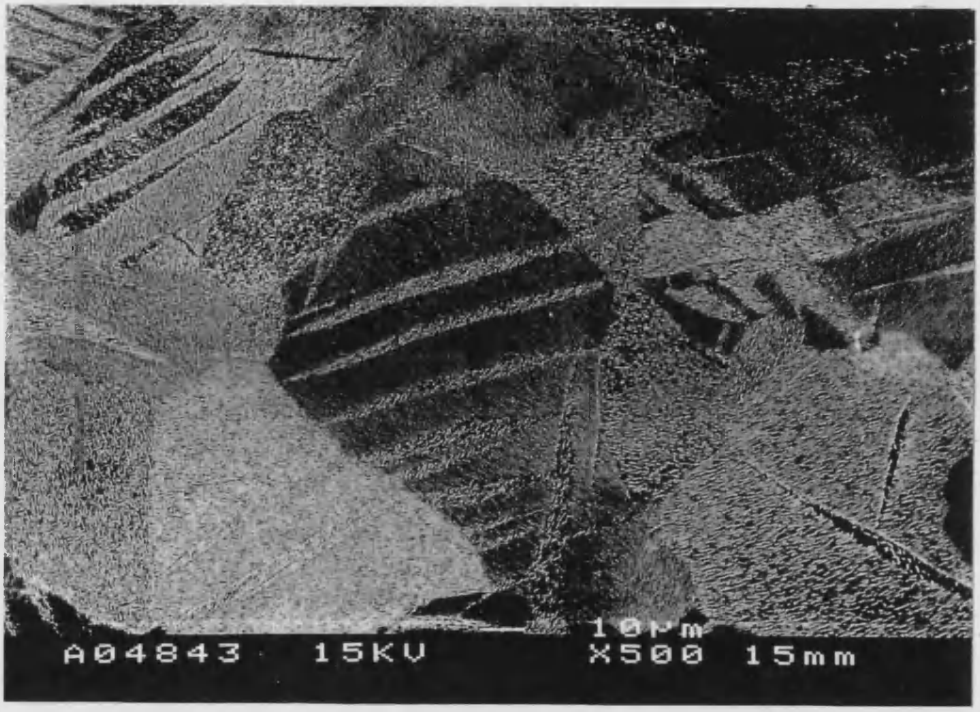

Figure 6.15. SEM micrograph of chemically etched, polished and revealed cadmium foil under x500 magnification

Figure 6.16 is an SEM image obtained of the same surface at higher magnification showing an individual grain created by the boundaries of other crystalline regions. Each area is composed of closely packed sheet-like structures which have a slightly undulating surface morphology. Within a single grain, these sheets stack horizontally and appear to face the same direction, whereas between adjacent grains their stacking orientation differs. This probably reflects their differing crystallographic orientation. Similar features are seen on etched titanium surfaces [8].

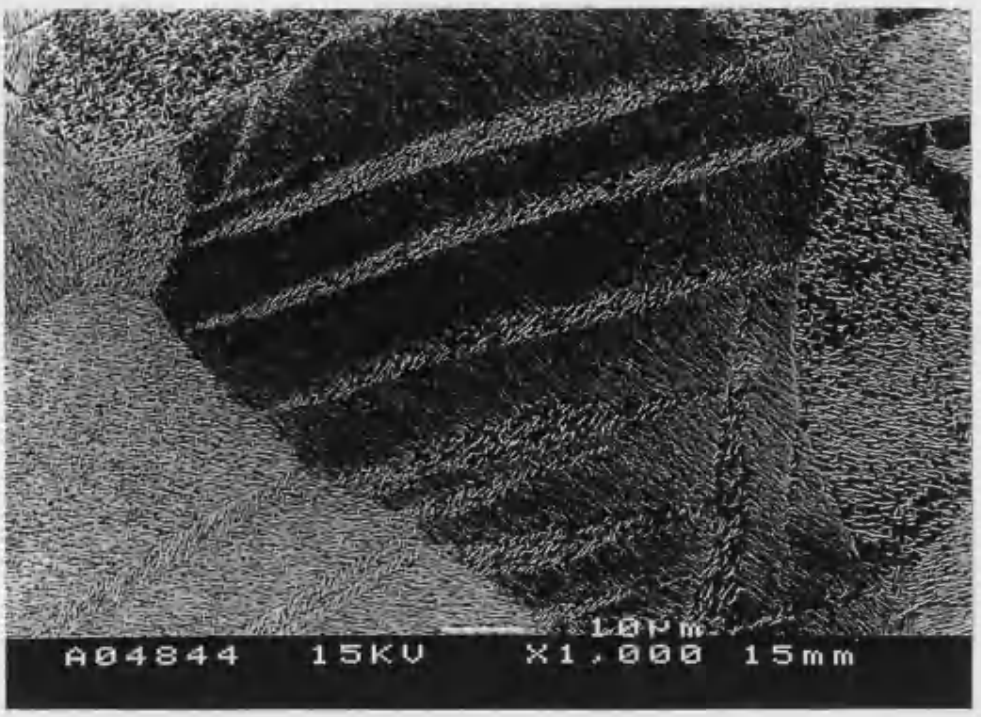

Figure 6.16. SEM micrograph of chemically etched, polished, and revealed cadmium foil under x1,000 magnification

To determine the orientation of the individual crystallites, electron diffraction measurements would have to be made. In both SEM and optical images of the cadmium surface, individual regions appear either light or dark due to the differing scattering effects of either of electrons in the case of the SEM or light in optical imagesat different features across the electrode surface. In a similar fashion to CdS films grown on chemically etched and polished Cd foils, the increased intricacy of the surface and presence of grains of differing orientation suggests anodisation will result in the growth of a particularly disordered layer of CdS. If the main criterion for choosing substrate pre-treatments for the growth of CdS was the band gap (relating to the stoichiometry) of the material, then chemical etch, polish, and reveal treatments would be prescribed, as values of E_g close to that obtained for single crystal CdS were obtained. However, in terms of their photocurrent conversion efficiency, the same CdS films appear to be the least desirable. The origin of this lies in the influence different substrate morphologies

have on promoting the growth of defective CdS in which recombination effects can occur. Therefore, it is important to consider the mechanisms involved in CdS film formation. The growth of CdS during anodisation at the highly intricate surface of chemically etched, polished, and revealed Cd is discussed as follows.

In figure 6.16 the most noticeable feature of the Cd electrode is the plate like structure, i, which extends across the surface of crystallite a. This is known as a twin and occurs as the result of stresses applied to the metal during its processing [32]. In twinning, the atoms within the crystallite are realigned as new crystallites. This produces the original structure but with a new orientation. Figure 6.17 illustrates a how a twin may be produced by a simple movement of atoms.

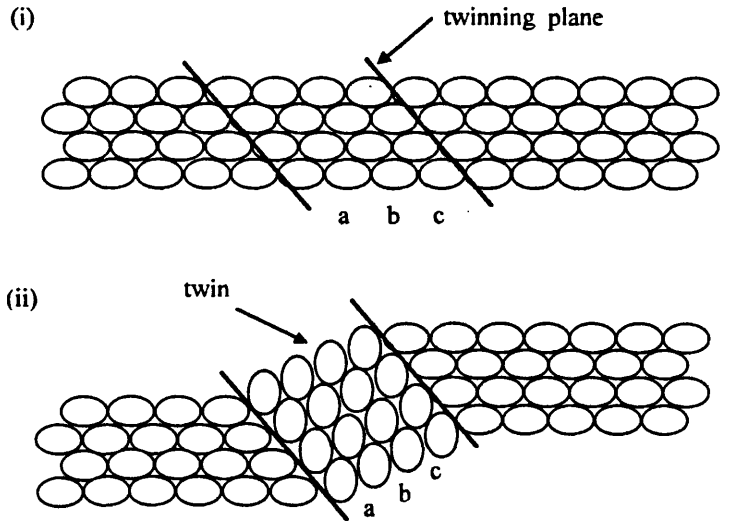

Figure 6.17. Twin formation due to movement between atomic layers.

In the SEM image it is evident that orientation of i is identical to that of crystallite b. A further observation is that the crystalline structure in this region appears to rise and fall at these twins. This distortion is due to the strain produced when two crystallites of differing orientation meet.

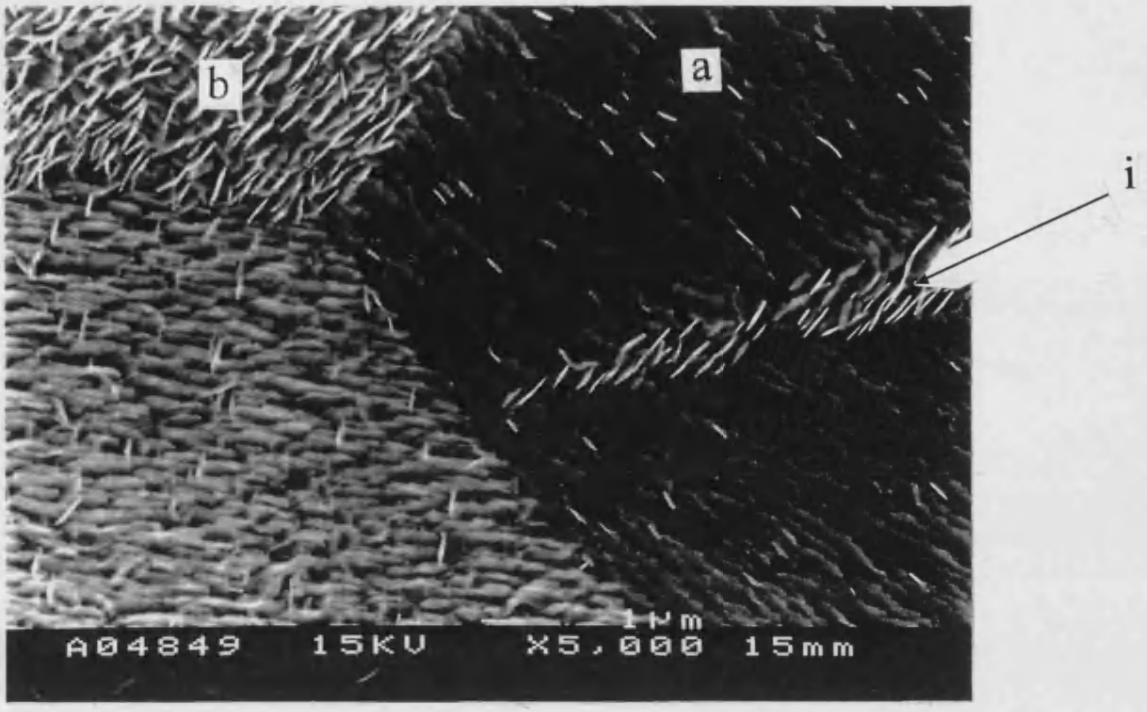

Figure 6.18. SEM micrograph of chemically etched, polished, and revealed cadmium foil under x5000 magnification

Illustrated in figure 6.18 is the intersection adjoining 3 crystallites of differing orientation. The bright region running through the darkest crystallite is a single twin. Figure 6.19 shows a high magnification image of the undulating sheets which comprise the bulk substrate structure.

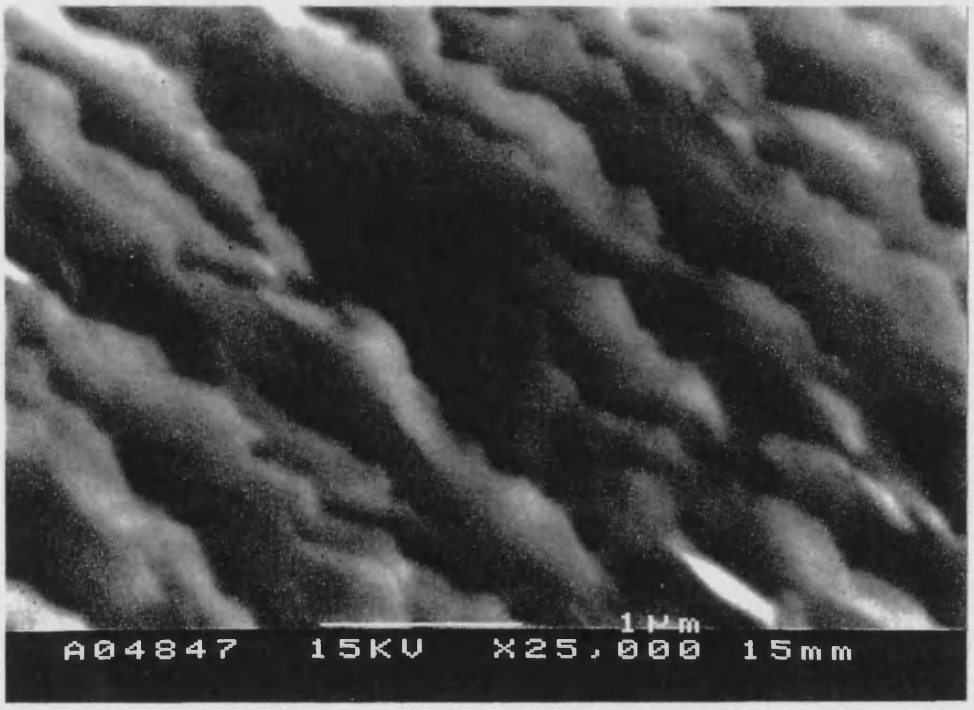

Figure 6.19. SEM micrograph of chemically etched, polished, and revealed cadmium foil under x25,000 magnification

During the early stages of nucleation and growth on an anodic film a thin continuous layer of insulating material is formed at the electrode surface. As these films are insulating, the only way that growth can continue is if ions migrate through the solid phase. From the SEM image of the undulating platelets shown in figure 6.19, it is proposed that film dissolution proceeds at the regions of greatest curvature where field strengths are enhanced. A schematic representation of disssolution and CdS nodule formation are illustrated in figure 6.20 (a) and (b), respectively.

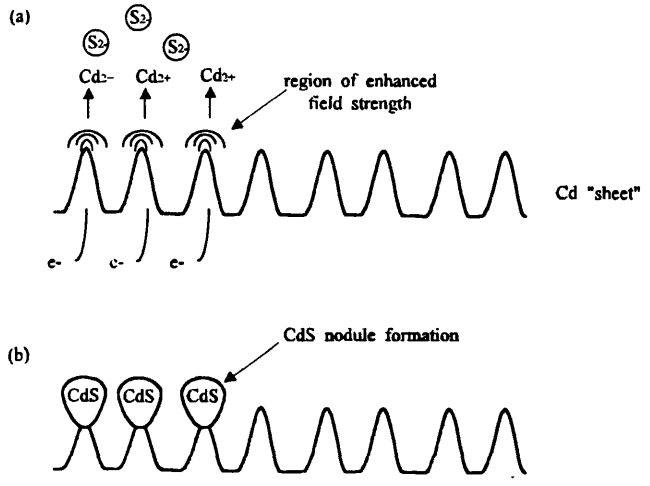

Figure 6.20. Schematic representation of (a) cadmium dissolution on the "sheet" surface and (b) subsequent nodule formation

If this process takes place across the entire surface, including at grain boundaries and twins, a particularly defective and rough surface will result, these parameters worsening if the field strength rises further resulting in dielectric breakdown and cracking of the film structure. It is proposed that extensive recombination of photogenerated charge carriers at these regions are responsible for the low quantum efficiency obtained for anodic films of CdS grown on chemically etched, polished, and revealed Cd foils.

The important influence of the underlying cadmium substrate on CdS film growth is clear, though it is evident that measurements made on the entire sample are not particularly informative in this respect. Localised photoelectrochemical measurements have shown that growth of CdS is clearly influenced at a microscopic level by substrate morphology. This is described in section 6.4.

6.3.3. Electrolyte Electroreflectance

Electrolyte electroreflectance measurements were made on CdS grown on chemically etched, polished, revealed cadmium foils. The SMSC set-up was employed but with incident light defocused so as to illuminate the entire sample area. The spectra recorded are plotted in figure 6.21.

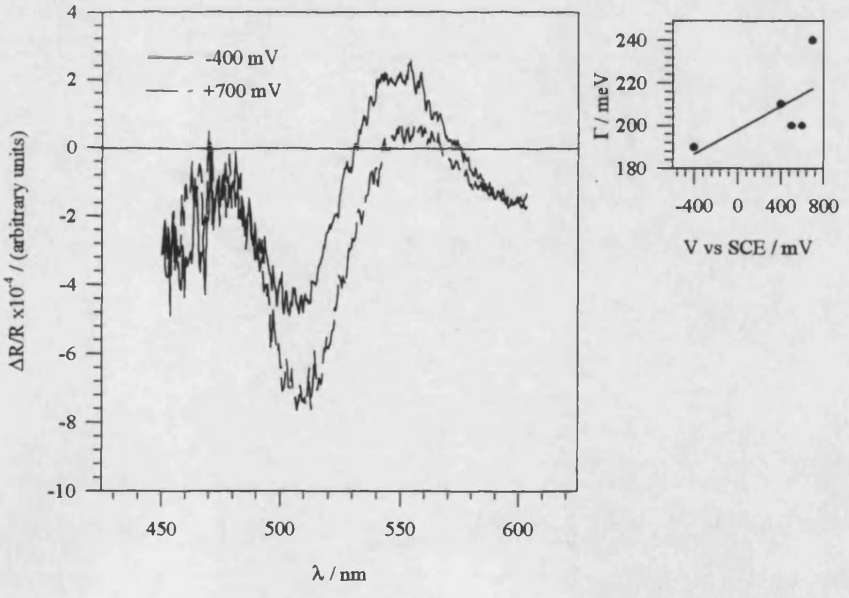

Figure 6.21. Electrolyte Electroreflectance spectra measured at different potentials for anodically grown CdS on Cd. The inset shows the variation in the broadening parameter with applied dc potential (V_{ac} = 150mV pk-pk, f = 270 Hz)

Table 6.6 gives values for the band gap (E_g) and broadening parameter (Γ / meV) determined by Aspnes [33] third derivative fitting function. Values for the band gap approach that for single crystal (E_g=2.42eV) as the electrode potential is made more positive. This was also found to be the case for values of E_g derived from photocurrent measurements.

V_{dc} *vs* SCE / V	E_g / eV	Γ / meV
-0.4	2.26	190
0.4	2.67	210
0.5	2.69	200
0.6	2.68	200
0.7	2.42	240

Table 6.6. Values for E_g and Γ determined by Aspnes [33] third derivative fitting function from EER measured for CdS deposited on a chemically etched, polished, and revealed cadmium foil.

The EER response for single crystal CdS is also given in figure 6.18. Of more interest is the broadening parameter, Γ, which is related to the crystallinity and defectiveness of the films. For single crystal CdS, $\Gamma \approx 50$ meV (see figure 5.10), whereas for the anodically grown films it is considerably higher. Comparing the thinnest to the thickest films obtained at -400 and +700 mV, respectively, the broadening parameter reflects a decrease in film "quality" with increasing film thickness. The band gap increases to a value very close to that for single crystal CdS. In the photocurrent analysis, it was suggested that an initially compact film of CdS was present up to the plateau region The values of the broadening parameter up to this region would seem to confirm this as at more positive potentials the more defective and porous film obtained is associated with higher values of Γ. The changes in broadening parameter therefore confirm the trends observed in the photocurrent results for growth under different applied dc potentials.

6.3.4. Localised Photoelectrochemical Imaging

The methods involved in the preparation and anodisation of cadmium foil prior to deposition were identical for the two imaging techniques. The mode of image acquisition has been used to describe the type of localised measurement made. The terms "direct" and "lock-in" detection refer to the PEM and SMSC techniques, respectively.

(i) Scanning Microscopy for Semiconductor Characterisation

Figure 6.22 (a) shows a video image taken of a chemically etched, polished, and revealed Cd foil in 0.5 mol dm^{-3} Na_2S. The boxed region represents the area scanned by the light spot to obtain the corresponding photocurrent image.

(a)

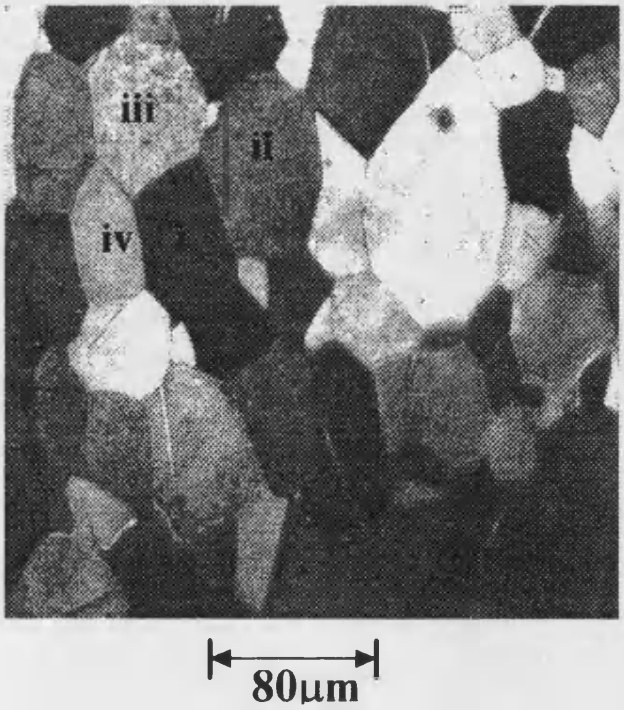

(b)

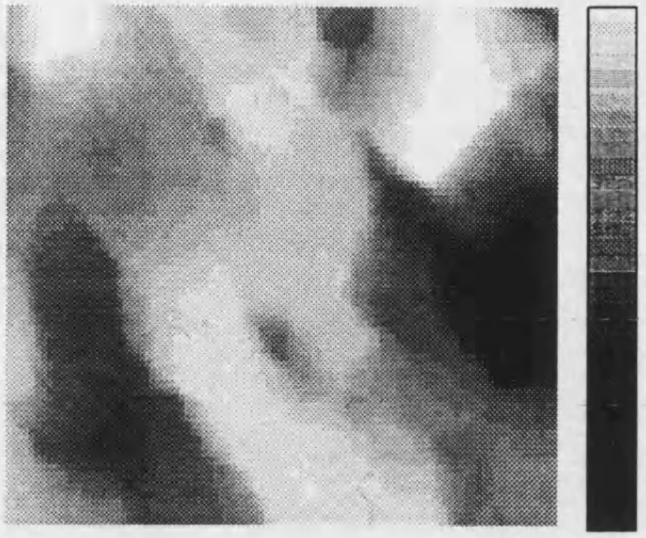

Figure 6.22. (a) Video image of the CdS/Cd electrode in contact with 0.5 mol dm^{-3} Na_2S (b) Photocurrent image of the same surface using monochromatic light of λ=514 nm at 0 mV vs SCE. Light "spot" diameter ≈6μm; f= 80 Hz. The scale bar on the right corresponds to 0 μA (black) and 125 μA (white).

Similarities between the crystalline morphology of the sample and the features seen in the SEM micrographs given in figures 6.15 and 6.16 are immediately apparent. However the microcrystalline texture of the individual grains suggests the surface was not fully revealed. The morphology is similar to the sample that was only chemically etched and polished. The corresponding photocurrent image is given in figure 6.22(b). The scale to the right of the image refers to the magnitude of the measured photocurrent over the range 0 μA (black) to 125 μA (white). Prior to obtaining the image, the sample was held at -1400 mV for 30 s to cathodically strip as much CdS from the electrode surface as possible. The potential was then ramped at 100 mVs^{-1} to 0 mV where the localised measurement was made. However, even after cathodic stripping a faint yellow layer remained on the surface. The only way the passive film could be stripped from the electrode surface was to scan the potential into the hydrogen evolution region. This was undesirable as gas evolution occurred rendering the electrode surface pitted. The

presence of this residual film leads to uncertainties in the determination of the total film thickness, i.e. the thickness determined from the charge passed during deposition excludes the presence of the initial passive layer. A number of interesting features are immediately obvious in the photocurrent. Firstly it appears that the photocurrent differs between individual grains across the electrode surface. Comparison of the video and photocurrent image reveals that areas of highest photocurrent correspond to the less reflective (darker) grains and regions of lower photocurrent correspond to the brighter, more reflecting areas. Under illumination, these regions appear light or dark due to scattering effects at their surface, the extent of which depends on their individual orientation. Scattering is an important phenomenon in localised measurements, especially if the whole electrode surface is photosensitive rather than the spot on which the laser is focused. For high magnification objectives necessary to achieve small spot sizes, scattering within the lens system and from the sample surface can illuminate a considerable area of the surface. Unlike the PEM system, the SMSC technique requires much time to be invested in ensuring an optimum focus of the laser beam at the electrode surface. The influence of scattering effects on photocurrent contrast will be discussed in section 6.3.4.

Comparing images (a) and (b) in figure 6.22, it appears that the photoresponse of the anodised CdS layer maps the grain structure of the underlying cadmium substrate. The main feature recognisable in both images is the central band of dark grains with a central brighter region formed from the inner edges of the surrounding grains. The brightest grain, (iv), evidently has the lowest photoresponse. Localised photocurrent voltammograms for the four regions were measured for a more quantitative description of the photocurrent distribution. The localised voltammograms were obtained by

"parking" the light spot on a given grain while the potential was scanned from -1400 mV to +400 mV at a scan rate of 250 mVs^{-1}. These are plotted in figure 6.23

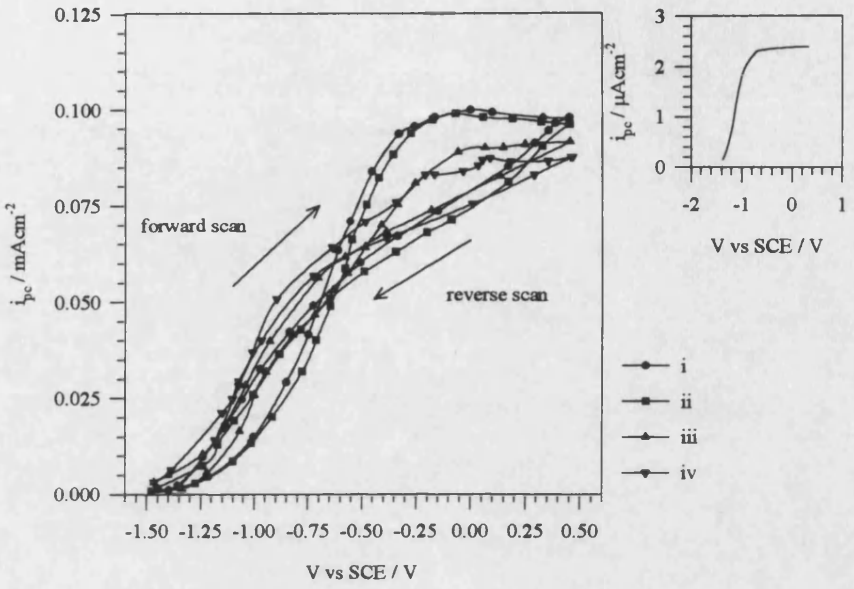

Figure 6.23. Localised photocurrent voltage curves for each of the regions (i) to (iv) labelled in figure 6.22 (a). Light "spot" diameter ≈ 6 μm; f = 80 Hz. The inset shows a photocurrent voltammogram for single crystal CdS (S-face) in 1.0 mol dm^{-3} Na_2SO_3 (λ=500 nm, f = 27 Hz).

Saturation in the photocurrent occurred at approximately +100 mV. The photocurrents measured at +400 mV were 0.087, 0.091, 0.096, and 0.099 μA for grains i, ii, iii, and iv, respectively.

The localised electrolyte electroreflectance response was determined for each of the four grains, also at 0 mV vs SCE. These are plotted in figure 6.24 (i) to (iv).

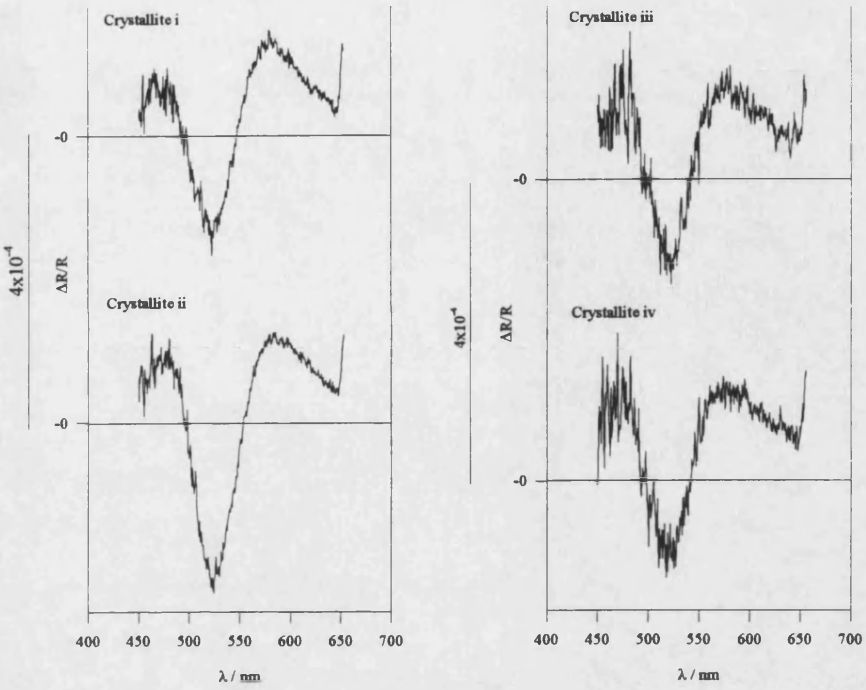

Figure 6.24 Electrolyte electroreflectance spectra measured at dc bias of 0 mV for grains (i) to (iv) in figure 6.22 (a). Light spot diameter ≈ 6μm; V_{ac} = 200 mV rms; f = 270 Hz.

Table 6.7 shows that the values for the band gap and broadening parameter determined using Aspnes [33] third derivative fitting are almost the same in the four regions. Based upon an assessment of the consistency of this determination, the accuracy of the fitting routine was found to be ± 0.08 eV for E_g and ± 4 meV for Γ. This suggests that EER is insensitive to variations in the properties of the photoactive layer that are responsible for the differing photocurrent intensity across the grains. The EER response indicates a relatively uniform coverage of CdS on each of the regions with respect to the stoichiometry of the deposit (as inferred from the band gap) and its crystallinity (as inferred from the broadening parameter).

	Crystallite i	Crystallite ii	Crystallite iii	Crystallite iv
E_g / eV	2.27	2.31	2.26	2.26
Γ / meV	247	250	230	237

Table 6.7. Values for the band gap (E_g) and broadening parameter (Γ) for grains (i) to (iv) illustrated in figure 6.22 (a). Light "spot" diameter ≈6 μm; V_{dc}= 0 mV; V_{ac}= 200mV rms; f= 270 Hz.

Not surprisingly, therefore EER images of the surface were featureless and of low contrast suggesting a uniform ΔR/R response over the anodised layer. The magnitude of the EER signals measured were typically $\Delta R/R = 10^{-6}$. Although at first the lack of image contrast was thought to be due to a problem of instrumental sensitivity at these detection limits, the fact that spot measurements could be obtained quite easily disproves this. Localised EER measurement have been made by a number of authors, although these have been performed on thick polycrystalline samples where their defect structure is better defined. Raccah *et al* [34] have measured localised EER spectra using a lock-in detection method to determine variations in composition for ternary semiconductors such as $Hg_xCd_{1-x}Te$ (MCT), with a spatial resolution of about 100 μm. Stoichiometries were determined based on the well known dependence of the energies of features in the EER spectrum on the composition x. It cannot be ruled out that variations in composition occur in the CdS films studies in this work, but at a resolution undetected by the size of the scanned light spot.

A video image of an anodised layer of CdS grown on a new sample is shown in figure 6.25 (a). In the boxed area two grains, i and ii, are separated by a darkened boundary. The surface of the upper grain appears smoother than the lower one which seems to have a slightly pitted surface. The unusual grain structure probably results from the thermal and stress induced crystallisation of the metal during manufacture and

corresponds to a rather extreme case of a boundary where two grains of widely differing orientation meet. Images (b) and (c) are enlarged photocurrent and reflectivity images of the two grains, i and ii. Unlike the video signal, the variation in the reflectivity across the surface could be obtained at the same time as the localised response by using the dual dc and phase sensitive inputs of the lock-in amplifier. Although the resolution of the reflectivity image was poorer than the video image, the former does reveal information on the topography of the surface as a result of light scattering effects. The most striking observation is that in the photocurrent image, the intensity on either side of the boundary is at its highest whereas at the boundary, the response is virtually zero. The reduction in photocurrent at the grain boundary is likely to reflect an enhanced rate of recombination at the defective region where two grains meet.

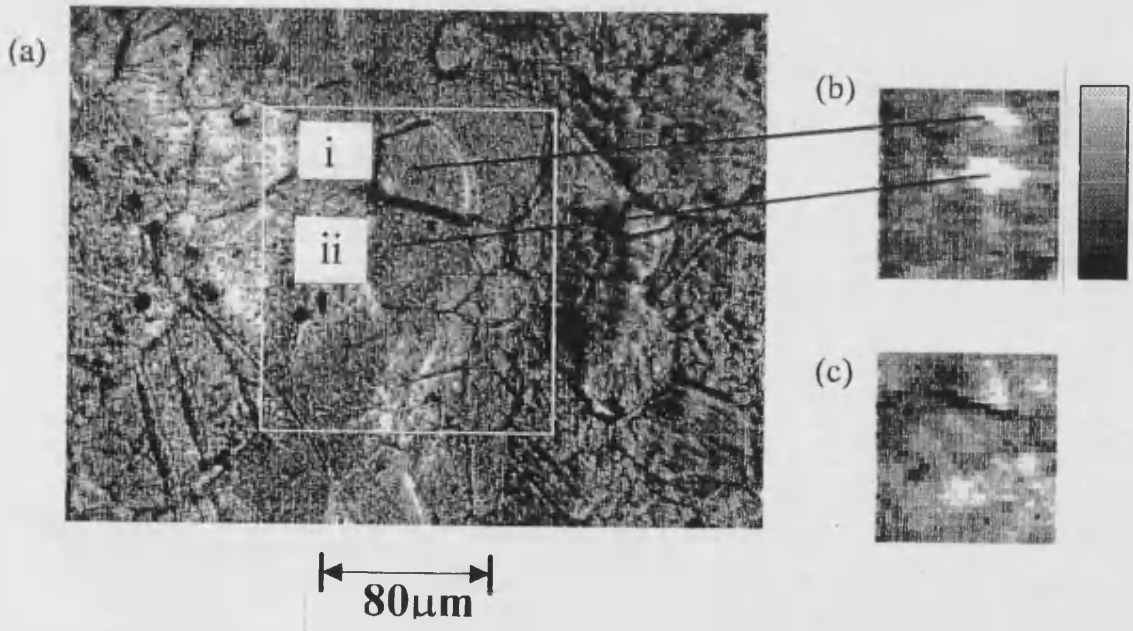

Figure 6.25. Video image of CdS/Cd electrode in contact with 0.5 mol dm^{-3} Na_2S (b) Enlarged photocurrent image of the grains i and ii obtained using monochromatic light of $\lambda = 514$ nm at 0 mV vs SCE. Light spot diameter ≈ 6μm; $f = 80$ Hz. The scale bar on the right corresponds to the magnitude of the photocurrent where 0 μA (black) and 125 μA (white). (c) Reflectivity image of the same region as in (b).

The effect of the underlying morphology on the substrate on photocurrent contrast was further investigated in the (a) reflectivity and (b) photocurrent images recorded in figure 6.26.

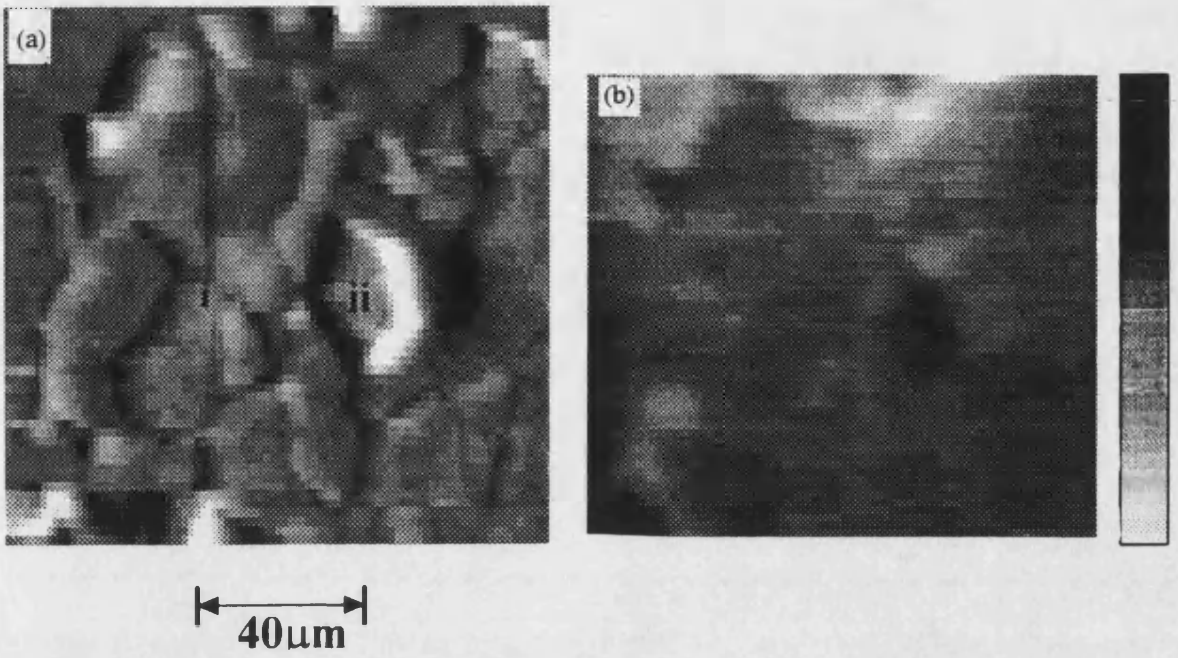

Figure 6.26 (a) Reflectivity image of anodised cadmium layer. (b) Photocurrent image of (a) obtained using monochromatic radiation of λ=514 nm at 0 mV vs SCE in 0.5 mol dm^{-3} Na_2S. Light spot diameter ≈8μm; f=80 Hz. The scale bar on the right corresponds to 0μA (black) and 125μA (white).

From the reflectivity image it appears the substrate is textured by intersecting grains across the electrode surface. The light and dark fringes around the area of the central six sided grain labelled (ii) are due to light scattering effects at the surface. In the corresponding localised image, (b) the photocurrent within the grain is considerably lower than in the surrounding region, (ii). (ignoring the artefact at the bottom left-hand corner of the image which was due to an error in the framestore). The photocurrent-voltage behaviour at (i) and (ii) was quantified by measuring localised photocurrent voltammograms from -1450 mV to +1450 mV at a scan rate of 100 mVs^{-1}. These are plotted in figure 6.27.

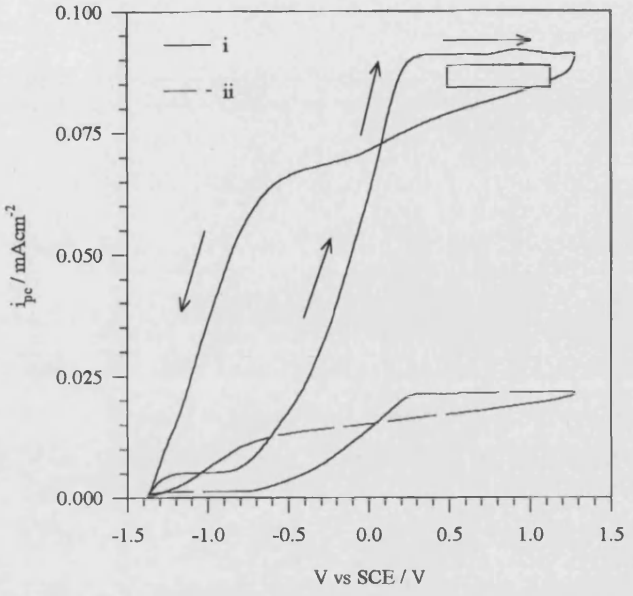

Figure 6.27. Localised photocurrent voltammograms measured using monochromatic light of λ=514 nm at regions i and ii labelled in figure 6.26 (a). Light "spot" diameter ≈ 6μm; f = 80 Hz.

(ii) Photoelectrochemical Microscopy

Figure 6.28 shows the (a) video and (b) photocurrent images obtained by the "direct detection" method for an anodically grown layer of CdS on Cd.

(a)

Figure 6.28. (a)Video and (b) photocurrent image of an anodised layer grown on Cd in 0.5 mol dm^{-3} Na_2S. Scan velocity = 17 cm/s (16 s per frame). Spot size = 2 μm.

The superior confocal imaging system and smaller spot size are responsible for the greatly enhanced resolution of the localised image. From this several features are immediately apparent from the image It appears that the photoresponse of the anodised layer maps the grain structure of the underlying substrate. Comparison of the photocurrent image with the video image shows that the photocurrent is highest on the darker grains, lower at the brighter grain, and virtually zero where grains of differing orientation meet. These results mirror those found using the lock-in detection technique, confirming that the responses obtained are not artefacts of the measuring system. The photocurrent intensity is also negligible in the dark regions or twins which traverse individual grains. Variations in image contrast are found to differ significantly between localised measurements made by the SMSC and PEM technique. With images detected by the lock-in method, the photoresponse appeared to map the underlying grain structure, whereas the direct method strongly identifies grain boundaries of the underlying substrate *as well as* the individual grains. To more consistently asses the difference in contrast between the two image acquisition modes, the signal detection

system in the PEM arrangement was modified to include the provision of a phase sensitive detector. In figure 6.29(a) the photocurrent response of the electrode was obtained using the direct detection mode of PEM. The corresponding lock-in image of the same surface is shown in figure 6.29(b).

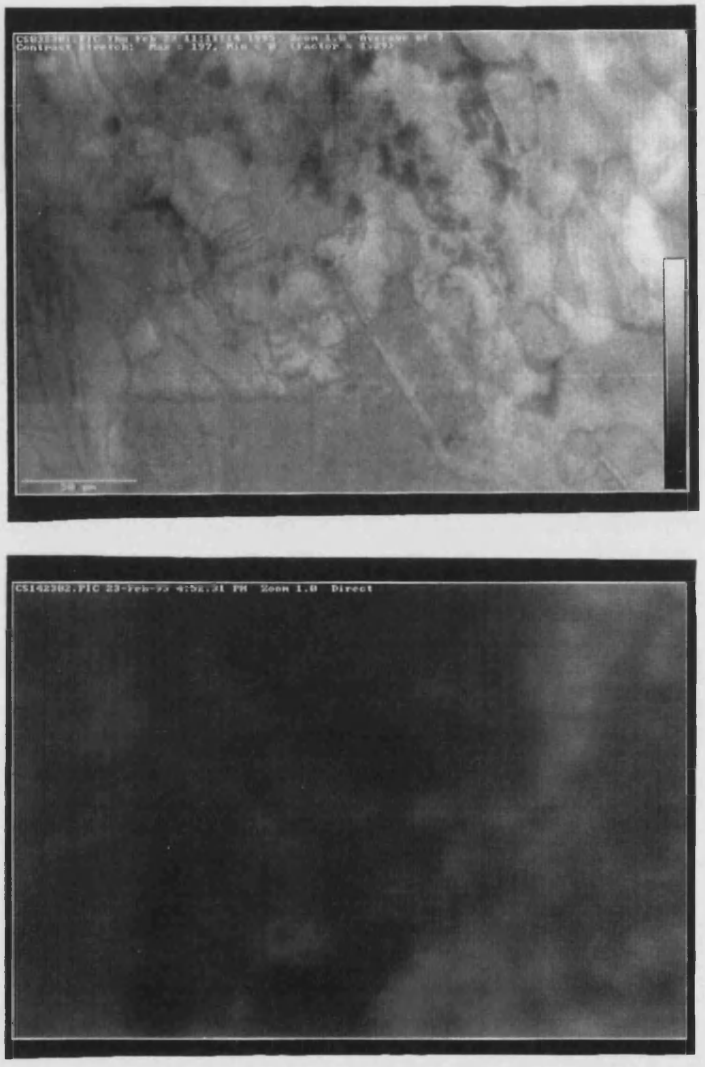

Figure 6.29. "Direct" and "lock-in" photocurrent images of Cd anodised in 0.5 mol dm^{-3} Na_2S at 0 mV dc bias. (a) Direct image with a scan velocity of 4.95 cm/s (2.9 s per frame). The scale bar on the right corresponds to the magnitude of the photocurrent where 2 μA (white) and 0 μA (black). (b) Lock-in image at 180 Hz and scan velocity of 4.95 cm/s (2.9s per frame). Pure white corresponds to 0.05 μA and black to 0 μA. Scale 10.5 mm =50 μm. In both cases spot size = 2 μm.

Comparison of the lock-in and direct detection images made on the PEM technique reveals the same trends. The only uncertainty in the comparison is that in the SMSC, the microscope stage is moved (step scan) whereas in PEM the beam is rastered across the surface (continuous scan). Finding similar features between the two images is not a

simple matter, but it appears that the bright patches in figure 3.29(b) correspond to the blurred grey regions in the direct image.

After illuminating the anodic film with the focused laser beam for half a minute or so, a permanent change in the localised photoresponse was observed. This is illustrated by the blackened rectangular area in figure 6.30.

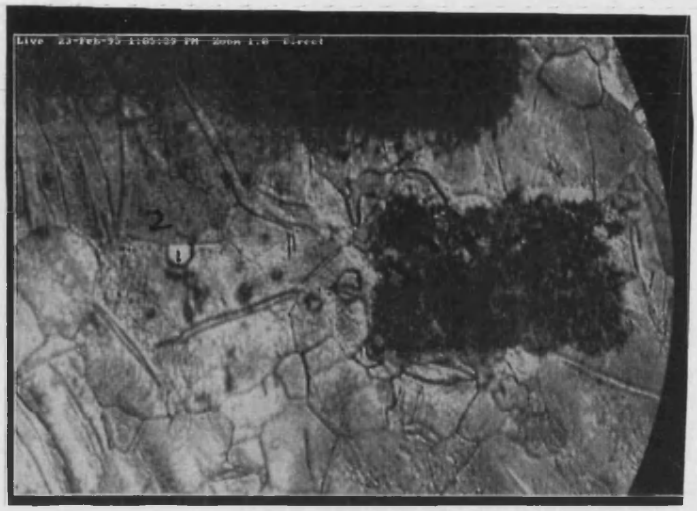

Figure 6.30. Video image of an area repetitively scanned by the incident laser beam for 1 minute. Scale 10.5 mm = 50 μm.

This "memory effect" depends on the length of previous illumination, the illumination intensity, and the bias during exposure. The memory effect was found to be accumulative and irreversible. Subsequent photocurrent images taken of a wider area including the blackened region showed zero photocurrent in the previously scanned area.

The localised photocurrent voltammograms for grains labelled (a) and (b) are plotted in figure 6.31

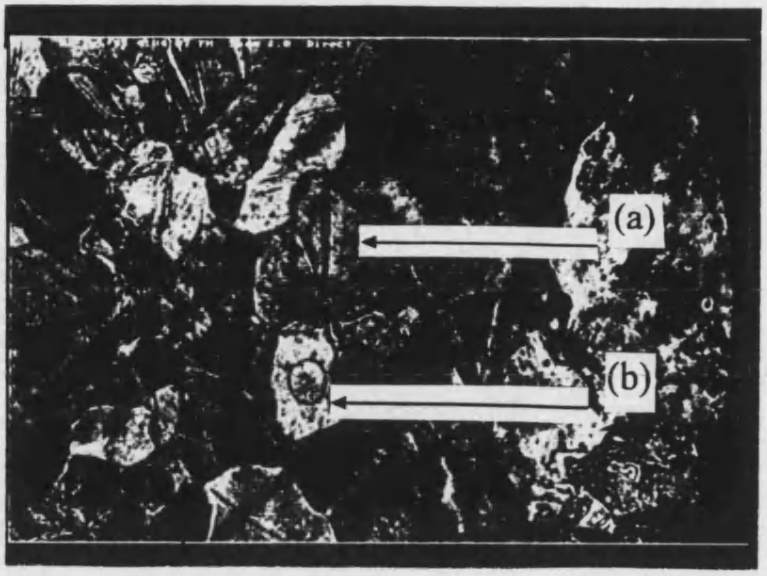

Figure 6.31. Video image of an anodised layer grown on Cd in 0.5 mol dm^{-3} Na_2S. Scale 1.5 cm =50 μm.

Due to the higher power of the laser used in the PEM investigations, the photocurrents obtained were considerably higher than those measured by SMSC. Photon fluxes striking the CdS/Cd surface in the PEM and SMSC techniques are $2.6x10^{12}$ and $6.4x10^{11}$ photons/s, respectively. The hysteresis observed between the forward and reverse scans is significantly larger than in the localised photocurrent voltammograms obtained by the SMSC technique, suggesting that a more drastic change in the surface has taken place between the scans. This is likely to be due to the higher beam residence time in the direct scan method which leads to increased photo- and possibly thermal- degradation of the photoactive layer.

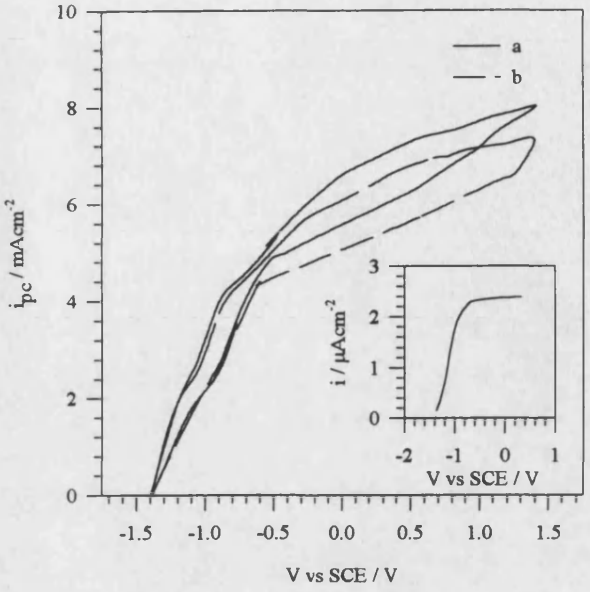

Figure 6.32. Localised photocurrent voltammograms measured using monochromatic light of λ=514 nm at regions (a) and (b) labelled in figure 3.32. Light spot diameter = 2 μm. The inset shows a photocurrent voltammogram for single crystal CdS (S-face) in 1.0 mol dm^{-3} Na_2SO_3 (λ=500 nm, f = 27 Hz).

The effect of dc bias on image contrast was also been examined, in particular the effects of recombination with increasing forwards bias. The images illustrated in figure 6.33 (i) to (viii) were obtained at -600 mV to +800 mV in 200 mV steps. Prior to recording the photocurrent image given in figure 6.33 (i), the electrode was held at -1400 mV for 30 s followed by scanning the potential at 100 mVs^{-1} to -600 mV. In each case the video image of the surface is given on the right hand side and corresponding photocurrent image on the left. The first image appears slightly blurred due to accidental vibration of the microscope stage. Several trends are immediately apparent. The images of greatest clarity have been obtained in the plateau region, but as the potential reaches the transpassive region the contrast drastically diminishes. Also, photocurrent enhancement seems to occur relatively uniformly across the entire electrode surface. As the dc bias increases, the contrast diminishes and features of the underlying substrate

(i)

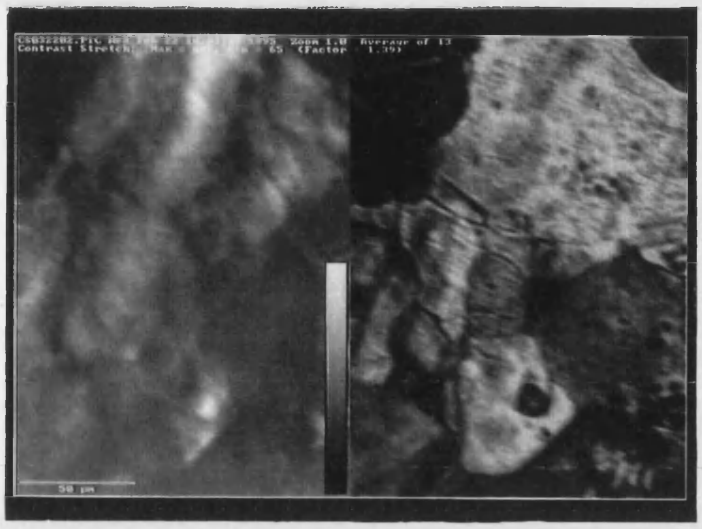

(ii)

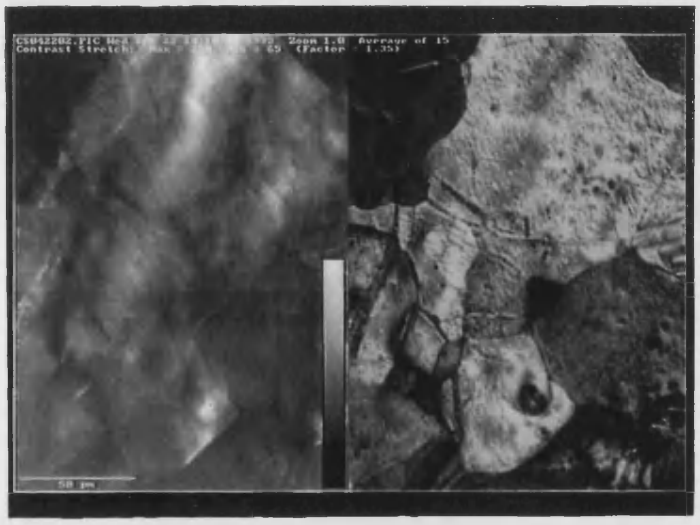

(iii)

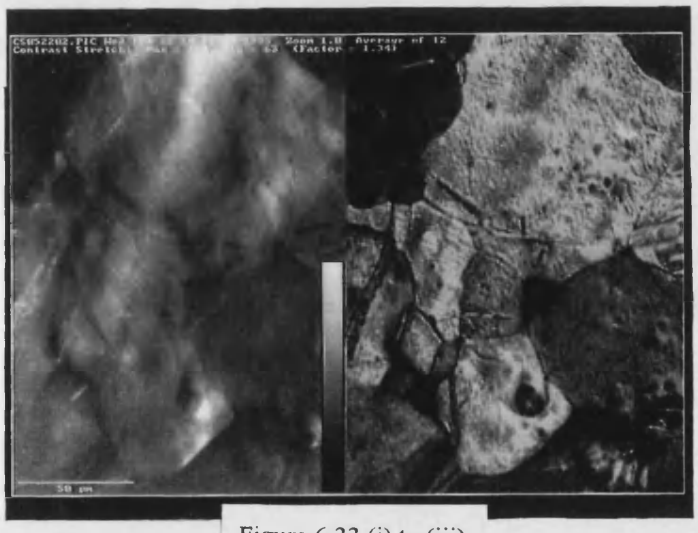

Figure 6.33 (i) to (iii)

(iv)

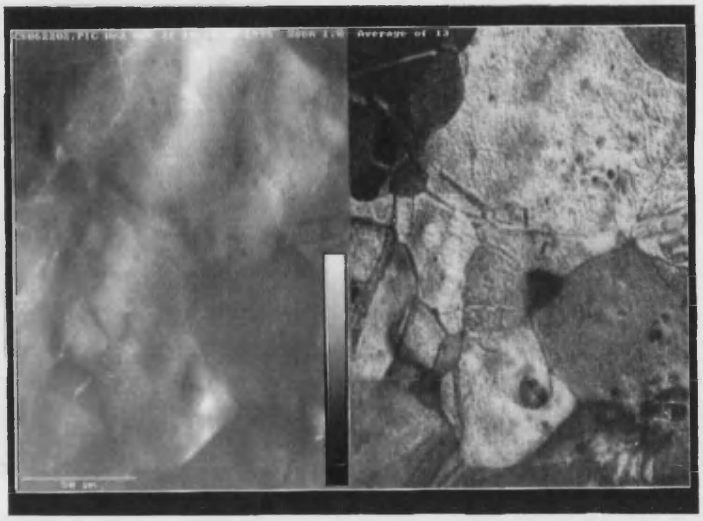

(v)

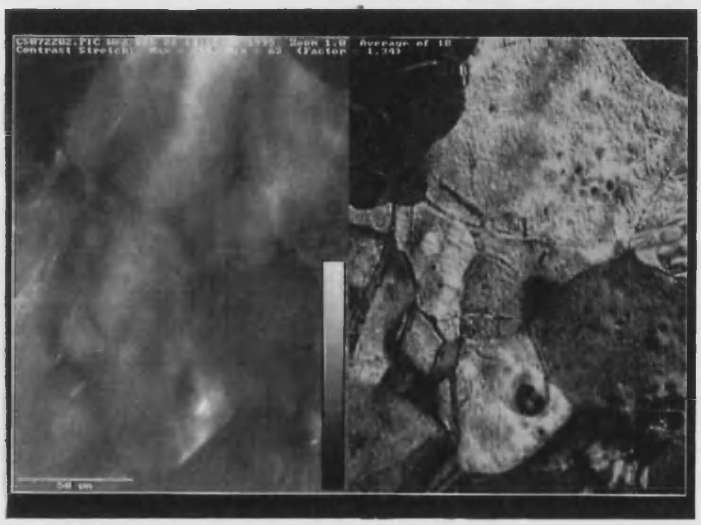

(vi)

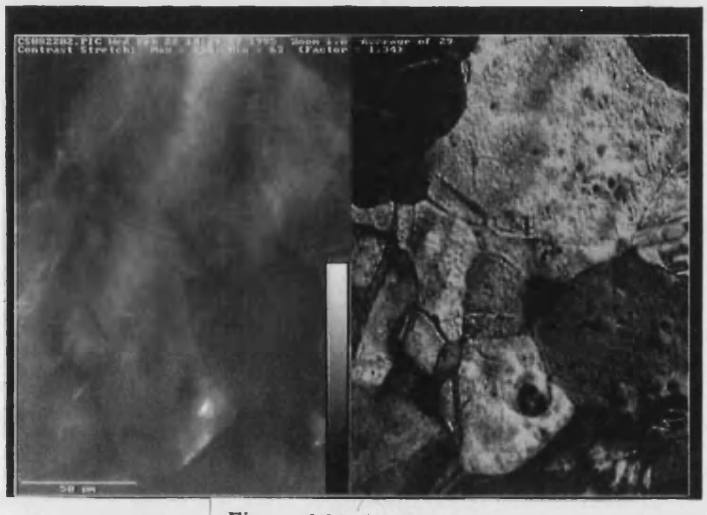

Figure 6.33 (iv) to (vi)

(vii)

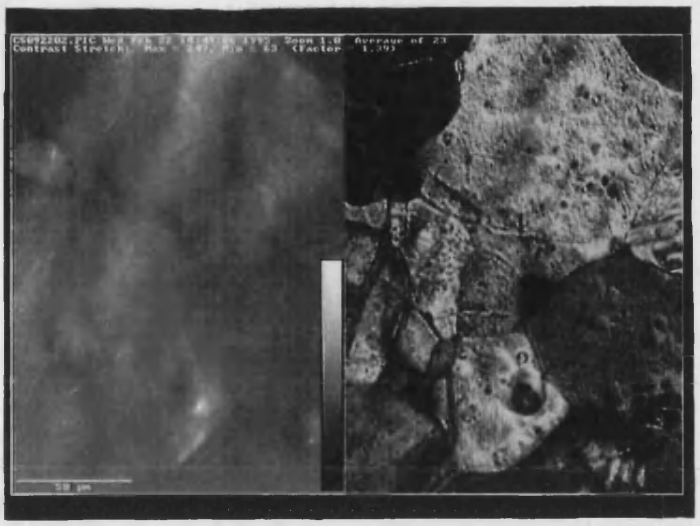

(viii)

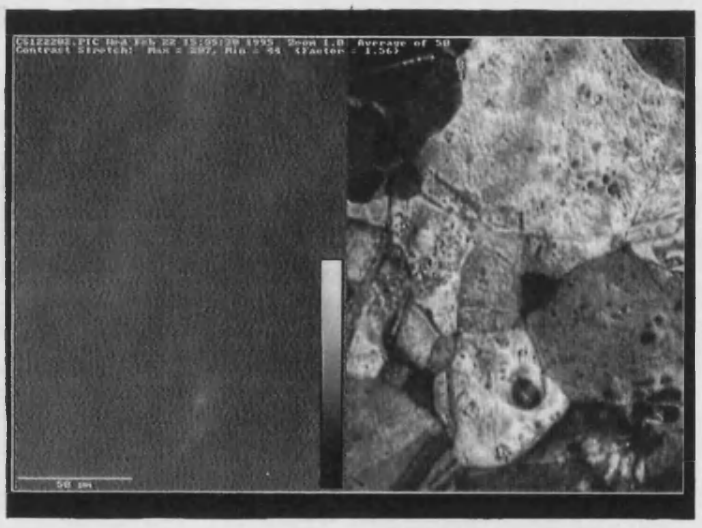

Figure 6.33 (i) to (viii). Photocurrent images of Cd anodised in 0.5 mol dm^{-3} Na_2S. Images were obtained at 200 mV intervals from -600 to +800 mV at a scan rate of 100 mVs^{-1}. Scan velocity 1.4 cm/s (5.3 s per frame). The scale bar on the right of the image corresponds to the magnitude of the photocurrent where 0.5 μA (white) and 0 μA (black). Light spot diameter = 2μm

becomes less apparent. This suggests the growth of a uniform and thick CdS layers across the electrode surface. At more positive potentials, rapid rates of film growth are accompanied by the formation of a porous and defective structure in which the photocurrent response is limited by enhanced recombination effects both in the bulk and at the surface of the film.

One feature which seems to remain in figure 6.33 (i) to (vii) is the diffuse white band that extends diagonally from the middle-top down towards the centre left of the photocurrent image. In the corresponding video image, these appear as dark patches that are slightly out of focus and were often observed randomly distributed across the electrode surface. Their photoresponse is unlikely to be associated with the initial stages of film formation, but rather with a precipitated and loosely adherent layer of CdS in electrical contact with the underlying substrate.

The resolution of the PEM images are sufficiently high that photocurrent distributions across individual twins within grains may be resolved. This is particularly well illustrated in figure 6.28(b). Across a single grain the photocurrent is relatively constant, though at twins a sharp reduction in the response is observed. As at grain boundaries, it is striking how sharp the photocurrent resolution at these regions are. Such features could not be resolved by the SMSC technique, however high the magnification.

6.4. Discussion

There are several possible explanations for the variations found in the image contrast across the surface. The first and most obvious is that the film thickness may vary between different grains, leading to a range of photogenerated charge carrier densities across the surface. If the film thickness is small compared to the penetration depth of the incident light ($1/\alpha$), the amount of light absorbed and thus the photocurrent will map the local thickness variations. The change in orientation from one grain to the next may alter the way in which CdS nucleates and grows at the film/solution interface. Parameters that are likely to affect the rate of film growth are the permeability of the film to ions and the crystallographic orientation of the substrate grains. It is difficult to accurately determine the thickness of the films deposited here due to the chemically formed layer of CdS on the electrode surface. According to the i-V curve in figure 6.2, film thicknesses should range from a few nm for image 6.33(i) to a few 100 nm for image 6.33(viii). The presence of a pre-existing CdS layer formed by corrosion will lead to underestimates of the total film thickness. The typical thickness of passivating layers are of the order of a few nm. For very thin films such as the oxide layers grown slowly (1 nm/min) on Ti by anodisation , heterogeneities in the photoresponse may often be due to variations in the metal substrate reflectivity due to surface crystallography. For example a completely reflecting surface could result in an oxide photoresponse twice that of an absorbing substrate surface. It appears from the images that for a series of grains of the same contrast, the photocurrent distribution is relatively uniform across the grain surface (ignoring any defects), suggesting a uniform coverage of CdS on individual grains.

For the majority of films grown here, their thickness is sufficient that the variations in contrast cannot be solely due to the incomplete absorption of light within the anodised layer. Instead some other mechanism is likely to be responsible, in

particular recombination of charge carriers. This will be an important process in determining the spatial variation in photocurrent and therefore contrast across the electrode surface. Recombination may occur at centres located either at the surface of the film or in the bulk of the deposit. For anodically grown CdS films, surface states are likely to include photocorrosion sites and loosely adherent clusters of CdS/S precipitates. Bulk states will originate from poorly crystalline CdS formed at grain boundaries. The contribution that these states make to the observed photocurrent response is determined by the band bending ($E - E_{fb}$). At potentials far from flatband the band bending is high and the space charge layers extends a significant distance across the width of the film. The electric field suppresses recombination in both bulk and surface states by promoting charge carrier separation. This effect is particularly enhanced at high field strengths found close to the electrode surface. At potentials close to flatband the space charge layer only extends a short distance away from the electrode surface. Charge carriers generated outside this region are therefore able to combine without producing a photocurrent, in which case the photocurrent is dominated by recombination effects. However, the difficulty is in precisely relating in these phenomena to variation in image contrast. For this reason, a number of contrast mechanisms are suggested in the following discussion.

The images recorded by PEM and SMSC techniques have highlighted the strong correlation between photocurrent intensity and different crystallographic features of the substrate surface. Of particular interest is the influence different structural features have on promoting the growth of CdS. During the early stages of anodisation, a particularly defective layer of CdS is formed to accommodate the large lattice mismatch between Cd (2.46 Å) and CdS (4.13 Å). As the film thickens the influence of the substrate becomes less important and the crystallinity of the CdS layer improves. However, at each grain

the photocurrent intensity appears to be different. This suggests that either (i) at different grains the thickness of CdS varies or (ii) recombination rates differ across the electrode surface. The first case implies that growth occurs preferentially at grains of particular orientations. Smyrl *et al* [8] have reported the formation of monocrystalline TiO_2 layers on Ti which replicate some of the crystallographic orientation of the underlying substrate. However, based on the large lattice mismatch between Cd and CdS, the formation of monocrystalline CdS layers seems unlikely. In this work, what is more probable is that the grains revealed by the chemical etch, polish, and reveal procedure are not all polycrystalline but contain a variety of crystallographic defects. At these regions the growth of defective layers of CdS is expected in which recombination will dominate the photocurrent response. These will appear as dark grains in the photocurrent image. However, less defective grains promote the growth of more crystalline CdS with a lower defect density. The higher photocurrents at these regions are therefore represented by the brighter grains in the localised image.

Many of the photocurrent images recorded by PEM show the presence of individual bright centres or "hot spots" where the saturation in the photocurrent occurs. In figure 6.33 (v) the arc shaped grain at the far left centre of the video image shows a thicker pair of boundaries traversing surface at 30° to the vertical. In the corresponding photocurrent image a random distribution of photocurrent "hot spots" is evident which follow the length of the grain. However, between the two boundaries the photocurrent is considerably lower. Smyrl *et al* [34] have shown the existence of trapping states in the anodic oxide on Ti at positions corresponding to grain boundaries in the underlying metal. Based on the similar morphology of the Cd structure to Ti, it could be argued that similar states exists at the grain boundaries of CdS films. This introduced the interesting possibility that at the defective region between grains, the reduction in

photocurrent is associated with the trapping of photogenerated holes. If holes accumulate at the film surface forming a high density of surface charge, the bands will flatten and recombination will be greater diminishing the photocurrent in this region. It is suggested that these holes are subsequently able to react in a number of ways according to reactions 6.12 to 6.14. The localised precipitation of photoactive CdS (reaction 6.14) may explain the photocurrent "hot spots" surrounding the grain boundary regions.

A more diffuse range of photocurrent "hot spots" can be seen to extend diagonally across the electrode surface in the photocurrent image shown in figure 6.33(v). This layer appears to be superficial to the electrode surface and so is likely to be associated with a precipitated form of CdS rather than the underlying layer of CdS associated with the initial stages of anodisation. During the early stages of growth the film may be considered as having a two layer structure: an inner compact layer formed chemically by the dissolution of cadmium at the electrode surface and a more porous outer layer formed by anodisation of the metal surface, suggesting the dark band corresponds to a superficial layer of CdS formed by dissolution precipitation. The lack of any relation between the position of the band and structural features of the underlying substrate suggest the layer is poorly adherent. As the beam scans over the electrode surface, convection induced by localised heating may result in slight drift across the electrode surface. However, electrical contact must be maintained to the substrate as photocurrents have been observed. This suggest some equilibrium mechanism of film formation/dissolution across the electrode surface if slight drift of the layer is involved.

In both of the above observations the photocurrent "hot spots" can also arise from light scattering effects at the electrode surface. As the beam scans across the

electrode surface it is effectively defocused when it strikes a scattering centre such as that illustrated in figure 6.34.

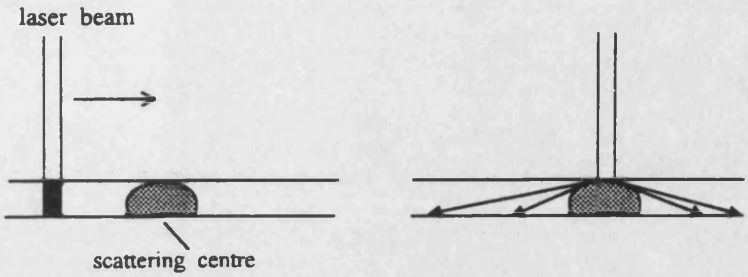

Figure 6.34. Effect of light scattering on illumination intensity at the surface of an electrode

At first it might seem that scattering should generally decrease the photocurrent response. However, the intensity (photons cm^2 s^{-1}) in the focused beam is much larger than in the scattered beam, even though the *total* photon flux (photons s^{-1}) is the same. At high light intensities the photocurrent no longer varies linearly with light intensity because second order recombination becomes dominant. Scattering therefore moves the response out of the sub-linear response and into the low intensity linear regime, so that the measured photocurrent actually increases. This is illustrated in figure 6.35.

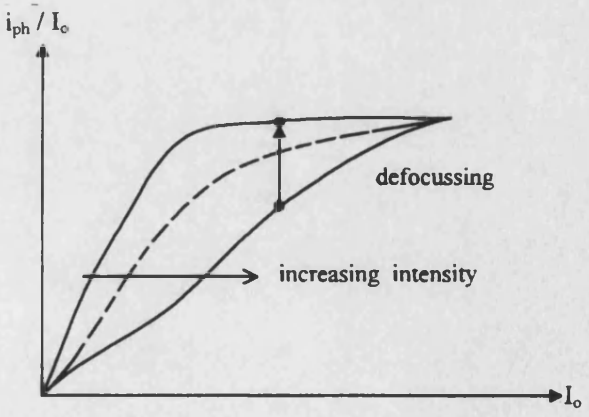

Figure 6.35. Schematic representation of the effect of laser defocusing on the photovoltage characteristics of an ideal single crystal CdS electrode

Comparing photocurrent images recorded in the monolayer and transpassive regimes reveals the position and intensity of the hot spots surrounding the arc-shaped grain at the far-left centre of images 6.33 (i) to (viii) are relatively unchanged. It was expected that for nodular films grown at high field strengths the effects of light scattering would be more predominant. These observations suggest that the most efficient centres originate from the growth of CdS at certain crystallographic features of the electrode surface.

Light scattering effects can also introduce variations in the illumination intensity as the beam strikes the electrode surface. For example, if the laser travels over neighbouring regions of smooth and nodular regions of CdS, the illumination intensity will vary as the beam is effectively focused and defocused over these areas at the electrode surface. Heller *et al* [35] have investigated the effect of varying light intensity on the photocurrent behaviour of etched and unetched single crystal CdS in a polysulfide electrolyte by flooding the surface of the crystal with a continuous laser beam whilst measuring the modulated component of the photocurrent produced by chopped illumination 100 W illumination. Spectra recorded for etched CdS showed a well defined saturation and little change following intense illumination by laser. However, for the unetched sample saturation was not observed and the photocurrent decreased rapidly to below the band edge. This is illustrated schematically in figure 6.36

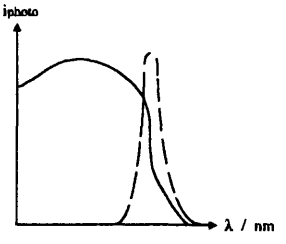

Figure 6.36 Effect of intense illumination on the photocurrent spectrum of unetched single crystal CdS in a polysulfide electrolyte. Both spectra were recorded under chopped illumination from a 100 W monochromatic light source. The dotted line shows the change in behaviour following intense illumination by laser (Reproduced from work by Heller *et al* [35])

The origin of this effect lies in the high density of surface traps which act as recombination centres at the etched electrode surface. If the carriers are not separated then at high levels of illumination the concentration of both minority and majority carriers rises sharply. This is accompanied by an increase in the rate of recombination which depresses the rate of photogeneration. In which case photocurrent efficiencies lower than expected are obtained. In terms of image contrast mechanisms this has two important effects: (i) At smooth regions across the electrode surface the beam is focused and the light intensity high. In which case the photoresponse is dominated by recombination effects at regions which contain a high density of traps. (ii) At centres where scattering is important the beam is effectively defocused and the illumination intensity reduced. Recombination becomes less important and saturation is observed when the rate of photogeneration equals the rate of recombination. In which case differences in contrast are more likely to reflect variations in scattering, films thickness, and reflectivity effects.

The photocurrent images obtained by the lock-in technique are quite different to the direct scan images. In the first case no information is revealed on the grain boundary structure of the electrode but rather the photocurrent contrast across the grains themselves. The origin for this lies in the frequency response of the parameters which have been shown to play a role in the contrast mechanism, i.e. g_1, G_1, and τ_1. Of particular interest is the relationship between the measuring frequency (ω) and the time constant ($1/\tau_{rec}$) associated with the rate of recombination (k_{rec}). At this point it is useful to use the IMPS signature illustrated in figure 6.37. to identify the regions over which contrast is observed.

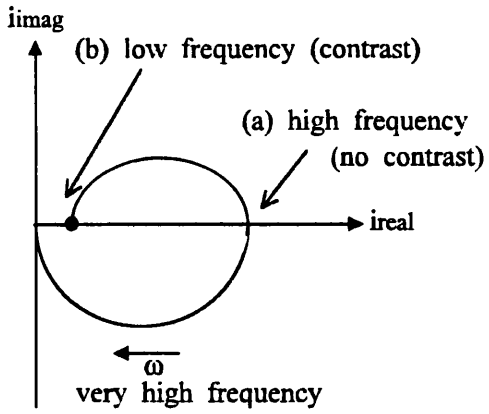

Figure 6.37. IMPS signature illustrating the relationship between measuring frequency (ω) and recombination rate (k_{rec}). Image contrast is only observed where $\omega < k_{rec}$.

In the upper loop which maps recombination, two situations may be identified: (i) At point (a) $\omega >> 1/\tau_{rec}$. The photocurrent is not attenuated in any way and shows no spatial variation across the electrode surface. The corresponding photocurrent image therefore shows no contrast. (b) $\omega < 1/\tau_{rec}$. Recombination effects can influence charge carrier generation. It $1/\tau_{rec}$ varies spatially across the electrode surface, contrast in the photocurrent image will be observed. It therefore follows that grain boundaries are not seen in the lock-in image because the modulation frequency is more rapid than the recombination rate, i.e. $\omega > k_{rec}$. This highlights one of the chief drawbacks of the step scan lock-in detection method, namely that only processes with time constants on the same scale of the frequency of modulation will be detected. For the case of non-modulated illumination, a much wider frequency spectrum is excited and detected. The gain in information is thus maximised as confirmed by the higher definition localised images recorded by the continuous scan direct detection method. However, due to the complex interplay between the parameters which determine image contrast, there is no single reason why differences in contrast are found between the lock-in and direct scan images.

The photocurrent images in figure 6.22 (b) and 6.26 (b) appear to have a "fuzziness" surrounding features which may be identified in the corresponding video image. This is especially evident in figure 6.22 (b). The step-wise reduction in photocurrent around a particular feature implies a transient decay in the response as the beam scans over the electrode surface at a rate dependent upon the relationship between the time constant of the lock-in amplifier (T_C) and the step scan frequency (ω_{step}). Figure 6.38 schematically illustrates the photocurrent time transients recorded for three equidistant points a, b, and c located across an electrode surface. At the same points the photocurrent is recorded by the framestore. If $T_C > \omega_{step}$, the photocurrent measured at a given point may include a contribution from the decaying signal associated with the previous point scanned. This is illustrated by the hatched area in figure 6.38 (i). In the corresponding photocurrent image this will lead to features with poorly defined or blurred edges. In figure 6.38 (ii), if $T_C < \omega_{step}$, the framestore only records a portion of the photocurrent transient and information relating to the photoresponse is lost. This will also lead to a reduction in image definition. Alternatively, by carefully matching the time constant of the lock-in amplifier to the step scan frequency, the entire i-t transient can be obtained. In which case sharp features in the photocurrent image are expected. This is illustrated in figure 6.38 (iii).

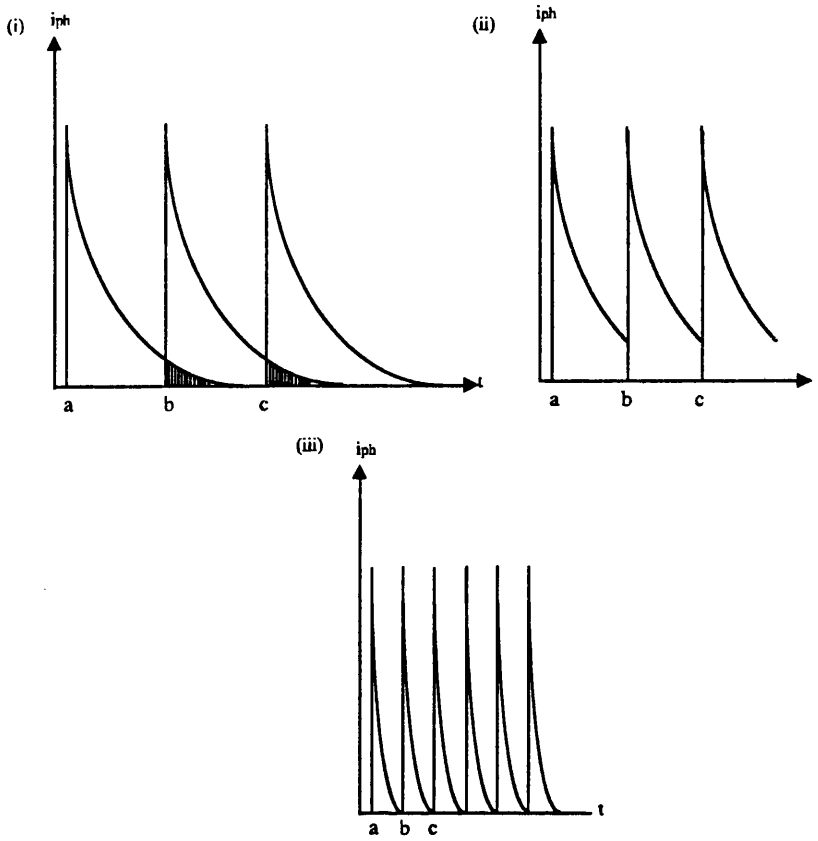

Figure 6.38. Schematic representation of photocurrent time transients recorded by lock-in detection at three equidistant points a, b, and c, across an electrode surface. (i) Overlapping transients with a low time constant, (ii) reduced time constant but same frequency as (i). (iii) Time constant matched to increased chopping frequency.

As the potential is varied, explanations for the changes in contrast observed in the sequence of images given in figure 6.33 (i) to (viii) are complicated by the fact that the film growth rate is not constant over the potentials at which the images were acquired. In a theoretical treatment of image contrast, the overall contrast would be determined by the bias dependent contribution of g_1, G_1, and τ_1. The decrease in the resolution appears to be quite gradual from 6.33 (i) to (vii), although a considerable reduction in image contrast is observed in image (viii). At the potential at which image (viii) was acquired, growth of CdS proceeds by the high field dissolution precipitation mechanism. The reduction in photocurrent and lack of image contrast suggests

extensive charge carrier recombination dominates the photoresponse in the porous defective layer.

The consequences of photo- and thermal degradation induced by illumination of the electrode surface have been illustrated in the video image in figure 6.30. It is probable that local dissolution of the anodised layer will result in immediate re-precipitation of CdS. If this layer is loosely adherent, it could appear dark in the corresponding photocurrent image if carrier collection rates are limited by poor electrical contact to the underlying substrate. Charge transfer will be further restricted if the resistivity is increased by the presence of excess S in the precipitated layer. Smyrl *et al* [34] have suggested that at anodically grown TiO_2 layers the most significant effect of beam damage is a reduction of the doping density, N_D, within the damaged oxide layer. If this is accompanied by the introduction of recombination centres, a reduction in photocurrent will be observed, even though the depletion layer width has increased.

Due to the high power of both laser sources used, the role of photocorrosion on the photocurrent response must be considered. Oxidation of CdS by photogenerated holes results in the formation of Cd^{2+} and S^{2-} ions. This process depends on the dc potential and thus band bending applied to the sample. Close to flat band the photocurrent response is dominated by recombination effects although the concentration of holes at the electrode surface is low. Conversely moving away from flat band potential in a positive direction the trend inverts. The band bending therefore determines the corrosion and recombination rates, both of which are important in image contrast mechanisms. In the following section a calculation is made to determine the effect the incident laser power has on photocorrosion of the anodised layer. It is assumed that the formation of CdS is a $2e^-$ process and that 100% of the incident light is absorbed by the

anodised layer. The charge required to deposit one monolayer of CdS in the hexagonal orientation is 230μC/cm^2.

(a) PEM

Laser power = 25 mW

Photon flux following beam attenuation by neutral density filters = 6.4x10^{12} photons s^{-1}

Beam diameter = 2 μm. Scattering effects at the rough electrode surface are likely to defocus the beam and thus increase its diameter. Estimating a two-fold increase in illumination area, the beam spot becomes 4 μm in diameter (area = 5.0x10^{-7} cm^2)

(i) *Local* photon flux = 6.4x10^{12} photons s^{-1} / 5.0x10^{-7} cm^2 = 1.3x10^{19} cm^2 s^{-1}

(ii) Local photocurrent produced, j_{photo} = 1.6x10^{-19} C x 1.3x10^{19} cm^2 s^{-1} = 2.05 Acm^{-2}

At these incredibly high currents, rapid dissolution of the CdS layer would be expected. However, it is important to consider that during illumination the layer continues to grow, not only by anodisation but also by reprecipitation of the products of photocorrosion. As the beam is not static but moves across the electrode surface, each point is illuminated for only a very short period of time (≈ 80 μs) compared with the duration over which the complete image is acquired (2.9 s per frame). The damaged region therefore has the opportunity to "repair" before the beam restrikes the same area. The extent of photocorrosion is strongly dependent on the duration the beam spends at a given point on the electrode surface, i.e. the beam residence time.

(iii) The beam residence time is determined by the spot diameter and its scan rate.

Beam residence time = spot diameter / scan speed

= 4x10^{-4} cm / 4.95 cm s^{-1} = 81 μs

(iv) The charge associated with photocorrsion is given by Q = it

Q = 2.05 Acm^{-2} x 81 μs = 166 μC/cm^2

This corresponds to less than 1 monolayer of CdS.

(b) SMSC

Summarising the same calculations for the conditions under which SMSC images were acquired:

Laser power = 10 mW

Photon flux following attenuation = 2.6×10^{11} photons s^{-1}

Beam diameter = 6 μm, estimated diameter due to scattering = 8 μm

Local photon flux = 1.3×10^{17} cm^2 s^{-1}; $j_{photo} = 0.02$ Acm^{-2}

Beam residence time between each step = 0.1 s

Q = 2069 $\mu C/cm^2$

Photocorrosion is therefore results in the dissolution of ≈ 9 monolayers or ≈ 4.5 nm of CdS at the electrode surface.

This comparison highlights the importance of photocorrosion following high intensity illumination of the electrode surface. Of particular concern are the very high rates of photocorrosion observed in the step-scan method. This may seem surprising as the laser power is significantly lower than the source of illumination used in the continuous scan technique. However, what is more important is the time the beam spends at every point across the electrode surface. The far longer times encountered in the step scan method will substantially increase the photon flux and rate of photocorrosion at the electrode surface. In which case, large changes in film structure are expected as reprecipitated CdS forms at the site of illumination. In the corresponding localised photocurrent image, the continuous perturbation of the film structure will introduce notable changes in both image contrast and resolution with time. This is likely to be one factor which contributes towards the poor resolution of SMSC

images. In PEM, the possibility of beam scanning at high rates limits the photon flux that reaches any point across the electrode surface. The corresponding rates of photocorrosion are therefore lower. Changes in image contrast across the electrode surface can therefore be more reliably associated with film structure rather than artefacts resulting from localised photodissolution. However, in this case photocorrsion rates are not negligible and it would be desirable to further limit film degradation by lowering the incident photon flux.

Damage of the electrode surface by repetitive scanning is therefore an important consideration in photocurrent contrast mechanisms. Photon fluxes should be used where sufficient contrast in the photocurrent image is obtained, but photocorrosion rates are negligible. This ensures the morphology and photoelectrochemical properties of the anodised layer remain constant between scans.

6.5 Conclusion

Preliminary photocurrent measurements made on CdS films grown anodically on Cd revealed that the photoresponse of the CdS layer is strongly influenced by the morphology of the underlying substrate. Following chemical etch and polish treatments of the Cd foils, scanning electron micrographs revealed a highly intricate surface morphology with a wide variety of crystallographic features. The highly defective nature of anodically grown CdS layers was confirmed by electrolyte electroreflectance measurements. Values of the broadening parameter were significantly higher than those obtained for single crystal CdS.

Localised photoelectrochemical measurements (Photoelectrochemical Microscopy (PEM) and Scanning Microscopy for Semiconductor Characterisation (SMSC)) revealed that the localised photocurrent response spatially maps the orientation of the underlying substrate. It was suggested that at grain boundaries and twins the photoresponse is dominated by recombination effects where the underlying substrate promotes the growth of a particularly defective form of CdS.

The variation in photocurrent intensity at different grains suggested that either (i) at different grains the thickness of CdS varies or (ii) recombination rates differ across the electrode surface. The first case corresponds to the preferential growth of CdS at grains of a particular orientation. An interesting study would be to use x-ray diffraction to determine if CdS layers grown on Cd were monocrystalline and whether they replicate the crystallographic orientation of the underlying substrate. The second case corresponds to the growth of poorly crystalline CdS at grains with differing crystallographic defects. Regions of low photocurrent may correspond to enhanced recombination rates. Localised intensity modulated photocurrent (IMPS) measurements

would reveal kinetic and mechanistic information on charge carrier recombination at regions across the electrode surface.

An assessment of the effect the incident laser power had on photocorrosion of the anodised layer revealed both techniques result in a significant rate of photodecomposition of the film surface. However, in the continuous scan method, the lower photon flux reaching the electrode surface suggests the effects of photocorrosion on image contrast are less severe.

In comparison with the step scan technique, image contrast and resolution is far superior in the direct scan method. In the first case only processes with time constants on the same scale of frequency modulation are detected whereas for the case of non-modulated illumination, a much wider frequency spectrum is excited and detected. The gain in information is thus maximised. The superior optics in the PEM technique will also contribute to the higher resolution of the localised images.

References

1 H. Gerisher, *J. Electroanal. Chem.*, **58**, 266 (1975)

2 B. Miller and A. Heller, *Nature*, **262**, 680 (1970)

3 L. M. Peter, *Electrochim. Acta*, **26**, 1076 (1978)

4 S. Dennison, *Electrochim. Acta*, **68**(16), 2695 (1996)

5 P. Salvador, A. M. Chaparro, B. Coll, M. Gonzalez, *Surface Sci.*, **296**, 160 (1996)

6 D. E. Williams, A. R. J. Kucernak, and R. Peat, *Faraday Discussions*, **94**, 149 (1992)

7 W. H. Smyrl, M. Kozlowski, LJ. Ananasoska, and R. Atanasoski, *Electrochim. Acta.*, **64**(12), 1766 (1989)

8 W. H. Smyrl, M. R. Kozlowski, P. S. Tyler, and R. T. Atanasoski, *Surface Sci.*, **194**, 505 (1988)

9 R. S. Hutton and D. E. Williams, *Electrochim. Acta*, **69**(5), 701 (1994)

10 P. Salvador, A. M. Chaparro, B. Coll, and M. Gonzalez, *Surface Science*, **296**, 960 (1996)

11 F. H. Pollak, C. E. Okeke, P. E. Vanier, and P. M. Raccah, *J. Appl. Phys.*, **49**(7), 4216 (1978)

12 R. S. Hutton and D. E. Williams, *J. Chem. Soc. Faraday Trans.*, **90**(2), 645 (1994)

13 A. M. Chaparro, P. Salvador, A. Mir, B. Coll, and V. Caselles, in *Proceedings of the 5th International Conference on Defect Recognition and Image Processing in Semiconductors and Devices, Santander*, 1994

14 M. A. Butler, *J. Electrochem. Soc.*, **161**, 2185 (1984)

15 D. E. Williams, R. Peat, A. R. J. Kucernak, *Electrochim. Acta*, **67**, 966 (1992)

16 U. Stander, H. H. Streblow, J. K. Dohrmann, *J. Phys. Chem.*, **85**, 477 (1981)

17 T. Yoshida, *J. Electrochem. Soc.*, **169**(8), 2656 (1992)

18 T. E. Furtak, D. C. Canfield, and B. A. Parkinson, *J. Appl. Phys.*, **51**, 6018 (1980)

19 S. U. Falk and A. J. Salkind, in Alkaline Storage Batteries. John Wiley, New York (1969)

[20] V. I. Birss and L. E. Kee, *J. Electrochem. Soc.*, **166**(10), 2097 (1986)

[21] L. M. Peter, *Electrochim. Acta*, **26**, 165 (1978)

[22] A. J. Arvia, S. B. Saidman, and J. R. Vilche, *Electrochim. Acta*, **62**(8), 1156 (1987)

[23] D. E. Williams, R. Peat, A. R. J. Kucernak, *Electrochim. Acta*, **68**(1), 57 (1996)

[24] L. M. Peter, *Chem. Rev.*, **90**, *756* (1990)

[25] M. W. Brieter and W. Vedder, *Electrochim. Acta*, **16**, 1405 (1968)

[26] N. Sato and M. Cohen, *J. Electrochem. Soc.*, **111**, 512 (1964)

[27] K. J. Vetter and J. W. Schultze, *J. Electroanal. Chem.*, **64**, 141 (1972)

[28] J. W. Schultze and J. W. Schultze, *Ber. Bunsenges. Phys. Chem.*, **75**, 470 (1971)

[29] S. R. Ray, II-VI Compounds, Chapter 6, Pergamon Press, Oxford (1969)

[30] J. P. Hirth and J. Lothe, Theory of Dislocations, 2nd Edn., John Wiley, New York (1982)

[31] M. E. Özsan, D. R. Johnson, M. Sadeghi, and D. Sivapathasundaram, 9th EUROCAD meeting, Zurich, 17-18 November 1994, p. 861

[32] R. E. Reed-Hill and R. Abbaschian in, Physical Metallurgy Principles, 6rd Edn., Chapter 17, PWS Publishing, Boston (1994).

[33] D. E. Aspnes, Surface Sci., 67, 418 (1976)

[34] W. H. Smyrl, C. Paik, M. R. Kozlowski, and P. S. Tyler, *J. Electrochem. Soc.*, **135**, 2385 (1988)

[35] A. Heller, K. C. Chang, and B. Miller, in *Proceedings of the conference on the electrochemistry and physics of semiconductor liquid interfaces under illumination*, Arlie, Virginia, May 3-5, p. 54, 1977